Reference Flux Linkage Selection and its Impact on Direct Torque Control Based Induction Motor Drive Performance

Amit Kumar Singh

Reference Flux Linkage Selection and its Impact on Direct Torque Control Based Induction Motor Drive Performance

A

Thesis Submitted

in Partial Fulfilment of the Requirements

for the Degree of

DOCTOR OF PHILOSOPHY

By

Amit Kumar Singh

Department of Electronics and Electrical Engineering

Indian Institute of Technology Guwahati

Guwahati - 781039, INDIA.

December, 2020

Certificate

This is to certify that the thesis entitled "**Reference Flux Linkage Selection and its Impact on Direct Torque Control Based Induction Motor Drive Performance**", submitted by **Amit Kumar Singh** (126102013), a research scholar in the *Department of Electronics & Electrical Engineering, Indian Institute of Technology Guwahati*, for the award of the degree of **Doctor of Philosophy**, has been carried out by him under my supervision and guidance. The thesis has fulfilled all requirements as per the regulations of the institute and in my opinion has reached the standard needed for submission. The results embodied in this thesis have not been submitted to any other University or Institute for the award of any degree or diploma.

Dated:

Guwahati.

Prof. Praveen Kumar
Dept. of Electronics and Electrical Engg.
Indian Institute of Technology Guwahati
Guwahati - 781039, Assam, India.

To

My supervisor

Prof. Praveen Kumar

for his guidance and inspiration

&

*My **family**, and **friends***

for their blessings, love and support

Acknowledgements

My doctoral dissertation would not have come to successful completion without the help of several people. I take this opportunity to express my sincere thankfulness to all of them. I would like to convey my acknowledgment to all of them who have provided help and guidance to complete my doctoral degree in the Department of Electronics and Electrical Engineering at the Indian Institute of Technology Guwahati, India.

I wish to express my deep sense of gratitude to my thesis supervisor, Prof. Praveen Kumar, for his excellent guidance, suggestions, and support. This thesis would not have been possible without his continuous guidance and support. I consider it as a pride and privilege to work with him. His patience, the freedom he provided me during the course of the project, along with his consistent encouragement, criticisms, and thorough planning, have aided a long way for the preparation of the present thesis. His true scientific spirit has helped me immensely to develop the quality of my research work. This achievement was possible only because of the strong support provided by him. I am very much thankful to him for transforming me from an unstructured form to a structured form in every aspect of my life and showing me a different path of life. Whatever knowledge I have gained during my research period, that is just because of him. Thank you very much, sir, for your exceptional help and support.

I would like to extend my profound sense of gratitude to my doctoral committee members Prof. Praveen Tripathy, Prof. Sisir Kumar Nayak, and Prof. A. Ravindranath for thorough inspiration and valuable suggestions. I am also grateful to faculty members and the office staff (Mr. Mukut Baruah) members of the Department of Electronics and Electrical Engineering, IIT Guwahati, for their kind cooperation in all respects. I thank specially to Mr. Dimpul, Mr. Bharali, Mr. Sanjib, Mr. Sonowal, and Mr. Sarma for providing the necessary lab facilities required for the research work.

My sincere thanks go to my colleagues Dr. C. Upendra Reddy and Dr. Kashyap Kumar Prabhakar, for their continued support and encouragement throughout the thesis work. I have the best memories of my early days at the institute with my friends Dr. Ankit Dalal, Mr. Gautam Rituraj, Dr. Mridul Kanti Malakar, Dr. Brijesh Kumar Kushwaha, Dr. Venkata Ramana Kasi, Mr. Umesh Chaudhary, Dr. Rakesh Roy, Mr. Rajendra Kumar, and Mr. Bikash Sah. I am very much thankful to my colleagues and friends for their ungrudging help and sympathetic encouragement.

No research is possible without financial support; I acknowledge the Ministry of Human Resource Development (MHRD) for fellowship under QIP category for the three years of the Ph.D. program.

The stay at this place also allowed me to know the rich diversity of the north-eastern states.

I want to extend my gratitude to the entire fraternity and staff of Sikkim Manipal Institute of Technology (SMIT) for their blessings, which made my path of success.

Finally, I want to convey my sincere gratitude to my parents and family members for their sustained help and encouragement in my personal and academic ventures. I feel proud and blessed to have such beloved parents, my father, Mr. Shambhu Singh, and my mother, Mrs. Urmila Singh, and family members; my younger brother Mr. Arun Kumar Singh, my wife Mrs. Menka Singh, my son Master Viraj Singh and my little princess Aaradhya Singh. I promise I shall never forget their uncountable help and encouragement during the journey of my life. Today, I am in this position that is just because of my family members. I do not find words to express my gratitude towards them, and they are always in my heart. I feel deeply indebted to them for whatever I have accomplished so far.

(Amit Kumar Singh)

Abstract

In recent years, the rise in developing nations' economic activities has resulted in the rapid expansion of cities. This expansion of cities has emanated an increase in vehicular traffic, which has lead to deterioration in air quality. Air quality deterioration is mainly because of the emission from internal combustion engine vehicles, which shared nearly 20-25% of the total air pollution. To address the problem of unprecedented air pollution caused by the internal combustion engine-based vehicle, governments worldwide have launched various programs, policies, and incentives to increase penetration of vehicles that are not fossil fuel-based. One of the acceptable solutions is to shift electricity-based transportation, i.e., adaptation of electric vehicles (EVs). The major challenge in the faster adoption of EVs is to develop affordable electric vehicles that fulfill the need of the market and mass users. One possible way to accomplish these targets is to develop an efficient and low-cost drivetrain, apart from high-capacity batteries, in a short span of time. To develop an EV drivetrain in reduce time, it is essential to adapt the available speed control methods proposed for industrial applications to modify for use in electric vehicles. In this thesis work, such an adaptation is presented for an EV drive with direct torque control (DTC) of induction motor (IM).

The EV drivetrains' primary subsystems are the battery, power converters, electric motor, and its controller. Of which the electric motor is one of the main subsystems of the EV drivetrains. The electric motor employed in the EV applications should have high torque and power densities and high efficiency over a wide range of operations. Thus rare earth permanent magnet (PM) motors have suited well in all these parameters. However, the rare-earth PM's price has increased over the past years; consequently, the PM motors are more expensive. Hence, it is essential to choose a suitable motor that is robust in construction and less expensive than PM motors. Therefore, in the recent past, the research work has gradually shifted towards magnet-less motors, which have performance characteristics similar to PM motors. Thus, the low-cost and rugged IMs have become a possible alternative for EV applications, and therefore, IM-based drive is considered in this thesis.

The IM's speed control for an EV application is challenging due to the wide range of operations and varying load conditions that the EVs practice during driving. Therefore, in the context of EV applications, a high-performance controller is essential for the IM drivetrain. The high dynamic performance of an IM is achieved by independently controlling the torque and flux linkages. The

field-oriented control (FOC) and direct torque control (DTC) strategies for the IM are best suited for a dynamic and wide speed range of operation. The DTC method gives a quick dynamic response compared to the FOC method. Furthermore, the DTC scheme's implementation is simple and does not demand any coordinate transformations and pulse width modulation techniques compared to the FOC strategy. Thus, in this thesis, the DTC-based IM drive is considered due to its simple control structure and competence to provide a high dynamic response.

Despite these advantages, DTC has some challenges like high torque ripple, higher inverter loss, high distortion in voltage, current waveform, variable switching frequency, and required low sampling time. Several modified DTC techniques have been proposed in the literature to improve the performance by either changing the switching strategy or modifying its basic structure. Moreover, the determination of optimal reference flux linkage (λ_s^*) over a wide range of speed operations is also challenging for DTC-based IM drive. It has a significant impact on drive performance. Therefore, in the thesis, the impact of λ_s^* on DTC-based IM drive is described.

In the DTC strategy, the λ_s^* also significantly impacts its performance. There are three basic methods for selecting λ_s^* for the IM drive system. Namely, variable flux control as a reference torque's function, loss model-based flux controller, and flux search controller based on minimum loss/minimum input power/minimum stator current. These methods give an acceptable solution for narrow speed and torque ranges, which is not favorable in EVs. In EV applications, the drive has to run over a wide operating range based on the vehicle driving cycles, which they regularly practice on the road. Moreover, it is found that the value of λ_s^* significantly impacts the DTC performance and plays an important role in improving the efficiency of the drivetrain. However, it is seen that there is no generalized accepted method for determining the λ_s^* value. It depends on individual applications.

Thus, in this thesis, the implementation of speed control DTC-based IM drive over a wide speed range is demonstrated. For the successful implementation of DTC based IM drive over a wide range of speed and torque, two methods are proposed for the selection of suitable λ_s^*:

1. Determination of λ_s^* using a Finite Element Analysis (FEA) based IM model.
2. Determination of λ_s^* using a non-linear equivalent circuit model of IM.

In the first work, the determination of λ_s^* is achieved using an FEA-based IM model. The FEA-based IM model is developed on the ANSYS Maxwell platform. The winding scheme and lamination designs of the motor are required to obtain an FEA-based IM model. The simulations are carried out with variations in motor speed (N_r), stator voltage (V_s), and stator voltage frequency (f_s). The FEA simulation's primary objective is to obtain suitable values of λ_s and T_e in lookup tables (LUTs)

format over a wide speed range. The obtained LUTs provide information about the suitable λ_s^* at required N_r and given T_e in context to the DTC strategy, with current and voltage constraints over a wide operating range. However, this method required a pre-knowledge about the motor's geometry, i.e., winding scheme, slot dimensions details, and lamination designs, to develop an FEA model of IM, which helps obtain accurate values of reference flux linkage in LUT format. This limitation is overthrown if a non-linear equivalent circuit model of IM will be developed and used.

Therefore, in the second work, the selection of λ_s^* is determined using a non-linear equivalent circuit model of IM. The no-load test, blocked rotor test, and non-linear magnetization curve test of the IM was performed to obtain equivalent circuit parameters. The non-linear magnetization curve has been plotted, and the dependency of magnetizing inductance (L_m) with magnetizing current (i_m) is determined. Thus, the obtained non-linear equivalent circuit model of IM with varying L_m has been used to determine the λ_s^* in LUT format.

Both these methods calculate λ_s^*, considering the reference speed, required torque, and given DC voltage. Moreover, the magnetic saturation effect is also considered while calculating an appropriate λ_s^* value. Finally, the two driving cycles, namely, the New York City Cycle (NYCC) and New European Driving Cycle (NEDC), are presented in this work to demonstrate the proposed method's suitability over a wide speed and torque range of operations for EV applications. The proposed method's performance evaluation over a wide operating range with the vehicle driving cycles (i.e., NYCC and NEDC) is carried out on the laboratory's developed experimental setup. Further, to check the robustness of the proposed methods, (i) the parameter sensitivity analysis is performed, and (ii) the comparative analysis of the proposed methods with other existing techniques is demonstrated, and experimental results are presented. The dynamic and steady-state responses for the considered cases are demonstrated, and it is observed that the proposed methods have fewer torque ripples. Besides, the input energy consumption and efficiency analysis of the considered vehicle driving cycles are also presented. The experimental observations show that the proposed methods yield improvement in drive efficiency with minimal input energy consumption. The proposed method is made acceptable for EV application with few modifications in the DTC algorithm.

Moreover, the second proposed technique (non-linear equivalent circuit model-based) is simple and does not require complex mathematical equations to determine λ_s^* values in the LUT format. It does not demand base speed calculation, which in general depends on the dc-link voltage, motor current, motor flux linkage, and machine parameters. The second proposed method presented in this thesis overcomes the drawback of the first proposed method (FEA-based approach).

CONTENTS

LIST OF FIGURES

भारतीय प्रौद्योगिकी संस्थान गुवाहाटी
Indian Institute of Technology Guwahati

LIST OF TABLES

NOMENCLATURE

Abbreviations

AC	Alternating current
A/D	Analog to digital conversion
ANN	Artificial neural network
AFO	Adaptive full order
AVV	Active voltage vector
B-EMF	Back electro motive force
D/A	Digital to analog conversion
DC	Direct current
DRFOC	Direct rotor flux field oriented control
DSP	Digital signal processor
DTC	Direct torque control
DTFC	Direct torque and flux control
EM	Electric motor
EMF	Electromagnetic force
EV	Electric vehicle
FOC	Field oriented control
FPGA	Field programmable gate array
HC	Hysteresis control
IM	Induction motor
IDRFOC	Indirect rotor flux field oriented control
IC	Internal combustion
MPC	Model predictive control
NEDC	New European drive cycle
NYCC	New York city drive cycle

PC	Personal computer
PM	Permanent magnet
PI	Proportional-integral
PWM	Pulse width modulation
RFOC	Rotor flux field oriented control
rpm	Revolutions per minute
RTI	Real time interface
SMC	Sliding mode control
SMO	Sliding mode observer
SPWM	Sinusoidal pulse width modulation
SRM	Switched reluctance motor
SyRl	Synchronous reluctance motor
ST	Switching table
SV	Space vector
SVM	Space vector modulation
SVM-DTC	Space vector modulation direct torque control
SVPWM	Space vector pulse width modulation
T	Time in seconds
VSI	Voltage source inverter

MATHEMATICAL NOTATIONS

f_s	stator voltage frequency.
$i_{Rs}\ i_{Ys}\ i_{Bs}$; $i_{Rr}\ i_{Yr}\ i_{Br}$	are the three-phase stator and rotor currents, respectively.
$\bar{i}_{\alpha\beta r}$	stationary two-phase rotor current in complex vector notation; i.e., $\bar{i}_{\alpha\beta r} = i_{\alpha r} + j\, i_{\beta r}$.
$\bar{i}_{\alpha\beta s}$	stationary two-phase stator current in complex vector notation; i.e., $\bar{i}_{\alpha\beta s} = i_{\alpha s} + j\, i_{\beta s}$.
$\bar{i}_{dqr}$	synchronously rotating rotor current in complex vector notation; i.e., $\bar{i}_{dqr} = i_{dr} + j\, i_{qr}$.
$\bar{i}_{dqs}$	synchronously rotating stator current in complex vector notation; i.e., $\bar{i}_{dqs} = i_{ds} + j\, i_{qs}$.
j	vector rotator (or) imaginary component.
k_p	proportional constant.
k_i	integral constant.
L_{lr}	rotor leakage inductance.
L_{ls}	stator leakage inductance.
L_m	magnetizing inductance.
L_r	rotor self inductance, $L_r = L_{lr} + L_m$.
L_r	stator self inductance, $L_s = L_{ls} + L_m$.
N_r	measured speed in rpm.
N_{ref} or N_r^*	reference speed in rpm.
N_{err}	error in speed rpm.
P_p	pole pairs.
R_s	stator resistance.
RYB	notation of three-phases.
R_r	rotor resistance.

S	slip of induction motor.
S_a , S_b , S_c	are the switching signals.
T_{act} , T_e	electromagnetic torque.
$\mathrm{T_{err}}$	relative torque error.
T_{ref} or T_e^*	reference torque.
TL	load torque.
V_{dc}	dc-link voltage.
v_{Rs} v_{Ys} v_{Bs}; v_{Rr} v_{Yr} v_{Br}	are the three-phase stator and rotor voltages, respectively.
$\overline{v}_{\alpha\beta r}$	stationary two-phase rotor voltage in complex vector notation; i.e., $\overline{v}_{\alpha\beta r} = v_{\alpha r} + j\,v_{\beta r}$.
$\overline{v}_{\alpha\beta s}$	stationary two-phase stator voltage in complex vector notation; i.e., $\overline{v}_{\alpha\beta s} = v_{\alpha s} + j\,v_{\beta s}$.
$\overline{v}_{dqr}$	synchronously rotating rotor voltage in complex vector notation; i.e., $\overline{v}_{dqr} = v_{dr} + j\,v_{qr}$.
$\overline{v}_{dqs}$	synchronously rotating stator voltage in complex vector notation; i.e., $\overline{v}_{dqs} = v_{ds} + j\,v_{qs}$.
λ_{Rs} λ_{Ys} λ_{Bs}; λ_{Rr} λ_{Yr} λ_{Br}	are the three-phase stator and rotor currents, respectively.
$\overline{\lambda}_{\alpha\beta r}$	stationary two-phase rotor flux linkage in complex vector notation; i.e., $\overline{\lambda}_{\alpha\beta r} = \lambda_{\alpha r} + j\,\lambda_{\beta r}$.
$\overline{\lambda}_{\alpha\beta s}$	stationary two-phase stator flux linkage in complex vector notation; i.e., $\overline{\lambda}_{\alpha\beta s} = \lambda_{\alpha s} + j\,\lambda_{\beta s}$.
$\overline{\lambda}_{dqr}$	synchronously rotating rotor flux linkage in complex vector notation; i.e., $\overline{\lambda}_{dqr} = \lambda_{dr} + j\,\lambda_{qr}$.
$\overline{\lambda}_{dqs}$	synchronously rotating stator flux linkage in complex vector notation; i.e., $\overline{\lambda}_{dqs} = \lambda_{ds} + j\,\lambda_{qs}$.
λ_s^*	reference stator flux linkage magnitude.
λ_s	stator flux linkage magnitude.
σ	leakage or coupling factor, $\sigma = 1 - \dfrac{L_m^2}{L_s L_r}$.
σ_{srm}	constant factor, $\sigma_{srm} = L_s L_r - L_m^2$.
σ_{T_e}	standard deviation.
τ_r	rotor time constant; $\dfrac{L_r}{R_r}$.

τ_s	stator time constant; $\frac{L_s}{R_s}$.
θ_e	synchronous angle between αs and ds (elec. rad.)
θ_s	stator flux linkage angle (elec. rad.) i.e., $\theta_s = \arctan \frac{\lambda_{\beta s}}{\lambda_{\alpha s}}$
θ_r	rotor flux angle (elec. rad.) i.e., $\theta_r = \arctan \frac{\lambda_{\beta r}}{\lambda_{\alpha r}}$
ω_e	synchronous speed (rad./s)
ω_r	rotor speed (rad./s)
ω_{sl}	motor slip speed (rad./s)
γ	angle between $\overline{\lambda}_s$ and $\overline{\lambda}_r$.
ΔT , Δt	sampling time.
ΔT_e	torque error band width.
$\Delta \lambda_s$	flux error band width.
$\otimes$	cross product.
$\odot$	dot product.
$\mathbf{I_{2\times 2}}$	an identity matrix; i.e., $\begin{bmatrix} 1 & 0 \\ 0 & 1 \end{bmatrix}$
$\mathbf{J_{2\times 2}}$	a rotational matrix; i.e., $\begin{bmatrix} 0 & -1 \\ 1 & 0 \end{bmatrix}$

Subscripts

ds , qs	denotes d-axis and q-axis of stator quantities in rotating reference frame.
dr , qr	denotes d-axis and q-axis of rotor quantities in rotating reference frame.
i, j	denotes integers vary from 1 to 4
αs , βs	denotes α-axis and β-axis of stator quantities in stationary reference frame.
αr , βr	denotes α-axis and β-axis of rotor quantities in stationary reference frame.

xr , yr	denotes x-axis and y-axis of rotor quantities in rotor rotating reference frame.

Superscripts

T	denotes transpose.
$*$	denotes a commanded or reference quantity.
$-$	denotes a vector.
$\sim$	denotes an error (reference - adjustable).
$\cdot$	denotes a differential operator.

CHAPTER 1

INTRODUCTION

1.1 Research Background

In recent years, the rise in developing nations' economic activities has resulted in the rapid expansion of cities [1]. This expansion of cities has emanated an increase in vehicular traffic, which has lead to deterioration in air quality. The deteriorated air quality had become a major concern around the world, and more specifically, in India. As per the World Health Organization (WHO) report, 37 Indian cities are listed as the most polluted cities [2]. The air pollution in these Indian cities is mainly because of the emission from the internal combustion engine (ICE) vehicles, which shared nearly 20-25% of the total air pollution in these cities [1]. To address the problem of unprecedented air pollution caused by the ICE-based vehicle, governments worldwide have launched various programs, policies, and incentives to increase penetration of vehicles that are not fossil fuel-based [3–8]. One of the acceptable solutions is to shift electricity-based transportation, i.e., adaptation of electric vehicles (EVs). The EVs ensure emission-free transportation, and it is efficient and environment friendliness. Thus, EVs will have the potential to have a significant impact on transportation, the environment, energy, new industry creation, and overall economic development.

For the rapid transition from ICE-based vehicles to EVs by 2030 [7, 9], India's government has reformed its policies, incentives, and support for research and development programs in academics, industry, and start-up initiatives. Therefore, the R & D's activities in academics and the automotive industries have boosted to meet the rise in demand for EVs. The major challenge in the faster adoption of EVs is to develop affordable EVs that fulfill the need of the market and mass users. One possible way to accomplish these targets is to develop an efficient and low-cost drivetrain, apart from high capacity batteries.

The EV drivetrains' primary subsystems are the battery, power converters, electric motor (EM), and its controller. Of which, EM is one of the main subsystems of the EV drivetrains. The EM employed in the EV applications should have high torque and power densities and high efficiency over a wide range of operations [10, 11]. Hence, rare-earth permanent magnet (PM) motors are preferred in EV applications as they are very well suited to all these parameters. However, the rare-earth PM's price has increased over the past years; consequently, the PM motors are more expensive [12]. Fig. 1.1 shows the rise in the magnet price over the past ten years. Of which, NdFeBDy (NH42SH) is mostly used for electric motors [13, 14]. Therefore, in the recent past, the research work

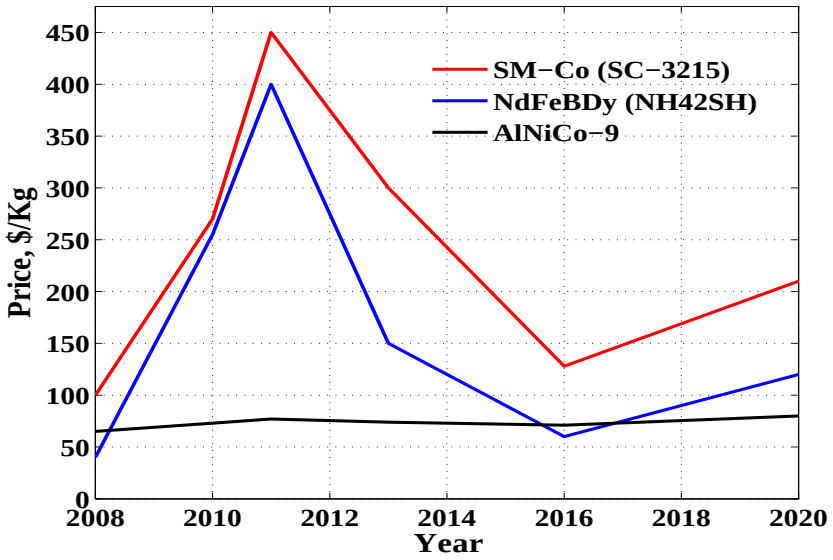

Fig. 1.1: Magnets price over the last ten years. These data are extracted from the report [13,14]. The magnets price for the year 2020 are projected values.

has gradually shifted towards magnet-less motors, which have performance characteristics similar to PM motors [15], such as induction motors (IMs), and switch reluctance motors (SRMs) [12]. It is essential to choose a suitable motor that is robust in construction and less expensive than PM motors. However, in industrial applications, drive operations are mostly predictable, which is not the case in electric vehicles. In EV applications, the drive operations are over the wide range of speed and with variable load conditions. Most EVs are used in the city areas where frequency start and stops, quick acceleration and deceleration, and low-speed operation are needed [16]. Thus, the challenge is to adapt the available speed control methods proposed for industrial applications to modify for use in EVs. From the above discussion, it is understood that the EV drivetrain should have the following features:

- Reliable,

- Maintenance-free,
- Low cost,
- Efficient over a wide speed range.

The literature review is carried out and discussed in the next subsequent section based on the above goals.

1.2 Literature Review

The classification of electric motors for EV applications is depicted in Fig. 1.2. The DC motors

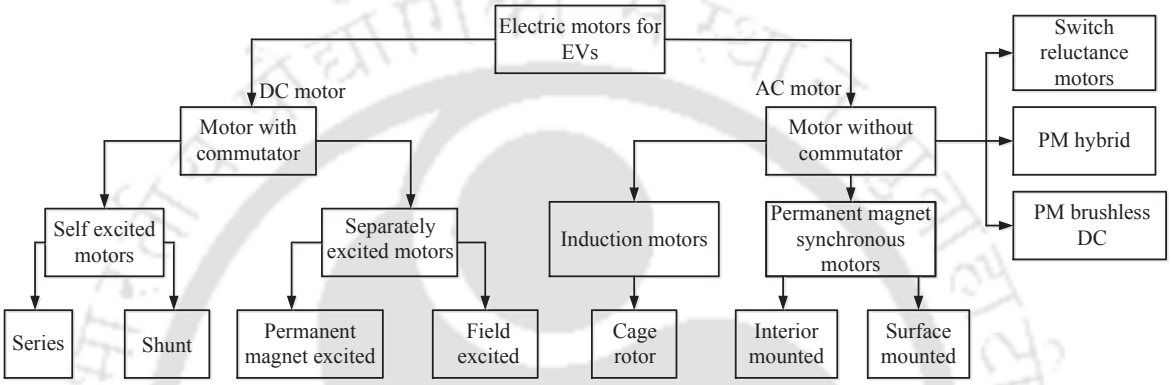

Fig. 1.2: Electric motor's classification for EV applications.

have well suited for electric propulsion because of their torque-speed characteristic and simple speed control methods. However, the DC motor requires regular maintenance because of the commutator segment [17]. The SRMs can be a possible option due to their low cost. However, the SRMs have some demerits like high torque ripple, high peak currents, and electromagnetic interference problems at high switching frequency [18]. The PM brushless dc motor may be the right choice for electric propulsion. However, at very high-speed, the system efficiency drops, and PM's demagnetization may be observed [17], which is undesirable for EV applications. Thus, the PM hybrid motors are introduced to overcome the limitation of PM brushless motor. The wider speed range and higher overall efficiency are observed with the PM hybrid motors, but it has complex construction [17].

However, IM is seen as one of the potential candidates for EV motors due to its robust construction and is less expensive than PM motors [12, 18–20]. Table 1.1 shows the detailed motor parameters comparison in context to the EV applications. A point-based grading system is adopted to evaluate electric motor performance, as shown in Table 1.1. The grading system comprises several major factors listed in Table 1.1, and each of these factors is graded in points from one to five, where five

points indicate the best. The grading system shows that the IM scores the most compared to other motors listed in the table.

Table. 1.1: Evaluation of electric motors performance for EV applications

Motor characteristics	DC motor	IM	PMSM	SRM
Mature Technology	5	4.5	4	3.5
Life time	3.5	5	4	4.5
Power density	2.5	4	5	3.5
Efficiency	2.5	4	5	4.5
Controllability	5	5	4	3
Torque ripple/noise	3.5	4.5	4.5	3
Reliability	3	5	4	5
Robustness	3	5	4	5
Torque density	3	4	5	4
Over-load capability	3	4	4	4
Speed range	2.5	4	4.5	4.5
Size and weight	3	4	5	4
Required maintenance	3	4	4	4
Cost	4	5	3	4
Total	46.5	62	60	56.5

Thus, the low-cost and rugged IMs have become a possible alternative for EV applications [21], and therefore, IM based drive is considered in this thesis.

The IM's speed control for an EV application is challenging due to the wide range of operations and varying load conditions that the EVs practice during driving. The high dynamic performance of an IM is achieved by independently controlling the torque and flux linkages. Therefore, the vector control schemes have come into existence, controlling the torque and flux linkage of an IM independently. The vector control techniques such as Field Oriented Control (FOC), Direct Torque Control (DTC), and their derived methods are better-suited control techniques in dynamic response [22–25] for EV applications.

In general, FOC has disadvantages, such as a complex control structure and requires coordinate transformation and pulse width modulator (PWM) signal generator [26, 27]. The DTC method gives a quick dynamic response compared to the FOC method [28]. Furthermore, the DTC scheme's implementation is simple and does not demand any coordinate transformations and pulse width modulation (PWM) techniques compared to the FOC strategy. Thus, among these methods [24, 25], DTC appears to be a suitable strategy for EV applications due to its simple control structure and competence to provide a high dynamic response [29, 30]. The classification of DTC schemes based on IM drives is shown in Fig. 1.3. As far as EV applications are concerned, DTC has some challenging issues which

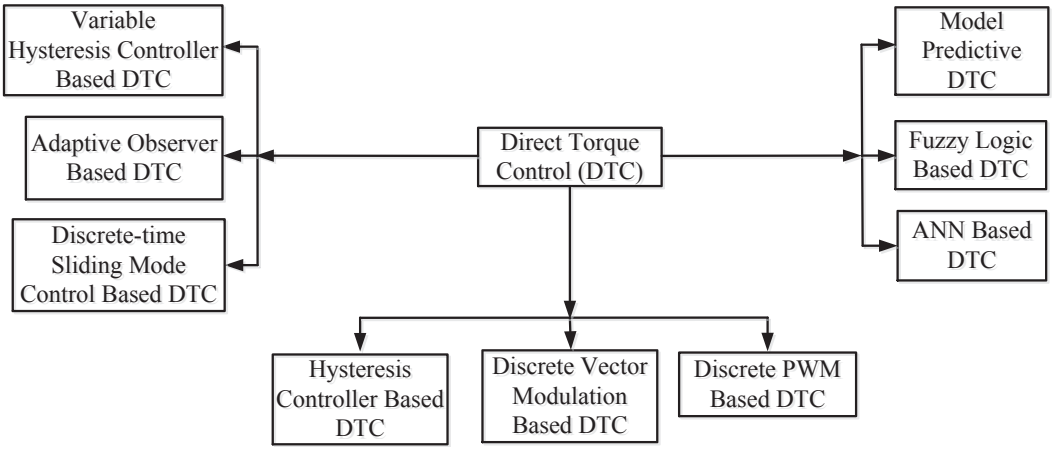

Fig. 1.3: DTC schemes for IM drive.

can be broadly classified as:

- High torque ripple, flux ripple, and variable switching frequency;
- Difficulty experienced at very low-speed operations for flux and torque control;
- Parameter variations, mainly stator resistance mismatch, which influences the flux linkage estimation at low-speed operations, and
- Determination of optimal λ_s^* for a wide range of speed operations.

With these broad objectives in mind, this section mainly emphasizes presenting the literature review. The first part of this section deals with the literature review on torque ripples, flux ripples, the difficulty encountered at low speed and parameter variation, and the methods to overcome these issues. The second part discusses the literature review on determining optimal λ_s^* for a wide range of speed operation.

1.2.1 Review on Torque and Flux Ripples Reduction, and Low Speed Performance of the DTC Method

The DTC technique, applied to induction machines, was initially proposed by I. Takahashi [28] and M. Depenbrock as Direct Self Control [31]. DTC's basic principle involves the direct control of the torque and the stator flux linkage (λ_s). It is done by selecting the inverter's accurate voltage vectors that feed the machine. The basic scheme of a DTC control depends on choosing an optimal switching vector table and two hysteresis comparators for both torque and stator λ_s. The estimated torque and stator λ_s are generally obtained from flux and torque estimators. Compared to the field-oriented control (FOC), the DTC has several advantages: less dependence on machine parameters, straightforward implementation, and better torque response dynamics. In DTC, the applied voltage

vector remains constant for each sampling period until there is a variation in the hysteresis regulators' output. Therefore, the switching frequency is not constant and depends on the rotational speed, load, and flux and torque regulators' bandwidth. Variable switching frequency is one of the drawbacks of the DTC control studied by several authors such as [32, 33].

The other major disadvantage of DTC control is the high level of torque and flux ripples, and the study in [34] has developed a method called a discrete vector modulation. In this method, the switching tables and the number of switching voltage vectors are increased within the defined time intervals over a fixed period to reduce the torque and flux ripples.

On the other hand, Takahashi (and others) proposes a new inverter structure (two three-phase inverters) in [35] to decrease the torque and flux ripples. While Mei (and others) use variable switching sectors [36] to reduce the switching frequency and the drooping characteristics of the estimated flux linkage.

In [37], a study has been carried out to predict the inverter's switching frequency based on the torque and flux regulators' hysteresis bands' width. The calculation depends on the variation of the average value of the torque slope equation of IM. Tests are carried out by the varying value of the width of the hysteresis bands. The switching frequency of the inverter is calculated by taking into account both the machine and inverter parameters. This work perhaps continues an idea proposed in [38] where the study of the variation of the hysteresis bandwidth with the machine parameters is carried out to obtain a constant switching frequency. A variable duty cycle control method is presented in [39, 40], which ascertained the proper operation under steady-state conditions with satisfactory values in the current distortion and the torque ripple.

In [41], a DTC algorithm for three-level inverter-fed induction motors has been presented to encounter problems such as the stator-flux drooping issues and undesirable torque control deterioration, mainly at low-speed operations. In this regard, to obtain a satisfactory performance at low-speed operation, an adaptive observer is proposed using the state variables and motor parameters' estimations.

The authors in [22] improved DTC's behavior by introducing a high frequency and low amplitude signal in the torque controller, with which they obtained improved performance. In [42, 43], the authors used the discrete-time sliding mode control (SMC) technique for improving the performance of the classical DTC technique. The SMC method robust to the parameter variations, and this method does not use current regulators for the generation of reference voltage vectors. These reference voltage vectors are the PWM block's input to provide switching pulses to the inverter with constant switching frequency. Though the method improves the drive's performance, complexity and

the computational burden are the limitations of this method. The work presented in [44] addresses current ripple optimization for the DTC-based IM drive. In [45], a predictive scheme is addressed with low computational requirements and low parameter sensitivity, reducing the flux and torque ripples for the DTC-based IM drive.

In [46–49], the authors propose a technique for improving DTC's dynamic performance using intelligent techniques; called fuzzy/direct neural control. In this study, the switching table and the hysteresis comparators are replaced by the fuzzy logic (FL)/ artificial neural network (ANN) controllers. The generated voltage vector from FL / ANN controllers make it possible to drive the flux and the torque towards their references in an optimal way.

Table. 1.2: Summary on the various forms of DTC strategies for IM drives as shown in Fig. 1.3

DTC Schemes	Torque ripple	Flux ripple	Switching frequency	Low-speed estimation	Remarks
Hysteresis Controller Based DTC	High	High	Variable	poor	Fast torque response and control structure is simple [32, 33].
Discrete Vector Modulation Based DTC	Low	Low	Constant	poor	Complex control structure [34].
Discrete PWM Based DTC	Low	Low	-	Satisfactory	With the two three-phase inverter in the circuit, control structure becomes complex [35, 36].
Variable Hysteresis Controller Based DTC	Medium	Medium	Constant	Satisfactory	Low-speed estimation is satisfactory [37, 38].
Adaptive Observer Based DTC	Medium	Medium	Constant	Satisfactory	Satisfactory response at the low-speed operations such as the issues of stator-flux linkage drooping and torque control are improved [41].
Discrete-time Sliding Mode Control Based DTC	Low	Low	-	Satisfactory	Drive performance improved, but control complexity, and the computational burden increased [42, 43].
Model Predictive DTC	Medium	Medium	-	Satisfactory	Low computational requirements and low parameter sensitivity, but control structure becomes complex [45].
Fuzzy Logic Based DTC	Medium	Medium	-	Satisfactory	Complex control structure [46, 47]
ANN Based DTC	Medium	Medium	-	Satisfactory	Complex control structure [48, 49]

Table 1.2 summarizes the evaluation of the DTC schemes for IM drives. It is seen that the DTC demerits (like torque ripples, flux ripples, high stator current, varying switching frequency, and low-speed stability) and the techniques to overcome these demerits are well reported in the literature. In the DTC strategy, the value of reference flux linkage (λ_s^*) also significantly impacts its performance. Therefore, the upcoming subsection is devoted to the literature review on determining optimal λ_s^* for a wide range of operations and its effects on the DTC strategy.

1.2.2 Review on Determination for Optimal Value of Reference Flux Linkage

According to the literature [15, 30, 50–55], several strategies for the determination of optimal λ_s^* in vector control IM drive are reported:

1. Variable flux controller (VFC) as a torque's function.
2. Flux search controller (SC)-based on minimum loss/ minimum input power/minimum stator

current.

3. Flux controller based on the Loss model.
4. Hybrid method.

Fig. 1.4 shows the classification of reference flux linkage determination techniques. VFC is a

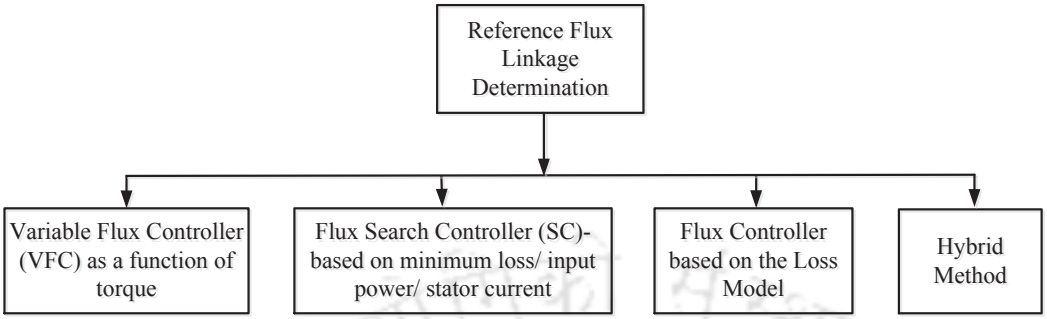

Fig. 1.4: Determination of reference flux linkage techniques.

well-known strategy and accepted in the industry because of its simplicity [28]. This method is based on the limit cycle control for flux linkage and torque using optimal PWM output voltage. Here, the limit cycle defines the hysteresis bands of flux linkage and torque. The method is simple and gives a satisfactory performance, but only for a narrow range of operations [56]. However, for an EV application, a wide speed range of operations are always desirable. Therefore, SCs methods are introduced [50, 57].

In the SCs method, the optimum value of λ_s^* is determined by the iteration process using the measured motor input power. The control variable for SCs stator current is more suitable since it is more sensitive to the flux variation than the input power and better statistical properties [51, 57]. Therefore, the SCs based on stator current minimization demonstrate better performance than input power as a control variable. The merit of the SCs is that they are independent of drive parameters and can be very accurate. However, this method suffers from slow convergence and torque ripples if the step changes of the flux command are abrupt [54]. Fuzzy and neuro-fuzzy-based SCs are proposed in [58–60] to improve the convergence performance to the optimum λ_s^*. Moreover, the load torque pulsations and measurement error may also lead to deterioration in the search algorithm's performance. Besides, it is observed for the drives with faster dynamics, the convergence issue and oscillation for flux's optimum value in the control algorithm are not desirable [15].

The λ_s^* selection using a loss model-based flux controller is introduced in [30, 52] to overcome the issue of convergence. The λ_s^* is obtained by minimizing the motor losses or combined with the inverter and DC-link capacitor [61]. The obtained λ_s^* values are stored and tabulated as a lookup table

(LUT) and implemented in the control algorithm. The loss model-based approach involves complex mathematical operations, which require high computing time and large memory size for feeding LUT (obtained from the offline calculation) in the control technique for efficiency improvement. This strategy's performance depends on the exact identification of motor parameters and their variation during operation [53, 62], and exact motor parameters determination is difficult [63].

There are also hybrid methods are reported [15, 25, 55] by combining the advantages of the loss model approach and the search controller for the improvement in the efficiency of a vector-controlled drive. In this method, a loss model-based approach calculates the initial value for the SC algorithm, followed by searching for the final flux's optimal value. The merit of this method is the fast determination of λ_s^* and is robust to parameters variation. However, the method's performance depends on the accurate measurement of the power signal, the type of search algorithm, and the determination of initial value calculation from the loss model approach [54].

Table. 1.3: Summary of reference flux linkage determination techniques

Methods	**Torque ripple**	**Wide speed range**	**Wide torque range**	**Computational complexity**	**Need for detailed motor parameters**	**Remarks**
Variable flux controller (VFC)	High	Limited	Limited	–	–	Simple but determination of the optimal λ_s value is not satisfactory and for limited speed range [56].
Flux search controller (SC) (Online estimation)	Medium	Yes	Yes	Yes	No	Slow convergence issues and ripples in torque are observed [25, 30, 51].
Flux search controller (SC) (Offline estimation)	Low	Limited	Limited	No	Yes	Limited range of operations [15, 25].
Flux controller based on the Loss model	Low	Yes	limited	Yes	Yes	Favorable for EV applications and optimal λ_s determination is possible, but dependant on the motor parameters' accuracy [62–64].
Hybrid method	Low	limited	limited	Medium	Yes	Dynamic performance is acceptable, but for limited operating ranges [54, 65–67].

Based on the literature, the summary of the determination of reference flux techniques is listed in Table 1.3. It is found that there is no generalized accepted method for determining the λ_s^* value. It depends on individual applications. Therefore, in the context of EV drivetrain, it is necessary to have an algorithm for λ_s^* selection over a wide range of operations, which is easy to implement in practice and free from convergence issues. It should not need an excessive computational resource and least sensitive to motor parameter variations. Furthermore, variable λ_s^* has a substantial impact on the DTC operation and is explained in the next subsection.

1.2.3 Impact of Variable Reference Flux Linkage on DTC Technique for an EV Application

In the DTC technique, the reference flux linkage (λ_s^*) also significantly impacts its performance. In conventional DTC, λ_s^* is kept at a constant value (usually at rated value) as these drives are set to operate at a constant speed [68]. However, this is not an optimum solution for the control strategies used in EV applications [69]. In these applications, the motor does not need to run at rated conditions for all the speed ranges [70]. As far as the EV applications are concerned, where the variations in load torque depend on the traffic and road conditions, it is not advisable to keep the λ_s^* at its rated value for speeds lower than the base speed. Moreover, keeping the rated value of λ_s^* for low-speed operations may result in a very high value of torque reference [70]. Besides, it is also observed that variable λ_s^* greatly influences the IM drive's efficiency and performance [28]. Hence, the optimal selection of λ_s^* is crucial in the DTC strategy over a wide operating range for EV applications.

In recent years, EVs have become a compulsion choice for green transportation. Therefore, a new way of study and research has been carried out in academia and industry to expedite EVs' penetration. The major challenge in the faster adoption of EVs is to develop low-cost EVs that fulfill the need of the market and users' daily needs. In the EV drivetrain, the EV motor, unlike industrial motors, has to operate over a wide speed and torque range of operations. Therefore, the challenge is to adapt the available speed control methods proposed for industrial applications to modify for use in EVs. Hence, it is essential to choose a controller with an excellent dynamic response over a wide range of speeds. Moreover, designing the cost-effective EV drivetrain; the IM is the preferred choice due to the several advantages over PM-based motors [21].

The IM's speed control techniques are well examined, and many methods, such as FOC and DTC, have been reported in the literature [24, 25]. Among these methods [24, 25], DTC appears to be a useful scheme for EV applications due to its simple control structure and competence to provide a high dynamic response [29, 30]. However, it is seen that the DTC demerits (like torque ripples, flux ripples, high stator current, varying switching frequency, and low-speed stability) [71] and the techniques to overcome these demerits are well investigated in the literature [23, 39, 40, 44, 72–74].

In the DTC strategy, the reference flux linkage (λ_s^*) also significantly impacts its performance. As reported in [15, 25, 30, 51, 56, 75–79], there are three basic methods for selecting λ_s^* for the IM drive system. Namely, variable flux control as a reference torque's function, loss model-based flux controller, and flux search controller based on minimum loss/minimum input power/minimum stator

current. The literature review gives an acceptable solution for narrow speed and torque ranges, which is not favorable in EVs. In EV applications, the drive has to run over a wide operating range based on the vehicle driving cycles, which they regularly practice on the road.

The work reported in the literature shows that the adaptation of DTC-based IM drive for EV applications in general and λ_s^* selection, in particular, has not been extensively examined. Besides, it is found that there is no generalized accepted method for determining the λ_s^*. The detailed literature review motivated to formulate the problem in the area of determination methods of appropriate λ_s^* for DTC-based IM drive over a wide range of operations.

1.3 Aim and Contributions

The IM employed in the EV drivetrain typically demands quick transient responses, better steady-state speed performance, and a wide range of operations. The IM's control for an EV application is challenging due to the wide range of speed operations and varying load conditions that the EVs practice on the road. Therefore, various research activities have been performed in IM speed control, and one among the control methods of an IM is the DTC. The DTC appears to be a suitable strategy for EV applications due to its simple control structure and competence to provide a high dynamic response. However, this scheme suffers from high torque and flux ripples, which directly impacts the drive performance. The DTC drawbacks and the methods to overcome those drawbacks are well reported by the researchers.

In the DTC strategy, the λ_s^* also significantly impacts its performance. As reported in [15, 25, 30, 51, 63, 76], the λ_s^* determination is one of the challenging problems in DTC-based IM drive for a wide speed range and varying load conditions. The work reported in the literature shows that the adaptation of DTC-based IM drive for EV applications in general and λ_s^* selection, in particular, has not been extensively examined. Therefore, this thesis presents a DTC-based IM for an EV application. The main contribution of this thesis is to develop methods for determining a suitable value of λ_s^*. In the EV applications, the variations in the available dc voltage from the battery source are observed as the state of charge (SoC) phenomenon and operating conditions [80]. Therefore, the proposed methods calculate λ_s^*, considering the reference speed, reference torque, and a given dc source voltage.

The thesis aims to design, develop, and implement a speed control DTC IM drive that can operate for a wide speed range and stable at various operating modes. For the successful implementation of DTC-based IM drive over a wide range of speed and torque, two methods are proposed for the

selection of suitable λ_s^*:

1. Determination of λ_s^* using a Finite Element Analysis (FEA) based IM model.
2. Determination of λ_s^* using a non-linear equivalent circuit model of IM.

In the first work, the determination of λ_s^* is achieved using an FEA-based IM model. The FEA-based IM model is developed on the ANSYS Maxwell platform. The winding scheme and lamination designs of the motor are required to obtain an FEA-based IM model. The simulations are carried out with variations in motor speed (N_r), stator voltage (V_s), and stator voltage frequency (f_s). The FEA simulation's primary objective is to obtain suitable values of λ_s and T_e in lookup tables (LUTs) format over a wide speed range. The obtained LUTs provide information about the suitable λ_s^* at required N_r and given T_e in context to the DTC strategy, with current and voltage constraints over a wide operating range. However, this method required a pre-knowledge about the motor's geometry, i.e., winding scheme, slot dimensions details, and lamination designs, to develop an FEA model of IM, which helps obtain accurate values of reference flux linkage in LUT format. This limitation is overthrown if a non-linear equivalent circuit model of IM will be developed and used.

Therefore, in the second work, the selection of λ_s^* is determined using a non-linear equivalent circuit model of IM. The no-load test, blocked rotor test, and non-linear magnetization curve test of the IM was performed to obtain equivalent circuit parameters. The non-linear magnetization curve has been plotted, and the dependency of magnetizing inductance (L_m) with the magnetizing current (i_m) is determined. Thus, the obtained non-linear equivalent circuit model of IM with varying L_m has been used to determine the λ_s^* in LUT format.

Both these methods calculate λ_s^*, considering the reference speed, required torque, and given DC voltage. Moreover, the magnetic saturation effect is also considered while calculating an appropriate λ_s^* value. Finally, the two driving cycles, namely, the New York City Cycle (NYCC) and New European Driving Cycle (NEDC), are presented in this work to demonstrate the proposed method's suitability over a wide speed and torque range of operations for the EV applications. The proposed method's performance evaluation over a wide operating range with the vehicle driving cycles (i.e., NYCC and NEDC) is carried out on the laboratory's developed experimental setup. The experimental setup of speed control for IM drive with the DTC technique is given in Appendix A.6. Further, consumption in input energy and efficiency analysis for considered driving cycles are also presented.

1.4 Organization of thesis

The remaining thesis chapters are organized as follows:

- **Chapter 2:** This chapter begins with the mathematical model of IM. In the first part, the detailed mathematical representation of the IM with different reference frame transformations used in the design of the control laws for steady-state and dynamic operation are discussed. The second part of the chapter describes the principle of operation of the vector control strategies, such as FOC and DTC methods, in brief.
- **Chapter 3:** This chapter first explains the impact of variable λ_s^* on DTC-based IM drive performance. A detailed analysis is presented in this chapter to explain the effects of variable λ_s on the motor's behavior. Besides, this chapter discusses the DTC scheme with variable λ_s^*. Further, a brief explanation of methods for determining the λ_s^* in context to the DTC scheme is presented. Finally, based on the determination methods of λ_s^*, the detailed discussion on its limitations in context to EV applications is summarized. Based on the finding of this chapter, the determination methods of λ_s^* are proposed for DTC based IM drive over a wide range of operations and are explained in the next subsequent chapters.
- **Chapter 4:** The FEA-based method to determine λ_s^* values is discussed in this chapter. A detailed methodology to get the suitable values of λ_s over a wide range of speed operations is explained in detail. This chapter also presents the parameter sensitivity analysis of the proposed technique. Further, to check the proposed FEA-based approach's robustness, the comparative analysis of the proposed method with other existing techniques is demonstrated. Experimental results are presented in this chapter. Lastly, the input energy consumption and efficiency analysis of the considered vehicle driving cycles are also presented. The method proposed in this chapter requires a pre-knowledge about the motor's geometry, i.e., winding scheme, slot dimensions details, and lamination designs, to develop an FEA model of IM, which helps obtain accurate values of reference flux in LUT format. This limitation is overthrown if a non-linear equivalent circuit model of IM will be developed and used. Therefore, the determination of reference flux linkage using a non-linear equivalent circuit model of IM is developed and discussed in the next chapter.
- **Chapter 5:** In this chapter, the determination of λ_s^* values using a non-linear equivalent circuit model of IM is presented. The chapter discusses the detailed procedure for determining non-linear equivalent circuit parameters (.i.e., magnetizing inductance, L_m) of IM. A detailed

methodology to get the suitable values of λ_s over a wide range of speed operations is explained in detail. Parameter sensitivity analysis of the proposed technique is investigated in this chapter. The comparative analysis of the proposed approach with (i) loss model-based approach and (ii) FEA based method (as presented in chapter-4), and the experimental results over a wide range of speed for the vehicle driving cycles (i.e., NYCC and NEDC) are demonstrated in this chapter. Further, the input energy consumption and the efficiency analysis of the presented vehicle driving cycles are also explained.

- **Chapter 6:** In this chapter, the conclusions drawn from the research work are outlined, and the scopes for future work are summarized.

भारतीय प्रौद्योगिकी संस्थान गुवाहाटी
Indian Institute of Technology Guwahati

भारतीय प्रौद्योगिकी संस्थान गुवाहाटी
Indian Institute of Technology Guwahati

CHAPTER 2

INDUCTION MOTOR MODELING AND CONTROL

2.1 Introduction

A variable-speed drive with accurate control of torque and speed are needed to achieve superior dynamic performance in EV drivetrains. In the past, to achieve high-performance, the DC machine drive had managed to fulfill the demand due to the absence of control strategies for the AC machine drive. However, with the advent of power electronics devices, the change in the constant voltage and frequency of the utility to variable voltage and variable frequency (VVVF) has been achieved [81]. The VVVF drive is achieved significant improvements in the control of AC drive under steady-state conditions. Moreover, the emergence in the vector control (VC) techniques (i.e., FOC, DTC, and their derived forms) has resulted in remarkable progress in the dynamics of VVVF drives [82].

The IM is used as an AC drive because of its robustness, ease of maintenance, reliability, and, most importantly, its low cost [83]. Due to the advantages of IM, this work focuses on EV drivetrain using IM. For an EV drivetrain, the selection of an accurate control strategy of IM is essential. The motor controller for EV application should have a fast dynamic response, high torque at low speed for starting and zero speed, and lower torque ripple. IM's VC techniques are better suited for EV applications because these control schemes can enable the IM to operate over a wide speed range and give an excellent dynamic response.

To design and implement the VC algorithm for an IM, it is required to understand the dynamic model of IM subjected to control. In this chapter, the IM's mathematical model that will eventually be used in VC techniques is explained, which can be used for analyzing the transient and steady-state performance and designing the control algorithm.

The remaining chapter is organized as follows: Section 2.2 describes IM's mathematical model in the different reference frames. A brief explanation of vector control strategies is presented in Section 2.3, and a detailed discussion of the direct torque control strategy is given in Section 2.3.2. The conclusions are drawn in Section 2.4.

2.2 Induction Motor Modeling

To understand and analyze the VC of IM, the mathematical model of the motor is necessary. The mathematical model of motor helps to explain the motor performance at transient and steady-state conditions. This model also assists in designing the controller and in estimating their parameters. For developing IMs mathematical model, the following assumptions are made [84]:

1. Balanced stator and rotor windings.
2. Sinusoidal distributed magnetomotive force in windings.
3. Uniform air gap.
4. Magnetic core saturation is neglected.

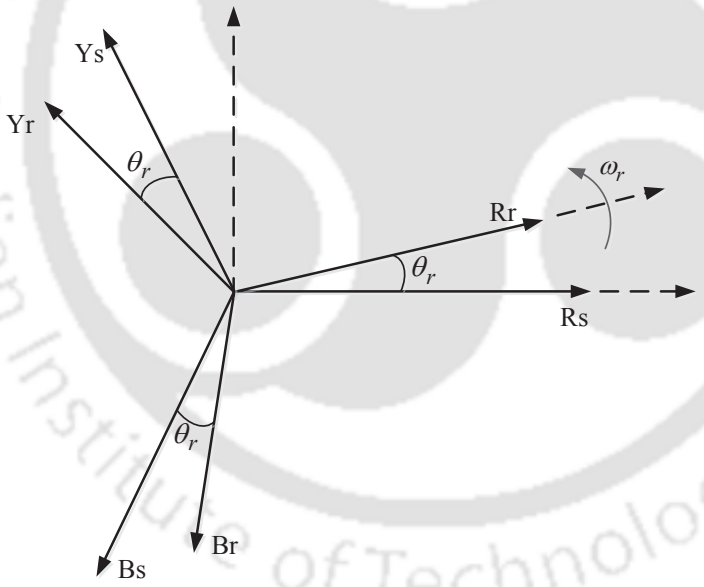

Fig. 2.1: Three phase representation of stator and rotor quantities.

For a three-phase IM, the stator voltages (V_{RYBs}) and stator flux linkages (λ_{RYBs}) are represented as [85]:

$$[V_{RYBs}] = [R_s]\,[i_{RYBs}] + p\,[\lambda_{RYBs}] \tag{2.1}$$

$$[\lambda_{RYBs}] = [L_s]\,[i_{RYBs}] + [M]\,[i_{RYBr}] \tag{2.2}$$

where, $[V_{RYBs}] = \begin{bmatrix} V_{Rs} \\ V_{Ys} \\ V_{Bs} \end{bmatrix}$, $[i_{RYBs}] = \begin{bmatrix} i_{Rs} \\ i_{Ys} \\ i_{Bs} \end{bmatrix}$, $[\lambda_{RYBs}] = \begin{bmatrix} \lambda_{Rs} \\ \lambda_{Ys} \\ \lambda_{Bs} \end{bmatrix}$,

$[R_s] = \begin{bmatrix} R_s & 0 & 0 \\ 0 & R_s & 0 \\ 0 & 0 & R_s \end{bmatrix}$, $[L_s] = \begin{bmatrix} L_{ls}+L_m & -\frac{L_m}{2} & -\frac{L_m}{2} \\ -\frac{L_m}{2} & L_{ls}+L_m & -\frac{L_m}{2} \\ -\frac{L_m}{2} & -\frac{L_m}{2} & L_{ls}+L_m \end{bmatrix}$, and

$[M] = L_m \begin{bmatrix} \cos\ \theta_r & \cos\left(\theta_r - \frac{2\pi}{3}\right) & \cos\left(\theta_r + \frac{2\pi}{3}\right) \\ \cos\left(\theta_r + \frac{2\pi}{3}\right) & \cos\ \theta_r & \cos\left(\theta_r - \frac{2\pi}{3}\right) \\ \cos\left(\theta_r - \frac{2\pi}{3}\right) & \cos\left(\theta_r + \frac{2\pi}{3}\right) & \cos\ \theta_r \end{bmatrix}$.

In equations (2.1) and (2.2), the terms i_{RYBs} and i_{RYBr} represent the three-phase stator and rotor currents, respectively; R_s represents the stator winging resistance; L_s, L_{ls}, and L_m represent the stator self-inductance, leakage inductance, and magnetizing inductance, respectively; θ_r represents the relative angle between the stator and rotor quantity as shown in Fig. 2.1; p represents the differential operator.

Similarly, the three-phase rotor voltages (V_{RYBr}) and rotor flux linkages (λ_{RYBr}) are given by [85]:

$$[V_{RYBr}] = [R_r]\,[i_{RYBr}] + p\,[\lambda_{RYBr}] \tag{2.3}$$

$$[\lambda_{RYBr}] = [L_r]\,[i_{RYBr}] + [M]\,[i_{RYBs}] \tag{2.4}$$

where, $[V_{RYBr}] = \begin{bmatrix} V_{Rr} \\ V_{Yr} \\ V_{Br} \end{bmatrix}$, $[i_{RYBr}] = \begin{bmatrix} i_{Rr} \\ i_{Yr} \\ i_{Br} \end{bmatrix}$, $[\lambda_{RYBr}] = \begin{bmatrix} \lambda_{Rr} \\ \lambda_{Yr} \\ \lambda_{Br} \end{bmatrix}$,

$[R_r] = \begin{bmatrix} R_r & 0 & 0 \\ 0 & R_r & 0 \\ 0 & 0 & R_r \end{bmatrix}$, $[L_r] = \begin{bmatrix} L_{lr}+L_m & -\frac{L_m}{2} & -\frac{L_m}{2} \\ -\frac{L_m}{2} & L_{lr}+L_m & -\frac{L_m}{2} \\ -\frac{L_m}{2} & -\frac{L_m}{2} & L_{lr}+L_m \end{bmatrix}$

In the above equations (2.3) and (2.4), R_r represents the rotor resistance; L_r, L_{lr}, and L_m represent the rotor self-inductance, leakage inductance, and magnetizing inductance, respectively. Due to the symmetry of the machine, the mutual inductance among stator-phases and rotor-phases are equal.

The differential equations given in (2.1) to (2.4) are the IM's governing equations, and all the steady-state and dynamic characteristics can be determined through these equations. In these expressions, the mutual inductance ($[M]$) varies wrt rotor position, which is complex to solve [86]. Therefore, to simplify these expressions (2.1) – (2.4), the three-phase quantities are converted into

two-phase direct and quadrature axes using Parks transform. The Parks transform also ensures that power is invariant [84]. The transformation matrices and different reference frames are discussed in the subsequent subsections.

2.2.1 Three-phase to Two-phase Transformation

The three-phase quantities can be converted into two-phase stationary reference frame (i.e., α-β) as [84–86]:

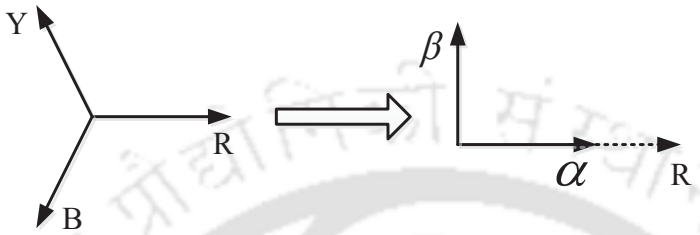

Fig. 2.2: Vector diagram for three-phase to two phase conversion.

$$\begin{bmatrix} X_\alpha \\ X_\beta \end{bmatrix} = \frac{2}{3}\begin{bmatrix} 1 & -\frac{1}{2} & -\frac{1}{2} \\ 0 & \frac{\sqrt{3}}{2} & -\frac{\sqrt{3}}{2} \end{bmatrix}\begin{bmatrix} X_R \\ X_Y \\ X_B \end{bmatrix} = T_{\alpha\beta}\begin{bmatrix} X_R \\ X_Y \\ X_B \end{bmatrix} \tag{2.5}$$

By introducing zero sequence component (X_0) in the equation (2.5), it is expressed as:

$$\begin{bmatrix} X_\alpha \\ X_\beta \\ X_0 \end{bmatrix} = \frac{2}{3}\begin{bmatrix} 1 & -\frac{1}{2} & -\frac{1}{2} \\ 0 & \frac{\sqrt{3}}{2} & -\frac{\sqrt{3}}{2} \\ \frac{1}{2} & \frac{1}{2} & \frac{1}{2} \end{bmatrix}\begin{bmatrix} X_R \\ X_Y \\ X_B \end{bmatrix} = T_{\alpha\beta}\begin{bmatrix} X_R \\ X_Y \\ X_B \end{bmatrix} \tag{2.6}$$

and, the inverse transformation matrix of $[T_{\alpha\beta}]$ is given as:

$$\begin{bmatrix} X_R \\ X_Y \\ X_B \end{bmatrix} = \begin{bmatrix} \frac{2}{3} & 0 & 1 \\ -\frac{1}{3} & \frac{1}{\sqrt{3}} & 1 \\ -\frac{1}{3} & -\frac{1}{\sqrt{3}} & 1 \end{bmatrix}\begin{bmatrix} X_\alpha \\ X_\beta \\ X_0 \end{bmatrix} = T_{RYB}\begin{bmatrix} X_\alpha \\ X_\beta \\ X_0 \end{bmatrix} \tag{2.7}$$

where, X can be voltage, current, and flux linkage; $X_{\alpha\beta}$ represents the two-phase components in stationary of respective entities. By applying the transformation matrices ($[T_{\alpha\beta}]$ (2.6); $[T_{RYB}]$ (2.7)), the three-phase quantities can be converted into two-phase quantities and vice-versa.

Fig. 2.3 shows the windings in natural frame RYB (for stator and rotor), $\alpha\beta 0$ stationary (for stator), and $xy0$ rotating (for rotor) reference frames. By projecting the reference frame RYB of the

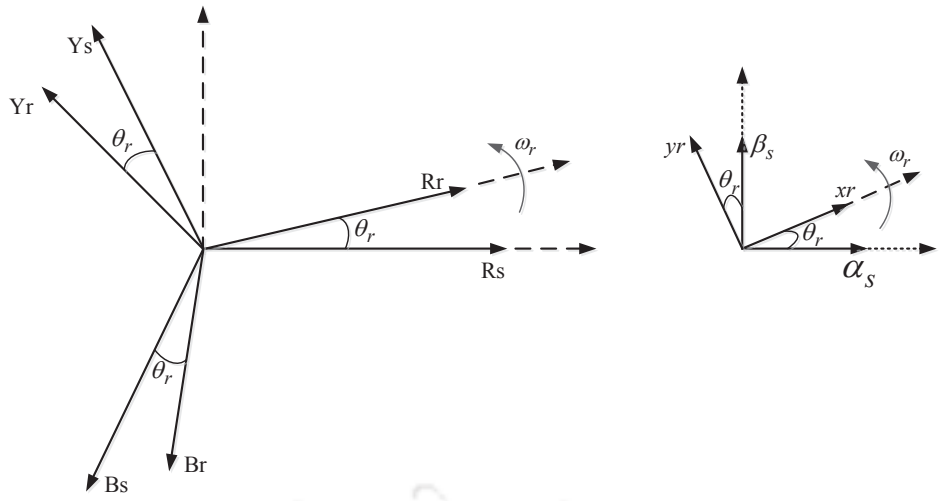

Fig. 2.3: Transformation of three-phase to two-phase reference frame.

stator and rotor quantities to the reference frames, $\alpha\beta 0$ (stator) and $xy0$ (rotor), and applying the transformation matrix ($[T_{\alpha\beta}]$ (2.6)) to the equations (2.1) and (2.3), the voltage equations become:

$$v_{\alpha s} = R_s i_{\alpha s} + \frac{d\lambda_{\alpha s}}{dt} \tag{2.8}$$

$$v_{\beta s} = R_s i_{\beta s} + \frac{d\lambda_{\beta s}}{dt} \tag{2.9}$$

$$v_{xr} = 0 = R_r i_{xr} + \frac{d\lambda_{xr}}{dt} \tag{2.10}$$

$$v_{yr} = 0 = R_r i_{yr} + \frac{d\lambda_{yr}}{dt} \tag{2.11}$$

Since the IM is squirrel-cage, the rotor voltage terms (v_{xr}, v_{yr}) in equations (2.10) and (2.11) are zero. By applying the three-phase to two-phase transformation to the flux linkage equations (2.2) and (2.4) we get;

$$\begin{bmatrix} \lambda_{\alpha s} \\ \lambda_{\beta s} \\ \lambda_{xr} \\ \lambda_{yr} \end{bmatrix} = \begin{bmatrix} L_s & 0 & M\cos\theta_r & -M\sin\theta_r \\ 0 & L_s & M\sin\theta_r & M\cos\theta_r \\ M\cos\theta_r & M\sin\theta_r & L_r & 0 \\ -M\sin\theta_r & M\cos\theta_r & 0 & L_r \end{bmatrix} \begin{bmatrix} i_{\alpha s} \\ i_{\beta s} \\ i_{xr} \\ i_{yr} \end{bmatrix} \tag{2.12}$$

Substituting the terms ($\lambda_{\alpha s}$, $\lambda_{\beta s}$, λ_{xr}, and λ_{yr}) of the equation (2.12) in the equations (2.8 - 2.11) and simplifying, we get;

$$\begin{bmatrix} v_{\alpha s} \\ v_{\beta s} \\ v_{xr} \\ v_{yr} \end{bmatrix} = \begin{bmatrix} R_s + \frac{d}{dt}L_s & 0 & \frac{d}{dt}[M\cos\theta_r] & -\frac{d}{dt}[M\sin\theta_r] \\ 0 & R_s + \frac{d}{dt}L_s & \frac{d}{dt}[M\sin\theta_r] & \frac{d}{dt}[M\cos\theta_r] \\ \frac{d}{dt}[M\cos\theta_r] & \frac{d}{dt}[M\sin\theta_r] & R_r + \frac{d}{dt}L_r & 0 \\ -\frac{d}{dt}[M\sin\theta_r] & \frac{d}{dt}[M\cos\theta_r] & 0 & R_r + \frac{d}{dt}L_r \end{bmatrix} \begin{bmatrix} i_{\alpha s} \\ i_{\beta s} \\ i_{xr} \\ i_{yr} \end{bmatrix} \tag{2.13}$$

The equation (2.13) model is in their respective reference frames, i.e., $v_{\alpha s}$ and $v_{\beta s}$ are in stationary reference frame while v_{xr} and v_{yr} are in the rotor rotating reference frame. Moreover, the rotor quantities in the equation (2.13) vary wrt rotor position, which is complex to solve [86].

For this reason, the model given by equation (2.13) has to be simplified such that the model is independent of rotor position and can do this by transforming the rotor quantities to the stationary reference frame.

Fig. 2.4 shows the transformation of rotor rotating quantities ($xy0$) to a stationary frame of reference ($\alpha\beta0$). The rotor rotating quantities in the $xy0$ reference frame can be transformed into a $\alpha\beta0$ stationary reference frame as:

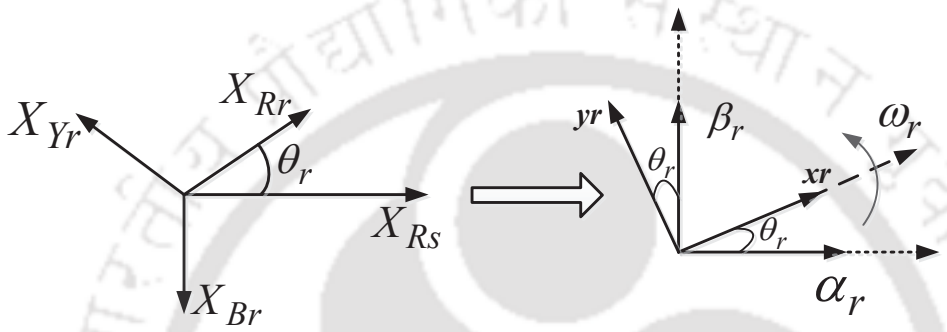

Fig. 2.4: Transformation of rotor rotating quantities to a stationary reference frame.

$$\begin{bmatrix} X_{\alpha r} \\ X_{\beta r} \\ X_{0r} \end{bmatrix} = \begin{bmatrix} \cos\theta_r & -\sin\theta_r & 0 \\ \sin\theta_r & \cos\theta_r & 0 \\ 0 & 0 & 1 \end{bmatrix} \begin{bmatrix} X_{xr} \\ X_{yr} \\ X_{0r} \end{bmatrix} = T_{\alpha\beta r} \begin{bmatrix} X_{xr} \\ X_{yr} \\ X_{0r} \end{bmatrix} \quad (2.14)$$

where $X_{\alpha\beta0r}$ and X_{xy0r} represent the direct and quadrature components of respective entities at stationary and rotor rotating reference frames, respectively.

Using the transformation matrix $[T_{\alpha\beta r}]$ (2.14), the rotor rotating quantities in the $xy0$ reference frame are transformed into a $\alpha\beta0$ stationary reference frame. Since the $v_{\alpha s}$ and $v_{\beta s}$ given in equation (2.13) are in a stationary reference frame, while v_{xr} and v_{yr} are in the rotor rotating reference frame.

For simplification of the model given by equation (2.13), all the rotor quantities are transformed to a stationary reference frame ($\alpha\beta$) using the transformation matrix $[T_{\alpha\beta r}]$ (2.14), as shown in equations (2.15- 2.18). As the stator of IM is excited by a balanced supply, zero sequence components are

neglected.

$$\begin{bmatrix} v_{\alpha s} \\ v_{\beta s} \\ v_{\alpha r} \\ v_{\beta r} \end{bmatrix} = \begin{bmatrix} 1 & 0 & 0 & 0 \\ 0 & 1 & 0 & 0 \\ 0 & 0 & cos\,\theta_r & -\sin\,\theta_r \\ 0 & 0 & \sin\,\theta_r & cos\,\theta_r \end{bmatrix} \begin{bmatrix} v_{\alpha s} \\ v_{\beta s} \\ v_{xr} \\ v_{yr} \end{bmatrix} \tag{2.15}$$

$$\begin{bmatrix} V_{\alpha\beta s} \\ V_{\alpha\beta r} \end{bmatrix} = \begin{bmatrix} U & 0 \\ 0 & T_{\alpha\beta r} \end{bmatrix} \begin{bmatrix} V_{\alpha\beta s} \\ V_{xyr} \end{bmatrix} \tag{2.16}$$

$$\begin{bmatrix} i_{\alpha s} \\ i_{\beta s} \\ i_{\alpha r} \\ i_{\beta r} \end{bmatrix} = \begin{bmatrix} 1 & 0 & 0 & 0 \\ 0 & 1 & 0 & 0 \\ 0 & 0 & cos\,\theta_r & -\sin\,\theta_r \\ 0 & 0 & \sin\,\theta_r & cos\,\theta_r \end{bmatrix} \begin{bmatrix} i_{\alpha s} \\ i_{\beta s} \\ i_{xr} \\ i_{yr} \end{bmatrix} \tag{2.17}$$

$$\begin{bmatrix} I_{\alpha\beta s} \\ I_{\alpha\beta r} \end{bmatrix} = \begin{bmatrix} U & 0 \\ 0 & T_{\alpha\beta r} \end{bmatrix} \begin{bmatrix} I_{\alpha\beta s} \\ I_{xyr} \end{bmatrix} \tag{2.18}$$

where $[U]$ is the identity matrix.

Substituting the equation (2.13) in the equations (2.15) and (2.17) and simplifying, we get;

$$\begin{bmatrix} v_{\alpha s} \\ v_{\beta s} \\ v_{\alpha r} \\ v_{\beta r} \end{bmatrix} = \begin{bmatrix} R_s + \frac{d}{dt}L_s & 0 & \frac{d}{dt}M & 0 \\ 0 & R_s + \frac{d}{dt}L_s & 0 & \frac{d}{dt}M \\ \frac{d}{dt}M & M\omega_r & R_r + \frac{d}{dt}L_r & L_r\omega_r \\ -M\omega_r & \frac{d}{dt}M & -L_r\omega_r & R_r + \frac{d}{dt}L_r \end{bmatrix} \begin{bmatrix} i_{\alpha s} \\ i_{\beta s} \\ i_{\alpha r} \\ i_{\beta r} \end{bmatrix} \tag{2.19}$$

where $\frac{d\theta_r}{dt} = \omega_r$. Equation (2.19) shows that all the quantities of equation (2.13) are referred to as a stationary $(\alpha\beta)$ frame of reference. Therefore, the model of equation (2.19) is independent of the rotor angle (θ_r).

From the above analysis, it is clear that the coupled equations in the RYB system are transferred into linear differential equations with two-coordinate transformations. Namely, the Clarke transformation (transformation of the three-phase system onto a two-phase system) and the Park transformation (transformation of the two-phase system onto an arbitrary rotating two-phase system). The subsequent subsection describes the transformation of the three-phase stator and rotor quantities (2.1 − 2.4) of IM into a two-phase arbitrary rotating reference frame.

2.2.2 IM Model in Reference Frame Rotating at Arbitrary Reference Speed

The transformation of a two-phase system onto an arbitrary($x^x - y^x$) rotating two-phase system can be achieved using the Park transformation. Fig. 2.5 shows the transformation of a two-phase stationary (α-β) system to an arbitrary ($x^x - y^x$) rotating system. The variable in the α-β reference frame can be transformed into an $x^x - y^x$ rotating reference frame as:

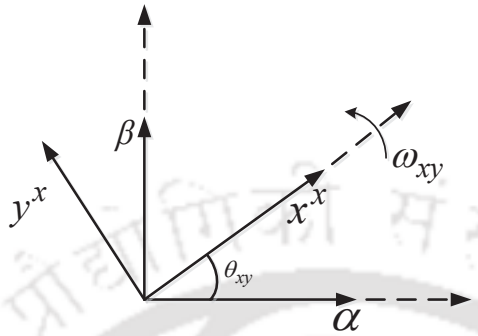

Fig. 2.5: Transformation of two-phase stationary to an arbitrary rotating two-phase reference frame.

$$\begin{bmatrix} X_x{}^x \\ X_y{}^x \end{bmatrix} = \begin{bmatrix} \cos\ \theta_{xy} & \sin\ \theta_{xy} \\ -\sin\ \theta_{xy} & \cos\ \theta_{xy} \end{bmatrix} \begin{bmatrix} X_\alpha \\ X_\beta \end{bmatrix} = T_{xy} \begin{bmatrix} X_\alpha \\ X_\beta \end{bmatrix} \tag{2.20}$$

The variables in arbitrary ($x^x - y^x$) rotating reference can be transformed into a stationary (α-β) reference frame using the transformation matrix $[T_{xy}^{-1}]$ as given below:

$$\begin{bmatrix} X_\alpha \\ X_\beta \end{bmatrix} = \begin{bmatrix} \cos\ \theta_{xy} & -\sin\ \theta_{xy} \\ \sin\ \theta_{xy} & \cos\ \theta_{xy} \end{bmatrix} \begin{bmatrix} X_x{}^x \\ X_y{}^x \end{bmatrix} = T_{xy}^{-1} \begin{bmatrix} X_x{}^x \\ X_y{}^x \end{bmatrix} \tag{2.21}$$

where θ_{xy} is an arbitrary angle between the stationary direct axis (α) and the real axis (x^x) of arbitrary reference frame, and $[X_{\alpha\beta}[$ and $[X_{xy}^x]$ represents the direct and quadrature components of the respective entities at stationary and arbitrary rotating reference frames, respectively.

By introducing zero sequence component in the equations (2.20) and (2.21), the transformation matrices $[T_{xy}]$ and $[T_{xy}^{-1}]$ are expressed as:

$$\begin{bmatrix} X_x{}^x \\ X_y{}^x \\ X_0{}^x \end{bmatrix} = \begin{bmatrix} \cos\ \theta_{xy} & \sin\ \theta_{xy} & 0 \\ -\sin\ \theta_{xy} & \cos\ \theta_{xy} & 0 \\ 0 & 0 & 1 \end{bmatrix} \begin{bmatrix} X_\alpha \\ X_\beta \\ X_0 \end{bmatrix} = T_{xy} \begin{bmatrix} X_\alpha \\ X_\beta \\ X_0 \end{bmatrix} \tag{2.22}$$

$$\begin{bmatrix} X_\alpha \\ X_\beta \\ X_0 \end{bmatrix} = \begin{bmatrix} \cos\ \theta_{xy} & -\sin\ \theta_{xy} & 0 \\ \sin\ \theta_{xy} & \cos\ \theta_{xy} & 0 \\ 0 & 0 & 1 \end{bmatrix} \begin{bmatrix} X_x{}^x \\ X_y{}^x \\ X_0{}^x \end{bmatrix} = T_{xy}^{-1} \begin{bmatrix} X_x{}^x \\ X_y{}^x \\ X_0{}^x \end{bmatrix} \tag{2.23}$$

In a generic form, the three-phase stator quantities (X_{Rs}, X_{Ys}, and X_{Bs}) can be transformed into two-phase arbitrary rotating quantities (X^x_{xs} and X^x_{ys}) using the transformation matrices $[T_{\alpha\beta}]$ (2.6) and $[T_{xy}]$ (2.22). Fig. 2.6 shows the transformation of three-phase stator quantities to two-phase arbitrary rotating quantities. By using equations (2.6) and (2.22), the three-phase stator quantities are

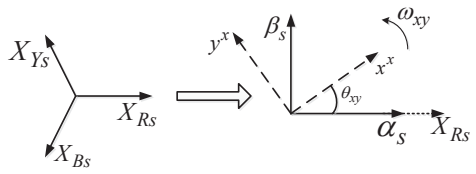

Fig. 2.6: Vector diagram for stator quantities conversion.

transformed into two-phase arbitrary rotating quantities as:

$$\begin{bmatrix} X^x_{xs} \\ X^x_{ys} \end{bmatrix} = \frac{2}{3} \begin{bmatrix} \cos\theta_{xy} & \sin\theta_{xy} & 0 \\ -\sin\theta_{xy} & \cos\theta_{xy} & 0 \\ 0 & 0 & 1 \end{bmatrix} \begin{bmatrix} 1 & -\frac{1}{2} & -\frac{1}{2} \\ 0 & \frac{\sqrt{3}}{2} & -\frac{\sqrt{3}}{2} \\ \frac{1}{2} & \frac{1}{2} & \frac{1}{2} \end{bmatrix} \begin{bmatrix} X_{Rs} \\ X_{Ys} \\ X_{Bs} \end{bmatrix} \tag{2.24}$$

$$\begin{bmatrix} X^x_{xs} \\ X^x_{ys} \end{bmatrix} = \frac{2}{3} \begin{bmatrix} \cos\theta_{xy} & \cos\left(\theta_{xy}-\frac{2\pi}{3}\right) & \cos\left(\theta_{xy}+\frac{2\pi}{3}\right) \\ -\sin\theta_{xy} & -\sin\left(\theta_{xy}-\frac{2\pi}{3}\right) & -\sin\left(\theta_{xy}+\frac{2\pi}{3}\right) \\ \frac{1}{2} & \frac{1}{2} & \frac{1}{2} \end{bmatrix} \begin{bmatrix} X_{Rs} \\ X_{Ys} \\ X_{Bs} \end{bmatrix} \tag{2.25}$$

Similarly, the three-phase rotor rotating quantities (X_{Rr}, X_{Yr}, and X_{Br}) can be transformed into two-phase arbitrary rotating quantities (X^x_{xr} and X^x_{yr}) using the transformation matrix (2.26). Fig. 2.7 shows the transformation of three-phase rotor quantities to two-phase arbitrary rotating quantities.

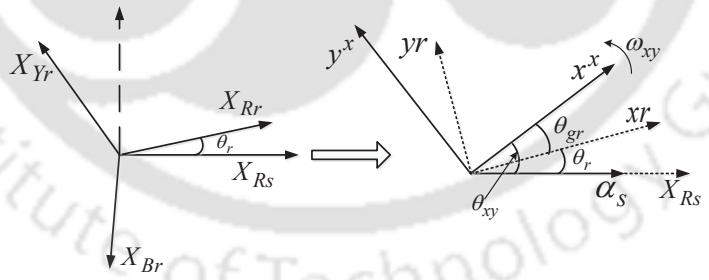

Fig. 2.7: Vector diagram for rotor quantities conversion.

$$\begin{bmatrix} X^x_{xr} \\ X^x_{yr} \end{bmatrix} = \frac{2}{3} \begin{bmatrix} \cos\theta_{gr} & \cos\left(\theta_{gr}-\frac{2\pi}{3}\right) & \cos\left(\theta_{gr}+\frac{2\pi}{3}\right) \\ -\sin\theta_{gr} & -\sin\left(\theta_{gr}-\frac{2\pi}{3}\right) & -\sin\left(\theta_{gr}+\frac{2\pi}{3}\right) \\ \frac{1}{2} & \frac{1}{2} & \frac{1}{2} \end{bmatrix} \begin{bmatrix} X_{Rr} \\ X_{Yr} \\ X_{Br} \end{bmatrix} \tag{2.26}$$

where θ_{gr}=θ_{xy}-θ_r.

The three-phase stator voltage and flux linkage expressions are given in (2.1 – 2.2) can be trans-

formed into a rotating reference (x^x-y^x) frame by using the transformation matrix (2.25). Then, the voltage expression of (2.1) in the x^x-y^x frame is represented as:

$$\left[X_{xys}^{x}\right]^{-1}\left[V_{xys}^{x}\right]=\left[R_s\right]\left[X_{xys}^{x}\right]^{-1}\left[i_{xys}^{x}\right]+p\left[\left[X_{xys}^{x}\right]^{-1}\left[\lambda_{xys}^{x}\right]\right] \tag{2.27}$$

Equation (2.28) is obtained after the multiplication of the matrix $[X_{xys}^{x}]$ with the (2.27).

$$\left[X_{xys}^{x}\right]\left[X_{xys}^{x}\right]^{-1}\left[V_{xys}^{x}\right]=\left[X_{xys}^{x}\right]\left[R_s\right]\left[X_{xys}^{x}\right]^{-1}\left[i_{xys}^{x}\right]+\left[X_{xys}^{x}\right]p\left[\left[X_{xys}^{x}\right]^{-1}\left[\lambda_{xys}^{x}\right]\right] \tag{2.28}$$

After the simplification, equation (2.28) is written as:

$$\left[V_{xys}^{x}\right]=\underbrace{\left[R_s\right]\left[i_{xys}^{x}\right]}_{1}+\underbrace{\left[X_{xys}^{x}\right]p\left[\left[X_{xys}^{x}\right]^{-1}\right]\left[\lambda_{xys}^{x}\right]}_{2}+\underbrace{\left[X_{xys}^{x}\right]\left[X_{xys}^{x}\right]^{-1}p\left[\left[\lambda_{xys}^{x}\right]\right]}_{3} \tag{2.29}$$

By solving the second and third term of (2.29), yields the simplified voltage expression in x^x-y^x frame as:

$$\left[V_{xys}^{x}\right]=\left[R_s\right]\left[i_{xys}^{x}\right]+\omega_{xy}\left[J\right]\left[\lambda_{xys}^{x}\right]+p\left[\left[\lambda_{xys}^{x}\right]\right] \tag{2.30}$$

where $J=\begin{bmatrix}0 & -1\\ 1 & 0\end{bmatrix}$

Similarly, the stator flux linkage expression (2.2) in x^x-y^x frame is given as:

$$\left[X_{xys}^{x}\right]^{-1}\left[\lambda_{xys}^{x}\right]=\left[L\right]\left[X_{xys}^{x}\right]^{-1}\left[i_{xys}^{x}\right]+\left[M\right]\left[\left[X_{xys}^{x}\right]^{-1}\left[i_{xyr}^{x}\right]\right] \tag{2.31}$$

After multiplying (2.31) with the matrix $[X_{xys}^{x}]$, equation (2.32) is obtained.

$$\left[X_{xys}^{x}\right]\left[X_{xys}^{x}\right]^{-1}\left[\lambda_{xys}^{x}\right]=\left[X_{xys}^{x}\right]\left[L\right]\left[X_{xys}^{x}\right]^{-1}\left[i_{xys}^{x}\right]+\left[\left[X_{xys}^{x}\right]\left[M\right]\left[X_{xys}^{x}\right]^{-1}\right]\left[i_{xyr}^{x}\right] \tag{2.32}$$

The stator flux linkage expression given in (2.33) in x^x-y^x frame is obtained by the simplifying the equation (2.32).

$$\left[\lambda_{xys}^{x}\right]=\left[L_s\right]\left[i_{xys}^{x}\right]+\left[L_m\right]\left[i_{xyr}^{x}\right] \tag{2.33}$$

Similarly, using the transformation matrix (2.26), the three-phase rotor voltage and flux linkage expressions (2.3-2.4) can be transformed into an arbitrary rotating reference (x^x-y^x) frame. The rotor voltage expressions (2.4) in the x^x-y^x frame is given as:

$$\left[X_{xyr}^{x}\right]^{-1}\left[V_{xyr}^{x}\right]=\left[R_r\right]\left[X_{xyr}^{x}\right]^{-1}\left[i_{xyr}^{x}\right]+p\left[\left[X_{xyr}^{x}\right]^{-1}\left[\lambda_{xyr}^{x}\right]\right] \tag{2.34}$$

After multiplying (2.34) with the matrix $[X^x_{xyr}]$, expression (2.35) is obtained.

$$\left[X^x_{xyr}\right]\left[X^x_{xyr}\right]^{-1}\left[V^x_{xyr}\right] = \underbrace{\left[X^x_{xyr}\right]\left[R_r\right]\left[X^x_{xyr}\right]^{-1}\left[i^x_{xyr}\right]}_{1} + \underbrace{\left[X^x_{xyr}\right] p\left[\left[X^x_{xyr}\right]^{-1}\left[\lambda^x_{xyr}\right]\right]}_{2} \tag{2.35}$$

Solving the first and second terms of (2.35), the rotor voltage expression in the $x^x - y^x$ frame is written as:

$$\left[V^x_{xyr}\right] = \left[R_r\right]\left[i^x_{xyr}\right] + \left(\omega_{xy} - \omega_r\right)\left[J\right]\left[\lambda^x_{xyr}\right] + p\left[\left[\lambda^x_{xyr}\right]\right] \tag{2.36}$$

Similarly, the rotor flux linkage expression given in (2.4) can be represented in the $x^x - y^x$ frame as:

$$\left[X^x_{xyr}\right]^{-1}\left[\lambda^x_{xyr}\right] = \left[L\right]\left[X^x_{xyr}\right]^{-1}\left[i^x_{xyr}\right] + \left[M\right]\left[\left[X^x_{xyr}\right]^{-1}\left[i^x_{xys}\right]\right] \tag{2.37}$$

By multiplying (2.37) with the matrix $[X^x_{xyr}]$, equation (2.38) is yielded.

$$\left[X^x_{xyr}\right]\left[X^x_{xyr}\right]^{-1}\left[\lambda^x_{xyr}\right] = \left[X^x_{xyr}\right]\left[L\right]\left[X^x_{xyr}\right]^{-1}\left[i^x_{xyr}\right] + \left[\left[X^x_{xyr}\right]\left[M\right]\left[X^x_{xyr}\right]^{-1}\right]\left[i^x_{xys}\right] \tag{2.38}$$

Solving (2.38), the simplified rotor flux linkage expression in the $x^x - y^x$ frame is given as:

$$\left[\lambda^x_{xyr}\right] = \left[L_r\right]\left[i^x_{xyr}\right] + \left[L_m\right]\left[i^x_{xys}\right] \tag{2.39}$$

Finally, the equations (2.30), (2.33), (2.36), and (2.39) represents the governing equations of the voltages and flux linkages of the stator and rotor quantities in the $x^x - y^x$ reference frame, and are given below:

$$\begin{aligned}
\left[V^x_{xys}\right] &= \left[R_s\right]\left[i^x_{xys}\right] + \omega_{xy}\left[J\right]\left[\lambda^x_{xys}\right] + p\left[\left[\lambda^x_{xys}\right]\right] \\
\left[V^x_{xyr}\right] &= \left[R_r\right]\left[i^x_{xyr}\right] + \left(\omega_{xy} - \omega_r\right)\left[J\right]\left[\lambda^x_{xyr}\right] + p\left[\left[\lambda^x_{xyr}\right]\right] \\
\left[\lambda^x_{xys}\right] &= \left[L_s\right]\left[i^x_{xys}\right] + \left[L_m\right]\left[i^x_{xyr}\right] \\
\left[\lambda^x_{xyr}\right] &= \left[L_r\right]\left[i^x_{xyr}\right] + \left[L_m\right]\left[i^x_{xys}\right]
\end{aligned} \tag{2.40}$$

The expended form of the matrices $[V^x_{xys}]$ and $[\lambda^x_{xys}]$ of (2.40) is written as:

$$\begin{aligned}
V^x_{xs} &= R_s i^x_{xs} - \omega_{xy}\lambda^x_{ys} + \frac{d\lambda^x_{xs}}{dt} \\
V^x_{ys} &= R_s i^x_{ys} + \omega_{xy}\lambda^x_{xs} + \frac{d\lambda^x_{ys}}{dt} \\
\lambda^x_{xs} &= L_s i^x_{xs} + L_m i^x_{xr} \\
\lambda^x_{ys} &= L_s i^x_{ys} + L_m i^x_{yr}
\end{aligned} \tag{2.41}$$

Similarly, the expended form of the matrices $[V^x_{xyr}]$ and $[\lambda^x_{xyr}]$ of (2.40) is given as:

$$\begin{aligned} V^x_{xr} &= R_r i^x_{xr} - (\omega_{xy} - \omega_r)\,\lambda^x_{yr} + \frac{d\lambda^x_{xr}}{dt} \\ V^x_{yr} &= R_r i^x_{yr} + (\omega_{xy} - \omega_r)\,\lambda^x_{xr} + \frac{d\lambda^x_{yr}}{dt} \\ \lambda^x_{xr} &= L_r i^x_{xr} + L_m i^x_{xs} \\ \lambda^x_{yr} &= L_r i^x_{yr} + L_m i^x_{ys} \end{aligned} \tag{2.42}$$

By using λ^x_{xs}, λ^x_{ys} of equation (2.41) and λ^x_{xr}, λ^x_{yr} of equation (2.42), the relation between λ^x_{xs} and λ^x_{xr}; λ^x_{ys} and λ^x_{yr} is given below.

$$\begin{aligned} \lambda^x_{xs} &= \sigma L_s i^x_{xs} + \frac{L_m}{L_r}\lambda^x_{xr} \\ \lambda^x_{ys} &= \sigma L_s i^x_{ys} + \frac{L_m}{L_r}\lambda^x_{yr} \end{aligned} \tag{2.43}$$

where, $\sigma = 1 - \frac{L_m^2}{L_s L_r}$.

The IM model in an arbitrary rotating reference ($x^x - y^x$) frame given in (2.41-2.43) can be represented in the different reference frames, such as stationary and synchronous. Therefore, the upcoming subsection presents the IM model equations in the stationary reference (α-β) frame and synchronously rotating reference ($d-q$) frame.

2.2.3 IM Model in Stationary Reference (α-β) Frame

The IM model expressions in α-β frame are derived by substituting ω_{xy} is equal to zero in (2.41) and (2.42); and replacing the subscripts $^x_{xs}$, $^x_{ys}$ of (2.41) and (2.42) with αs and βs, respectively. Then, the voltages and flux linkages expressions of the stator and rotor quantities in α-β frame are given as follows:

$$V_{\alpha s} = R_s i_{\alpha s} + \frac{d\lambda_{\alpha s}}{dt} \tag{2.44a}$$

$$V_{\beta s} = R_s i_{\beta s} + \frac{d\lambda_{\beta s}}{dt} \tag{2.44b}$$

$$\lambda_{\alpha s} = L_s i_{\alpha s} + L_m i_{\alpha r} \tag{2.44c}$$

$$\lambda_{\beta s} = L_s i_{\beta s} + L_m i_{\beta r} \tag{2.44d}$$

$$V_{\alpha r} = R_r i_{\alpha r} - \omega_r \lambda_{\beta r} + \frac{d\lambda_{\alpha r}}{dt} \tag{2.45a}$$

$$V_{\beta r} = R_r i_{\beta r} + \omega_r \lambda_{\alpha r} + \frac{d\lambda_{\beta r}}{dt} \tag{2.45b}$$

$$\lambda_{\alpha r} = L_r i_{\alpha r} + L_m i_{\alpha s} \tag{2.45c}$$

$$\lambda_{\beta r} = L_r i_{\beta r} + L_m i_{\beta s} \tag{2.45d}$$

In α-β frame, using linear transformations, the three phases quantities (i.e., voltages, currents, and flux linkages) are referred to as a set of orthogonal co-ordinate axes that are stationary with respect to the stator [87]. Thus, the resulting differential equations in α-β frame are linear and have constant coefficients for the case when the rotor speed (ω_r) is constant. The equations in α-β are readily soluble by the operational methods. The control structures which required to deal with stator quantities only, and less dependent upon rotor quantities, mainly employ a stationary frame of reference for the transformations (RYB to α β transformation).

2.2.4 IM Model in Synchronous Rotating Reference ($d-q$) Frame

The IM model in the synchronously rotating reference ($d-q$) frame is derived by replacing ω_{xy}, and the subscripts x, y of (2.41) and (2.42) with ω_s, d, and q, respectively. Then, the voltages and flux linkages equations in the $d-q$ frame are written as follows:

$$V_{ds} = R_s i_{ds} - \omega_s \lambda_{qs} + \frac{d\lambda_{ds}}{dt} \tag{2.46a}$$

$$V_{qs} = R_s i_{qs} + \omega_s \lambda_{ds} + \frac{d\lambda_{qs}}{dt} \tag{2.46b}$$

$$\lambda_{ds} = L_s i_{ds} + L_m i_{dr} \tag{2.46c}$$

$$\lambda_{qs} = L_s i_{qs} + L_m i_{qr} \tag{2.46d}$$

$$0 = R_r i_{dr} - (\omega_s - \omega_r)\lambda_{qr} + \frac{d\lambda_{dr}}{dt} \tag{2.47a}$$

$$0 = R_r i_{qr} + (\omega_s - \omega_r)\lambda_{dr} + \frac{d\lambda_{qr}}{dt} \tag{2.47b}$$

$$\lambda_{dr} = L_r i_{dr} + L_m i_{ds} \tag{2.47c}$$

$$\lambda_{qr} = L_r i_{qr} + L_m i_{qs} \tag{2.47d}$$

In $d-q$, the current (I_{ds} & I_{qs}) frequency is consistent with the rotating frequency and is behaved

like a dc current. Then by controlling dc current, the ac current in the reference frame is controlled indirectly. The control structures with more number of PI regulators preferred $d-q$ frame of reference. As the PI controller in a stationary reference frame holds a finite gain for ac component, thus cannot guarantees the system to track ac reference without steady-state error [88,89]. However, the PI controller in the $d-q$ frame holds an infinite gain for the input signals whose frequency is consistent with rotating frequency, and thus achieves zero steady-state error.

The IM equations defined in the $\alpha-\beta$ frame (2.44-2.45) and $d-q$ frame (2.46-2.47) are used to analyze IM performance in both transient and steady-state conditions. In the control algorithm, the IM model equations given in (2.44-2.47) are used for the real-time implementation as well as in simulation. The next subsection describes the electromagnetic torque (T_e) expression in the different reference frames.

2.2.5 Electromagnetic Torque Expression in Different Reference Frame

Fig. 2.8 shows the three-phase (RYB) and two-phase (dq) windings. Assuming that each of the three-phase windings has N_1 turns per phase and equal current magnitudes, the two-phase windings will have $\frac{3N_1}{2}$ turns per phase for mmf equality [84]. In other words, for power equivalence, the power input to the three-phase motor model has to be equal to the power input to the two-phase motor model.

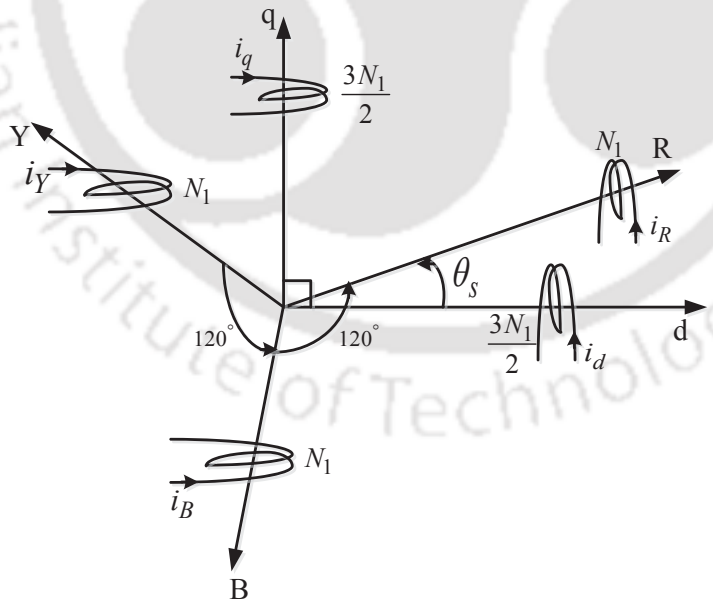

Fig. 2.8: Three-phase (RYB) and two-phase (dq) stator windings.

The torque expression in different reference frames can be derived using the motor input power.

The motor input power (P_{in}) in the $d-q$ frame is given as [84]:

$$P_{in} = \frac{3}{2}\left(V_{ds}i_{ds} + V_{qs}i_{qs}\right) \tag{2.48}$$

By substituting the stator voltages from (2.46) in (2.48), P_{in}'s expression is rewritten as:

$$P_{in} = \underbrace{\frac{3}{2}R_s\left(i_{ds}^2 + i_{qs}^2\right)}_{1} + \underbrace{\frac{3}{2}\left(i_{ds}\frac{d\lambda_{ds}}{dt} + i_{qs}\frac{d\lambda_{qs}}{dt}\right)}_{2} + \underbrace{\frac{3}{2}\omega_s\left(\lambda_{ds}i_{qs} - \lambda_{qs}i_{ds}\right)}_{3} \tag{2.49}$$

In (2.49), the right side first term (1) represents the copper loss (P_{cu}) in the stator; second terms (2) represents the stored magnetic energy (P_{mag}), and the third term (3) is the actual air-gap power(P_{gap}).

$$\begin{aligned} P_{cu} &= \tfrac{3}{2}R_s\left(i_{ds}^2 + i_{qs}^2\right) \\ P_{mag} &= \tfrac{3}{2}\left(i_{ds}\tfrac{d\lambda_{ds}}{dt} + i_{qs}\tfrac{d\lambda_{qs}}{dt}\right) \\ P_{gap} &= \tfrac{3}{2}\omega_s\left(\lambda_{ds}i_{qs} - \lambda_{qs}i_{ds}\right) \end{aligned} \tag{2.50}$$

The P_{gap} can be determined using T_e and ω_s as:

$$P_{gap} = T_e\frac{\omega_s}{P_p} \tag{2.51}$$

Thus, by using P_{gap} from (2.50) and (2.51), the T_e can be determined as:

$$T_e = \frac{3P_p}{2}\left(\lambda_{ds}i_{qs} - \lambda_{qs}i_{ds}\right) \tag{2.52}$$

By using the transformation matrix (2.20), (2.52) can be represented in $\alpha-\beta$ frame as:

$$T_e = \frac{3P_p}{2}\left(\lambda_{\alpha s}i_{\beta s} - \lambda_{\beta s}i_{\alpha s}\right) \tag{2.53}$$

The expression given in (2.52) and (2.53) can be used indirectly and directly in IM control methods to estimate the T_e value.

This section discussed the mathematical model of IM and transformation of three-phase quantities into an equivalent two-phase arbitrary rotating reference frame. The reduced IM model expressions in α-β and $d-q$ reference frames are described. Further, the T_e expression is explained in $d-q$ and α-β frame. The developed IM model in the different reference frames can be employed in the vector control algorithms to achieve the desired control action. The control techniques are discussed in the next section.

2.3 Vector Control Strategies

The most common control techniques for high-performance AC motor drives are vector control (VC) techniques. In the VC strategy, independent control of the flux linkage and torque can be achieved, which is similar to separately excited direct current (DC) motor control. This control develops a fast dynamic response, better transient and steady-state motor performance [25, 26].

Such control techniques are preferred in high-performance applications, such as EV drives, high-speed motor drives, robotics, servos, and multilevel converter-based motor drives. Various derived forms of VC techniques are developed in the late sixties and early seventies, and still in works are continuing to improve their performance for the desired application. The most popular VC strategies are field-oriented control (FOC) and direct torque control (DTC) [90]. Fig. 2.9 shows the classification of VC strategies with derived form of FOC and DTC [91]. In recent times, the FOC strategy became the industry benchmark for high-performance applications. Therefore, most of the EV drive-train controllers use a FOC strategy to control the IM. In the upcoming subsection, the basic principle of FOC strategy and its variants is discussed.

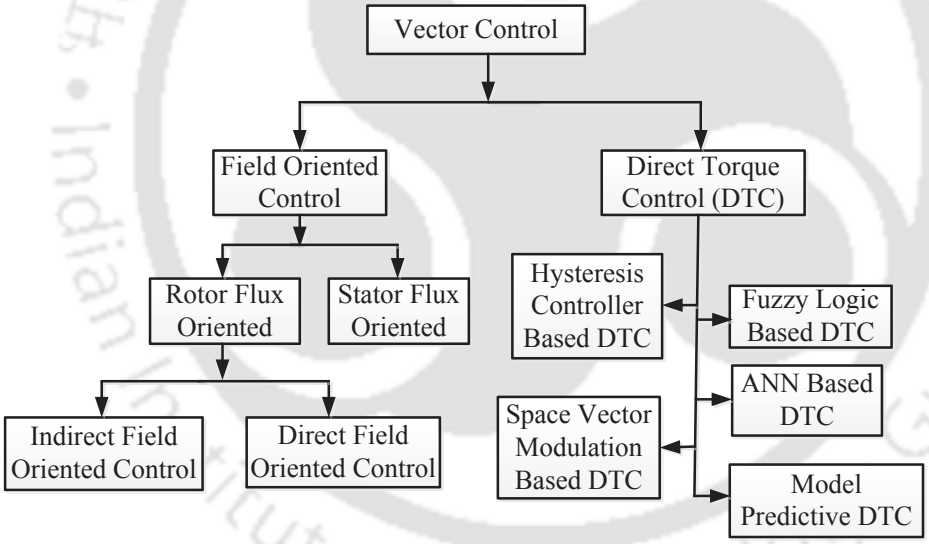

Fig. 2.9: IM vector control strategies classification.

2.3.1 Field Oriented Control Technique

In this scheme, the independent control of torque and flux is achieved by controlling the decoupled stator current components (i.e., i_{ds} and i_{qs}). These currents i_{ds} and i_{qs} are responsible for producing the flux and torque, respectively. For controlling the torque and flux, the values i_{ds} and i_{qs} are compared with their actual values. In the FOC strategy, all quantities are converted into a rotor flux rotating

reference frame, which is DC in nature. Hence, the control variable is preferred in DC value since it is easy to handle, and a better control action is achieved. The electromagnetic torque given in (2.52) can be represented with rotor flux quantities as:

$$T_e = \frac{3}{2}\frac{P}{2}\frac{L_m}{L_r}\left(\lambda_{dr} i_{qs} - \lambda_{qr} i_{ds}\right) \tag{2.54}$$

Based on the flux linkage vector orientation, the FOC scheme is classified into; 1) FOC scheme with stator flux linkage orientation, 2) FOC scheme with airgap flux linkage orientation, and 3) FOC scheme with rotor flux linkage orientation. The rotor flux linkage vector-oriented FOC scheme is widely adopted due to the less complexity, and easy to achieve decoupling of torque and flux linkage [92].

In the rotor flux linkage vector orientation, the q-axis rotor flux linkage (λ_{qr}) is always equal to zero since the d-axis rotor flux is aligned with the rotating reference frame real axis, as shown in Fig. 2.10. Therefore, (2.54) can be rewritten as:

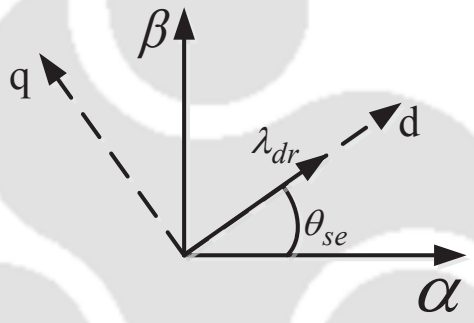

Fig. 2.10: Vector representation of FOC principle

$$T_e = K_t \lambda_{dr} i_{qs} \tag{2.55}$$

where, $K_t = \frac{3}{2}\frac{P}{2}\frac{L_m}{L_r}$ is the torque constant.

Substituting $\lambda_{qr} = 0$ in (2.47a) and using (2.47c), λ_{dr} can be determined as:

$$\lambda_{dr} = \left(\frac{L_m}{\tau_r p + 1}\right) i_{ds} \tag{2.56}$$

where, $\tau_r = \frac{L_r}{R_r}$ is the rotor time constant. Thus, the λ_{dr} can be controlled by adjusting the i_{ds}. In (2.56), when i_{ds} is kept constant, λ_{dr} can be approximately equal to $L_m i_{ds}$. Then, the (2.55) can be further simplified as:

$$T_e = \frac{3}{2}\frac{P}{2}\frac{L_m^2}{L_r} i_{ds} i_{qs} \tag{2.57}$$

In (2.57), i_{ds} is called a flux producing stator current component, and i_{qs} is torque producing part of stator current. Thus, by means of the FOC scheme, the value of T_e can be effectively controlled by adjusting the i_{qs} keeping i_{ds} constant.

The FOC scheme with rotor flux linkages orientation requires the positions of rotor flux linkages for every instant of time to control IM. Based on the acquired rotor flux linkage phasor position (θ_r), FOC technique can be classified as direct rotor flux linkage-oriented control (DRFOC) scheme and indirect rotor flux linkage-oriented control (IRFOC) scheme [93]. A brief description of these two control strategies is given in subsequent subsections.

2.3.1.1 DRFOC Strategy

Fig. 2.11 shows the schematic block diagram of the DRFOC scheme. In this scheme, the estimated rotor flux linkage (λ_r) helps to determine θ_r. The estimation of λ_r is achieved using measured stator currents and rotor speed. Here, θ_r is used to convert the stator current components in the stator reference frame ($i_{\alpha s}$ and $i_{\beta s}$) into a synchronous rotating reference frame, i.e., i_{ds} and i_{qs} currents. These currents are compared with their reference values (i_{ds}^* and i_{qs}^*), and the generated errors are passed through PI regulators. Based on the stator currents error, the reference voltages (V_{ds}^* and V_{qs}^*) are obtained and transformed into stationary reference frame voltages ($V_{\alpha s}{}^*$ and $V_{\beta s}{}^*$) to generate the required inverter switching sequence for achieving desired control action. The error (λ_r^*-λ_r) value of rotor flux linkage is passed through a PI regulator to obtained i_{ds}^*. However, the value of i_{qs}^* is determined from the torque controller after comparing the reference torque (T_e^*) and estimated torque (T_e) values whereas, T_e^* is obtained from the speed controller shown in Fig. 2.11.

The control algorithm's performance depends on the accurate positioning of θ_r for coordinate transformation and maintaining the correct field orientation. Complex estimators or observers are required to estimate the rotor flux position or angle.

2.3.1.2 IRFOC Strategy

The detailed schematic of the IRFOC scheme is illustrated in Fig. 2.12. In this technique, θ_{se} is determined by integrating the summation of calculated slip speed and the estimated (or) measured rotor speed (ω_r) as given in (2.42).

$$\theta_{se} = \int (\omega_{sl} + \omega_r)\, dt \tag{2.58}$$

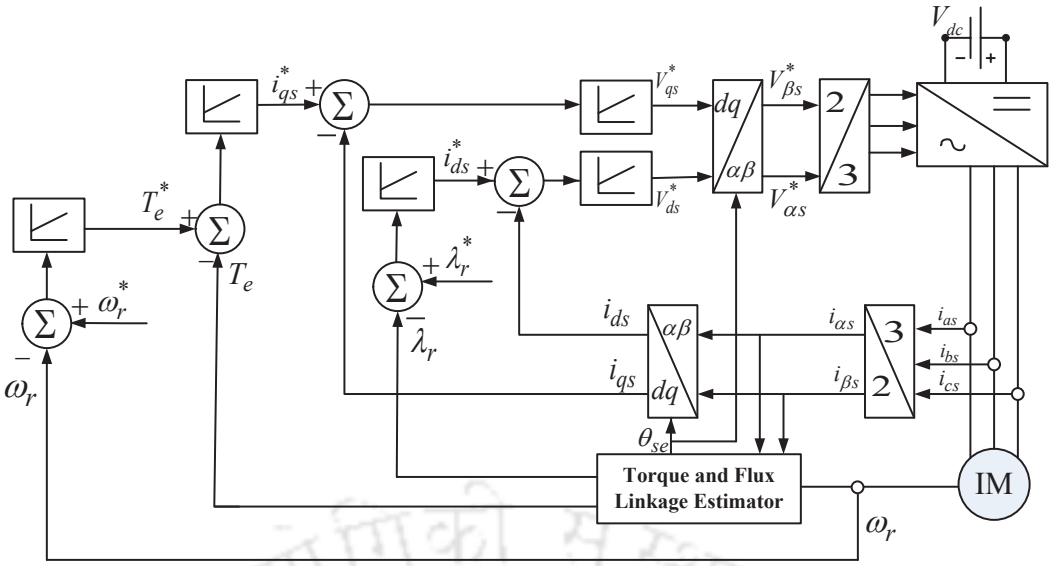

Fig. 2.11: Direct rotor flux linkage oriented FOC strategy

where, $\omega_{sl} = \frac{R_r}{L_r}\frac{i_{qs}^*}{i_{ds}^*}$ [93].

The required slip speed (ω_{sl}) is calculated from the values of reference currents, i.e. i_{ds}^* and i_{qs}^*. Here, λ_r is indirectly controlled by adjusting the i_{ds}^* current. The remaining operation of this control scheme is similar to the DRFOC scheme.

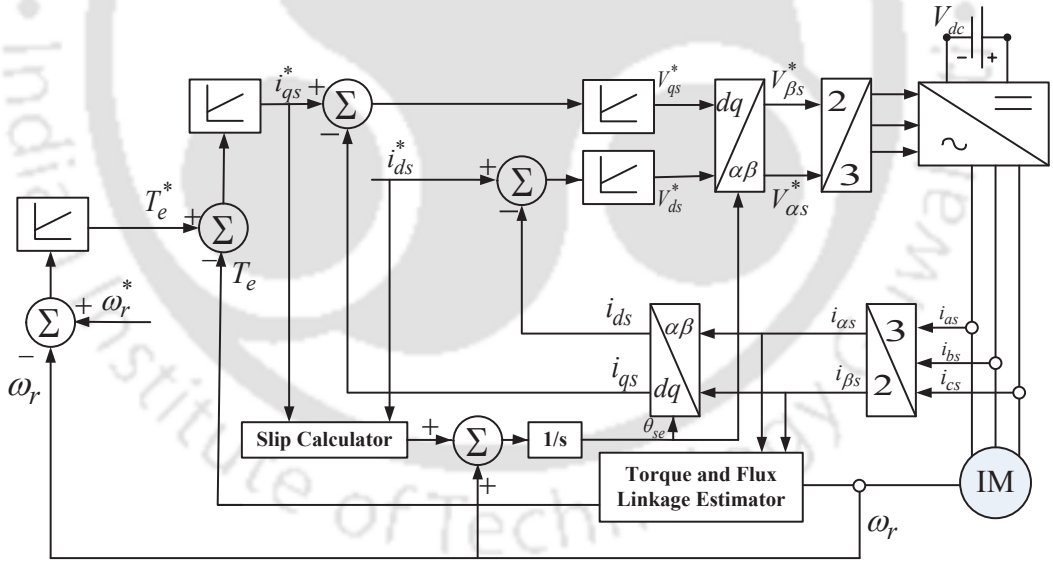

Fig. 2.12: Indirect rotor flux linkage oriented FOC strategy

Both control strategies are extensively studied in the literature and widely used in motor drive applications. However, the major drawbacks of DRFOC and IRFOC schemes are [94]:

- Parameter dependency R_r, L_r in IRFOC, and R_s for the DRFOC.
- Transformations from one reference frame to another reference frame is essential.

- Require accurate location of the flux linkage angle.
- PWM signal generator required.
- Complex control architecture.

Whereas the advantages of these techniques are:

- Good dynamic performance.
- Low torque ripple and current harmonics.
- Operates at the constant switching frequency.

In this subsection, the basic principle of FOC strategy and its variant in the rotor flux orientation scheme, i.e., DRFOC and IRFOC, are described. Also, the detailed schematic diagram with the merits and demerits of both control schemes is explained. However, another type of vector control technique is reported in the literature, i.e., DTC, which has a faster dynamic response than the FOC scheme and a simpler structure. In the next subsequent subsection, the basic principle of the DTC scheme is discussed.

2.3.2 Direct Torque Control

The DTC scheme was proposed by Takahashi (1986) [28] and Depenbrock (1988) [31]. In this scheme, direct and independent control of torque and stator flux linkage is achieved by applying the optimal switching voltage vectors for the voltage source inverter. The selection of switching voltage vectors is made such that the torque and flux errors are restricted within the respective hysteresis bands.

For an IM, the electromagnetic torque (T_e) of the motor can be written as follows [95]:

$$\begin{aligned} T_e &= \tfrac{3}{2}P\tfrac{L_m}{\sigma L_s L_r}\overline{\lambda_r}\otimes\overline{\lambda_s} \\ &= \tfrac{3}{2}P\tfrac{L_m}{\sigma L_s L_r}\left|\overline{\lambda_r}\right|\left|\overline{\lambda_s}\right|\sin(\theta_s-\theta_r) \\ &= \tfrac{3}{2}P\tfrac{L_m}{\sigma L_s L_r}\left|\overline{\lambda_r}\right|\left|\overline{\lambda_s}\right|\sin(\gamma) \end{aligned} \tag{2.59}$$

where $\otimes$ represents the cross product; $\gamma=(\theta_s-\theta_r)$, and γ is the angle between the rotor and stator flux linkage vector, θ_s and θ_r are the angles of stator and rotor flux vectors with respect to the stationary axis, respectively.

Fig. 2.13 shows the vector diagram of the stator and rotor flux linkage vector in the stationary reference frame. The equation (2.59) depicts that the value of T_e is controlled by adjusting γ, if the magnitude of the stator flux linkage vector ($|\lambda_s|$) is held constant. The appropriate value of γ is achieved by selecting the optimal stator voltage vector.

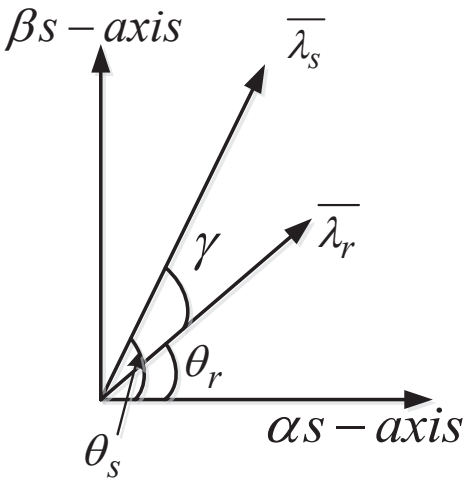

Fig. 2.13: Vector representation of stator and rotor flux linkage vectors with respect to stationary axis.

Fig. 2.14(a) shows the schematic diagram of a two-level voltage source inverter. The total number of possible switching voltage vectors are eight, of which six are active voltage vectors, and the rest are zero voltage vectors. A zero voltage vector is produced if the upper switches of three limbs are either ON or OFF state. Fig. 2.14(b) shows the graphical representation of active voltage vectors. The mathematical description of voltage space vector using inverter switching states is expressed as follows.

$$\overline{v_s} = \frac{2}{3} V_{dc} \left[S_a + S_b e^{j\frac{2\pi}{3}} + S_c e^{-j\frac{2\pi}{3}} \right] \tag{2.60}$$

where S_a, S_b, and S_c are the the inverter switches states as depicted in Fig. 2.14(a).

The stator flux linkage is obtained by integrating the stator back-EMF ($\overline{v_s} - R_s \overline{i_s}$) as follows:

$$\overline{\lambda_s} = \int \left(\overline{v_s} - R_s \overline{i_s} \right) \tag{2.61}$$

where $\overline{\lambda_s} = \lambda_{\alpha s} + j\lambda_{\beta s}$, $\overline{v_s} = V_{\alpha s} + jV_{\beta s}$, and $\overline{i_s} = i_{\alpha s} + ji_{\beta s}$.

Neglecting the stator resistance voltage drop (only for analysis purpose) in the equation (2.61), the change in stator flux linkage vector is given as follows [86]:

$$\Delta \overline{\lambda_s} = \overline{v_s} \, \Delta T \tag{2.62}$$

The equation (2.62) concludes that the change in stator flux linkage vector, $\Delta\overline{\lambda_s}$, is proportional to the space vector, $\overline{v_s}$, applied for the shorter interval of time, ΔT. Therefore, $\Delta\overline{\lambda_s}$ follows the voltage space vector, $\overline{v_s}$, and the magnitude of change in $\Delta\overline{\lambda_s}$ depends on the magnitude of $\overline{v_s}$ applied.

Thus, applying an appropriate voltage vector based on the instantaneous stator flux linkage vector location, a constant magnitude and continuous movement of the stator flux linkage vector is achieved.

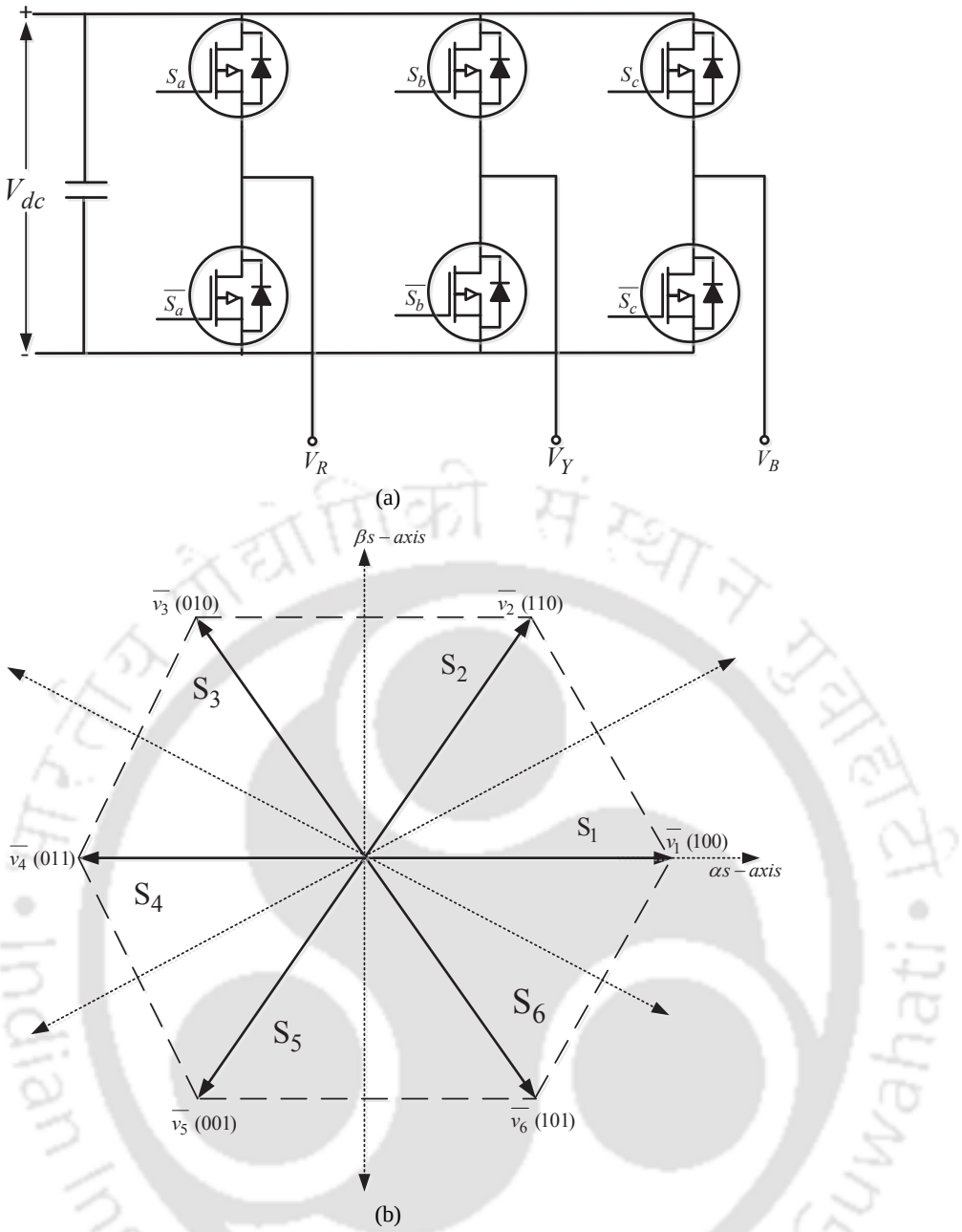

Fig. 2.14: (a) Schematic diagram of voltage source inverter (VSI) and output voltage vectors (b) Representation of instantaneous voltage vectors.

The stator flux linkage vector trajectory depicted in Fig. 2.15 rotates in an anti-clockwise direction along with the selected voltage vectors. The lookup table for the selection of voltage space vectors is given in Table 2.1.

This section explains the basic principle of the DTC scheme with independent control of T_e and stator λ_s. Based on the DTC principle, a detailed control architecture for the IM drivetrain is explained in the subsequent subsection.

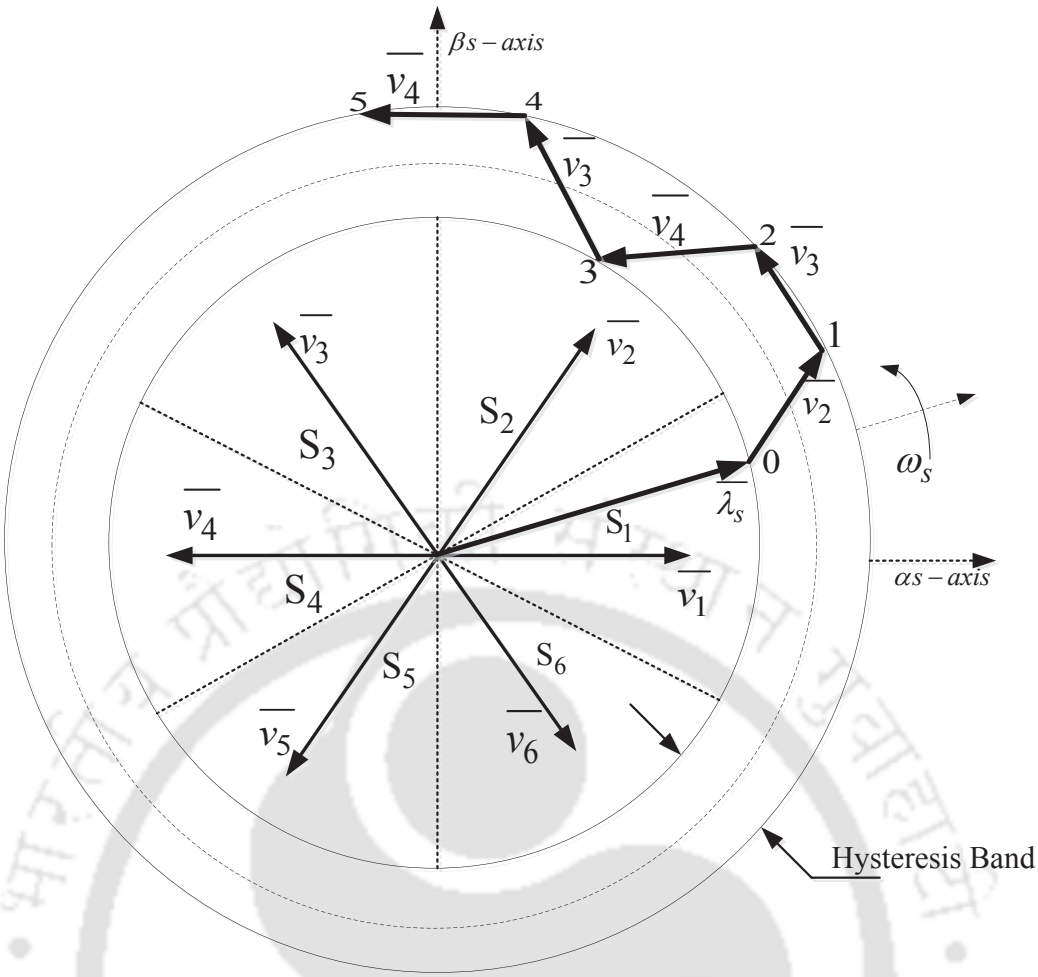

Fig. 2.15: Trajectory of stator flux linkage vector control in anti-clockwise direction.

2.3.2.1 Hysteresis Controller based DTC Scheme

Fig. 2.16 shows the detailed schematic block diagram of the hysteresis controller-based DTC (HC-DTC). The HC-DTC scheme requires a torque controller, flux controller, and voltage vector switching table. These are the main blocks of the HC-DTC scheme, which are explained in the subsequent subsections.

2.3.2.2 Torque Controller

The torque controller is a three-level hysteresis comparator. The comparator output can be either $+1$ or 0 or -1, depends on the error of the torque. When the output is $+1$, a torque increasing active voltage vector is applied, and if the output is -1, a decreasing torque vector is employed. If the comparator output is zero, it means the torque error is small, and a null voltage vector has to be

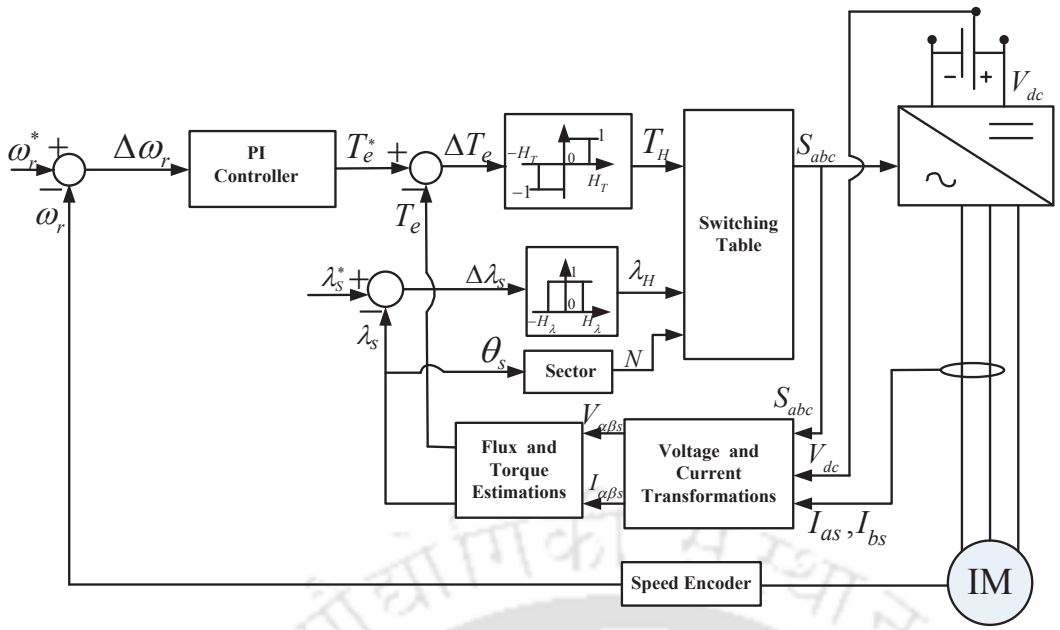

Fig. 2.16: Hysteresis controller based direct torque control strategy.

selected. The representation of torque error status is given as follows:

$$d_{T_e}(k) = \begin{cases} +1, & if\ T_e^* - \frac{\Delta T_e}{2} \geq T_e \\ -1, & if\ T_e^* + \frac{\Delta T_e}{2} \leq T_e \\ 0, & otherwise \end{cases} \tag{2.63}$$

where $\frac{\Delta T_e}{2}$ is the torque hysteresis comparator band width.

2.3.2.3 Flux Controller

The flux controller is a two-level hysteresis comparator. The output of the comparator is either $+1$ or -1 depending on the flux error. A voltage vector with increasing in flux is applied when the output is $+1$, and if the output is -1, a flux decreasing voltage vector is employed. Depending on the flux error, the comparator outputs either $+1$ or -1. The general representation of the flux error controller is given as,

$$d_{\lambda_s}(k) = \begin{cases} +1, & if\ \lambda_s^* - \frac{\Delta\lambda_s}{2} \geq \lambda_s \\ -1, & if\ \lambda_s^* + \frac{\Delta\lambda_s}{2} \leq \lambda_s \end{cases} \tag{2.64}$$

where $\frac{\Delta\lambda_s}{2}$ is the flux hysteresis comparator band width.

2.3.2.4 Voltage Vector Switching Table

Table 2.1 shows the voltage vector switching table consisting of optimal voltage vectors. The outputs of the flux and torque controllers are the inputs to the switching table. Moreover, to obtain the optimal voltage vectors from the switching table, sector information based on the stator flux linkage position is also required. Based on the switching table's inputs, the desired voltage vector is selected, regulating both the stator flux linkage and the torque in the required way.

Table. 2.1: DTC Switching table scheme.

$\Delta\lambda$	ΔT_e	S_1	S_2	S_3	S_4	S_5	S_6
$+1$	$+1$	V_2	V_3	V_4	V_5	V_6	V_1
$+1$	-1	V_6	V_1	V_2	V_3	V_4	V_5
$+1$	0	V_7	V_8	V_7	V_8	V_7	V_8
-1	$+1$	V_3	V_4	V_5	V_6	V_1	V_2
-1	-1	V_5	V_6	V_1	V_2	V_3	V_4
-1	0	V_8	V_7	V_8	V_7	V_8	V_7

The DTC-based speed control of IM is achieved by considering the measured or estimated speed (ω_r in rad/sec or N_r in rpm) as the feedback term. The feedback speed (ω_r or N_r) signal is compared with the reference speed (ω_r^* or N_r^*) and generated speed error is passed through a PI regulator. The output of the PI regulator is considered as T_e^* (shown in Fig. 2.16). The inner loop estimates the magnitudes of estimated torque (T_e) and flux linkage (λ_s) based on stator voltages and currents. The T_e and λ_s are compared with their reference (T_e^*, λ_s^*) values, which are inputs to respective hysteresis comparators. An optimized voltage vector is applied on the motor through the inverter based on the generated error status from hysteresis comparators and sector information. The selected voltage vector sequence reduces the errors and achieves the desired control operation.

The HC-DTC scheme provides a fast torque response, and due to the absence of the current controller, PWM generator, coordinate transformation, its control structure is simple [28]. However, it has some limitations like high torque ripple, high flux ripple, variable switching frequency, and flux drooping at low-speed operation. Several methods are proposed in the literature to improve HC-DTC performance. Out of these methods, the Space Vector Modulation DTC is popular and considered as an alternate of HC-DTC scheme. In the next subsection, the Space Vector Modulation DTC strategy is presented.

2.3.3 Space Vector Modulation based DTC Strategy

The Space Vector Modulation (SVM) based DTC control scheme is shown in Fig.2.17. It has two control blocks, one for the stator flux (λ_s) and another for electromagnetic torque (T_e). In the scheme, the generation of stator voltage signals ($V^*_{\alpha s}$ and $V^*_{\beta s}$) is accomplished by employing PI regulators for achieving desired control action. The PI controller, whose input is the electromagnetic torque's error ($T^*_e - T_e$), gives the output voltage value V^*_{qs} required to minimize electromagnetic torque error. On the other hand, the PI controller's output, whose input is the stator flux error ($\lambda^*_s - \lambda_s$), provides the voltage value V^*_{ds} required to minimize stator flux error. The coordinate transform block transforms the voltages v^*_{ds} and v^*_{qs} which are in the reference system fixed at the stator flux (with an angle θ_s) to the stationary reference system. The voltages resulting from the transformation are modulated through the SVM block to generate the inverter's required switching signals. A trial and error method is used to tuned PI controllers to achieve desired control action. However, with more PI regulators' introduction to the control structure, the control algorithm becomes complex.

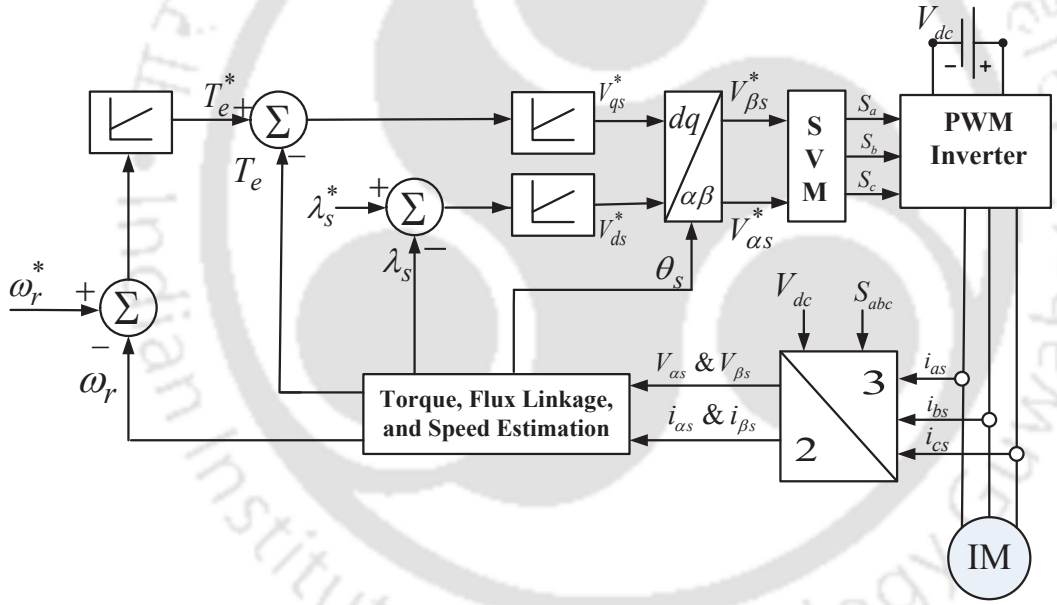

Fig. 2.17: Space vector modulation based direct torque control scheme.

In another variant of the DCT scheme, the methods such as fuzzy logic (FL) based DTC, artificial neural network (ANN) based DTC, and model predictive (MP) DTC have also provided a significant contribution in improving the performance of DTC. In the FL-based DTC scheme, predefined rules are used to select the switching signals. The switching signals are obtained from the Mamdani de-fuzzification method, and the number of rules has to be increased for better performance control [67]. Though, it results in improved transient response but not much reduction in torque and flux ripples

under steady-state [96]. Most researches have focused on modified DTC techniques, namely, the two-fuzzy controllers in the SVM-DTC technique, FL-DTC-duty ratio control, FL-DTC- predictive control, and even in the multilevel inverter domain [67, 96]. In the ANN-based DTC model, the control algorithms are employed with SVM-DTC using two separate ANN to improve control performance and reduce torque and flux ripples [97]. The first ANN model has been used to select the appropriate inverter switching states, and the second one is used to determine the stator flux vector region. In the MP-DTC technique, the switching signals are generated based on flux and torque error minimization of cost function [98–100]. These modified techniques have obtained improvement in terms of torque and flux ripples reduction. However, these techniques make the control structure more complicated, and it negates the merits of simplicity in the DTC.

Table 2.2 summarizes the conclusions for the control methods discussed in this section from the viewpoint of the controller's features, the easiness of operation at low speeds, high speed, dynamic performance, and implementation complexity. Since the DTC method gives a quick dynamic response. Its implementation is simple and does not require any coordinate transformations and PWM techniques. Despite these advantages, DTC has some challenges like high torque ripple, higher inverter loss, high distortion in voltage, current waveform, variable switching frequency, and required low sampling time [71, 101–104]. Several modified DTC techniques have been proposed in the literature to improve the performance [23, 27, 39, 40, 44, 45, 72–74] by either changing the switching strategy or modifying its basic structure. Moreover, the determination of optimal λ_s^* over a wide range of speed operations is also a challenging problem for DTC-based IM drive. It has a significant impact on drive performance. Therefore, in the next chapter, the impact of λ_s^* on DTC-based IM drive is described.

Table. 2.2: Summary on the various forms of vector control strategies as shown in Fig. 2.9

Properties/ Performance	FOC			DTC				
	SFOC	**DRFOC**	**IRFOC**	**HC-DTC**	**SVM-DTC**	**FL-DTC**	**ANN-DTC**	**MP-DTC**
Defined switching frequency	Yes	Yes	Yes	No	Yes	–	–	–
Torque ripple	Low	Low	Low	High	Medium	Medium	Medium	Medium
Low speed	Favorable	Favorable	Favorable	Neutral	Neutral	Favorable	Favorable	Favorable
High speed	Neutral	Neutral	Neutral	Favorable	Unfavorable	–	–	–
Dynamic response	Fast	Fast	Fast	Very fast	Very fast	Very fast	Very fast	Very fast
Parameter sensitivity	High	High	High	Low	Low	Low	Low	Low
Coordinate transformation	Yes	Yes	Yes	No	No	No	No	No
PWM Modulator	Yes	Yes	Yes	No	Yes	No	No	No
Control tuning	PI gains	PI gains	PI gains	Hysteresis bands	PI gains	PI gains	PI gains	PI gains
Complexity and processing requirements	High	High	High	Lower	Medium	Medium	Medium	Medium

2.4 Conclusion

This chapter explains the motor modeling, and types of reference frame transformations (*R-Y-B* to α-β and α-β to *d-q*) used to design the control laws for steady-state and dynamic operation of the IM. Generally, for the high dynamic performance application, the vector control schemes are preferred. Hence, this chapter explains the principle of operation of the vector control strategies, such as FOC and DTC methods, in brief. The hysteresis controller-based DTC scheme is a highly encouraging non-FOC method due to its ability to regulate the machine torque quickly and correctly. This scheme evades the problem of field orientation.

Besides the advantages of DTC, it has some drawbacks, and one of them's the selection of λ_s^*. The correct determination of λ_s^* for DTC-based IM drive is crucial, and it plays a vital role over a wide range of speed operations. Therefore, in the next chapter, the impact of λ_s^* on DTC-IM drive over a wide range of operations is explained in detail.

भारतीय प्रौद्योगिकी संस्थान गुवाहाटी
Indian Institute of Technology Guwahati

भारतीय प्रौद्योगिकी संस्थान गुवाहाटी
Indian Institute of Technology Guwahati

भारतीय प्रौद्योगिकी संस्थान गुवाहाटी
Indian Institute of Technology Guwahati

CHAPTER 3

IMPACT OF REFERENCE FLUX LINKAGE ON DIRECT TORQUE CONTROL

3.1 Introduction

As discussed in chapters-1 and 2, the DTC technique has some limitations like high torque ripple, flux ripple, high stator current distortion, and variable switching frequency [71]. Several methods are presented in the literature to address the issues of torque and flux ripples in DTC [23,39,40,44,72–74]. The work addressed in [39, 40] introduces a control technique with a variable duty cycle to ensure current distortion's satisfactory and a lower torque ripple under steady-state conditions. In [44], an IM drive-based DTC scheme is presented to optimize the current ripple. A predictive method with low computational complexity and low parameter sensitivity is addressed in [45], which reduces the torque and flux ripples in a DTC IM drive. Since the issues of torque and flux ripple, variable switching frequency, and high current ripples are well explained in the literature [23, 39, 40, 44, 45, 71–74].

In the DTC scheme, the reference flux linkage (λ_s^*) also significantly impacts its performance. In conventional DTC IM drive, the λ_s^* is to use at its rated value for speeds lower than base speed, and a λ_s vary inversely to the rotor speed above the base speed [68]. However, this solution is not suitable for the control schemes used for EV applications [69]. In these applications, it is not necessary that the motor will operate at rated conditions for speeds below the base speed [70]. As far as EV applications are concerned, where the load torque varies depending on the traffic and road condition, it is not suitable to set the λ_s^* to its rated value for speeds lower than base speed. Moreover, setting the λ_s^* to its rated value for low-speed operation may result in a very high reference torque [70]. Thus, the determination of the suitable value of λ_s^* is significant over a wide range of operations and varying load torque in EV applications.

As reported in [15, 25, 30, 51, 56, 75–79], there are three basic methods for selecting λ_s^* for the IM drive system. Namely, variable flux control as a reference torque's function, flux control based on loss model, and flux control using a search controller with minimum loss/minimum input power/minimum stator current. In this chapter, the impact of variable λ_s^* and methods of its determination for DTC-based IM drive is discussed.

The remaining chapter is organized as follows: Section 3.2 describes the impact of variable λ_s^* on an IM drive over a wide range of operations. A detailed analysis is presented in this section to explain the effects of variable λ_s on the motor's behavior. Besides, the DTC scheme with variable λ_s^* is discussed. Section 3.3 presents a brief explanation of methods for determining the λ_s^*. Further, a detailed discussion of its limitation in context to EV applications is discussed. The conclusions are drawn in section 3.4.

3.2 Variable Flux Linkage And Its Impact

This section discusses the impact of variable λ_s over a wide range of operations for an EV application. The discussion starts with the analysis of the desired torque-speed characteristics of an EV drivetrain. It is observed that the desired torque-speed characteristics of an EV drivetrain are influenced by motor λ_s which is variable. An equivalent circuit approach is used to obtain the desired torque-speed characteristics and is presented in the next subsequent section. Further, it is shown in the analysis that the motor λ_s greatly influences the motor's performance. In an EV drivetrain, to tune the motor's characteristics with the desired characteristics, a controller, is needed. In this thesis, the controller chosen is DTC. The highlights of this section are as follows and are discussed in the next subsequent sections.

- EV Drivetrain and its desired torque-speed characteristics
- Equivalent Circuit Approach To Obtain The Desired Characteristics
- Influence of flux linkage on the motor's performance
- DTC scheme with variable reference flux linkage

3.2.1 EV Drivetrain And Its Desired Torque-Speed Characteristics

An EV drivetrain has mainly the subsystems consisting of a battery pack, power converters, controller, and the EM viz. IM. The schematic of the EV drivetrain is shown in Fig. 3.1 with the DTC scheme.

The major subsystem of the EV drivetrain is the EM. The motor's functioning completely de-

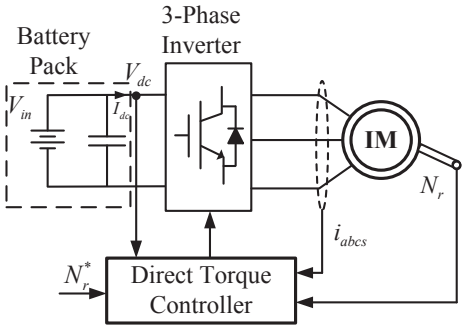

Fig. 3.1: EV drivetrain configuration with battery pack, power converter, DTC controller and IM.

termines the EV drivetrain's performance over a wide range of operations [105]. Therefore, it is necessary to understand the desired characteristics of EM used for an EV application. The typical desired characteristics of the EM for EV applications are shown in Fig. 3.2 [105]. The desirable

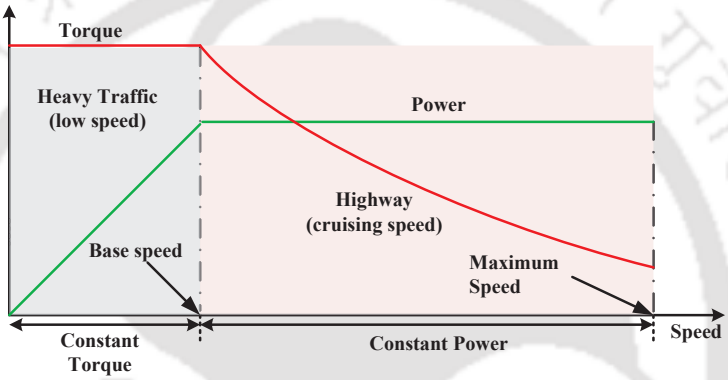

Fig. 3.2: Electric motor's desired torque-speed characteristics for an EV application.

driving conditions for EM in EV applications comprise the low-speed region (i.e., heavy traffic) and maximum cruising speed region (highway speed), as shown in Fig. 3.2. At the low-speed region (less than the base speed as marked in Fig. 3.2), the motor has to operate at constant torque mode. In the high-speed region (higher than the base speed), the motor has to operate at constant power mode.

The desired characteristics of EM shown in Fig. 3.2 are obtained if the motor voltage, current, and λ_s exhibit the characteristics, as shown in Fig. 3.3. The characteristics are shown in Fig. 3.3 show that the voltage supplied to the motor increases with the increase in speed, while λ_s is kept constant in low-speed operation. This low-speed region, preferably in and around the city area, is regarded as heavy traffic. At the point of base speed, the excitation voltage to the motor reaches its rated value. After the base speed, the motor voltage is kept constant and λ_s weakened. This region is regarded as a highway region, where the motor can attain its maximum cruising speed.

As shown in Fig. 3.3, the characteristics are the required characteristics of voltage, current, and

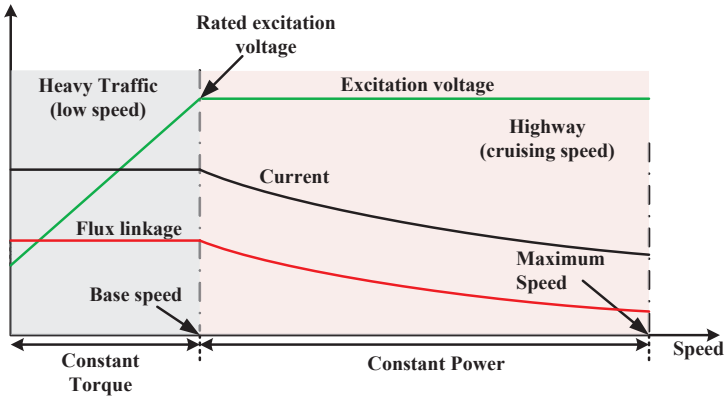

Fig. 3.3: Required characteristics of motor voltage, current and flux linkage for an EV application.

λ_s for the motor to obtain the desired characteristics, as shown in Fig. 3.2, in EV applications. As discussed in chapter- 1, the rugged and low-cost induction motors (IM) have become a viable alternative for EV applications [21]. Thus, IM based drive for an EV application is considered in this thesis. The characteristics shown in Fig. 3.3 are the required attributes of the motor to be used for EV application; therefore, it is essential to analyze IM's performance. The performance of the motor is evaluated by examining its equivalent circuit. Since IM is considered in this thesis, its equivalent circuit analysis is presented in the next subsection.

3.2.2 Equivalent Circuit Approach To Obtain The Desired Characteristics

The equivalent circuit of IM is shown in Fig. 3.4. To obtain the characteristics, as shown in Fig. 3.3, the following analysis is made using IM's equivalent circuit.

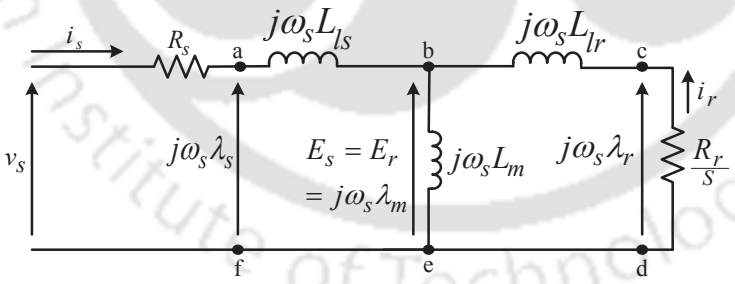

Fig. 3.4: Per-phase equivalent circuit of IM with rotor quantities referred to the stator.

Using the equivalent circuit, as shown in Fig. 3.4, the stator λ_s and stator current (i_s) are expressed as [62]:

$$\overline{\lambda_s} = L_s\overline{i_s} + L_m\overline{i_r} \tag{3.1}$$

$$\overline{i_s} = -\overline{i_r}\frac{j\omega_s L_r + \frac{R_r}{s}}{j\omega_s L_m} \tag{3.2}$$

where $\omega_s = 2\pi f_s$ and f_s is supply voltage frequency applied to stator winding.

Substituting the expression of i_s shown in (3.2) into (3.1), and taking the magnitude and square of (3.1), the stator flux linkage is expressed, as shown in (3.3):

$$\lambda_s^2 = i_r^2 \left(\frac{R_r L_s}{L_m}\right)^2 \left[\left(\frac{\sigma L_r}{R_r}\right)^2 + \left(\frac{1}{\omega_{sl}}\right)^2\right] \tag{3.3}$$

where ω_{sl} is slip frequency. Upon using a valid approximation, i.e.,

$$\frac{\sigma L_r}{R_r} \ll \frac{1}{\omega_{sl}} \tag{3.4}$$

(3.3) can be simplified as:

$$\lambda_s = i_r \left(\frac{R_r L_s}{L_m \omega_{sl}}\right) \tag{3.5}$$

Based on the equivalent circuit model, as shown in Fig. 3.4, the mechanical output power (P_o) is obtained as:

$$P_o = T_e \omega_{rm} = \frac{3}{2} i_r^2 R_r \frac{(1-s)}{s} = \frac{3}{2} i_r^2 R_r \frac{\omega_r}{\omega_{sl}} \tag{3.6}$$

where ω_{rm} and ω_r are mechanical and electrical velocity of rotor, respectively. From (3.6), the rotor current is written as:

$$i_r^2 = \left(\frac{4}{3p}\right) \frac{T_e \omega_{sl}}{R_r} \tag{3.7}$$

Moveover, from (3.5) slip frequency (ω_{sl}) in terms of i_r and λ_s is evaluated as:

$$\omega_{sl} = \left(\frac{R_r L_s}{L_m}\right) \frac{i_r}{\lambda_s} \tag{3.8}$$

Substituting (3.8) in (3.7), the rotor current is expressed in terms of λ_s, T_e, and motor parameters as:

$$i_r^2 = \left(\frac{16}{9p^2}\right) \frac{T_e^2}{\lambda_s^2} \left(\frac{L_s}{L_m}\right)^2 \tag{3.9}$$

Taking magnitude and square of (3.2) and solving (3.9) and (3.5), stator current (i_s) is determined as:

$$i_s^2 = \left(\frac{16}{9p^2}\right) \frac{T_e^2}{\lambda_s^2} \left(\frac{L_s L_r}{L_m^2}\right)^2 + \left(\frac{\lambda_s^2}{L_s^2}\right) \tag{3.10}$$

From (3.10), the motor torque (T_e) is given by (3.11),

$$T_e = \left(\frac{3p}{4}\right) \left(\frac{\lambda_s L_m^2}{L_s L_r}\right) \sqrt{i_s^2 - \frac{\lambda_s^2}{L_s^2}} \tag{3.11}$$

where i_s is stator current and λ_s is stator flux linkage of IM respectively. The relation in (3.11), shows the dependency of T_e with λ_s and i_s, assuming all other parameters of IM (p, L_m, L_s, and L_r) as

constant.

Solving (3.11) and simplifying for stator flux linkage, we get:

$$\lambda_s = \frac{L_s i_s}{\sqrt{2}} \sqrt{1 + \sqrt{1 - \left(\frac{64}{9} \frac{L_r^2}{L_m^4 p^2} \frac{T_e^2}{i_s^4}\right)}} \tag{3.12}$$

(3.12) shows the expression of motor λ_s, which is a function of T_e and i_s. At the low-speed region (less than the base speed), the motor has to operate at constant torque mode, as shown in Fig. 3.2. To obtain the desired T_e characteristic, the λ_s must follow the relation (3.12) upto base speed, as shown in Fig. 3.3. Moreover, upto base speed, motor current (i_s) is kept constant at its maximum value. In this mode, T_e is constant, and power is proportional to speed and is linear increases with speed, as shown in Fig. 3.2. The motor output power (P_o) is obtained using (3.6).

In the high-speed region (higher than the base speed), the motor has to operate at constant power mode. Upto base speed, the motor runs at maximum T_e. From the equivalent circuit shown in Fig. 3.4, the expression of maximum torque is given by (3.13);

$$T_{em} = \left(\frac{3p}{4}\right) \left(\frac{1-S}{\omega_r}\right) \left(\frac{v_s^2}{R_s + \sqrt{R_s^2 + \omega_s^2 (L_s + L_r)^2}}\right) \tag{3.13}$$

Substituting (3.13) in (3.6), the motor output power (P_o) is re-written as;

$$P_o = \left(\frac{3p}{4}\right) \left(\frac{v_s^2 (1-S)}{R_s + \sqrt{R_s^2 + \omega_s^2 (L_s + L_r)^2}}\right) \tag{3.14}$$

The expression (3.14) shows that the motor output power is dependent on excitation voltage (v_s) at/beyond the base speed and remains constant. The excitation voltage (v_s) to the motor reaches its rated value (see Fig. 3.3), and further increment in v_s is not preferred due to the motor rating. Thus, the high-speed region is also regarded as a constant power mode.

In order to obtain the expression of λ_s beyond the base speed, i_s in (3.11) is replaced by (3.15) [106]:

$$i_s = \frac{v_s - \omega_s \lambda_s}{R_s} \tag{3.15}$$

The expression (3.15) is obtained, considering the steady-state condition of IM. From the equivalent circuit of IM, as shown in Fig. 3.4, the stator voltage equation viewed from the terminal af is given by:

$$v_s = R_s i_s + j \omega_s \lambda_s \tag{3.16}$$

Taking the magnitude and solving for i_s, one can obtain the expression, as shown in (3.15).

Solving (3.11), (3.15), and (3.13), the expression of λ_s is determined by (3.17), which is applicable for speed beyond the base speed.

$$\lambda_s = \frac{v_s L_s^2 \left(-\omega_s L_m + R_s L_r \sqrt{L_s^2 \omega_s^2 + \frac{L_m^2}{L_s^2 L_r^2} - R_s^2} \right)}{L_m (R_s^2 - L_s^2 \omega_s^2)} \tag{3.17}$$

The relation (3.17) determines the expression of λ_s at maximum T_e and rated v_s. Therefore, the desired torque characteristic shown in Fig. 3.2 beyond the base speed is obtained if λ_s follows the relation, as shown in (3.17).

1. **Consider the equivalent circuit of IM, as shown in Figure 3.4.**
2. Perform IEEE standard tests, no-load and blocked rotor tests at rated conditions, to obtain the parameters of IM.
3. Solve the equivalent circuit to obtain the expressions of *Te* and λs for speeds below and above the base speed as shown in steps below:

Upto Base Speed	**Above Base Speed**
1. To obtain the desired *Te,* λs must follow the relation shown in (3.12), at maximum stator current . 2. The desired value of *Te* is obtained using (3.13), assuming all other parameters of IM (*p*, *Lm*, *Ls* and *Lr*) as constant. 3. Upto the base speed, *Te* is constant, as shown in Figure 3.2. 4. In this mode, *Pm* is proportional to speed and increases linearly with speed, as shown in Figure 3.2, and is obtained using (3.6). **Note:** In this region, to obtain the desired *Te, stator current* and λs must be constant, as shown in Figure 3.3. **Note:** At base speed, v_s reaches its rated value.	1. To obtain the desired value of *Te,* λs is first determined using (3.17). 2. Again, *stator current* is determined using (3.15). 3. Thereafter, the desired *Te* is obtained using (3.11), assuming all other parameters of IM (*p*, *Lm*, *Ls* and *Lr*) as constant. 4. In this mode, *Pm* is constant, and is obtained using (3.14), as shown in Figure 3.2. **Note:** Here, v_s is maintained constant at its rated value.

Fig. 3.5: Steps wise procedure to obtained desired characteristics as shown in Fig. 3.2

The relations (3.11) to (3.17) show that λ_s, T_e, V_s, I_s, and ω_r are all interrelated. These quantities have a significant impact on a wide range of operations in EV applications. The step-wise procedure and its flowchart to obtain the desired characteristics (see Fig. 3.2) for electric motor are shown in Fig.(s) 3.5 and 3.6. These characteristics are obtained at rated conditions, assuming all other IM parameters as constant (magnetic saturation ignored). For a wide range of operations, it is observed that variable λ_s is desirable. Besides, it is also accepted that λ_s greatly influences the performance of the motor. In the next subsection, the impact of λ_s on the motor's performance is addressed.

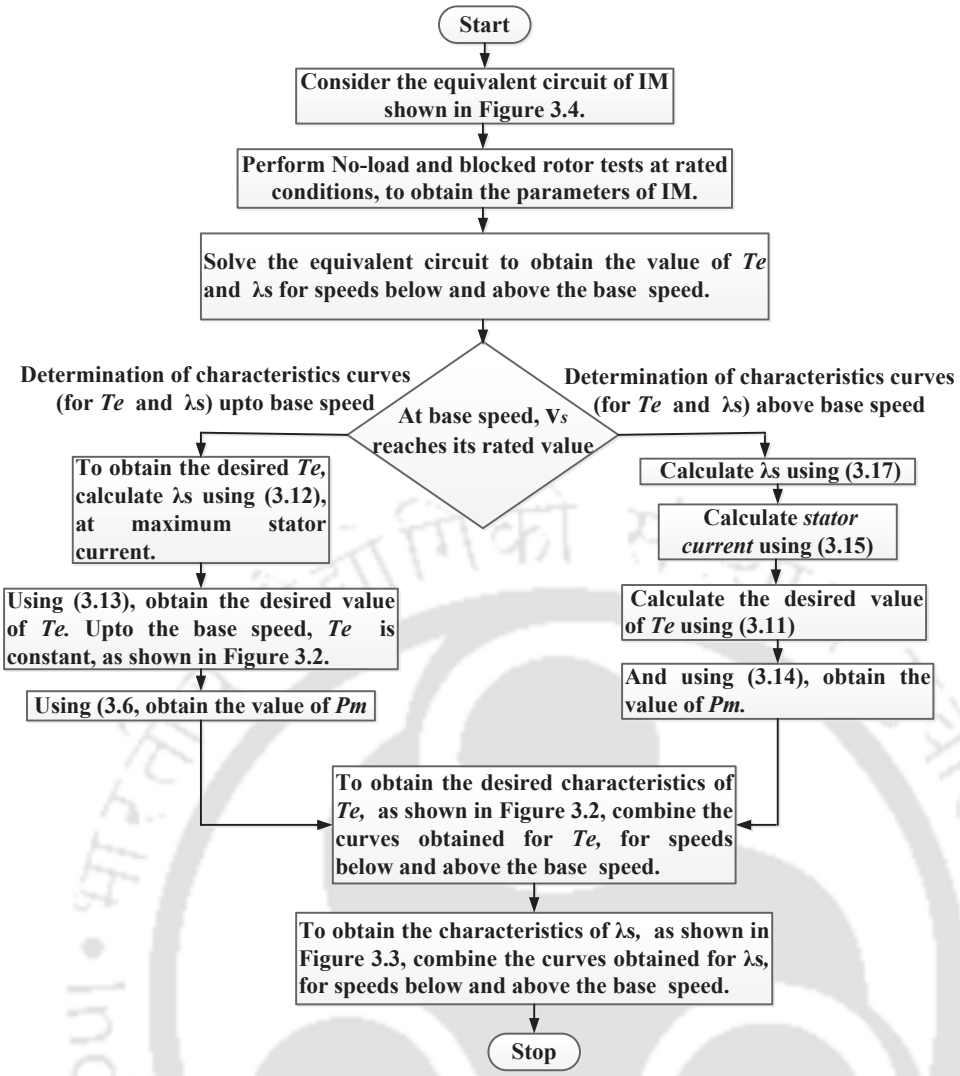

Fig. 3.6: Flow chart to obtained desired characteristics as shown in Fig. 3.2

3.2.3 Impact of Flux Linkage on the Motor's Performance

The issue of variable λ_s is addressed in this section. Fig. 3.7 shows the vectors of magnetic flux density in the air-gap of the IM at no-load and load. The resultant magnetic field (B_{net}) of IM is the vector sum of the stator magnetic field (B_S) and the rotor magnetic field (B_R) and is given by (3.18) [107]

$$\overrightarrow{B_{net}} = \overrightarrow{B_S} + \overrightarrow{B_R} \tag{3.18}$$

The electromagnetic torque, which keeps the rotor turning, is given by (3.19)

$$T_e = k\overrightarrow{B_R} \times \overrightarrow{B_{net}} \tag{3.19}$$

where k is the motor constant. The magnitude of the electromagnetic torque is given by

$$T_e = k\,|B_R|\,|B_{net}|\sin\delta \tag{3.20}$$

Each term in the expression (3.18)−(3.20) must be considered separately to understand the IM's

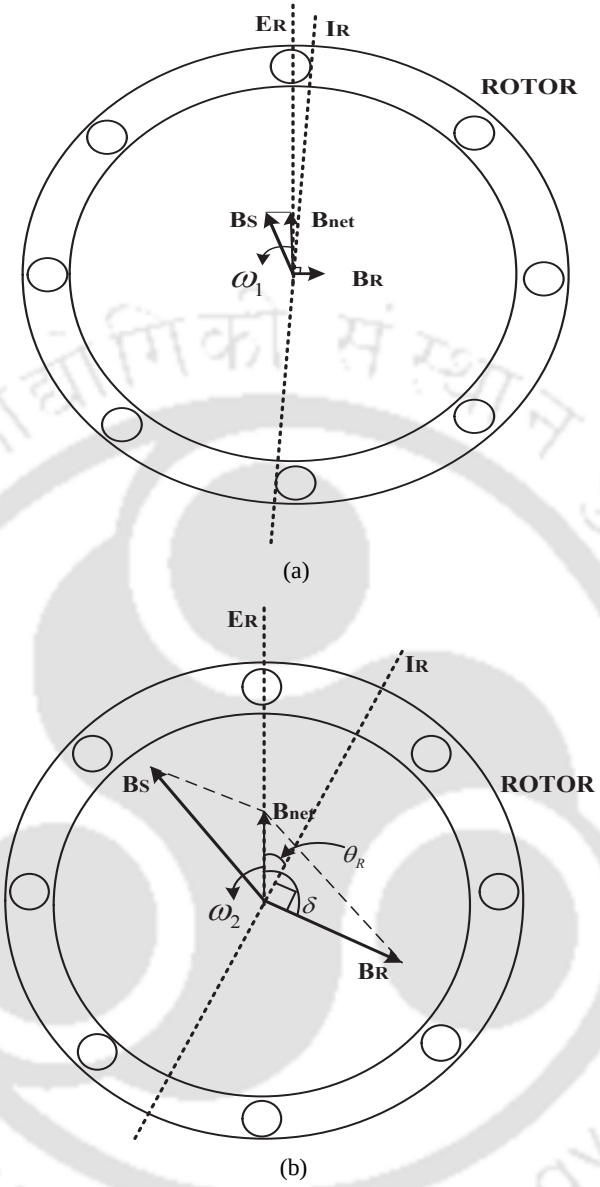

Fig. 3.7: Magnetic fields in an induction motor at two rotor speeds (a) at ω_1 rad/sec and slip (S_1) (b) at ω_2 rad/sec and slip (S_2) (where $\omega_1 > \omega_2$ and $S_1 < S_2$).

overall behavior.

- B_S: The stator magnetic field is directly proportional to the current flowing in the stator, as long as the stator core is unsaturated.
- B_R: The rotor magnetic field is directly proportional to the current flowing in the rotor, as long as the rotor core is unsaturated. The current flow in the rotor increases with increasing slip.
- B_{net}: The net magnetic field is proportional to the B_S and B_R as given by (3.18), which are

eventually proportional to the currents flowing through IM's stator and rotor. The current flowing through the IM depends and proportionate to the applied voltage. Therefore, the B_{net} in the motor is proportional to the applied voltage and the stator current.

- $\sin\delta$: The angle δ is the angle between net and rotor magnetic fields. With the change in speed, slip changes lead to a change in the rotor-induced (E_R) e.m.f.'s frequency. As rotor reactance is a function of E_R frequency, a change in rotor current (I_R) will be observed. As a result, I_R now lags further behind the E_R, and the rotor magnetic fields (B_R) shift with the I_R, changing in angle δ is observed as shown in Fig. 3.7. Therefore, the change in rotor speed eventually leads to the change in angle δ.

The expression (3.20) shows that the torque is directly proportional to the net magnetic field, rotor magnetic field, and angle δ. The net magnetic field can also be analyzed in terms of flux linked by the stator of IM. The calculation of flux linked by the coils is explained in [108] and given by

$$\lambda_{ph\_coil}(t) = l_m N_c \int_{\zeta_{ph\_i}-\varepsilon/2}^{\zeta_{ph\_i}+\varepsilon/2} B^r_{net}(R_s,\theta,t)\,d\theta \qquad \{ph = a,b,c\} \tag{3.21}$$

where B^r_{net} is the radial component of the resultant magnetic field, R_s is the stator inner radius, θ is the spatial angle, l_m is the motor length, and N_c is the turns per coil . ζ_{ph_i} and $\varepsilon/2$ represents angle of axis and coil pitch for one coil of any phase.

The total flux linkage for a phase, λ_{ph}, is determined using the flux of individual coils of that phase as given by

$$\lambda_{\mathrm{ph}}(\mathrm{t}) = \mathrm{P}\sum_{\mathrm{i}=1}^{\mathrm{coils}} \lambda_{\mathrm{coil}} \qquad \{\mathrm{ph} = \mathrm{a},\mathrm{b},\mathrm{c}\} \tag{3.22}$$

Using $abc-to-dq$ transformation, direct and quadrature axes (λ_d and λ_q) flux linkages can be obtained. Thus, the total flux linked by the stator of an IM is given by

$$\lambda_s = \sqrt{(\lambda_d^2 + \lambda_q^2)} \tag{3.23}$$

The flux linked (λ_s) by the IM's stator is fundamentally the function of B_{net} and which is eventually the function of stator current. As the stator current changes, the angle δ changes. It is also clear that the torque will also change given by (3.20). The change in B_{net} indicates the change in λ_s. Moreover, in a wide range of operations with the change in rotor speed, the back e.m.f. induced in the stator winding changes; as a result, stator current changes. As a consequence, the changes are seen in motor λ_s as well as in T_e.

It is seen from the above discussion that the motor λ_s has influenced on the torque-speed charac-

teristics of the motor. As EV applications are concerned, it is not necessary that the motor operates at rated conditions over a wide varying speed and torque range. Therefore, to tune the motor's characteristics with the required attributes for EV applications, a controller is needed. Moreover, it is observed that the variable λ_s is desirable for a wide range of operations. Thus, to obtain the desired characteristics, as shown in Fig. 3.2, the input feed to the controller must be of nature, as shown in Fig.3.3. In this thesis, the controller chosen is DTC. The better performance of DTC strategy depends on the accurate determination of λ_s^* over a wide speed range, in EV applications. In the next subsection, the DTC strategy with variable λ_s^* is explained.

3.2.4 DTC Overview

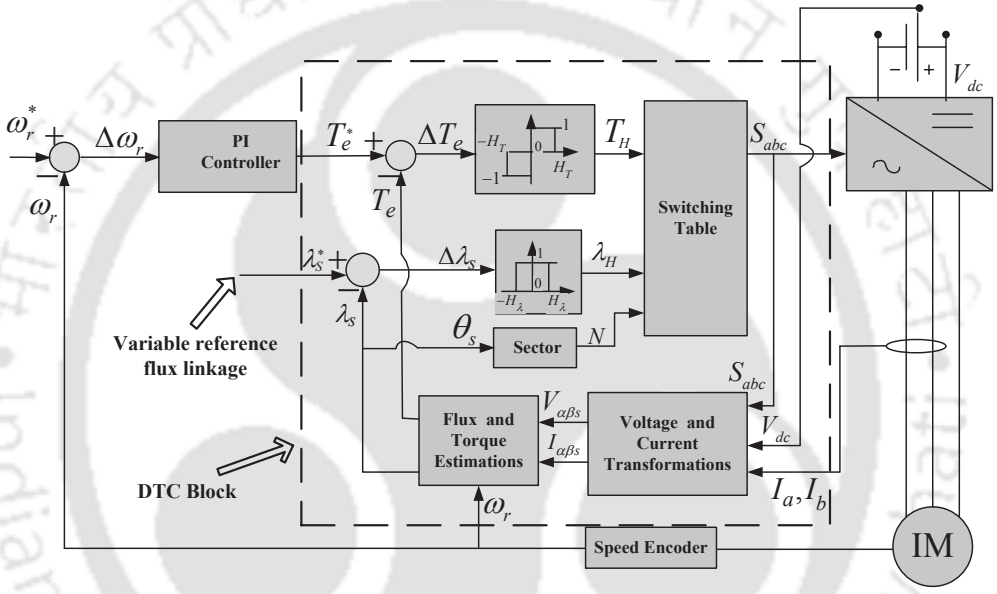

Fig. 3.8: Block diagram representation of DTC based IM drive. The sub-blocks, voltage & current transformation, and flux and torque estimation block with its detailed implementations are shown in Fig. 3.9.

A brief description of the DTC strategy is explained in chapter 2. In this section, DTC with variable flux linkage (as one of the reference command signals) is discussed. A block diagram of the DTC-based IM drive is shown in Fig. 3.8. DTC algorithm aims is to control the instantaneous values of T_e and λ_s of an IM directly and independently. The control action is carried out with the selection of a suitable voltage vector from a switching table. The selection of voltage vector is decided based on error status (i.e., torque error (T_H), flux linkage error (λ_H)), and sector position (N). The errors status is generated by the comparison between the respective reference and estimated values, respectively.

The DTC based speed control of IM, as shown in Fig. 3.8, is achieved by considering the follow-

ing blocks:

- **Voltage and current transformations block**: The actual motor voltage and currents are measured, and *abc* to $\alpha-\beta$ transformation is performed as discussed in chapter 2, section 2.2.3. In the stationary reference, i.e., $\alpha-\beta$ frame, using the measured actual stator phase currents (i.e., i_{as} and i_{bs}), V_{dc}, and inverter gate switching signals (S_a, S_b, and S_c), the $\alpha-\beta$ components of stator voltage and current are determined as:

$$\begin{aligned} V_{\alpha s} &= \left(\frac{V_{dc}}{3}\right)\ (2S_a - S_b - S_c) \\ V_{\beta s} &= \left(\frac{V_{dc}}{\sqrt{3}}\right)\ (S_b - S_c) \end{aligned} \tag{3.24}$$

$$\begin{aligned} i_{\alpha s} &= i_{as} \\ i_{\beta s} &= \left(\frac{1}{\sqrt{3}}\right)\ (i_{as} + 2i_{bs}) \end{aligned} \tag{3.25}$$

- **Flux linkage and torque estimations block**: The performance of the DTC scheme depends on the accurate estimation of λ_s and T_e. Several estimation methods for λ_s and T_e are proposed in the literature for DTC-based IM drive [109]. Most of the methods are based either on the voltage model or on the current model. The estimation method based on the voltage model has the inaccuracy in the low-speed region, whereas the current model's technique is sensitive to machine parameters. In [110], a voltage-current model (VCM) is introduced and widely accepted as the λ_s and T_e estimation technique for DTC over a wide range of operations. The VCM scheme is explained in detail in the next subsequent section.
- **Encoder block for rotor speed measurement**: An incremental optical encoder is used to measure the motor's speed. Generally, the encoder is mounted to the shaft of the machine set. The encoder's output is directly fed to the high computing processors (i.e., DS1103, DSP, and FPGA) measurement unit, which gives the IM's measured speed.

3.2.4.1 Voltage-Current Model Based Flux Linkage and Torque Estimation

Using (2.44) from chapter 2, section 2.2.3, in $\alpha-\beta$ frame, the $\lambda_{\alpha s}$ and $\lambda_{\beta s}$ can be determined as:

$$\begin{aligned} \lambda_{\alpha s} &= \int (V_{\alpha s} - i_{\alpha s}R_s)\, dt \\ \lambda_{\beta s} &= \int \left(V_{\beta s} - i_{\beta s}R_s\right) dt \end{aligned} \tag{3.26}$$

The relation in (3.26) shows that the estimation of $\lambda_{\alpha s}$ and $\lambda_{\beta s}$ uses α and β components of the stator voltage and current. The α and β components of stator voltage and current (i.e., $V_{\alpha s}$, $V_{\beta s}$, $i_{\alpha s}$, and $i_{\beta s}$) are obtained using (3.24) and (3.25).

The accurate estimation of $\lambda_{\alpha s}$ and $\lambda_{\beta s}$ in (3.26) depends on the actual measured signals' accuracy. The actual signals, i.e., i_{as} and i_{bs}, and V_{dc}, as shown in Fig. 3.8, are measured by using sensors. The sensors used for measurement have inherent noise and dc-offset, which leads to an inaccuracy in the flux linkage's estimation. Therefore, to achieve the accurate stator flux linkages estimation, (3.26) is modified for a wide speed operation. Using the voltage model, (3.26) is modified to estimate $\lambda_{\alpha s}$ and $\lambda_{\beta s}$ as:

$$\begin{aligned} \lambda_{\alpha s} &= \int \left((V_{\alpha s} - i_{\alpha s} R_s) + \gamma_{\alpha c} \right) dt \\ \lambda_{\beta s} &= \int \left((V_{\beta s} - i_{\beta s} R_s) + \gamma_{\beta c} \right) dt \end{aligned} \tag{3.27}$$

where, $\gamma_{\alpha c}$ and $\gamma_{\beta c}$ are the error compensation factor for the estimation of $\lambda_{\alpha s}$ and $\lambda_{\beta s}$, respectively. The error compensation factors are determined using the current model. In the current model, the estimation of rotor flux linkages, i.e., $\lambda'_{\alpha r}$ and $\lambda'_{\beta r}$, are achieved using rotor voltage expression of (2.45). The terms $V_{\alpha r}$ and $V_{\beta r}$ in (2.45) are equal to zero as the rotor windings are shorted. The rotor voltage expressions are modified as:

$$\begin{aligned} 0 &= R_r i_{\alpha r} - \omega_r \lambda'_{\beta r} + \frac{d\lambda'_{\alpha r}}{dt} \\ 0 &= R_r i_{\beta r} + \omega_r \lambda'_{\alpha r} + \frac{d\lambda'_{\beta r}}{dt} \end{aligned} \tag{3.28}$$

Using (3.28), the $\lambda'_{\alpha r}$ and $\lambda'_{\beta r}$ are estimated as:

$$\begin{aligned} \lambda'_{\alpha r} &= \int \left(\frac{1}{\tau_r} \left(L_m i_{\alpha s} - \lambda'_{\alpha r} \right) + \omega_r \lambda'_{\beta r} \right) dt \\ \lambda'_{\beta r} &= \int \left(\frac{1}{\tau_r} \left(L_m i_{\beta s} - \lambda'_{\beta r} \right) - \omega_r \lambda'_{\alpha r} \right) dt \end{aligned} \tag{3.29}$$

where $\tau_r = \frac{L_r}{R_r}$ is the rotor time constant.

The rotor flux linkages ($\lambda'_{\alpha r}$ and $\lambda'_{\beta r}$) from the current model are estimated using (3.29). The relation between stator and rotor flux linkages are obtained using the expression of (2.44) and (2.45) as:

$$\begin{aligned} \lambda'_{\alpha s} &= \left(\frac{L_m}{L_r} \right) \lambda'_{\alpha r} + (\sigma L_s i_{\alpha s}) \\ \lambda'_{\beta s} &= \left(\frac{L_m}{L_r} \right) \lambda'_{\beta r} + (\sigma L_s i_{\beta s}) \end{aligned} \tag{3.30}$$

where $\sigma = 1 - \frac{L_m^2}{L_s L_r}$ is the leakage factor.

Finally, the error compensation factor's ($\gamma_{\alpha c}$ and $\gamma_{\beta c}$) values are determined from a PI controller by passing the difference of estimated stator flux linkages (i.e., ($\lambda_{\alpha s}$-$\lambda'_{\alpha s}$) and ($\lambda_{\beta s}$-$\lambda'_{\beta s}$) using (3.27) and (3.30).

The final values of $\lambda_{\alpha s}$ and $\lambda_{\beta s}$ are estimated using (3.27) after substitution of $\gamma_{\alpha c}$ and $\gamma_{\beta c}$ values,

respectively. Thus, the magnitude and angle of λ_s can be evaluated using (3.28) as:

$$\lambda_s = \sqrt{\left(\lambda_{\alpha s}^2 + \lambda_{\beta s}^2\right)}$$
$$\theta_s = \arctan\left(\frac{\lambda_{\beta s}}{\lambda_{\alpha s}}\right) \tag{3.31}$$

The T_e can be estimated using (3.27) and (3.25), as discussed in chapter 2, section 2.2.5:

$$T_e = \frac{3}{2}\frac{P}{2}\left(\lambda_{\alpha s} i_{\beta s} - \lambda_{\beta s} i_{\alpha s}\right) \tag{3.32}$$

The accurate estimation of λ_s and T_e is essential for the satisfactory performance of the DTC strategy over a wide range of operations. The detailed implementation block diagram of the VCM scheme and transformation block (voltage and current) are shown in Fig. 3.9. Moreover, a precise

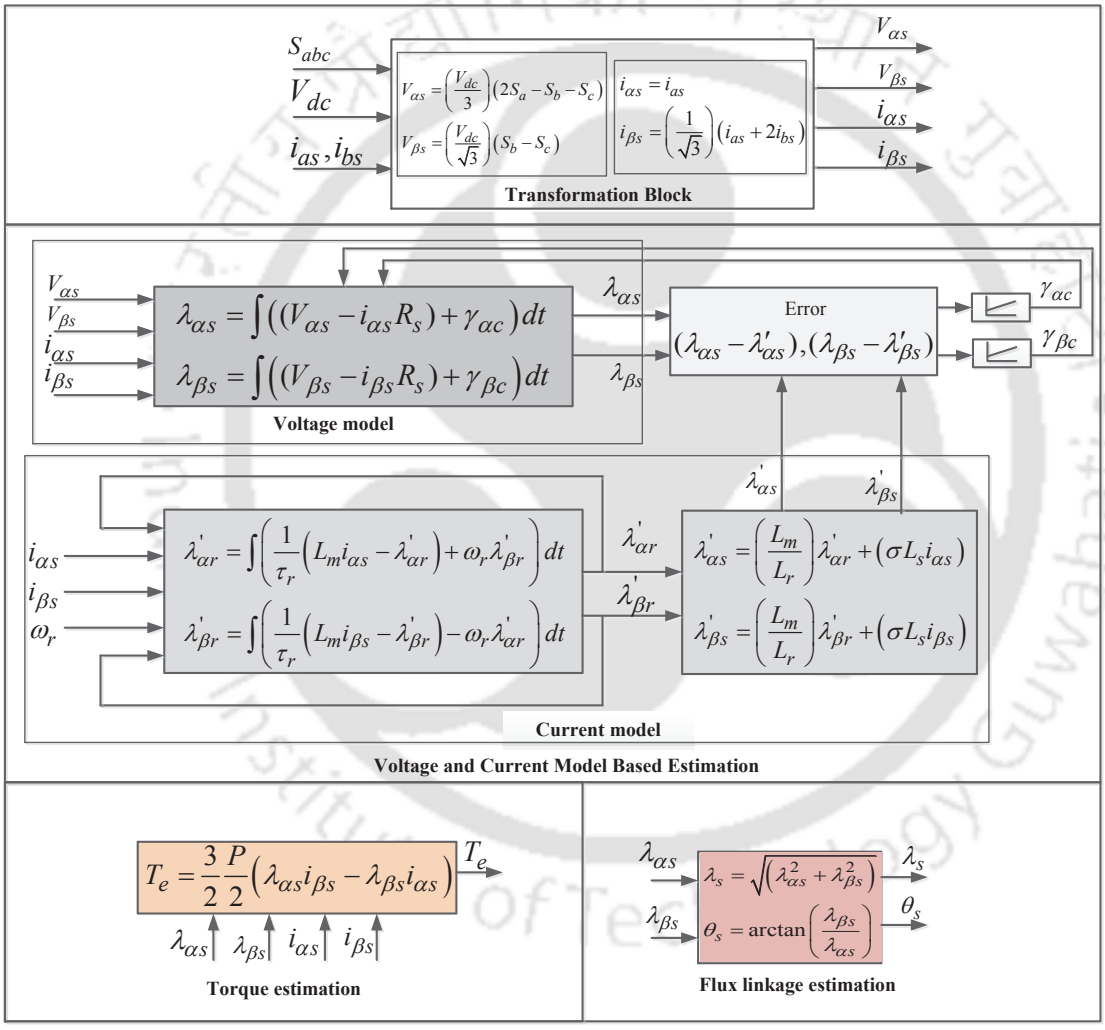

Fig. 3.9: Implementation block diagram of VCM scheme and transformation block. The diagram shows in this figure are the sub-block diagram of voltage & current transformation, and flux and torque estimation block for the DTC strategy shown in Fig. 3.8.

and accurate estimation of λ_s and T_e is possible in the DTC strategy when a motor operates with suitable λ_s^*. For an applied voltage and current in the DTC strategy, a motor can always estimate the

λ_s and T_e. The estimated values of λ_s and T_e are whether the actual required values of the λ_s and T_e, considering the motor's voltage and current rating constraints, are decided by comparing with their respective reference (i.e., λ_s^* & T_e^*) values in the DTC strategy.

In conventional DTC, λ_s^* is kept at a constant value (usually at rated value) as those drives are set to run at a constant speed. However, in EV applications, the motor usually does not operate at rated conditions for all the speed ranges [70]. For a wide range of operations (see Fig. 3.2), a variable λ_s^* (see Fig. 3.3) is desirable in the DTC scheme. For proper and precise control over a wide range of speed and torque, the λ_s^* in the DTC scheme is shown in Fig. 3.8 should be variable. Moreover, a suitable selection of λ_s^* will also help in estimating the accurate λ_s values and T_e over a wide range of operations.

Thus, the selection of optimal λ_s^* is very critical for EV applications over a wide range of operations [111]. From the above discussion, it can be seen that variable λ_s is preferred over a wide range of operations and will impact the performance of the motor. Moreover, the EV drivetrain efficiency can also be improved by adjusting the λ_s^* command depending upon the control algorithm over wide operating conditions. Numerous techniques on determining optimal λ_s^* for IM drive have been reported in recent years [15, 25, 30, 51, 63, 76]. Some of the reference flux linkage value determination techniques for IM drive are discussed in the upcoming section.

3.3 Determination of Optimal Reference Flux Linkage for an Induction Motor Drive

According to the literature, the three basic strategies for the determination of optimal λ_s^* in vector control IM drive are reported:

1. Variable flux controller as a torque's function.
2. Flux controller based on the Loss model.
3. Flux search controller-based on minimum loss/ minimum input power/minimum stator current.

3.3.1 Variable Flux Controller

This method is a well-known technique and widely used in industry because of its simplicity [28]. In this scheme, the determination of λ_s^* is evaluated based on the desired torque value (3.33):

$$|\lambda_s^*| = |\lambda_{sn}| \sqrt{\frac{T_e^*}{T_{en}}} \tag{3.33}$$

where λ_{sn} is the nominal flux linkage, T_{en} is the machine's nominal torque, and T_e^* is the desired torque. This method is based on the limit cycle control of flux linkage and torque using optimum pulse width modulation (PWM) output voltage. Here, the limit cycle defines the hysteresis bands of flux linkage and torque. The instantaneous values of the flux linkage and torque are calculated from the primary variables (i.e., voltage and current applied to the IM). These primary variables can be controlled directly and independently by selecting optimum inverter switching modes. In this strategy, one of the variables is controlled and is measured or estimated. This measured or estimated value is used in the drive's feedback control for predefined reference values, as shown in Fig. 3.10. In Fig. 3.10, the command signal C_1 can be stator flux or stator direct axis current, and C_2 can be T_e^* or stator quadrature axis current.

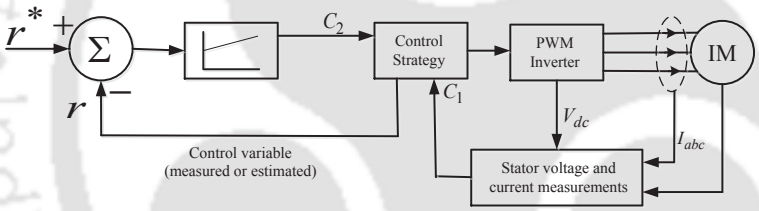

Fig. 3.10: Block diagram of flux controller.

Fig. 3.11 shows the block diagram representation of the DTC strategy with a variable flux controller. The control strategy block is shown in Fig. 3.10 is replaced with the DTC strategy block, as shown in Fig. 3.11. The λ_s^* in this scheme is the reference torque function i.e., T_e^* given by relation (3.33). The complete control strategy was developed on the synchronously rotating reference $(d-q)$ frame [28]. The method is simple and gives satisfactory performance, but only for a narrow range of operations. Moreover, it is sensitive to the motor's parameter variations due to temperature changes and magnetic circuit saturation [56].

3.3.2 Loss Model-Based Flux Controller

This technique for flux control is based on the IM's loss model to determine an optimal λ_s^* at desired conditions. In [62], the optimum value of λ_s^* is determined from the IM loss minimization algorithm,

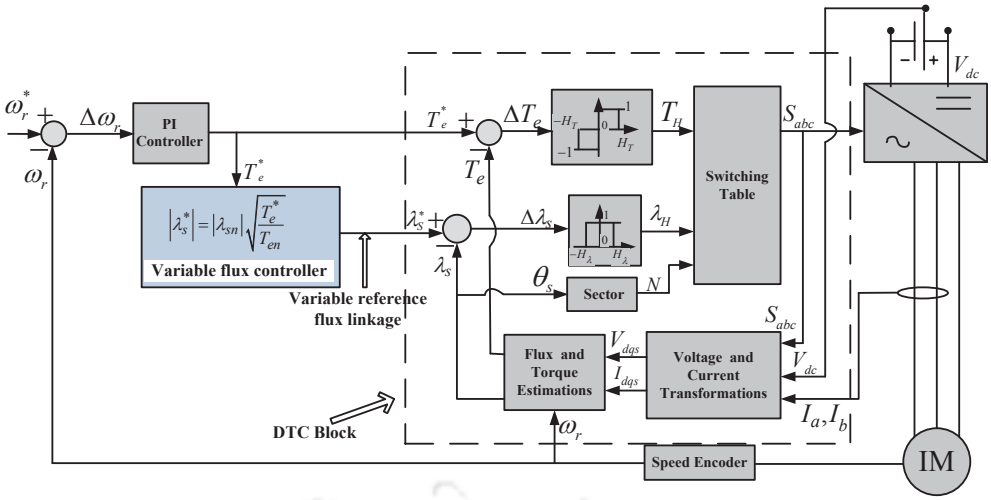

Fig. 3.11: Block diagram of the DTC strategy with a variable flux controller. The control strategy block of Fig. 3.10 is replaced with the DTC block. The control strategy developed on the synchronously rotating reference frame.

and a loss model has been developed in terms of λ_s, T_e, N_r, and motor parameters. In literature, the copper and iron losses of an IM are usually modeled as follows:

$$P_{cu} = \frac{3}{2} i_s^2 R_s + \frac{3}{2} i_r^2 R_r \tag{3.34}$$

$$P_{core} = K_e f_s^2 \lambda_s^2 + K_h f_s \lambda_s^2 \tag{3.35}$$

The copper loss model (3.34) includes ohmic losses on the stator and the rotor, and the approximate iron loss model (3.35) includes eddy current losses and hysteresis losses. The constant K_e and K_h represent the eddy current loss and hysteresis loss coefficient. The values of K_e and K_h values can be determined by performing a no-load experiment on IM.

In (3.34) and (3.35), the terms i_s, i_r and f_s have to be determined in terms of motor parameters, ω_r, T_e and λ_s.

The i_s, i_r, and f_s are determined using (3.36), (3.37), and (3.38), and are discussed in section 3.2.2:

$$i_s^2 = \frac{16}{9P^2} \frac{T_e^2}{\lambda_s^2} \frac{L_s^2 L_r^2}{L_m^4} + \frac{\lambda_s^2}{L_s^2} \tag{3.36}$$

$$i_r^2 = \frac{16}{9P^2} \frac{T_e^2}{\lambda_s^2} \frac{L_s^2}{L_m^2} \tag{3.37}$$

$$f_s = \frac{1}{2\pi} \left[\omega_r + \frac{4}{3P} \frac{T_e}{\lambda_s^2} \frac{R_r L_s^2}{L_m^2} \right] \tag{3.38}$$

By substituting (3.36) and (3.37) in (3.34) and solving, the P_{cu} is rewritten as:

$$P_{cu} = \frac{8}{3P^2}\left[\frac{T_e}{\lambda_s}\right]^2\left(1+\frac{L_{1s}}{L_m}\right)^2\left[R_s\left(1+\frac{L_{1r}}{L_m}\right)^2+R_r\right]+\frac{3}{2}R_s\left(\frac{\lambda_s}{L_{1s}+L_m}\right)^2 \tag{3.39}$$

Similarly, by substituting (3.38) in (3.35) and solving, the P_{core} is determined as:

$$P_{core} = K_e\frac{1}{4\pi}\left[\omega_r+\frac{4}{3P}\frac{T_e}{\lambda_s^2}\frac{R_rL_s^2}{L_m^2}\right]^2\lambda_s^2+K_h\lambda_s^2\frac{1}{2\pi}\left[\omega_r+\frac{4}{3P}\frac{T_e}{\lambda_s^2}\frac{R_rL_s^2}{L_m^2}\right] \tag{3.40}$$

Finally, the total motor loss (P_{total}) is determined as:

$$P_{total} = P_{cu}+P_{core} \tag{3.41}$$

The optimum λ_s^* for a given condition can be determined by minimizing (3.41) w.r.t. λ_s. Fig. 3.12 shows the block diagram representation of the loss model-based flux controller. In Fig. 3.12, the command signal C_1 can be stator flux or stator direct axis current, and C_2 can be T_e^* or stator quadrature axis current. The required optimal value of C_1 is determined from the loss model approach by minimizing (3.41) wrt λ_s.

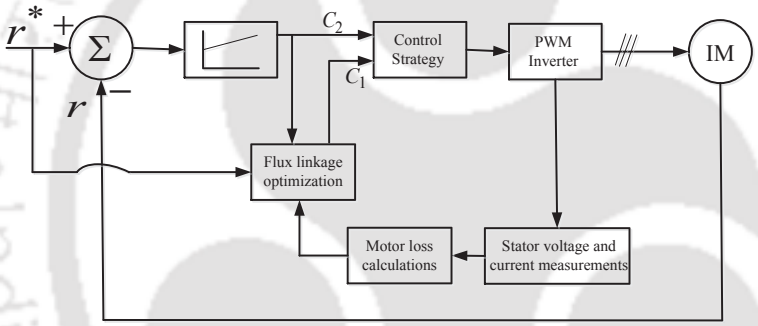

Fig. 3.12: Block diagram of loss model-based flux controller.

Several methods are reported in the literature for the loss minimization approach and its improvement. The method is equally acceptable in the FOC strategy as well as in the DTC strategy [15, 30]. The control strategy was developed in the synchronously rotating reference ($d-q$) frame. Fig. 3.13 shows the block diagram representation of the DTC strategy with a loss model-based flux controller. The control strategy block is shown in Fig. 3.12 is replaced with the DTC strategy block, as shown in Fig. 3.13. The λ_s^* is optimized based on the T_e^* and ω_r^*.

The algorithm's execution response is fast, as the optimal λ_s is calculated directly from the loss model. The optimal operating point can be calculated from this strategy with the acceptance of the exact determination of losses in the drive. However, for the following reasons, it cannot be possible in practice [58]:

- The determination of losses such as stray load loss, iron losses in case of saturation, and copper

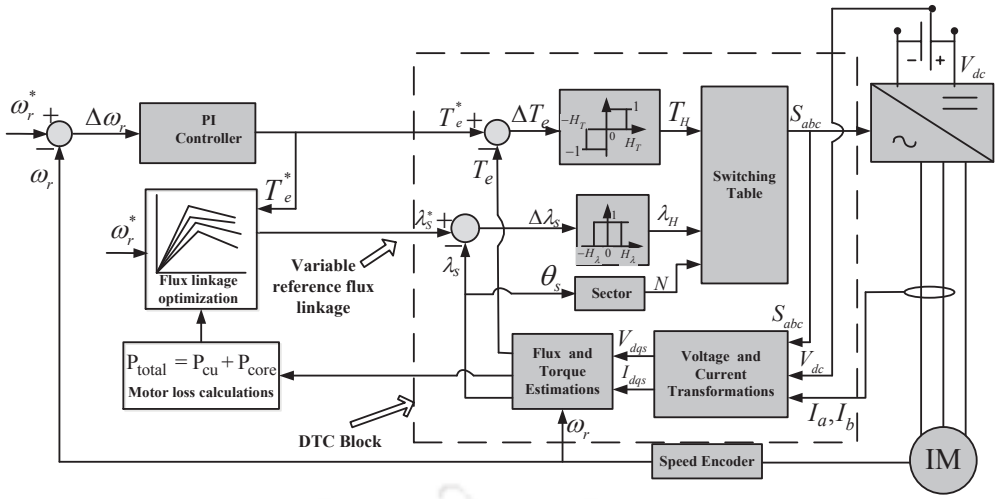

Fig. 3.13: Block diagram of the DTC strategy with a loss model-based flux controller. The control strategy block of Fig. 3.12 is replaced with the DTC block. Here the synchronously rotating reference frame is used to develop the control strategy.

loss because of temperature rise are difficult to predict.

- The measurement of all control signals using sensors cannot be possible due to its cost limitation. It means that the estimation process for certain quantities is being performed, which naturally leads to an error.

This strategy's performance depends on the accurate motor parameters identification and their variation during operation [62], and accurate determination of motor parameters is difficult [63].

3.3.3 Flux Search Controller

The search control (SC) techniques employ iterative adjustment of the flux command in the machine controller. The iteration process is carried till the measured variables settle down to the lowest value for a given torque and speed. Fig. 3.14 shows the block diagram implementation of the SC algorithm. In this algorithm, the input power (or current) has been minimized for a given T_e^* and ω_r^* by adjusting a λ_s^* value [30, 51]. The SC algorithm iteratively changes the flux level searching for the optimal excitation that gives the minimum input power (current) for the existing operating condition.

The SC algorithm's basic flow chart is shown in Fig. 3.15, where f is the measured quantity (motor input power, DC input power, and stator current), and x is the control variable (stator or rotor flux linkages). In Fig. 3.14, the command signal C_1 can be stator flux or rotor flux or stator direct axis current, and C_2 can be T_e^* or stator quadrature axis current. The required optimal value of C_1 is determined from the SC-based algorithm on the measured variable. Fig. 3.16 shows the block diagram representation of the DTC strategy with a flux search controller. The control strategy block

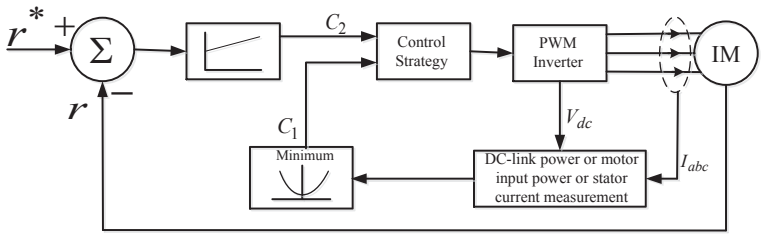

Fig. 3.14: Block diagram of search controller algorithm.

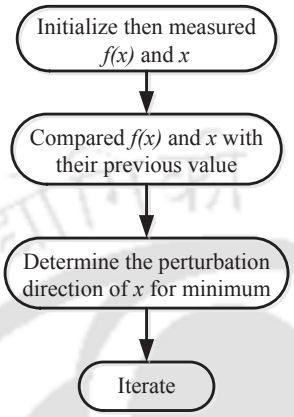

Fig. 3.15: Flow chart of search controller algorithm.

is shown in Fig. 3.14 is replaced with the DTC strategy block, as shown in Fig. 3.16. The λ_s^* value is optimized for a given T_e^* and ω_r^* to achieve the minimum input power for the desired operating condition. The complete control strategy developed on the synchronously rotating reference $(d-q)$ frame.

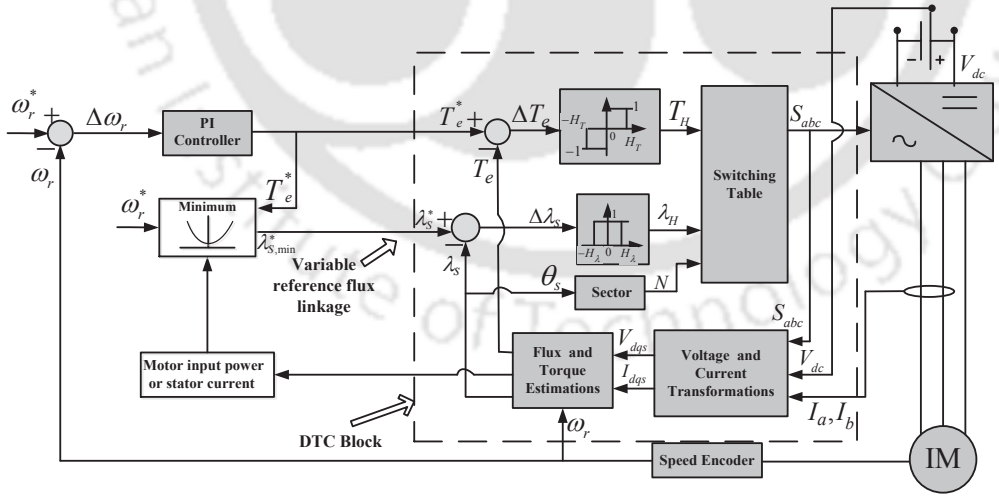

Fig. 3.16: Block diagram of the DTC strategy with flux search controller. The control strategy block of Fig. 3.14 is replaced with the DTC block. Here the control strategy developed on the synchronously rotating reference frame.

As the input power is a parabolic function of the machine controller, various SC methods such as

fuzzy [112] and neuro-fuzzy methods [59] are available for minimizing the input power (or current) for a given output. The merit of the SCs is that they are independent of drive parameters and can be very accurate. However, this method suffers from slow convergence and torque ripples if the step changes of the flux command are abrupt [15, 25]. The load torque pulsations and measurement error may also lead to deterioration in the search algorithm's performance. Moreover, it is observed for the drives with faster dynamics, the convergence issue and oscillation for flux's optimum value in the control algorithm are not desirable [15].

There are also hybrid methods are reported [15, 25] by combining the advantages of the loss model approach and the search controller. In this method, a loss model-based approach calculates the initial value (C_0) for the SC algorithm, followed by searching for the final flux's optimal value. Fig. 3.17 shows the block diagram representation of the hybrid model scheme. The merit of this method is the fast determination of λ_s^* and is robust to parameters variation. However, the method's

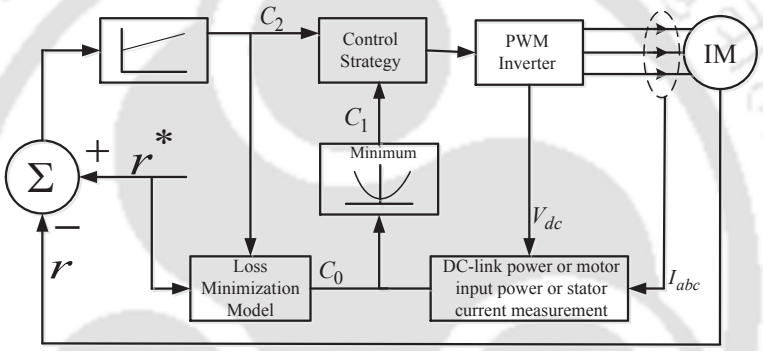

Fig. 3.17: Block diagram of hybrid algorithm.

performance depends on the accurate measurement of the power signal, the type of search algorithm, and the determination of initial value calculation from the loss model approach.

3.3.4 Limitations

Based on the published reports in the literature, Table 3.1 shows a summary of reported techniques from aspects such as torque ripples, wide speed range, wide torque range, and computational complexity.

Table. 3.1: Summary of reported techniques for selection of reference flux linkage

Methods	**Torque ripple**	**Wide speed range**	**Wide torque range**	**Computational complexity**	**Need for detailed motor parameters**	**Remarks**
Conventional	High	No	No	–	–	Constant flux approach (not suitable for EV applications [69]).
Variable flux method	High	Limited	Limited	–	–	Simple but determination of the optimal value of λ_s is not satisfactory and for limited speed range [56].
Loss model based (optimal DTC)	Low	Yes	limited	Yes	Yes	Suitable for EV application and can determine optimal λ_s, but depends highly on the accuracy of motor parameters [62–64].
Flux search controller (Online estimation)	Medium	Yes	Yes	Yes	No	Slow convergence issues and torque ripples [25, 30, 51].
Flux search controller (Offline estimation)	Low	Limited	Limited	No	Yes	Does not account for all operating range [15, 25].
Maximum torque per ampere flux controller	Medium	limited	limited	Yes	Yes	Suitable for EV applications, with limited range of operation [65].
New online loss minimization	Medium	limited	limited	No	Yes	Optimum flux and power savings for minimum losses are obtained, but, convergence time is not defined [66].
Fuzzy logic based stator flux linkage sector selection	Low	limited	limited	Medium	No	Dynamic performance is good, but limited ranges of speed and torque [67].

It is concluded that the technique proposed in [69] is not desirable for EV applications with a wide range of speed operations. This technique sets the machine to operate at a rated λ_s^* with constant speed (N_r). The method, such as a variable flux method in [56], cannot determine the λ_s^* optimal value and operates for a limited speed range. The loss model-based technique (also referred to as optimal DTC) in [62–64] exhibits low torque ripples with a limited operating range. However, the algorithms associated with optimal DTC are complicated and required detailed knowledge of motor parameters. The method proposed in [30, 51] is the flux search controller based on online estimation. The process is independent of motor parameters but suffers from slow convergence and torque ripples [25]. In [15, 25], the flux search controller technique based on offline estimation is proposed. This method exhibits low torque ripples with satisfactory performance but does not account for all operating conditions. The method proposed in [64–66] has an acceptable performance in the low-speed region. The demerits of this method are; it is defined with limited N_r and T_e ranges and exhibits torque ripples. In [67], the presented method has a satisfactory performance with low torque ripples but accounts for limited ranges of N_r and T_e.

This section discussed the three methods for the determination of λ_s^* in vector control IM drive. The detailed implementation procedure for each method is explained. Each method has its own merits and demerits; hence the selection methods for λ_s^* depend on the dedicated application. The selection of λ_s^* is crucial for a wide range of operations as well as for the efficiency improvement of the EV drivetrains.

3.4 Conclusion

This chapter explains the impact of variable λ_s^* on the performance of DTC-based IM drive. It is clear that the characteristics shown in Fig. 3.2 cannot be achieved by the constant λ_s method. For a wide range of speed and torque, a variable λ_s^* (see Fig. 3.3) is desirable in the DTC scheme. Hence, the selection of optimal λ_s^* is critical and has a substantial impact on IM drive performance for EV applications over a wide range of operations and the EV drivetrain's efficiency improvement. The determination methods of λ_s^* are broadly classified into three categories. For each method, merits and demerits are discussed. It is found that there is no generalized accepted method for determining the reference flux linkage.

Thus, the determination of optimal λ_s^* is one of the challenging issues in DTC of IM for a wide range of operations and variable load conditions. Hence, there is a need for revisiting the DTC

technique over wide speed and torque ranges in EV applications. Therefore, in the next subsequent chapters, the determination methods of λ_s^* are proposed for DTC based IM drive over a wide range of operations.

CHAPTER 4

REFERENCE FLUX LINKAGE DETERMINATION FOR DIRECT TORQUE CONTROL INDUCTION MOTOR DRIVE BASED ON FINITE ELEMENT ANALYSIS MODEL

4.1 Introduction

As discussed in chapter -3, the λ_s^* significantly impacts the motor's performance in the DTC scheme. As reported in [15, 25, 30, 51, 56, 75–79], the optimal λ_s^* determination is also one of the challenging issues in DTC-based IM for a wide range of operations in EV application.

As per literature, there are three ways of λ_s^* determination for the IM drive system, namely, variable flux control as a torque's function, flux controller based on the loss model, and flux search controller (SC)-based on the minimization of loss/input power/stator current. The first method is simple and gives an acceptable performance, but only for a narrow range of operations [56]. In the second method, the λ_s^* is obtained by minimizing the motor's losses or combined with the inverter and DC-link capacitor [61]. The obtained optimal λ_s^* values are stored in the lookup table (LUT) format and implemented in the control algorithm. In [15], an offline method is presented to determine λ_s^* by minimizing the motor's losses. The major demerit of the loss minimization technique is sensitive to motor parameter variations [62]. Besides, the performance of loss minimization techniques depends on the accurate identification of motor parameters, and precise motor parameters identification is

difficult [63].

In the third method, the optimum value of λ_s^* is determined by the iteration process using measured motor input power [30, 51]. Also, fuzzy and neuro-fuzzy-based SCs are proposed in [58–60] to improve the optimum λ_s^* value's convergence performance. Search-based algorithms' main advantage is the robustness to parameter variations since they work on the real-time measured variables. Besides, a LUT-based offline SC method for selecting the optimal value of λ_s is presented in [25]. In this offline method, the obtained data of suitable λ_s are stored in LUT format and fed to the machine controller for efficiency optimization. This method's disadvantage is that it has only a narrow range of operations [25]. The SC suffers from convergence issues and torque ripples if the step changes of the flux command are abrupt [15, 25]. The load torque pulsations and measurement error may also lead to deterioration in the search algorithm's performance. It is observed for the drives with faster dynamics, the convergence issue and oscillation for flux's optimum value in the control algorithm are not desirable (for example, in EV applications) [15].

As far as the LUT based works for the selection of λ_s^* are concerned, the reported works are either sensitive to motor parameter variations or do not account for a wide range of operations [15, 25]. Moreover, these works do not explain the technique's performance for vehicle driving cycles (especially the speed and the torque) which an EV is ascertained to experience on the road. The work reported shows that the use of DTC-based IM drive, for EV application in general and λ_s^* selection in particular, have not been extensively studied. Besides, it is found that there is no generalized accepted method for determining the λ_s^*. The literature review gives an acceptable solution for a narrow torque and speed range, which is not favorable in EVs. In EV applications, the drive has to run over a wide range of operations based on the driving cycle, which they might predict on the road.

Since research activities in DTC for IM drive have mostly concentrated on industrial application and not towards application to EVs. However, in EV applications, it is desirable to have an algorithm for λ_s^* selection, with the following features;

- It should account for magnetic saturation in the motor.
- It should not use excessive computational resources and should be fast.
- It should be least sensitive to the motor's parameter variation.
- It should be applicable for a wide speed range.

Therefore, this chapter presents a selection method of λ_s^* for DTC-based IM drive over a wide range of operations in the context of EV drivetrain. The work's primary objective is to propose a method for determining a suitable value of variable λ_s^* for DTC of IM over a wide range of operations.

The two driving cycles, namely, the New York City Cycle (NYCC) and New European Driving Cycle (NEDC), are considered in this work to illustrate the proposed method's validity over a wide range of operations. In EV applications, the DC voltage variation is experienced wrt the discharge of the battery and operating conditions [80]. Thus, the proposed method first sets the maximum torque limit based on the available DC voltage and then determines the proper λ_s^*. The proposed method calculates λ_s^*, considering the reference speed, torque (T_e), and DC voltage. The contributions of this chapter are:

- A technique is proposed to determine a suitable value of λ_s^* for the DTC of IM.
- The proposed approach uses a Finite Element Analysis (FEA) based IM model to consider the magnetic saturation effect for calculating an appropriate λ_s^* value.
- The proposed method calculates λ_s^* considering the reference speed, torque (T_e), and DC voltage.
- The offline calculated values of λ_s^* are collected and stored in the lookup table (LUT) format and is fed to the DTC algorithm.
- It is less sensitive to the motor's parameter variation, such as stator resistance and leakage inductance, and magnetization inductance.

The performance evaluation of the proposed method over a wide speed range with the vehicle driving cycles (i.e., NYCC and NEDC) is carried out on the developed experimental setup in the laboratory. The technical details of the experimental setup are given in Appendix A.6. The comparison of the proposed methodology is made in terms of the speed, torque, and flux linkage responses, dynamic, and steady-state performance, with conventional DTC (constant λ_s^*) and variable flux technique, for various vehicle driving cycles. Further, the input energy consumption and efficiency analysis for considered driving cycles are also discussed.

The remainder of this chapter is organized as follows: Section 4.2 explains the FEA-based method to determine λ_s^* values. An FEA-based IM model is developed, and simulations are carried out on the developed model to obtain the λ_s values. A detailed methodology to get the suitable values of λ_s over a wide range of speed operations is explained in Section 4.2. Section 4.3 presents the parameter sensitivity analysis of the proposed method. Section 4.4 defines the implementation of obtained λ_s as a reference flux linkage (λ_s^*) in the DTC algorithm. Section 4.5 shows the comparative study of the proposed LUT-based DTC with conventional DTC (constant λ_s^*) and variable flux technique. The comparison is carried out in terms of the speed, torque, and flux linkage responses for driving cycles, dynamic and steady-state performance, and the demonstrated experimental results. Moreover, the

input energy consumption and efficiency analysis of the considered driving cycles are also discussed in Section 4.5. Finally, Section 4.6 presents the conclusion of the chapter.

4.2 Finite Element Analysis (FEA) based IM model

This section explains the methodology for the determination of λ_s^* in context to DTC-based IM drive over a wide range of operations in EV applications. The determination of λ_s^* is achieved by using the Finite Element Analysis (FEA) based IM model. The FEA-based IM model using ANSYS Maxwell 2D is developed, and simulations are carried out to determine the suitable values of λ_s over a wide range of speed. Fig. 4.1 shows the machine's geometry, and the dimension details of stator and rotor slots are given in Table 4.1. The parameters of the IM are listed in Appendix A.2.

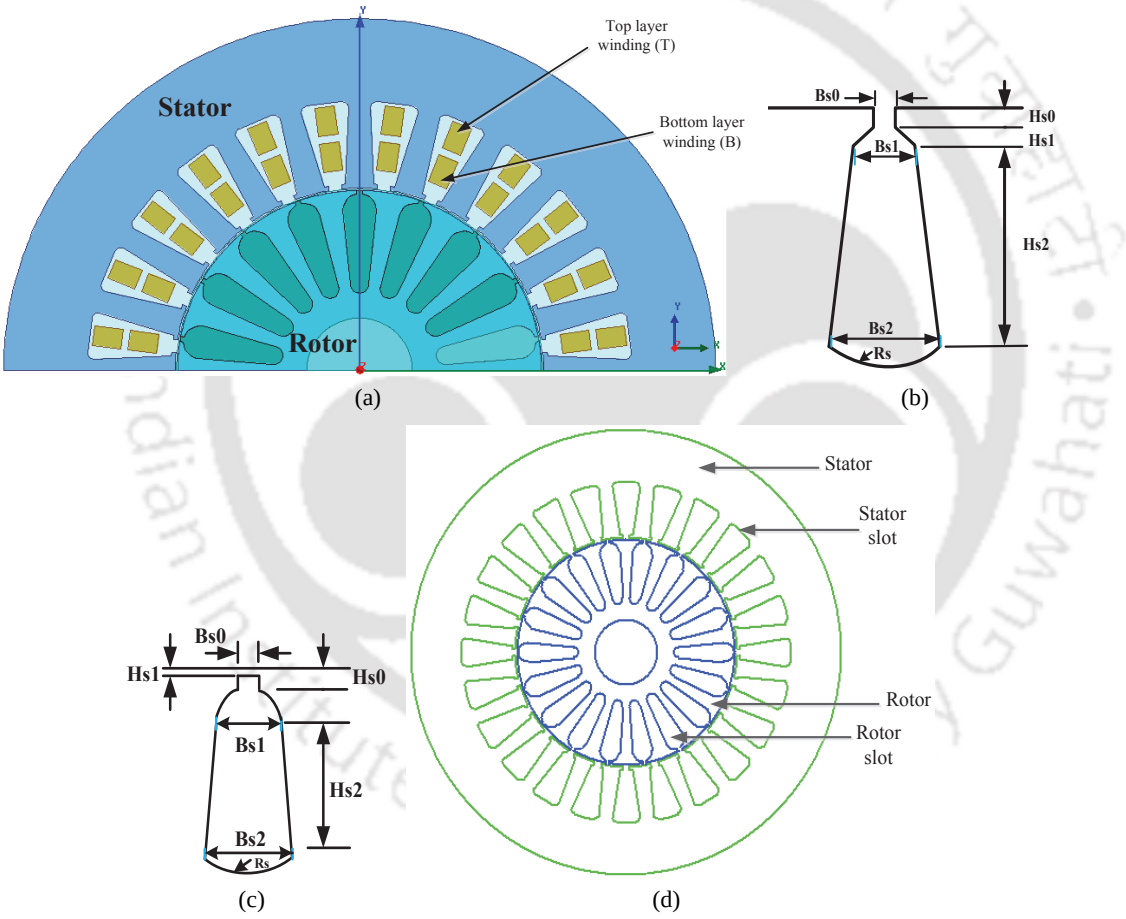

Fig. 4.1: ANSYS Maxwell three-phase induction motor model (a) Maxwell 2D (Half view) (b) Stator slot (c) Rotor slot (d) Lamination sheet.

Fig. 4.2 shows the B-H characteristic of the ferromagnetic core used in the FEA model of the IM. The winding scheme of the stator is listed in Table 4.2. The stator winding has two layers with four slots per pole per phase. Each phase has 28 turns and a coil in to 1T slot and out from 11B slot with a

Table. 4.1: Dimension details of stator and rotor slots

Dimension	Stator	Rotor	Unit
Outer diameter	135	69	*mm*
Inner diameter	70	20	*mm*
Hs0	0.8	0.65	*mm*
Hs1	0	0	*mm*
Hs2	14.6	14.2	*mm*
Bs0	2.5	1	*mm*
Bs1	4	6.27	*mm*
Bs2	9	3.5	*mm*
Rs	1.2	0.41	*mm*

slot pitch of 10 (T and B stand for top and bottom layer windings of the slot, respectively), as shown in Fig. 4.3(b).

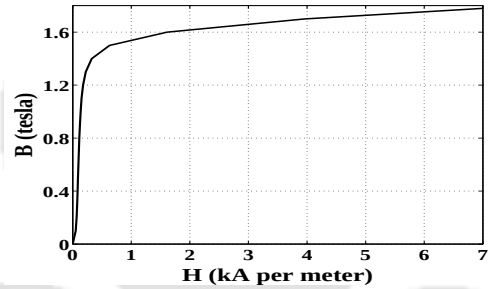

Fig. 4.2: B-H curve of the core material.

Table. 4.2: Two layers winding scheme of the stator

Phase	Turns	In slot	Out slot
A	28	1T	11B
A	28	2T	12B
A	28	3T	13B
A	28	4T	14B
-C	28	5T	15B
-C	28	6T	16B
-C	28	7T	17B
-C	28	8T	18B
B	28	9T	19B
B	28	10T	20B
B	28	11T	21B
B	28	12T	22B

With the required machine's geometry (see Fig. 4.1), the slot dimension details (see Table 4.1),

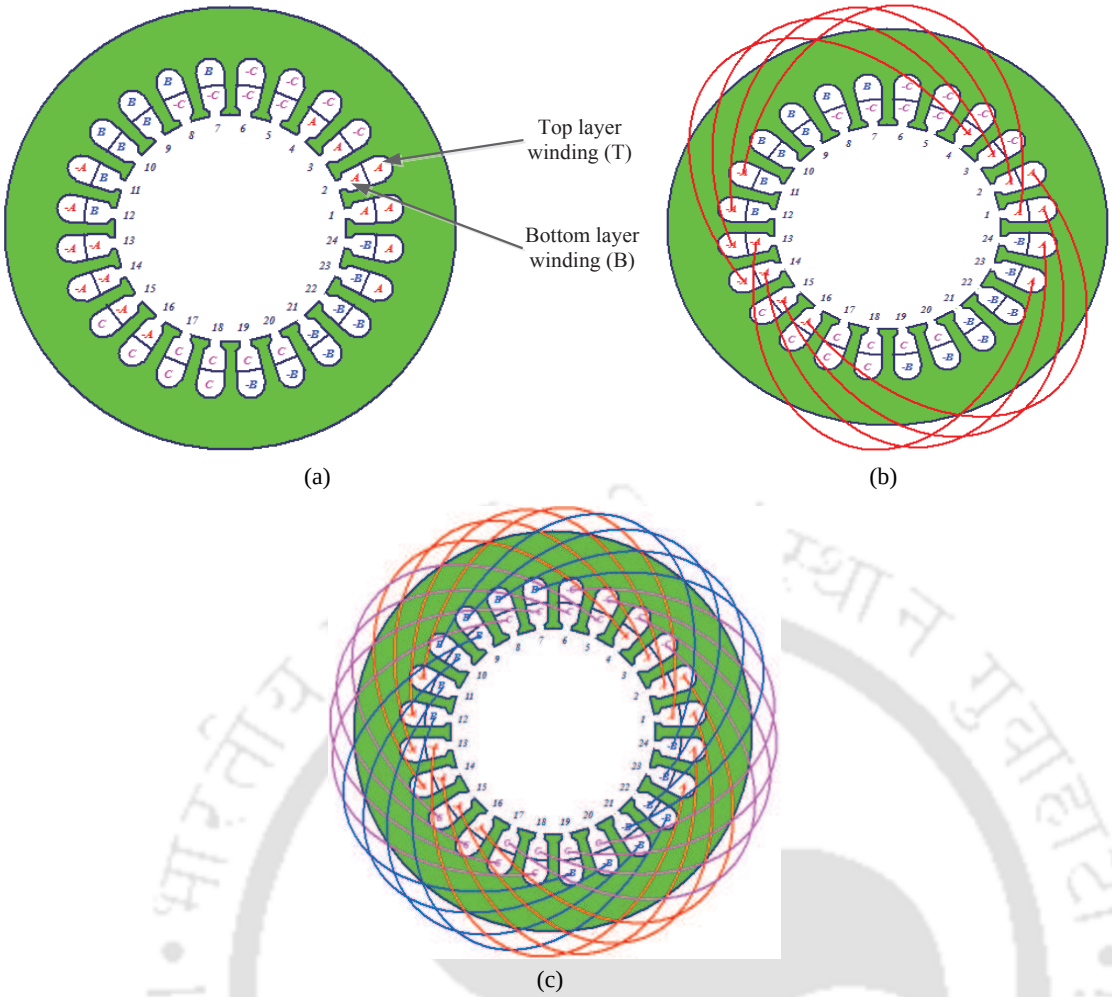

Fig. 4.3: Two layer winding scheme of the three-phase induction motor model shown in Fig. 4.1 (a) Stator winding scheme with two layers (b) Stator phase-A two layers winding (c) Complete two layers winding of the stator. The winding scheme is designed with 4 slots per pole per phase as per Table 4.2.

and the winding scheme (see Table 4.2), the IM FEA model is developed on ANSYS Maxwell. The simulations are carried out with variations in motor speed (N_r), stator voltage (V_s), and stator voltage frequency (f_s). The FEA simulation's primary objective is to obtain suitable values of λ_s and T_e in lookup tables (LUTs) format over a wide speed range. The obtained LUTs provide information about the suitable λ_s^* at required N_r and given T_e in context to the DTC strategy, with voltage and current constraints over a wide speed range.

The multiple sets of simulations are carried out with N_r varying from 100 rpm to 2850 rpm (rated) in 50rpm steps. For each N_r, f_s is chosen at a 5% slip, and few f_s with respective N_r are shown in Table 4.3. The V_s is varied from 10 V to 110 V with steps of 10V. The motor is supplied with the 50% of the rated phase voltage. This is due to the limited dc input voltage for the inverter. For each value of V_s and N_r, the corresponding values of stator current, flux linkage, and torque are obtained. The

obtained values of stator current, flux linkage, and torque are the instantaneous values. Therefore, they are further processed to get per phase rms quantities. The obtained rms values of quantities are arranged in tabular form, as shown in Table 4.4. The execution steps shown in Fig. 4.4 explain the process to be followed for FEA simulations and obtaining the rms values of stator current (I_s), flux linked (λ_s) by the stator coil, and the motor torque (T_e) in tabular form. Fig. 4.5 shows the flowchart of the process explained in Fig. 4.4.

Table. 4.3: Few stator frequencies at slip of 5%

Rotor speed (N_r)(rpm)	Synchronous speed (N_s) (rpm)	Frequency (f_s)(Hz)
100	105.26	1.76
300	315.78	5.26
500	526.32	8.77
1000	1052.63	17.54
1500	1578.95	26.32
2000	2105.26	35.09
2500	2631.58	43.86
2850	3000	50

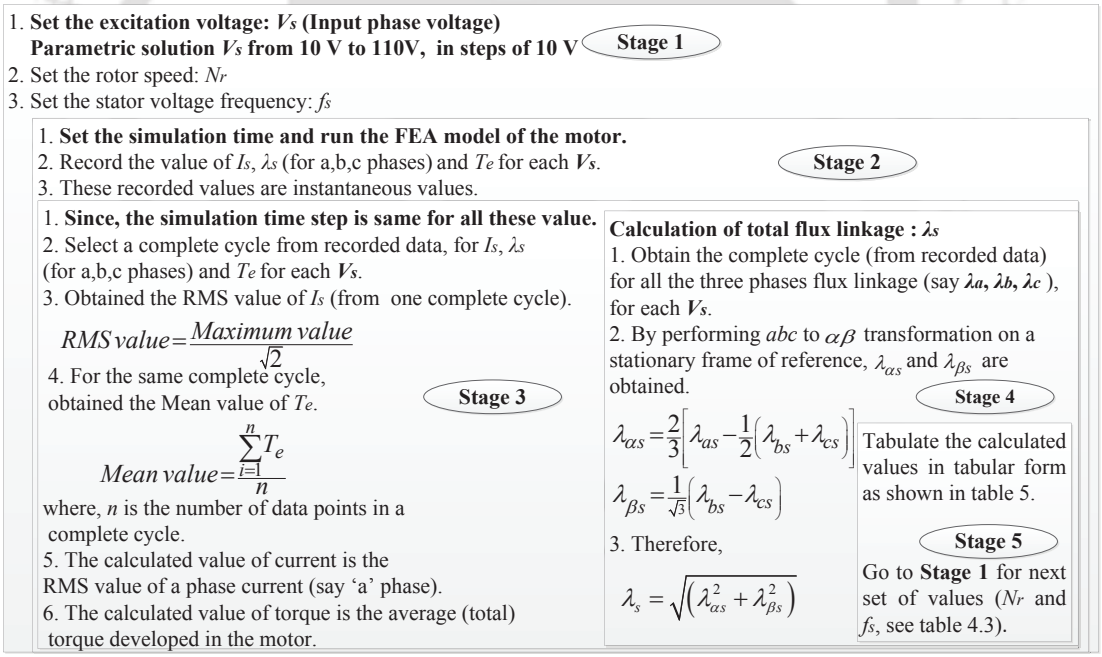

Fig. 4.4: Execution steps for the FEA simulation to obtain the values in tabulated form as shown in Tables 4.4 and 4.5.

Tables 4.4 and 4.5 shows some of the obtained tabulated values at different N_r and its corresponding f_s with the variation of V_s from 10 V to 110 V. In a similar manner, for all N_r between 100 rpm to 2850 rpm at 50 rpm steps, the corresponding values of I_s, λ_s, and T_e are obtained and arranged in

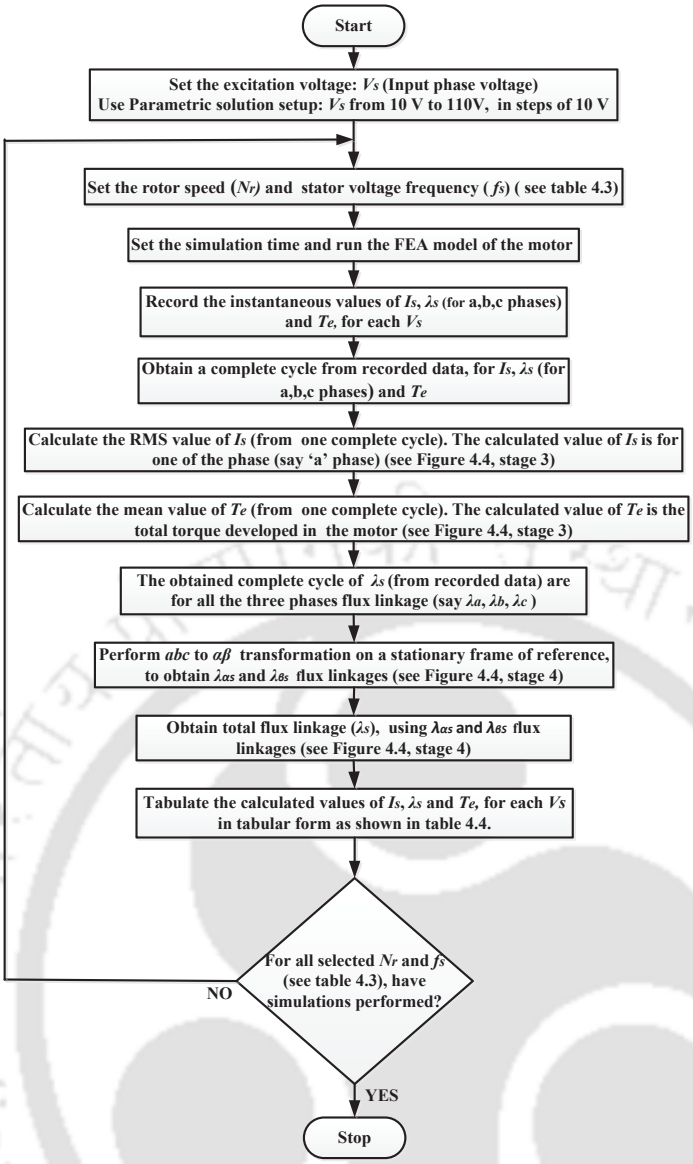

Fig. 4.5: Flow chart of the process explained in the Fig. 4.4, to run the FEA simulation and to obtain the values in tabulated form as shown in Tables 4.4 and 4.5.

tabular form.

The tabulated values show that the high value of I_s and λ_s are observed at lower speeds, which are impracticable for the IM used in this experiment. Since the nameplate current rating of IM is 2.5 A. This work's primary concern is for EV application, where the drive needs to operate over a wide speed and torque range with varying load conditions. So, limiting the current to its nominal rated values is not a preferable condition. Therefore, considering the IM used in this work with its electrical design constraint, it is overburden to twice the rated current value.

Thus, considering IM's overloading factor to twice its rated current value, processing of calculated data values of I_s, T_e, and λ_s are concluded. While processing the calculated values, the data points

Table. 4.4: Calculated values at 300 rpm motor speed and 5.26 Hz stator voltage frequency

Stator current(rms) (A)	Flux linkage (Wb)	Torque (Nm)	Input phase voltage(rms) (V)
0.47	0.57	0.17	10
1.94	1.08	0.52	20
4.33	1.45	0.76	30
6.76	1.78	0.96	40
9.32	2.06	1.16	50
12.05	2.28	1.34	60
14.85	2.46	1.49	70
17.79	2.61	1.59	80
20.66	2.72	1.66	90
23.50	2.82	1.72	100
26.31	2.91	1.78	110

Table. 4.5: Calculated values at 2500 rpm motor speed and 43.86 Hz stator voltage frequency

Stator current(rms) (A)	Flux linkage (Wb)	Torque (Nm)	Input phase voltage(rms) (V)
0.21	0.07	0.02	10
0.42	0.14	0.07	20
0.62	0.21	0.15	30
0.83	0.28	0.26	40
1.03	0.35	0.41	50
1.24	0.42	0.59	60
1.45	0.49	0.81	70
1.65	0.56	1.05	80
1.86	0.63	1.33	90
2.06	0.70	1.63	100
2.28	0.77	1.94	110

corresponding to the high value of I_s, i.e.,$>$ 5 A, are discarded from all the obtained tabulated values. For example, Table 4.4 has few values corresponding to $I_s > 5$ A. For such cases, the obtained tabulated values are again sorted with the current limit, ensuring the corresponding values to high current are discarded from the respective tables. The sorted values are again tabulated, as shown in Table 4.6.

Further, some tables have the calculated values within the acceptable current limit, as shown in

Table. 4.6: Sorted values at 300 rpm motor speed and 5.26 Hz stator voltage frequency

Stator current(rms) (A)	Flux linkage (Wb)	Torque (Nm)	Input phase voltage(rms) (V)
0.47	0.57	0.17	10
1.94	1.08	0.52	20
4.33	1.45	0.76	30

Table 4.5. In Table 4.5, all the values are within the acceptable current limit. Therefore, for such tables, further sorting of data points is not required. In like manner, the processing and sorting of calculated values for all the tables are completed and arranged in tabular form, and a few of them are as shown in Tables 4.5 and 4.6. These sorted data are further tabulated based on V_s variations. Since the variations in V_s are observed from 10 V to 110 V with 10 V steps, a total of 11 tables are further framed. In each table, the variations in N_r are observed from 100 rpm to 2850 rpm. For example, Table 4.7 is shown for 50 V.

Table. 4.7: Few of chosen values at phase voltage 50 V

Rotor speed(rpm)	Stator current(A)	Torque (Nm)	Flux Linkage(Wb)
250	3.91	0.89	0.49
500	3.86	0.91	0.5
1000	3.73	0.96	0.51
2000	3.12	1.09	0.53
2500	1.03	0.41	0.35
2850	1.01	0.39	0.31
250	4.30	1.10	0.52
1000	3.93	1.24	0.54
2000	2.40	1.26	0.62
1750	2.43	1.40	0.67
100	4.93	5.95	0.88

Table 4.7 is obtained by choosing corresponding 50 V data from Table 4.5, 4.6, and the rest of similar Tables (not shown). However, Table 4.6 does not have 50 V data. In such cases, the particular table can be ignored.

In similar manner, these eleven voltage tables are framed for 10 V to 110 V. For each V_s, the torque and flux linkage curves are plotted as shown in Figures 4.6 and 4.7.

- Fig. 4.6 shows T_e vs. N_r: The torque curves are plotted wrt N_r, for each V_s. This is used as torque LUT. Using curve fitting, these curves are further refined, as shown in Fig. 4.11.
- Fig. 4.7 shows λ_s vs. N_r: This curve shows the flux linkage curves wrt N_r, for each V_s. However, to get flux linkage LUT, λ_s vs. N_r curves are needed, at different T_e values, which is discussed in detail in the last paragraph of this section.

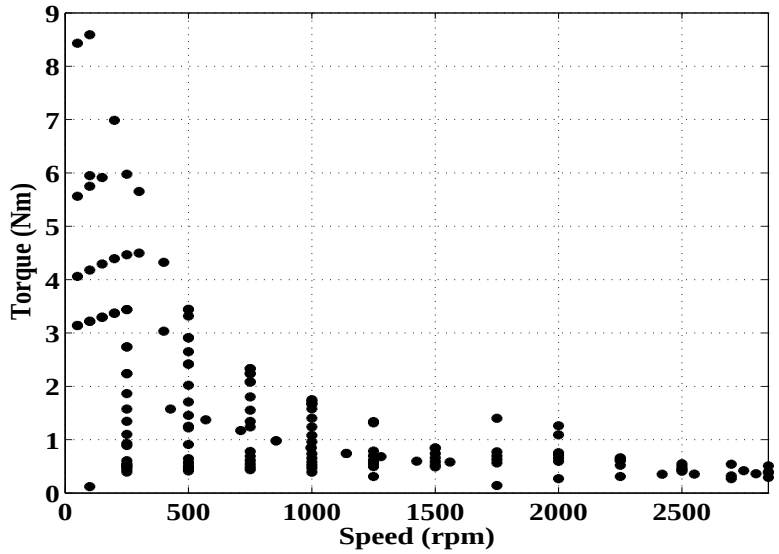

Fig. 4.6: T_e variations at 50 V wrt N_r.

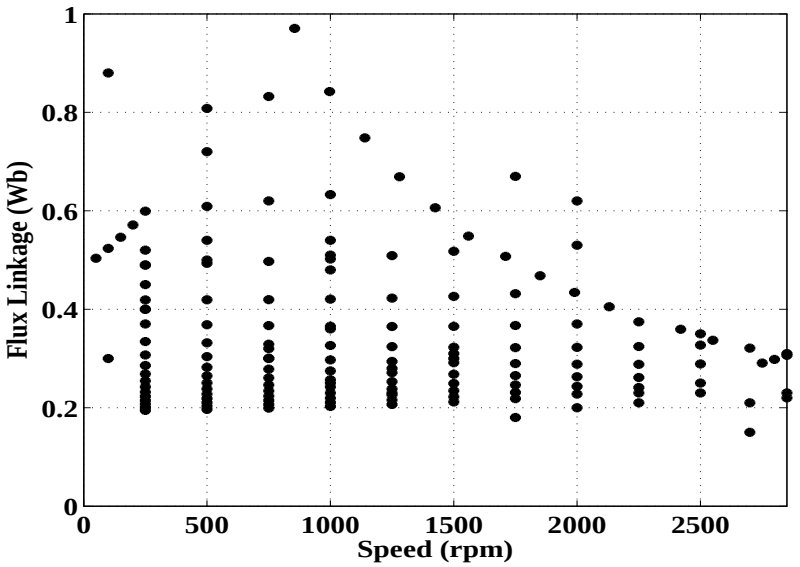

Fig. 4.7: λ_s variation at 50 V wrt N_r.

These graphs (see Fig(s). 4.6 and 4.7) are plotted with variations in N_r and f_s (for T_e and λ_s) at a particular V_s. As a result, multiple data points are observed at a particular value of N_r. If these sets

of data points are fed to the machine controller, pulsations in speed and torque can be seen, which, of course, is unacceptable for a drive system. Thus, the graphs are shown in Fig(s). 4.6 and 4.7 are further defined with limits such as λ_s limit, base speed, and T_e limit. These limits are explained in detail using relations (3.11) to (3.17) in chapter- 3. In the next subsequent sections, using these relations the λ_s limit, base speed, and T_e limit are defined to obtained suitable values of λ_s and T_e in LUT format.

4.2.1 Flux linkage limit calculation

The flux linkage limit is calculated, considering (3.15), which can be written as shown in (4.1),

$$\lambda_s = \frac{V_s - I_s R_s}{\omega_s} \tag{4.1}$$

In this work, the IM used is excited with 50% of its rated phase voltage i.e., 110 V (rms). Therefore, the stator λ_s must be calculated at 110 V voltage to obtain the maximum flux linked by the stator coil. So, (4.1) can be re-framed as shown in (4.2),

$$\left|\lambda_{s(110\,V)}\right| = \left|\frac{V_{ind}}{\omega_s}\right| \tag{4.2}$$

where V_{ind} is the maximum voltage across the stator winding of induction motor [107] and also termed as stator winding back-emf. The stator winding back-emf is the voltage difference of stator input voltage and stator resistance drop. Thus, V_{ind} is defined using (4.3),

$$V_{ind} = \left(\sqrt{2}\sqrt{3}\,V_s\right) - \left(\sqrt{2}\,I_s\,R_s\right) \tag{4.3}$$

where, V_s and I_s are the phase rms values of stator input voltage and current, respectively. The stator winding of the IM used is connected in a star fashion. Under the above-stated conditions, the λ_s is calculated and is found to 0.8 Wb. Therefore, in this thesis, 0.8 Wb is considered as the maximum flux linked by the stator coil. The same value of flux linkage is used wherever the rated λ_s is required.

4.2.2 Base speed calculation

For the base speed determination, the relation between ω_s and ω_r is examined and is determined using (4.4).

$$\omega_s = \omega_r + \frac{1}{\sigma\,\tau_r} \tag{4.4}$$

where ω_r is rotor speed in rad/sec, $\sigma = 1 - \frac{L_m^2}{L_s L_r}$ is the leakage coefficient, and $\tau_r = \frac{L_r}{r_r}$ is the rotor time constant [69]. Using (4.4), the base speed is determined as;

$$\omega_r = \omega_s - \frac{1}{\sigma \tau_r} \tag{4.5}$$

Here, ω_r is considered as base speed in rad/sec. Table 4.8 shows the calculation of base speed wrt variable λ_s. It is found that with variable λ_s, base speed is not changing, and it remains constant for all values of V_s. In this thesis, the base speed is calculated as 47.37 rad/sec. Thus, the equivalent speed in rpm, i.e., 500 rpm, is considered as base speed.

Table. 4.8: Base speed calculation with varaible flux

Phase voltage(rms) (V)	110	100	90	80	70	60	50
Flux linkage(Wb)	0.809	0.731	0.653	0.575	0.496	0.420	0.342
Maximum voltage induced (V_{ind}) (V)	254.276	229.782	205.287	180.792	156.30	131.80	107.31
$\omega_s(rad/sec)$	181.38	181.38	181.38	181.38	181.38	181.38	181.38
$\omega_r(rad/sec)$	47.37	47.37	47.37	47.37	47.37	47.37	47.37

4.2.3 Torque limit calculation, and LUTs for T_e and λ_s

This section determines the suitable values of λ_s and T_e in the lookup table (LUT) format. The calculated T_e defines the maximal value of T_e at a reference speed and dc source voltage in the DTC algorithm. Therefore, it is mandatory to limit the torque value. Using relation (3.11), the maximum value of torque is obtained. This will ensure the limit of torque value for corresponding λ_s, V_s and N_r. The observation chart for T_e and λ_s wrt rotor speed at different phase voltages is shown in Table 4.9.

The obtained curves for λ_s and T_e are shown in Fig.(s) 4.8 and 4.9. If these sets of data points are used in the DTC, vibrations in the motor speed are observed. For acceptable motor operation, the obtained curves of λ_s and T_e (shown in Fig.(s) 4.8 and 4.9) are refined using a cubic spline interpolation curve fitting. The obtained smoothened curves are shown in Fig.(s) 4.10 and 4.11. Few torque LUT entries are shown in Table 4.10, and the complete detailed LUT table is given in Appendix A.1.2.

The torque lines are shown in Fig. 4.11 ensure that at a given V_s (say 30 V, 40 V, 50 V), the motor can develop the torque (maximum) shown by these lines. For example, if the motor is operating at 30 V, it can achieve a maximal torque of 0.49 Nm upto base speed. As speed increases, the torque capability developed by the motor reduces. And, if a torque of 0.49 Nm is needed at any other speed ($>$ base speed), the voltage level must be increased to meet torque demand.

Fig. 4.10 shows λ_s variations wrt N_r, and V_s. The λ_s LUT is obtained by determining the λ_s verses

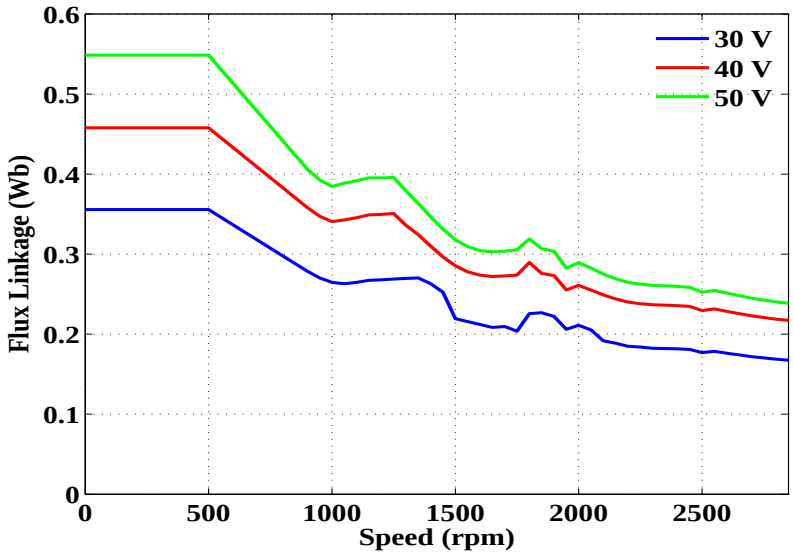

Fig. 4.8: Flux linkage variation wrt speed at different phase voltages. The flux linkages are not smooth; if used in the DTC as reference flux, it causes oscillations in motor speed.

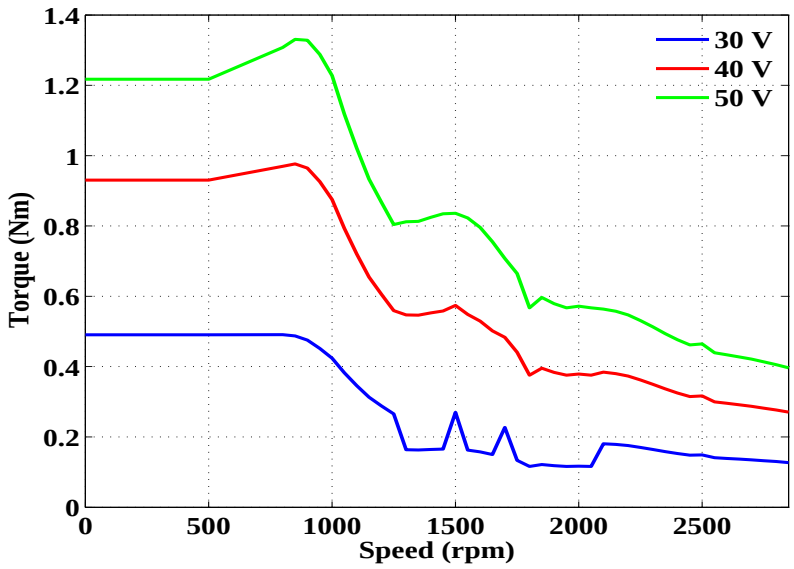

Fig. 4.9: Torque variation wrt speed at different phase voltages. The torques are not smooth; if used in DTC, it causes oscillations in motor speed.

N_r curves at distinct values of T_e. Therefore, curve fitting is further executed on the obtained sets of data to accomplish λ_s verses N_r plots.

For example, at 1000 rpm, complete data points of T_e and λ_s values are available with variations of V_s, as shown in Table 4.9. Using curve fitting, the fitted-model at 1000 rpm has been determined. This fitted-model shows λ_s variation wrt T_e at 1000 rpm. Similar steps are carried out for the remaining N_r values to obtain the fitted-models. These fitted-models show variations between λ_s and T_e values at

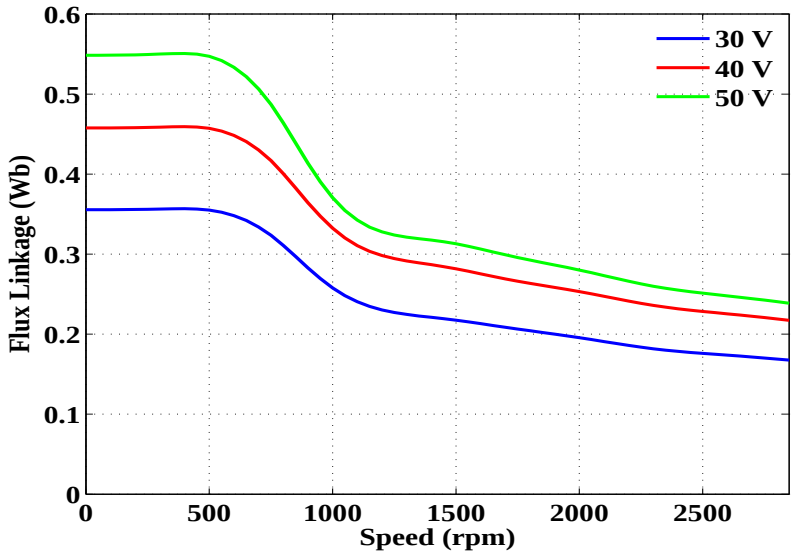

Fig. 4.10: Flux linkage variation wrt speed at different phase voltages. The flux linkages are smooth, and it is acceptable for DTC.

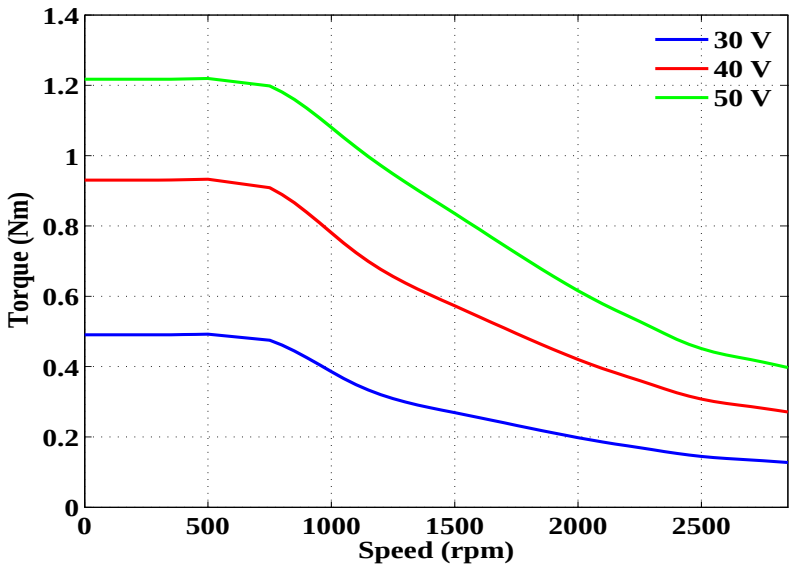

Fig. 4.11: Torque variation wrt speed at different phase voltages. The torques are smooth, and it is acceptable for the DTC.

all possible speeds from 100 rpm to 2850 rpm. The obtained λ_s and T_e values at distinct speeds are arranged in tabular form to get the required λ_s LUT. Few λ_s LUT entries are shown in Table 4.11, and the complete detailed LUT table is given in Appendix A.1.1. A Flow chart to determine the suitable values of λ_s and T_e in LUT format is shown in Fig. 4.12.

The obtained LUT for λ_s shows flux variations wrt N_r and T_e. The T_e LUT shows motor torque variations wrt N_r and V_s. In EV applications, the variation in DC voltage is experienced wrt the discharge of the battery and operating conditions [80]. Therefore, for inverter fed IM, the relation

Table. 4.9: Torque lookup table and flux linkage table wrt speed at different phase voltage

$N_r\ (rpm)/$ $V_s\ (V)$		500 rpm	1000 rpm	1500 rpm	2500 rpm	2850 rpm
30	T_e	0.49	0.39	0.27	0.14	0.12
	λ_s	0.356	0.256	0.218	0.176	0.167
40	T_e	0.93	0.78	0.57	0.31	0.27
	λ_s	0.45	0.32	0.28	0.23	0.21
50	T_e	1.22	1.08	0.84	0.45	0.39
	λ_s	0.54	0.36	0.31	0.25	0.23

Table. 4.10: Torque lookup table wrt motor speed and phase voltage (as shown in Fig. 4.11).

Speed/ voltage	500 rpm	1000 rpm	1500 rpm	2500 rpm	2850 rpm
30 V	0.49	0.39	0.27	0.14	0.12
40 V	0.93	0.78	0.57	0.31	0.27
50 V	1.22	1.08	0.84	0.45	0.39

Table. 4.11: Lookup Table of flux linkage which is used as reference flux in the DTC scheme

Speed/ torque	500 rpm	1000 rpm	1500 rpm	2500 rpm	2850 rpm
0.3 Nm	0.30	0.21	0.18	0.15	0.14
0.7 Nm	0.45	0.32	0.28	0.23	0.21
1.5 Nm	0.72	0.48	0.41	0.33	0.31

between the stator excitation voltage (V_s) and inverter input dc voltage (V_{dc}) must be considered and is calculated using (4.6) [113].

$$|V_s| = \frac{0.8 * V_{dc}}{\sqrt{3}} \tag{4.6}$$

Using (4.6), V_{dc} is calculated as:

$$V_{dc} = \frac{\sqrt{3}|V_s|}{0.8} \tag{4.7}$$

This section explains the determination method of λ_s^* using an FEA-based IM model. The obtained λ_s^* values are stored in LUT format, with λ_s, base speed, and torque limits. The suitable value of λ_s^* is chosen from its LUT at reference speed and T_e. In addition, a proper value of maximum T_e (i.e., T_{em}) is also chosen from its LUT at reference speed and dc source input voltage. To check the robustness of the proposed method, the parameters (i.e., R_s and L_{1s}) sensitivity analysis has performed and is discussed in the next section.

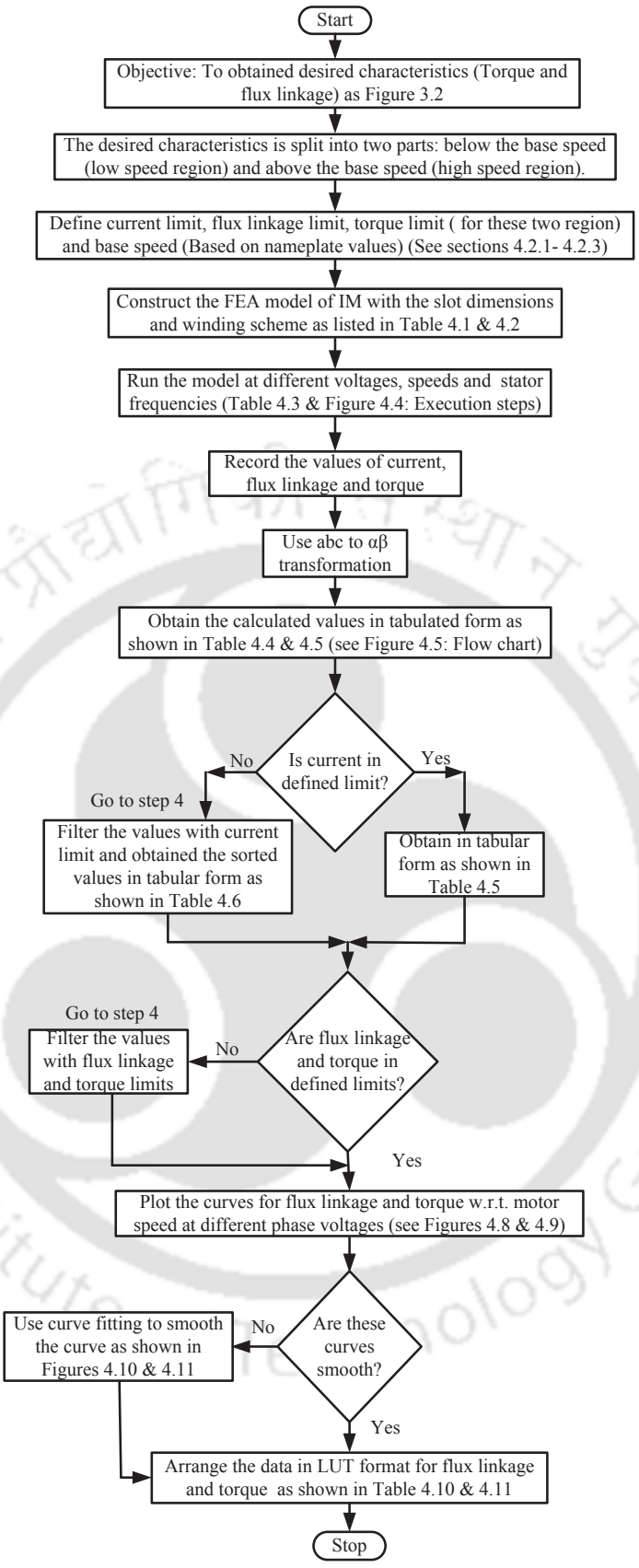

Fig. 4.12: Flow chart to obtain LUTs for flux linkage and torque using FEA-based IM model.

4.3 Parameter Sensitivity Analysis

In this section, the robustness of the proposed method is examined by performing parameter sensitivity analysis. The effect of parameter sensitivity on the proposed method is observed with ±5 percent (%) variations in R_s and L_{ls}. The FEA motor model is made ready with these variations, and the sets of simulations are performed. The calculated values are shown in Tables 4.12-4.15. These values are obtained from the simulations test of the modified FEA model with change in parameters values by ±5%. Tables 4.12-4.15 show the obtained values with parameter variations at 300 rpm and 2500 rpm, with respect to Tables 4.4 and 4.5.

Table. 4.12: Calculated values at 300 rpm motor speed and 5.26 Hz stator voltage frequency with ±5% R_s variations and constant L_{ls} wrt Table 4.4 (here, $\pm\delta$ indicates ±5%).

Stator current(I_{as}) (A)		Flux linkage (λ_s) (wb)		Torque (T_e) (Nm)		Input phase voltage(rms)(V)
With $(R_s+\delta R_s)$	With $(R_s-\delta R_s)$	With $(R_s+\delta R_s)$	With $(R_s-\delta R_s)$	With $(R_s+\delta R_s)$	With $(R_s-\delta R_s)$	
0.46	0.475	0.568	0.58	0.167	0.172	10
1.91	1.98	1.07	1.085	0.51	0.523	20
4.24	4.45	1.44	1.46	0.75	0.767	30
6.60	6.92	1.76	1.80	0.94	0.977	40
9.05	9.60	2.03	2.08	1.13	1.18	50
11.70	12.45	2.25	2.31	1.31	1.36	60
14.32	15.42	2.43	2.49	1.46	1.52	70
17.12	18.53	2.57	2.63	1.55	1.61	80
19.90	21.55	2.69	2.75	1.62	1.67	90
22.60	24.51	2.79	2.85	1.68	1.73	100
25.26	27.49	2.88	2.94	1.74	1.79	110

Table 4.12 and 4.13 show calculated values at stator voltage frequency 5.26 Hz and motor speed 300 rpm, with ±5% variations in R_s and L_{ls}, respectively, wrt Table 4.4. In Table 4.12 and 4.13, the first three values are within the acceptable current limit (i.e., 5 A). As discussed in section 4.2, the values that are not in the current limit range are discarded from the respective tables. Therefore, from the tables (Table 4.12 and 4.13), the values corresponding to high current are discarded. Fig. 4.13 shows the plot for calculated values of Table 4.12 at 300 rpm and 5.26 Hz with ±5% R_s variations and at constant L_{ls} (wrt Table 4.4). Fig. 4.14 shows the plot for calculated values of Table 4.13 at 300 rpm and 5.26 Hz with ±5% L_{ls} variations and at constant R_s (wrt Table 4.4). In Fig(s). 4.13 and 4.14, an arrow is pointed to show the values within the acceptable current limit of 5 A, and remaining values beyond the limit are discarded. The percentage change in calculated values with variations in

Table. 4.13: Calculated values at 300 rpm motor speed and 5.26 Hz stator voltage frequency with $\pm 5\%$ L_{ls} variations and constant R_s wrt Table 4.4 (here, $\pm\delta$ indicates $\pm 5\%$).

Stator current(I_{as}) (A)		Flux linkage(λ_s) (wb)		Torque(T_e) (Nm)		Input phase voltage(rms)(V)
With $(L_{ls}+\delta L_{ls})$	With $(L_{ls}-\delta L_{ls})$	With $(L_{ls}+\delta L_{ls})$	With $(L_{ls}-\delta L_{ls})$	With $(L_{ls}+\delta L_{ls})$	With $(L_{ls}-\delta L_{ls})$	
0.46	0.472	0.569	0.575	0.164	0.165	10
1.93	1.95	1.07	1.081	0.512	0.514	20
4.32	4.36	1.44	1.452	0.752	0.755	30
6.72	6.78	1.77	1.782	0.953	0.956	40
9.27	9.36	2.05	2.061	1.15	1.157	50
11.98	12.10	2.27	2.284	1.33	1.341	60
14.78	14.91	2.45	2.465	1.48	1.487	70
17.71	17.86	2.60	2.618	1.58	1.585	80
20.60	20.76	2.71	2.723	1.65	1.65	90
23.42	23.56	2.81	2.822	1.71	1.739	100
26.23	26.41	2.90	2.911	1.76	1.81	110

Table. 4.14: Calculated values at 2500 rpm motor speed and 43.86 Hz stator voltage frequency with $\pm 5\%$ R_s variations and constant L_{ls} wrt Table 4.5 (here, $\pm\delta$ indicates $\pm 5\%$).

Stator current(I_{as}) (A)		Flux linkage(λ_s) (wb)		Torque(T_e) (Nm)		Input phase voltage(rms)(V)
With $(R_s+\delta R_s)$	With $(R_s-\delta R_s)$	With $(R_s+\delta R_s)$	With $(R_s-\delta R_s)$	With $(R_s+\delta R_s)$	With $(R_s-\delta R_s)$	
0.207	0.212	0.069	0.071	0.0199	0.0203	10
0.414	0.425	0.138	0.141	0.0695	0.0701	20
0.619	0.623	0.209	0.212	0.149	0.151	30
0.825	0.832	0.278	0.283	0.264	0.267	40
1.025	1.036	0.348	0.353	0.413	0.418	50
1.236	1.234	0.417	0.424	0.596	0.603	60
1.442	1.454	0.488	0.495	0.811	0.821	70
1.646	1.655	0.556	0.566	1.059	1.071	80
1.852	1.862	0.629	0.636	1.336	1.352	90
2.059	2.07	0.698	0.71	1.634	1.652	100
2.273	2.285	0.768	0.775	1.949	1.97	110

parameters for 300 rpm and 5.26 Hz wrt Table 4.4 are shown in Table 4.16 and 4.17. The tables show that the maximum change in percentage, within the acceptable current limit, for the calculated values are $(+2.12$ to $-2.77)\%$ for I_s, $(+0.92$ to $-1.75)\%$ for λ_s, $(+3.52$ to $-1.17)\%$ for T_e.

Table 4.14 and 4.15 show calculated values at 2500 rpm and 43.86 Hz, with $\pm 5\%$ R_s and L_{ls} variations, respectively, wrt Table 4.5. The obtained values in these tables are within the acceptable current limit. Fig. 4.15 shows the plot for the calculated values of Table 4.14 at 2500 rpm and 43.86 Hz, with $\pm 5\%$ R_s variations and constant L_{ls}, wrt Table 4.5. Fig. 4.16 shows the plot for calculated

Table. 4.15: Calculated values at 2500 rpm motor speed and 43.86 Hz stator voltage frequency with $\pm 5\%$ L_{ls} variations and constant R_s wrt Table 4.5 (here, $\pm\delta$ indicates $\pm 5\%$).

Stator current(I_{as}) (A)		Flux linkage(λ_s) (wb)		Torque(T_e) (Nm)		Input phase voltage(rms)(V)
With $(L_{ls}+\delta L_{ls})$	With $(L_{ls}-\delta L_{ls})$	With $(L_{ls}+\delta L_{ls})$	With $(L_{ls}-\delta L_{ls})$	With $(L_{ls}+\delta L_{ls})$	With $(L_{ls}-\delta L_{ls})$	
0.207	0.212	0.0699	0.0704	0.0197	0.0201	10
0.414	0.421	0.1399	0.141	0.0696	0.0706	20
0.619	0.623	0.2096	0.212	0.1491	0.1501	30
0.825	0.832	0.2789	0.282	0.2654	0.2672	40
1.024	1.036	0.3498	0.353	0.415	0.4177	50
1.237	1.242	0.4198	0.424	0.5977	0.6017	60
1.442	1.454	0.4893	0.494	0.8136	0.8188	70
1.648	1.655	0.5586	0.565	1.0622	1.0691	80
1.853	1.861	0.6299	0.635	1.34	1.3485	90
2.059	2.071	0.6998	0.705	1.6385	1.6492	100
2.273	2.286	0.7698	0.774	1.9531	1.966	110

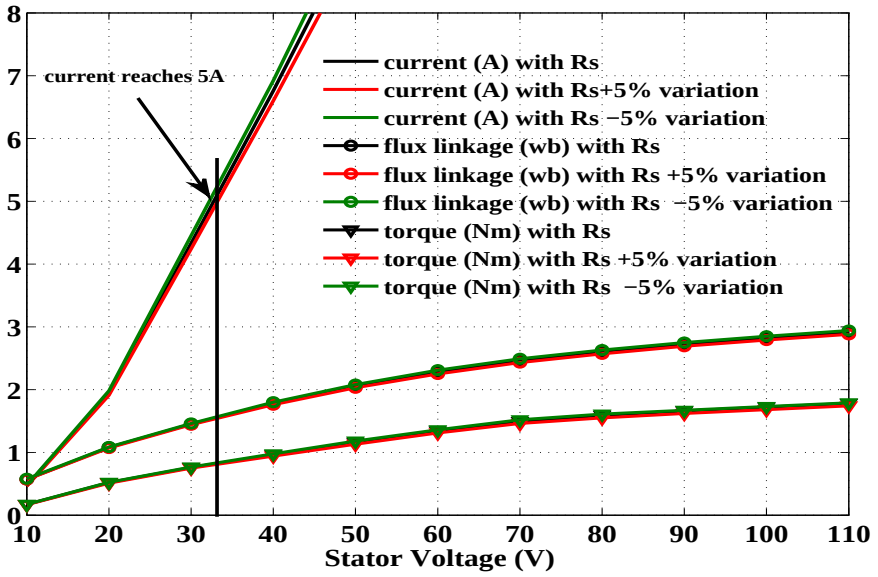

Fig. 4.13: Calculated values (Table 4.12) with stator resistance (R_s) variations of 5% for 300 rpm at stator voltage frequency of 5.26 Hz wrt Table 4.4.

values of Table 4.15 at 2500 rpm and 43.86 Hz, with $\pm 5\%$ L_{ls} variations and constant R_s (wrt Table 4.5). The percentage change in calculated values with variations in parameters for 2500 rpm and 43.86 Hz wrt Table 4.5 are shown in Table 4.18 and 4.19. The tables show that the maximum change in percentage for the calculated value are $(+1.42$ to $-1.19)\%$ for I_s, $(\pm 1.42)\%$ for λ_s, $(+1.5$ to $-2.76)\%$ for T_e.

These observations show that, for $\pm 5\%$ parameter variations, the maximum variations in λ_s and T_e are $(+0.92$ to $-1.75)$ % and $(+3.52$ to $-1.17)\%$, respectively, up to the base speed. Beyond the base

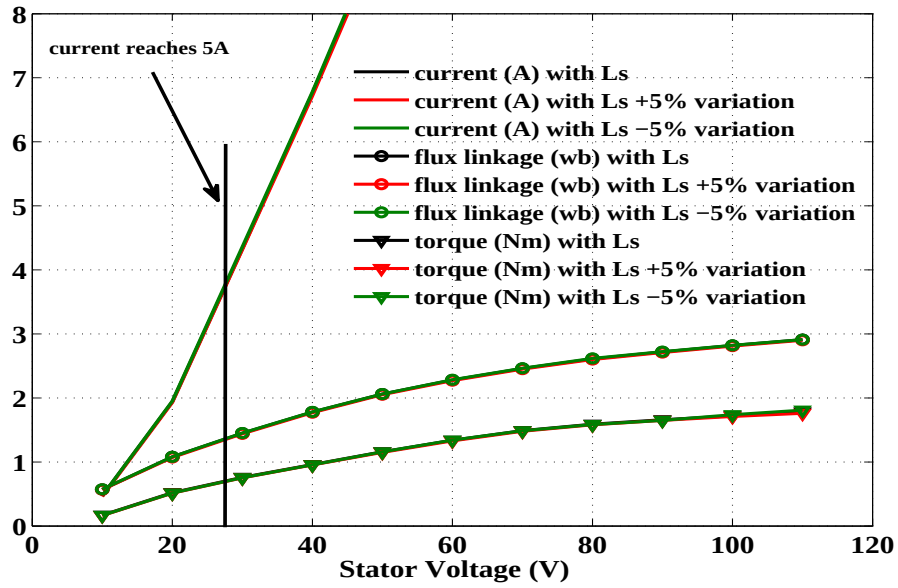

Fig. 4.14: Calculated values (Table 4.13) with stator leakage inductance (L_{ls}) variations of 5% for 300 rpm at stator voltage frequency of 5.26 Hz wrt Table 4.4.

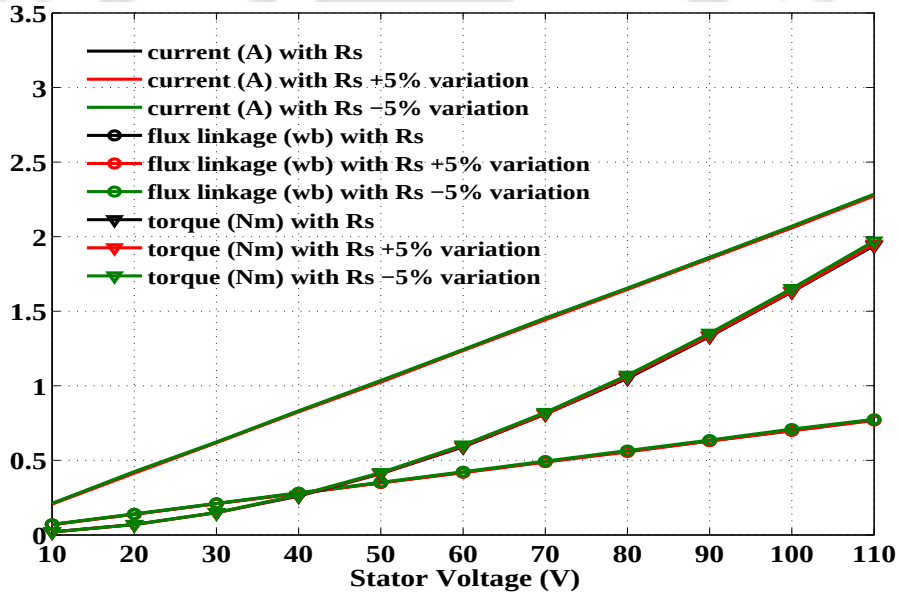

Fig. 4.15: Calculated values (Table 4.14) with stator resistance (R_s) variations of 5% for 2500 rpm at stator voltage frequency of 43.86 Hz wrt Table 4.5.

speed, the variations in λ_s and T_e are (± 1.42)% and ($+1.5$ to -2.76)%, respectively. The observations confirm that the proposed approach is least sensitive to the variations of parameters. These offline obtained values of λ_s^* and T_e are arranged in LUT format and are fed to the DTC algorithm, which is discussed in the next section.

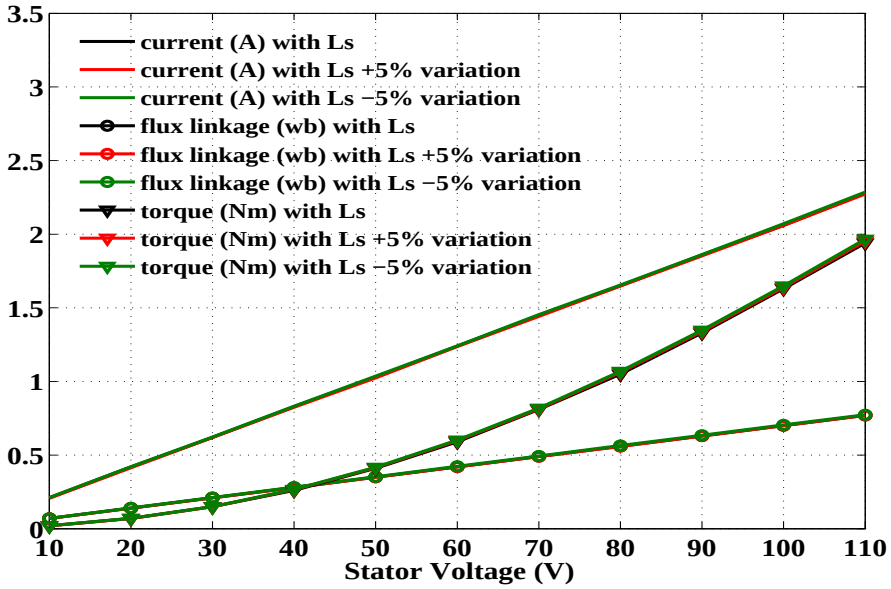

Fig. 4.16: Calculated values (Table 4.15) with stator leakage inductance (L_{ls}) variations of 5% for 2500 rpm at stator voltage frequency of 43.86 Hz wrt Table 4.5.

Table. 4.16: Percentage (%) change in calculated values of Table 4.12 at 300 rpm motor speed and 5.26 Hz stator voltage frequency with $\pm 5\%$ R_s variations and constant L_{ls} wrt Table 4.4 (here, $\pm\delta$ indicates $\pm 5\%$).

% change in stator current (I_{as})		% change in flux linkage (λ_s)		% change in torque (T_e)		Input phase voltage(V_{as})(V)
With $(R_s + \delta R_s)$	With $(R_s - \delta R_s)$	With $(R_s + \delta R_s)$	With $(R_s - \delta R_s)$	With $(R_s + \delta R_s)$	With $(R_s - \delta R_s)$	
2.12	−1.06	0.35	−1.75	1.76	−1.17	10
1.54	−2.06	0.92	−0.46	1.92	−0.57	20
2.07	−2.77	0.68	−0.68	1.31	−0.92	30
2.36	−2.36	1.12	−1.12	2.08	−1.77	40
2.89	−3.00	1.45	−0.97	2.58	−1.72	50
2.90	−3.31	1.31	−1.31	2.23	−1.49	60
3.56	−3.83	1.21	−1.21	2.01	−2.01	70
3.76	−4.15	1.53	−0.76	2.51	−1.25	80
3.67	−4.30	1.10	−1.10	2.40	−0.60	90
3.82	−4.29	1.06	−1.06	2.32	−0.58	100
3.99	−4.48	1.03	−1.03	2.24	−0.56	110

4.4 Implementation of Proposed Method

Fig. 4.17 shows the schematic block diagram of the closed-loop IM speed control technique with the DTC strategy. The inner loop determines the estimated torque (T_e) magnitude and flux linkage (λ_s) magnitude based on stator voltages and currents, as discussed in chapter-3, section 3.2.4. The T_e and λ_s are compared with their reference values, and the corresponding errors are generated. These

Table. 4.17: Percentage (%) change in calculated values (Table 4.13) at 300 rpm motor speed and 5.26 Hz stator voltage frequency with $\pm 5\%$ L_{ls} variations and constant R_s wrt Table 4.4 (here, $\pm\delta$ indicates $\pm 5\%$).

% change in stator current (I_{as})		% change in flux linkage (λ_s)		% change in torque (T_e)		Input phase voltage(V_{as})(V)
With $(L_{ls}+\delta L_{ls})$	With $(L_{ls}-\delta L_{ls})$	With $(L_{ls}+\delta L_{ls})$	With $(L_{ls}-\delta L_{ls})$	With $(L_{ls}+\delta L_{ls})$	With $(L_{ls}-\delta L_{ls})$	
2.12	−0.42	0.17	−0.87	3.52	2.94	10
0.51	−0.51	0.92	−0.09	1.53	1.15	20
0.23	−0.69	0.68	−0.13	1.05	0.65	30
0.59	−0.29	0.56	−0.11	0.72	0.41	40
0.53	−0.42	0.48	−0.04	0.86	0.25	50
0.58	−0.41	0.43	−0.17	0.74	−0.70	60
0.47	−0.40	0.40	−0.20	0.67	0.20	70
0.44	−0.39	0.38	−0.30	0.62	0.31	80
0.29	−0.48	0.36	−0.11	0.60	0.60	90
0.34	−0.25	0.35	−0.07	0.58	−1.10	100
0.30	−0.38	0.34	−0.03	1.12	−1.68	110

Table. 4.18: Percentage (%) change in calculated values (Table 4.14) at 2500 rpm motor speed and 43.86 Hz stator voltage frequency with $\pm 5\%$ R_s variations and constant L_{1s} wrt Table 4.5 (here, $\pm\delta$ indicates $\pm 5\%$).

% change in stator current (I_{as})		% change in flux linkage (λ_s)		% change in torque (T_e)		Input phase voltage(V_{as})(V)
With $(R_s+\delta R_s)$	With $(R_s-\delta R_s)$	With $(R_s+\delta R_s)$	With $(R_s-\delta R_s)$	With $(R_s+\delta R_s)$	With $(R_s-\delta R_s)$	
1.42	−0.95	1.42	−1.42	0.50	−1.50	10
1.42	−1.19	1.42	−0.71	0.71	−0.14	20
0.16	−0.48	0.47	−0.95	0.66	−0.66	30
0.60	−0.24	0.71	−1.07	−1.53	−2.69	40
0.48	−0.58	0.57	−0.85	−0.73	−1.95	50
0.32	−0.24	0.71	−0.95	−1.01	−2.20	60
0.55	−0.27	0.40	−1.02	−0.12	−1.35	70
0.24	−0.30	0.71	−1.07	−0.85	−2.00	80
0.43	−0.10	0.15	−0.95	−0.45	−1.65	90
0.05	−0.48	0.28	−1.42	−0.24	−1.34	100
0.31	−0.21	0.25	−0.64	−0.46	−1.54	110

generated errors are the inputs to respective comparators, i.e., torque error is input to the torque hysteresis comparator, and flux error is input to the flux hysteresis comparator. The torque hysteresis comparator outputs are +1,-1,0, and flux hysteresis comparator outputs are +1,-1 (where +1 indicates for an increment, -1 for decrement, and 0 to remains unchanged). The two hysteresis comparators output along with the sector information (N) are the three inputs to an inverter switching table. The

Table. 4.19: Percentage (%) change in calculated values (Table 4.15) at 2500 rpm motor speed and 43.86 Hz stator voltage frequency with $\pm 5\%$ L_{1s} variations and constant R_s wrt Table 4.5 (here, $\pm\delta$ indicates $\pm 5\%$).

% change in stator current (I_{as})		% change in flux linkage (λ_s)		% change in torque (T_e)		Input phase voltage(V_{as})(V)
With $(L_{ls}+\delta L_{ls})$	With $(L_{ls}-\delta L_{ls})$	With $(L_{ls}+\delta L_{ls})$	With $(L_{ls}-\delta L_{ls})$	With $(L_{ls}+\delta L_{ls})$	With $(L_{ls}-\delta L_{ls})$	
1.42	−0.95	0.14	−0.57	1.5	−0.5	10
1.42	−0.23	0.07	−0.71	0.57	−0.85	20
0.16	−0.48	0.19	−0.95	0.6	−0.06	30
0.60	−0.24	0.39	−0.71	−2.07	−2.76	40
0.58	−0.58	0.05	−0.85	−1.21	−1.87	50
0.24	−0.16	0.04	−0.95	−1.30	−1.98	60
0.55	−0.27	0.14	−0.81	−0.44	−1.08	70
0.12	−0.30	0.25	−0.89	−1.16	−1.81	80
0.37	−0.05	0.01	−0.79	−0.75	−1.39	90
0.05	−0.53	0.02	−0.71	−0.52	−1.17	100
0.31	−0.26	0.02	−0.51	−0.67	−1.34	110

switching table output is switching signals (S_{abc}), which are generated for inverter switches.

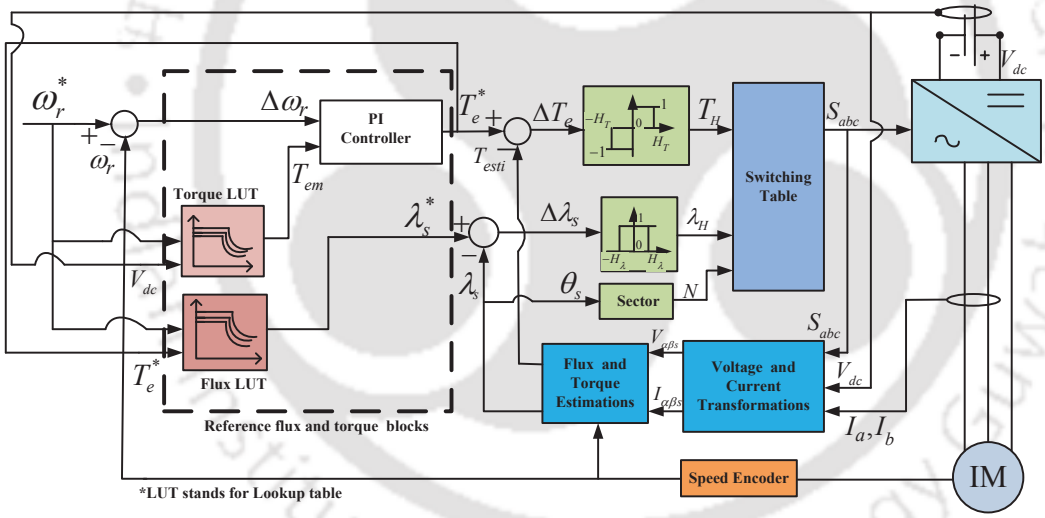

Fig. 4.17: Block diagram of the speed control of IM with DTC drive system. The LUTs for λ_s and T_e obtained in the previous section are included here. The transformation and estimations blocks are explained in chapter-3, section 3.2.4.

The obtained λ_s and T_e LUTs are used in the DTC algorithm as the reference flux and torque, as shown in Fig. 4.17. The λ_s^* LUT has two inputs, namely reference torque (T_e^*) and reference speed (ω_r^*). Based on these two inputs, proper λ_s^* is selected from its respective LUT. For each ω_r^*, the value of maximum torque (T_{em}) given to the controller changes. The T_{em} is selected from its respective LUT wrt ω_r^* and dc source voltage (V_{dc}). The PI controller block's output is T_e^*. The PI controller output,

T_e^*, is monitored by torque LUT for desired speed and given dc source voltage.

Besides, for the calculation of accurate λ_s^* and T_{em} in the LUTs, an average of two nearest possible values from the LUTs are considered by the algorithm. For this reason, a step size for speed, dc voltage, and torque is considered as 50 rpm, 10 V, and 0.1 Nm, respectively. These step sizes are chosen to ensure that the algorithm execution time is faster and obtain accurate λ_s^* and T_{em} values from their respective LUTs.

4.5 Result and discussion

The experimental setup of speed control for IM drive with the DTC scheme is shown in Appendix A.6. The complete system has been developed in the laboratory test-bed to mimic the EV conditions as far as possible. The developed setup is facilitated to run the motor for different driving cycles. It has tested and examined the performance of the controller over a wide torque and speed range. The control algorithm is realized on a dSPACE1103 platform, and its sampling time is chosen as 40 μsec.

To check the effectiveness of the proposed method, a comparison with (i) conventional technique with constant reference flux and (ii) variable flux technique (as discussed in chapter 3, and as given in (3.33)) is carried out (as shown in Table 4.20).

Table. 4.20: Comparison table for the considered cases

Method	Driving cycle response	Energy consumption
Case I : Conventional	Speed,	For different
Case II : Variable flux (see chapter-3, section 3.3)	Torque	driving
Case III : Proposed LUT based	and Flux linkage	cycles

A multiple series of experiments are conducted and investigated in the laboratory with the developed test-bed setup. Comparative evaluations are figure-out and discussed in the next subsequent sections. The proposed approach (Cases III) is compared with the existing methods (Cases I and II) in terms of performance indices of the drive (such as N_r, T_e, and λ_s responses), ripples in T_e and λ_s. Besides, input energy consumption and efficiency analysis are also discussed in detail and presented in sections 4.5.3 and 4.5.4, respectively.

4.5.1 Drive cycle response

The proposed technique and the other two existing methods (listed in Table 4.20) are tested experimentally on the following vehicle driving cycles:

- New York City Cycle (NYCC)

- New European Driving Cycle (NEDC)

The speed, torque, and flux linkage responses with the considered cases are demonstrated for NYCC and NEDC driving cycles. Further, the root mean square errors (RMSEs) for the response are calculated using (4.8) with each considered case, and a comparative analysis is shown in Table 4.21.

$$RMSE = \sqrt{\frac{\sum_{n=1}^{m} e^2[n]}{m}} \tag{4.8}$$

where e is the error between reference and estimated values, and m is the sample's number of points.

Table. 4.21: RMSE results chart

	NYCC			NEDC		
	Case I	Case II	Case III	Case I	Case II	Case III
Speed (rpm)	172.68	88.78	63.00	57.43	27.68	15.57
Torque (Nm)	0.16	0.10	0.07	0.15	0.11	0.06
Flux linkage (Wb)	0.34	0.15	0.04	0.27	0.13	0.08

Fig. 4.18 shows speed responses of the considered cases for the NYCC. Fig. 4.18(c) is the DTC speed response for the proposed method (case III), and Fig.(s) 4.18(a)-4.18(b) are speed responses for the conventional technique (case I) and variable flux technique (case II), respectively. The responses for torque and flux are shown in Fig.(s) 4.19 and 4.20, respectively. Fig.(s) 4.19(a) and 4.19(b) shows the torque responses for the case I and II. The observation indicates that the torque responses with cases I and II are not acceptable, as ripples are detected. Since the motor is not able to produce the required torque, as the flux selection in these cases is not proper. Fig. 4.19(c) shows the torque response with the proposed approach (case III). The observation shows that the torque response is satisfactory with a low ripple. The flux linkage response for case III is shown in Fig.4.20(c). The observation shows that the proper λ_s^* is selected for the proposed method. As a result, the motor is able to develop the required torque with case III. The flux response is shown in Fig.4.20(c) confirms that the variations in flux (reference as well as estimated) is desirable for a wide range of operation. Besides, close observation of 15 sec is made for the NYCC as shown in Fig.(s) 4.21- 4.23. These results show that the case I and II have convergence issues; consequently, the accurate tracking of reference speed, torque and flux is not acceptable. Whereas case III shows comparatively fair performance in terms of speed tracking, torque, and flux tracking.

Similar observations are reported with NEDC, and the observations are presented as in Fig.(s) 4.24- 4.26. As observed, the existing techniques (case I and II) with the DTC strategy are unacceptable for a wide speed range. Whereas observations are fair with case III (in terms of speed, torque, and

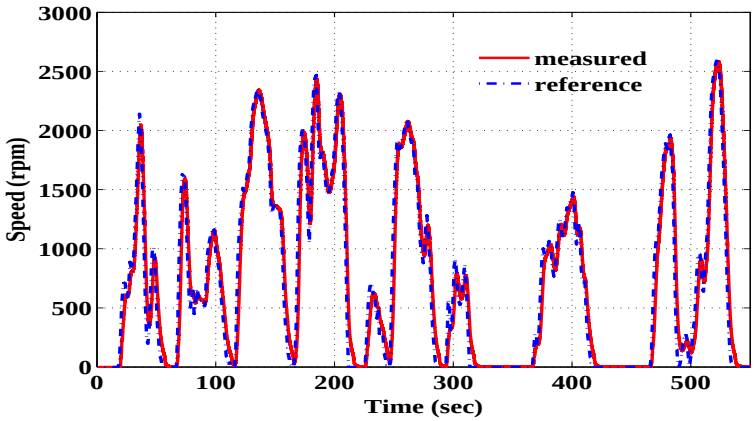

(a)

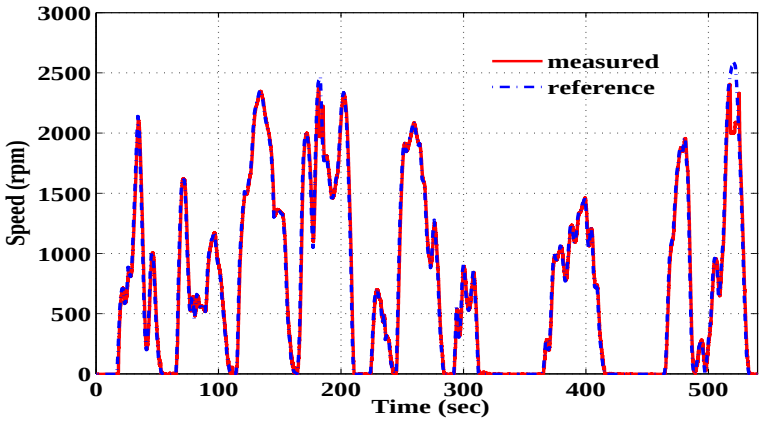

(b)

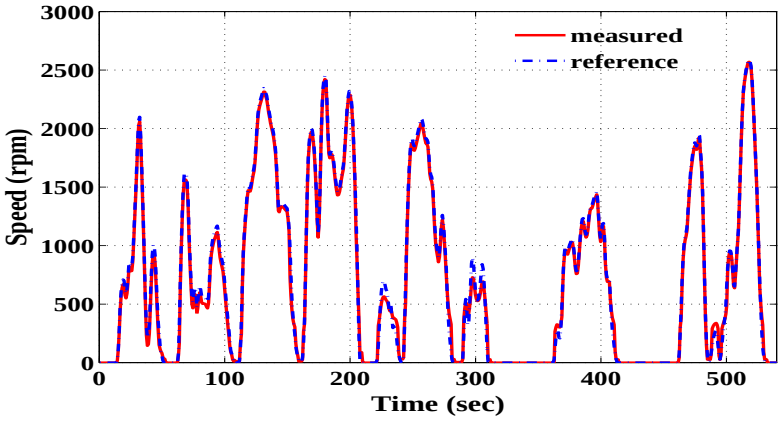

(c)

Fig. 4.18: NYCC speed response (a) Case I (b) Case II (c) Case III. Speed tracking is better for Case III compared to cases I and II. The RMSE for Case III is 63.00, while for Cases I and II are 172.68 and 88.78, respectively.

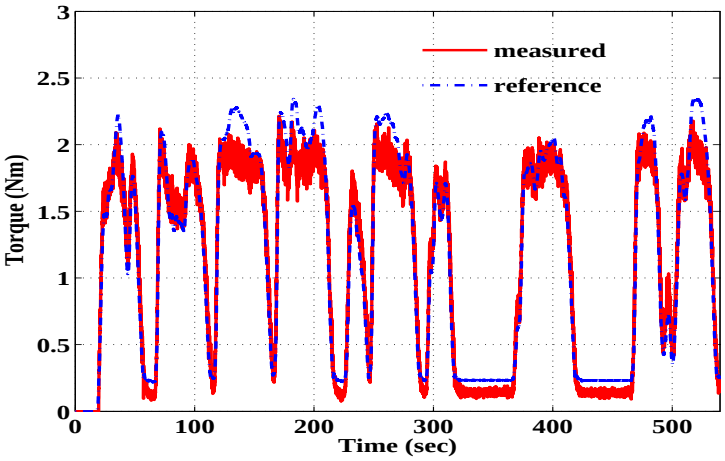

(a)

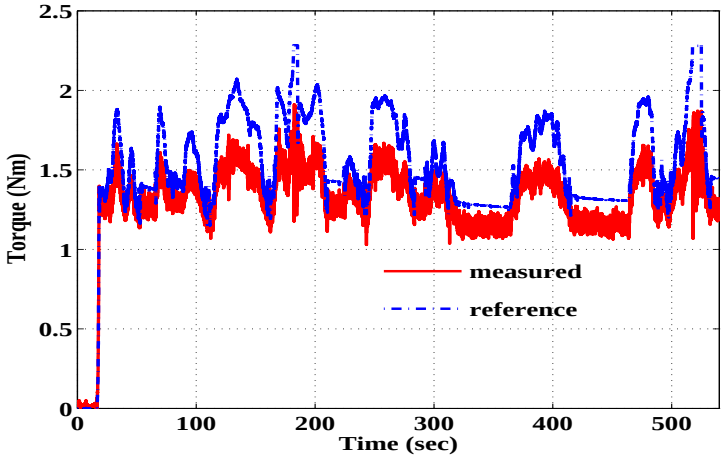

(b)

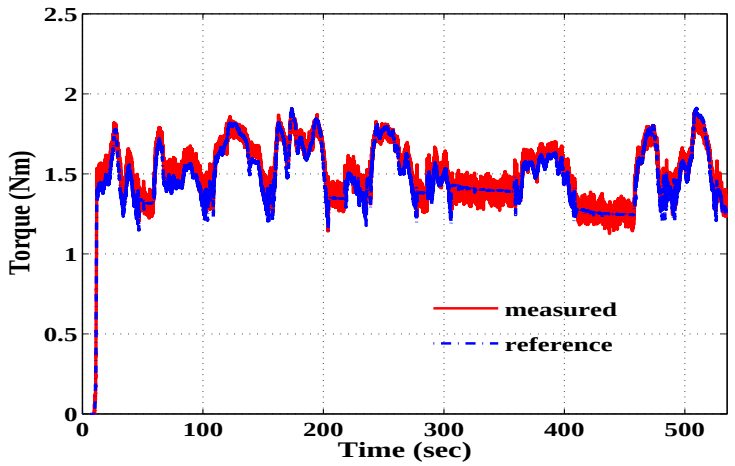

(c)

Fig. 4.19: NYCC torque response (a) Case I(b) Case II (b) Case III. Proper tracking of T_e^* is not possible with cases I and II for a wide speed range. Torque's response is satisfactory with case III. The RMSE for Case III is 0.07, while for Cases I and II are 0.16 and 0.10, respectively.

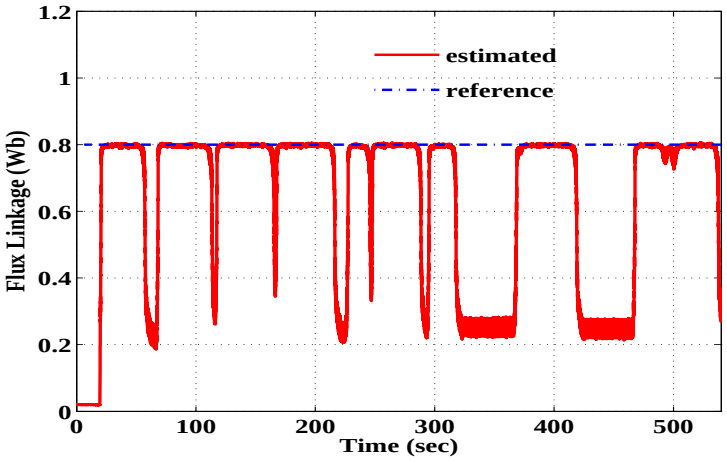

(a)

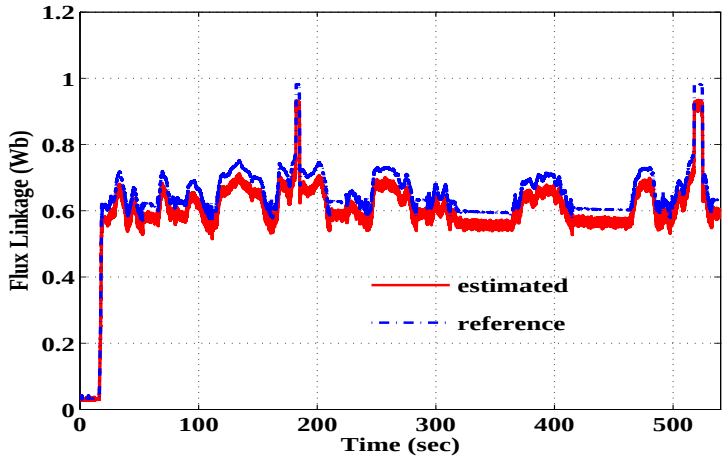

(b)

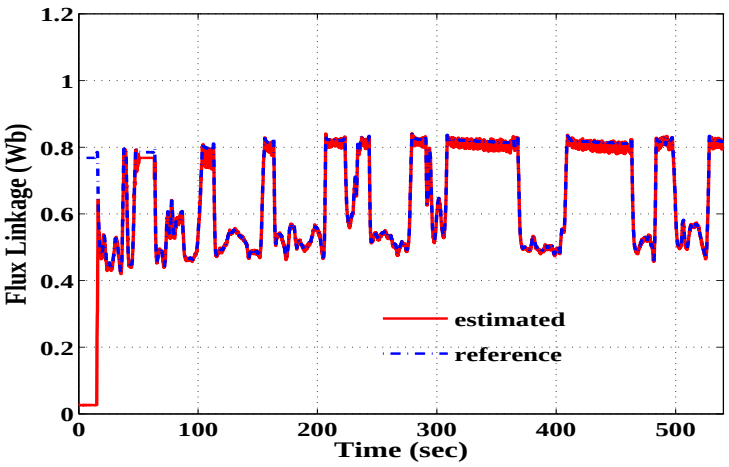

(c)

Fig. 4.20: NYCC flux linkage response (a) Case I (b) Case II (b) Case III. With Cases I and II, the selection of λ_s^* is not appropriate, due to which the motor cannot estimate the required T_e. The flux linkage response with case III is satisfactory. The RMSE for Case III is 0.04, while for Cases I and II are 0.34 and 0.15, respectively.

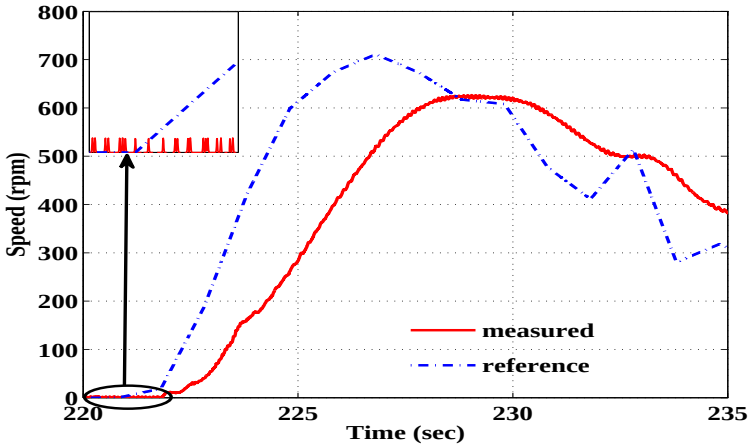

(a)

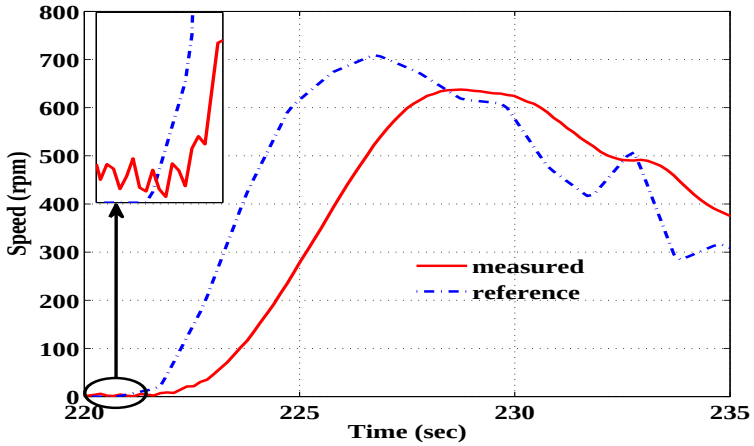

(b)

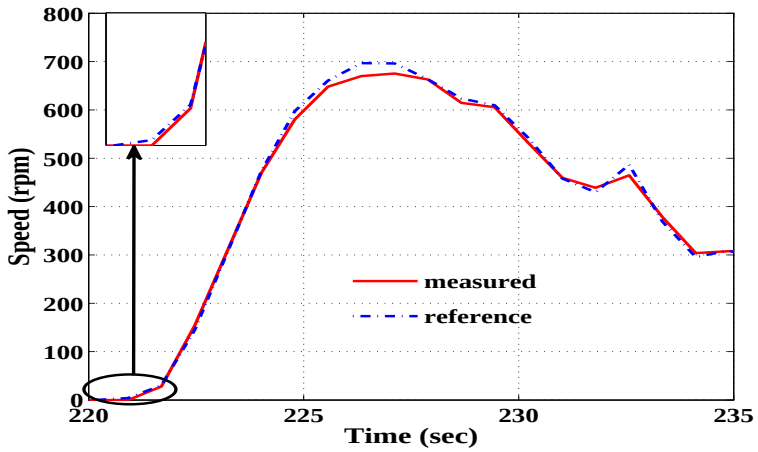

(c)

Fig. 4.21: NYCC speed response for a period of 15 sec (a) Case I (b) Case II (b) Case III. Speed tracking is better for Case III compared to Cases I and II.

flux responses). Moreover, the ripples in measured torque are small with case III, and appropriate λ_s^* selection (so as estimated λ_s) is achievable to develop the motor's required T_e. Besides, case III

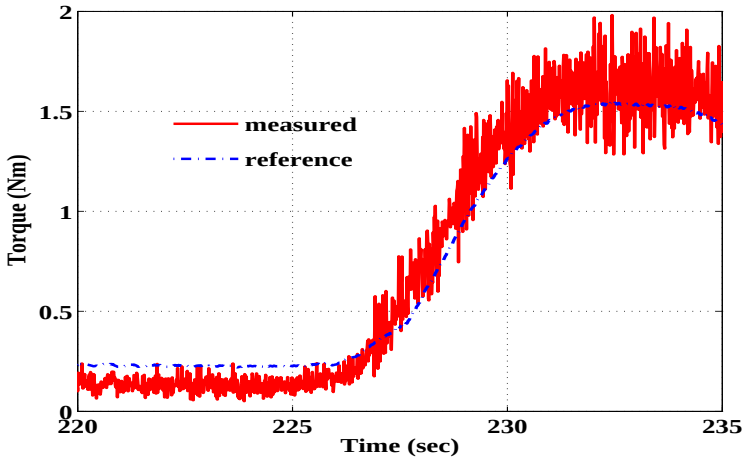

(a)

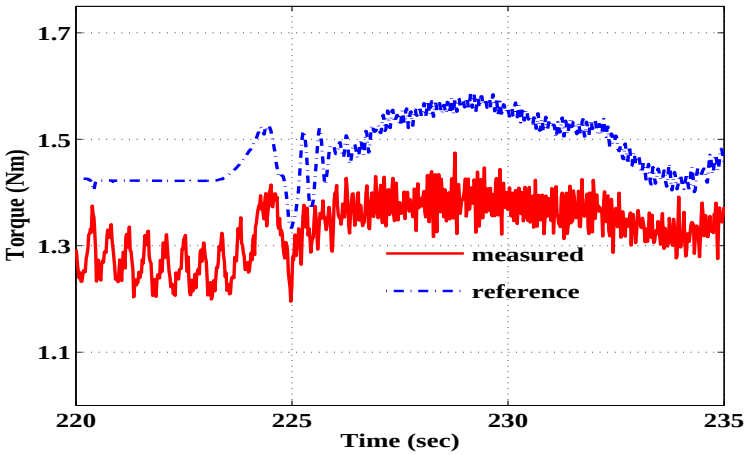

(b)

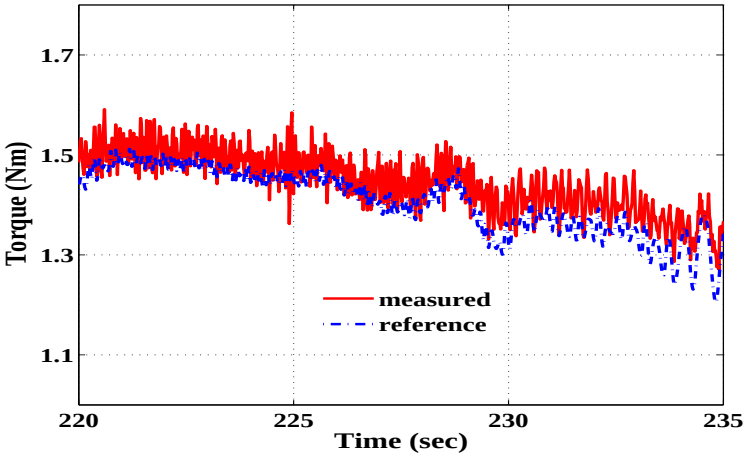

(c)

Fig. 4.22: NYCC torque response for a period of 15 sec (a) Case I(b) Case II (b) Case III. Proper tracking of T_e^* is not possible with Cases I and II for a wide speed range. Torque's response is satisfactory with Case III.

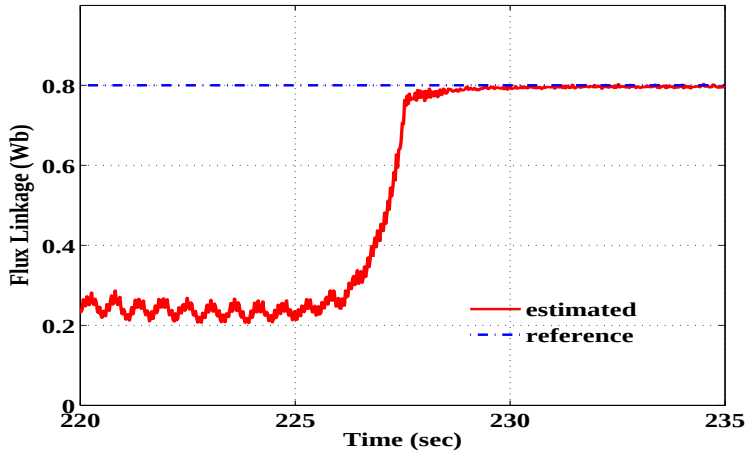

(a)

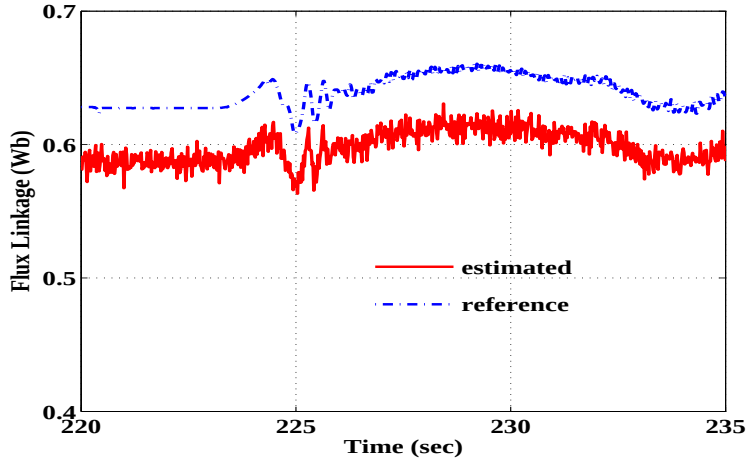

(b)

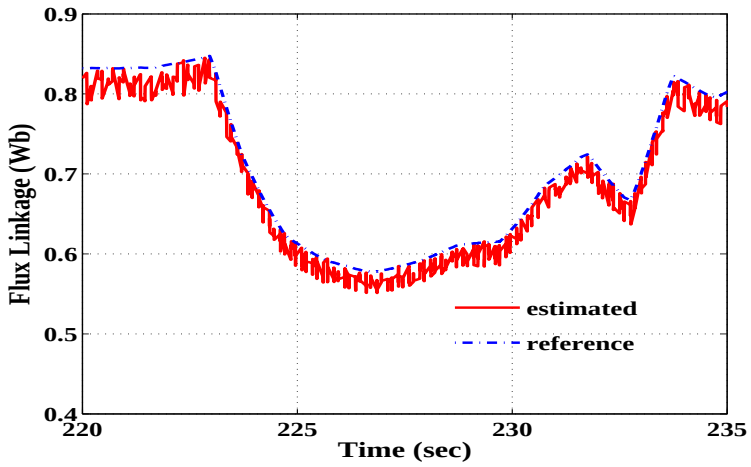

(c)

Fig. 4.23: NYCC flux response for a period of 15 sec (a) Case I (b) Case II (b) Case III. With Cases I and II, the selection of λ_s^* is not appropriate, due to which the motor is not able to estimate required torque (see Fig. 4.19(a) and 4.19(b)). The flux linkage response with Case III is satisfactory.

determines the low value of flux compared to cases I and II for speed higher than the base speed. This is acceptable for EV applications with a wide speed range.

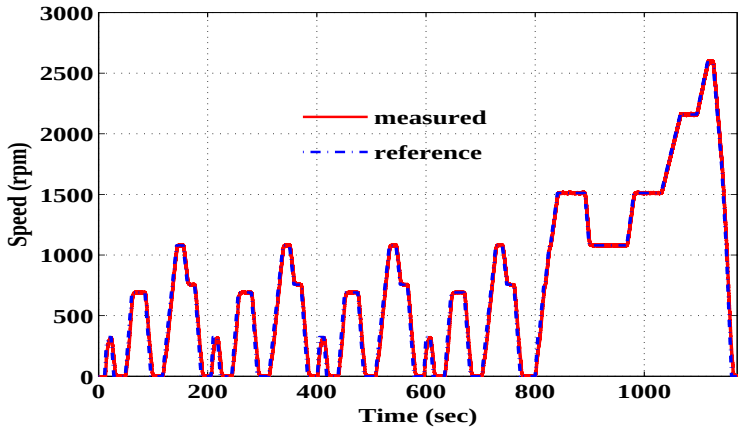

(a)

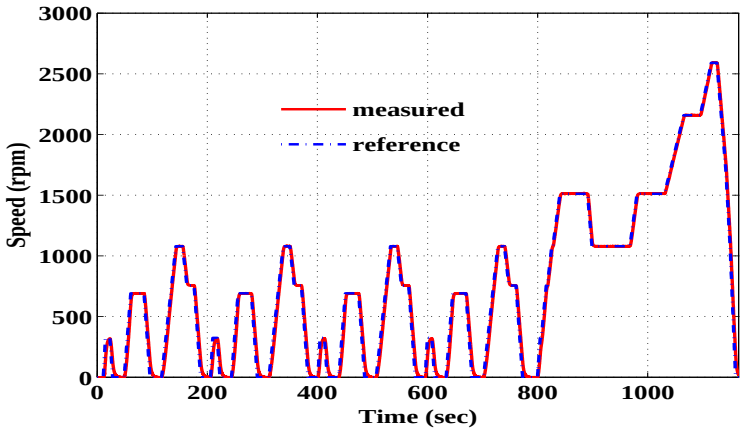

(b)

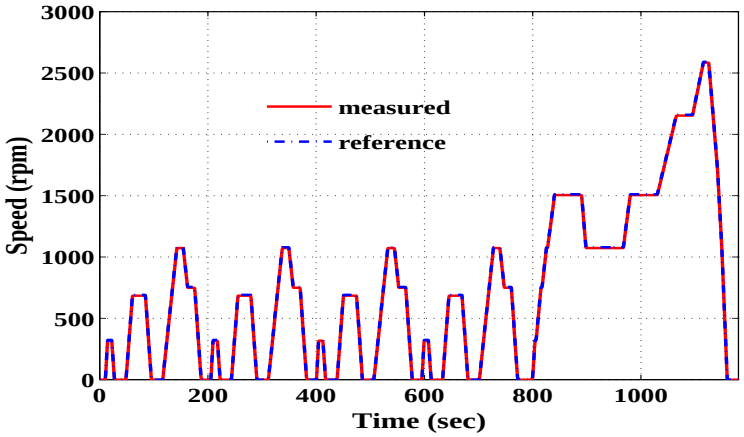

(c)

Fig. 4.24: NEDC speed response (a) Case I (b) Case II (c) Case III. Speed tracking is better for Case III compared to Cases I and II. The RMSE for Case III is 15.57, while for Cases I and II are 57.43 and 27.68, respectively.

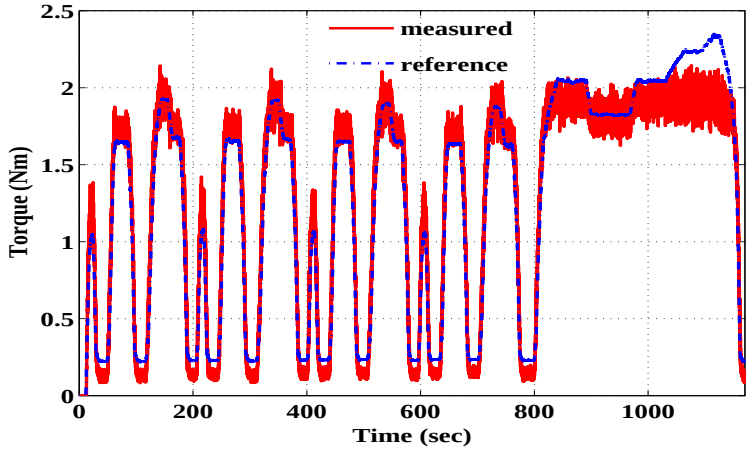

(a)

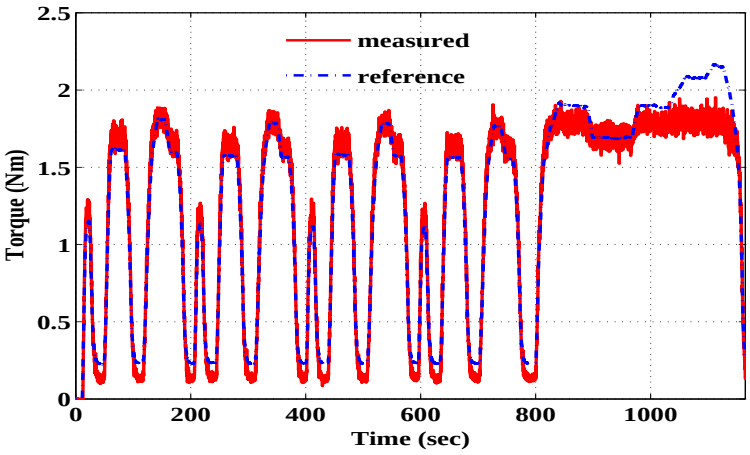

(b)

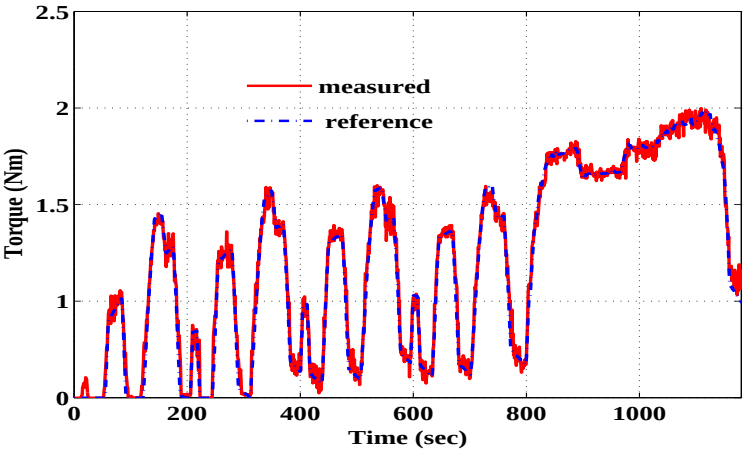

(c)

Fig. 4.25: NEDC torque response (a) Case I(b) Case II (c) Case III. Proper tracking of T_e^* is not possible with cases I and II for a wide speed range. Torque response is satisfactory with case III. The RMSE for Case III is 0.06, while for Cases I and II are 0.15 and 0.11, respectively.

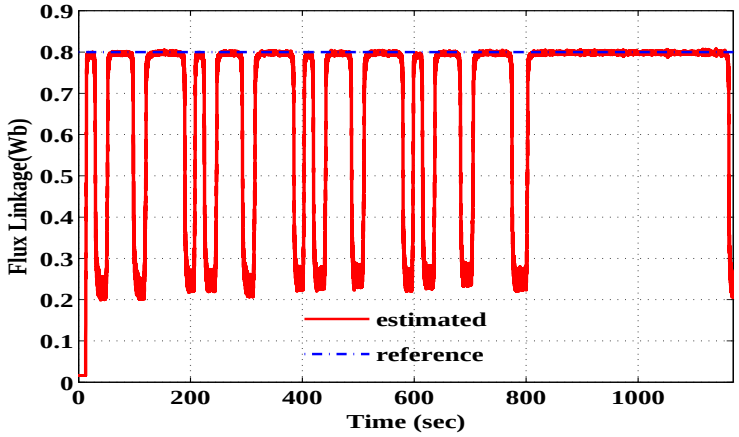

(a)

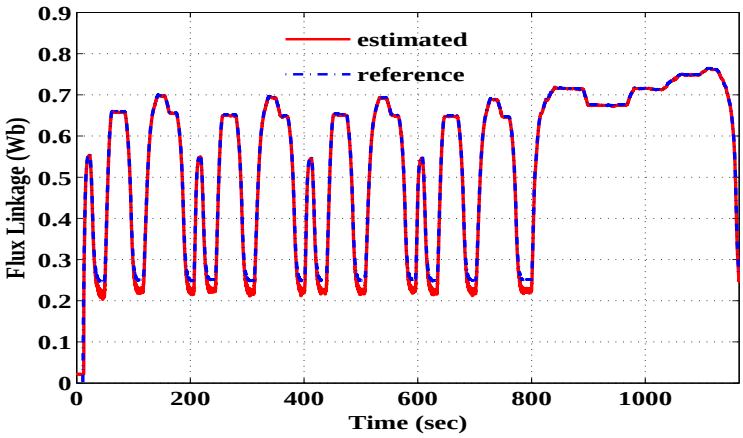

(b)

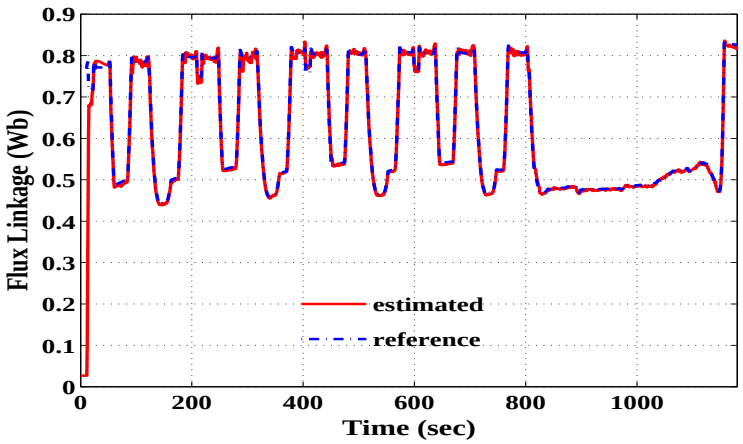

(c)

Fig. 4.26: NEDC flux response (a) Case I (b) Case II (c) Case III. With Cases I and II, the selection of λ_s^* is not appropriate, due to which the motor is not able to estimate the required T_e. The flux linkage response with case III is satisfactory. The RMSE for Case III is 0.08, while for Cases I and II are 0.27 and 0.13, respectively.

Table 4.21 shows the speed RMSE value for cases I and II are high. And torque ripples are seen for cases I and II. Since, the flux level is either constant over the changing operating conditions or does not get the acceptable range of variations to settle for an optimal value. The result ensures that cases I and II are not able to determine the accurate λ_s^* value. Thus, cases I and II may not be acceptable for drives with fast dynamics. Table 4.21 clearly marks that case III provides comparatively satisfactory performance. Further, to check the reliability of the proposed method, the dynamic and steady-state responses are observed and discussed in the next subsequent section.

4.5.2 Dynamic and steady state response

The steady-state response and the transient at starting with step response at different speeds are analyzed and demonstrated in this section. The performance indicators such as torque ripple expressed in standard deviation (σT_e), relative torque error (T_{err}), and relative flux error (λ_{err}) are calculated for the considered cases. Fig. 4.27 illustrates the dynamic speed response of the DTC-based IM drive with step-change in speed. The speed response is tested by changing the speed from 0 rpm to 1000 rpm and back to 250 rpm, as shown in Fig. 4.27.

The torque response (reference and measured) with the proposed method (case III) shown in Fig. 4.27(c) are comparatively fair. Also, fewer torque ripples are observed with case III as compared to cases I and II.

To understand the impact of the proposed technique on torque and flux ripples, torque ripple expressed in standard deviation (σT_e), relative torque error (T_{err}), and relative flux error(λ_{err}) are calculated using (4.9)-(4.11) [114] for the considered cases at different operating points. The experimental observations at 100 rpm with considered cases are shown in Fig(s). 4.28- 4.31.

$$\%\sigma_{\hat{T}_e} = \sqrt{\frac{1}{n-1}\sum_{i=1}^{n}\left(\hat{T}_{ei} - \hat{T}_{emn}\right)^2} \times 100 \tag{4.9}$$

$$\hat{T}_{emn} = \frac{1}{n}\sum_{i=1}^{n}\hat{T}_{ei} \tag{4.10}$$

$$\%X_{error} = \frac{Avg(X_{ref}) - Avg(X_{esti})}{Avg(X_{ref})} \times 100 \tag{4.11}$$

where $\hat{T}_{ei}$ is the actual sample, n represents sample's number, X represents torque or flux linkage used for the calculation of error, Avg is an average value, ref is the reference value, and $esti$ is either measured or estimated value.

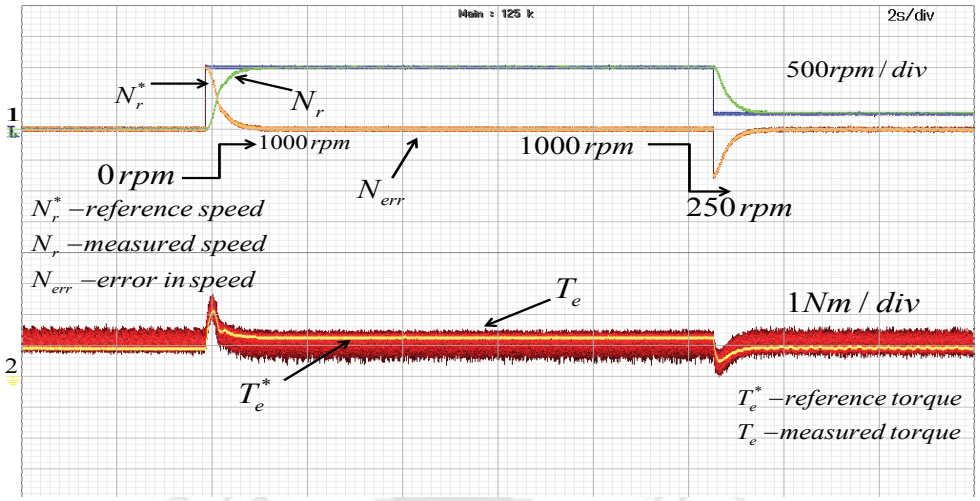

(a)

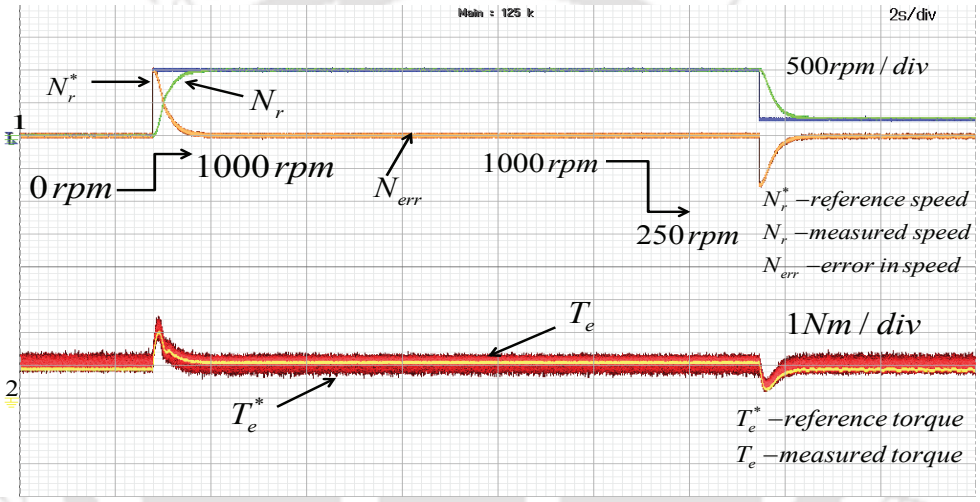

(b)

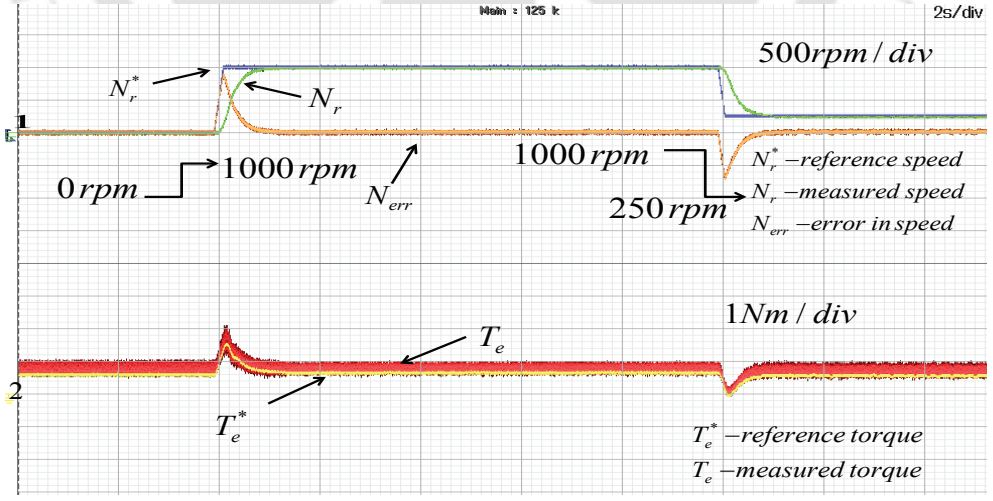

(c)

Fig. 4.27: Dynamic response with step change in speed (a) Case I (b) Case II (c) Case III.

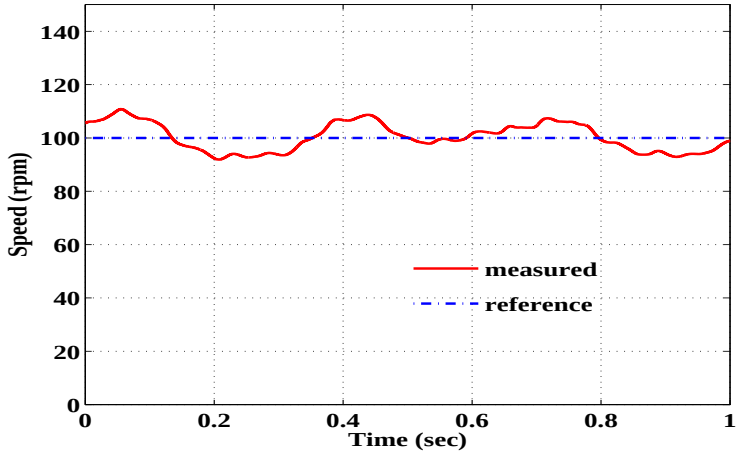

(a)

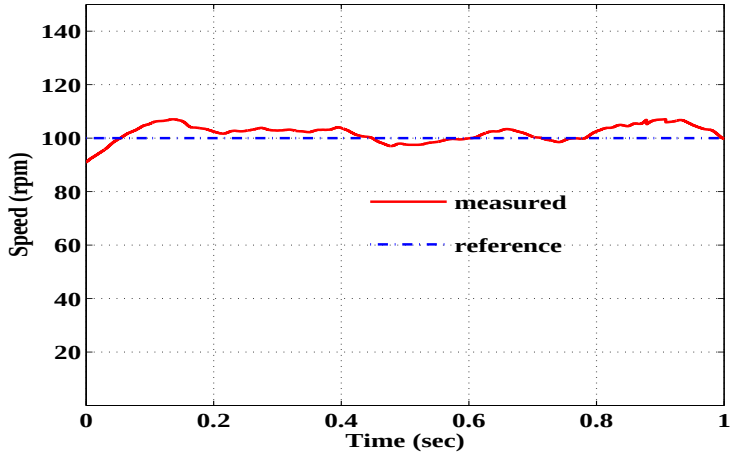

(b)

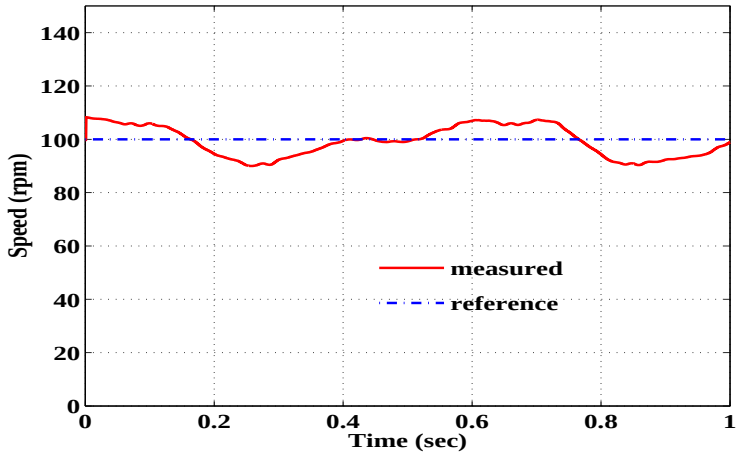

(c)

Fig. 4.28: Steady state speed response at 100 rpm (a) Case I (b) Case II (c) Case III.

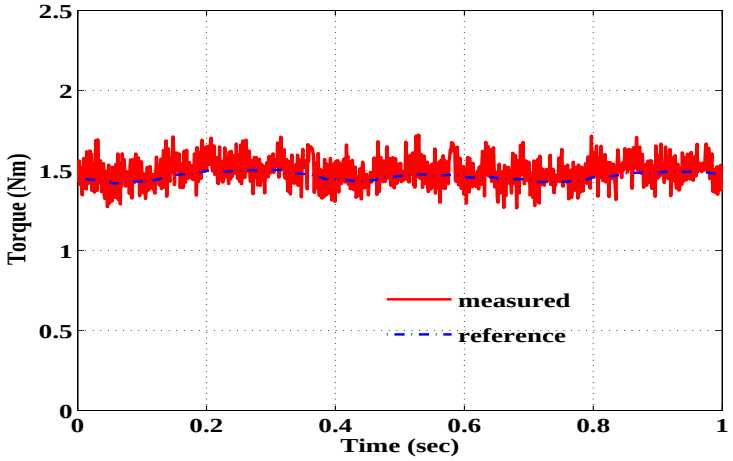

(a)

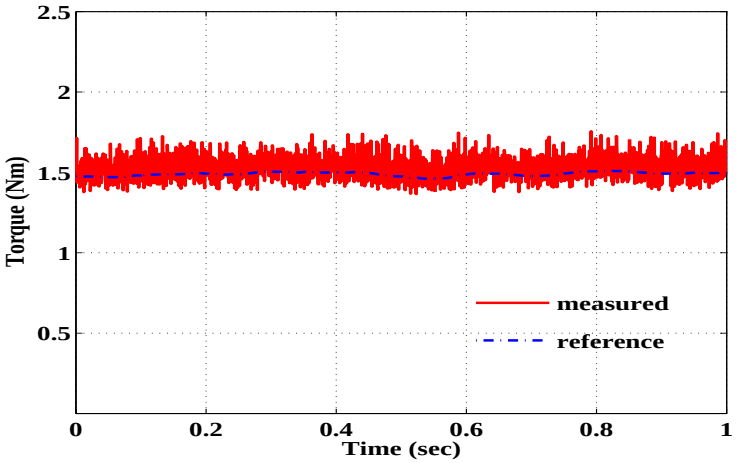

(b)

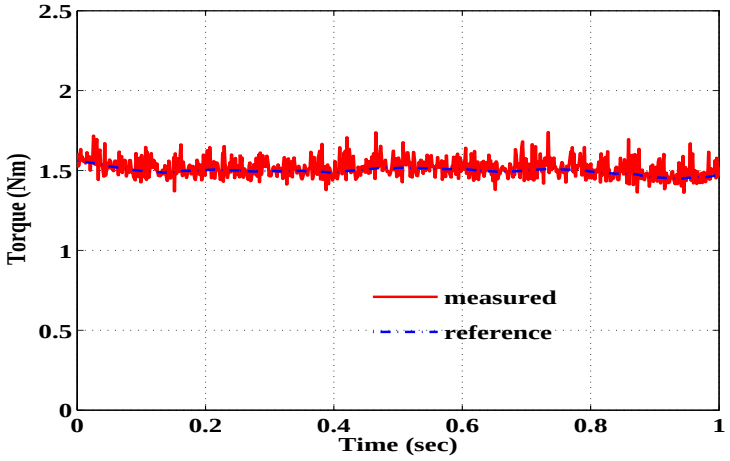

(c)

Fig. 4.29: Steady state torque response at 100 rpm (a) Case I (b) Case II (b) Case III. The % torque ripple (σT_e) in standard deviation with Case III is 6.89%, while for Cases I and II are 9.59% and 8.72%, respectively.

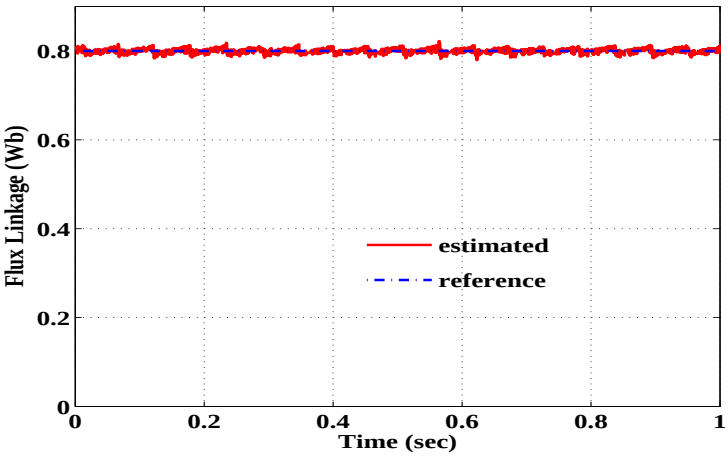

(a)

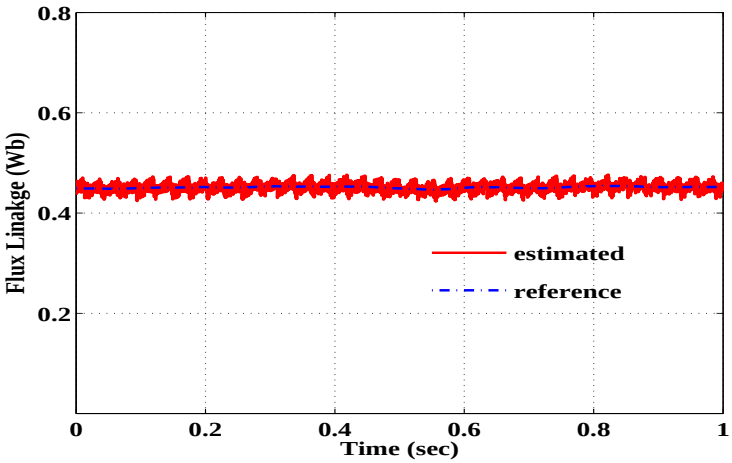

(b)

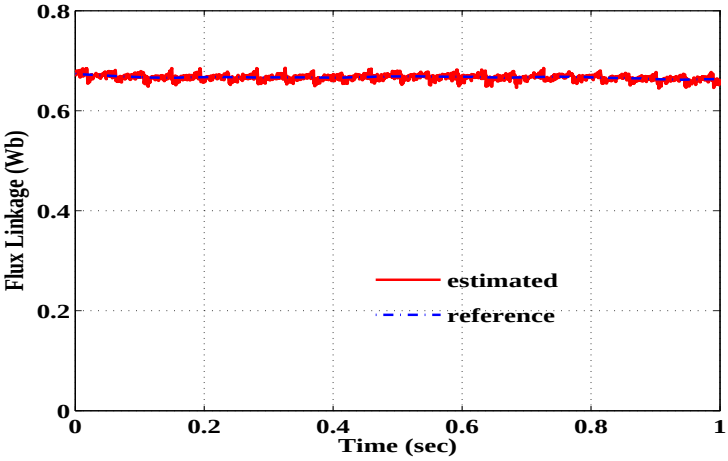

(c)

Fig. 4.30: Steady state flux linkage response at 100 rpm (a) Case I (b) Case II (b) Case III. The % relative flux error (λ_{err}) with case III is 0.0059%, while for Cases I and II are 0.032% and 0.025%, respectively.

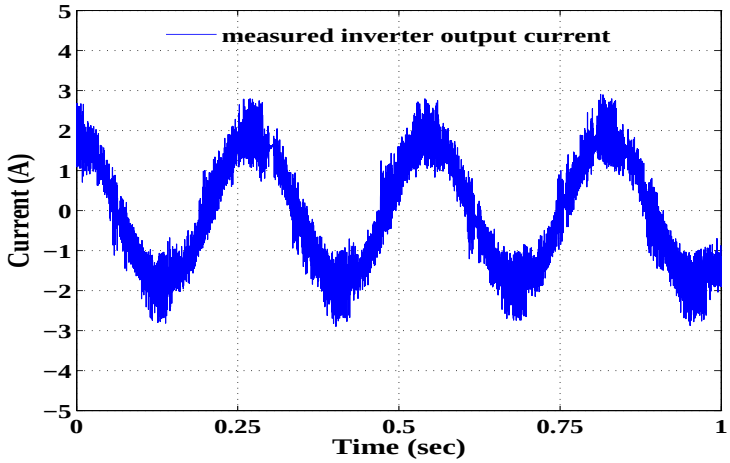

(a)

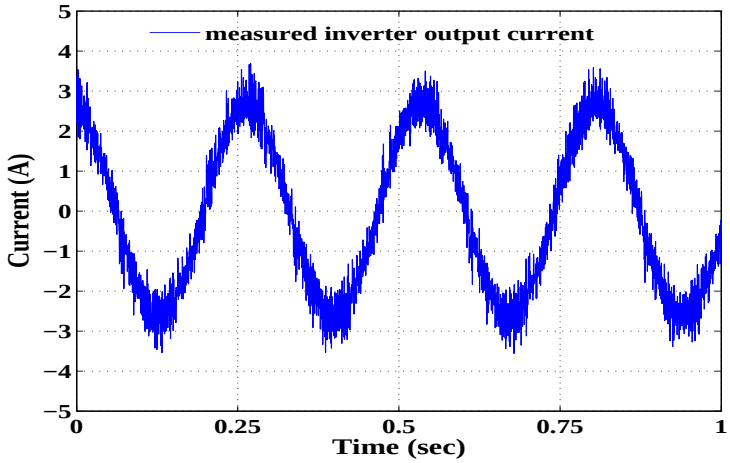

(b)

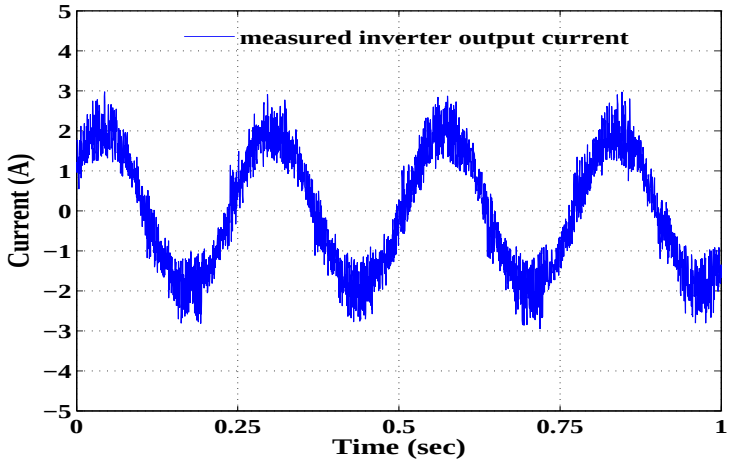

(c)

Fig. 4.31: Steady state current response at 100 rpm (a) Case I (b) Case II (c) Case III.

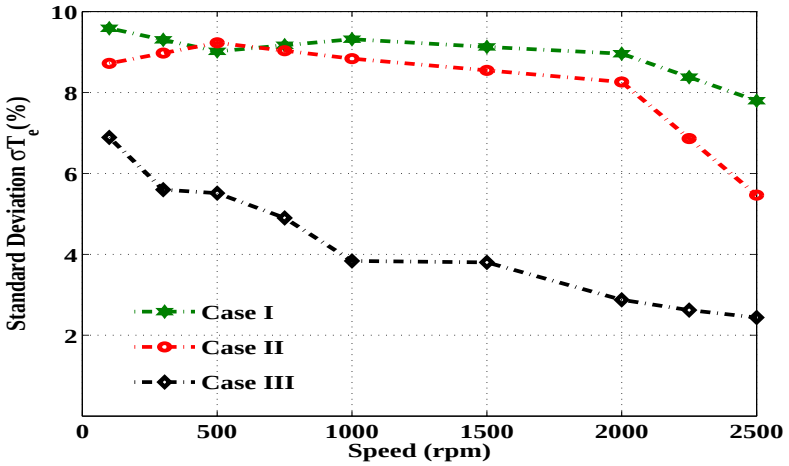

(a)

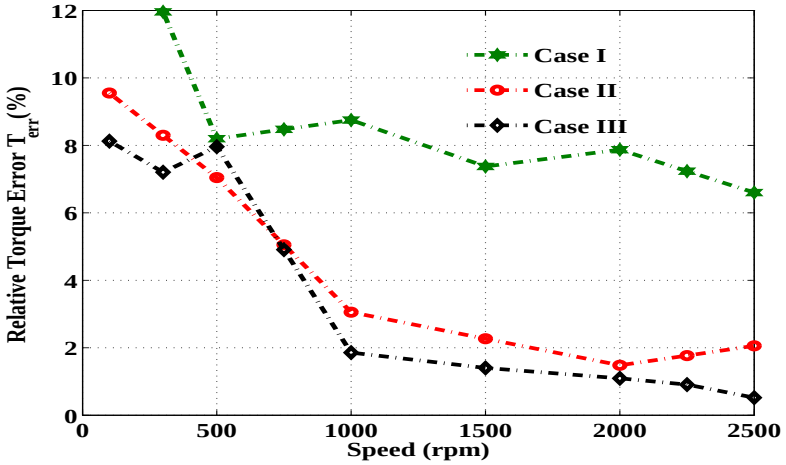

(b)

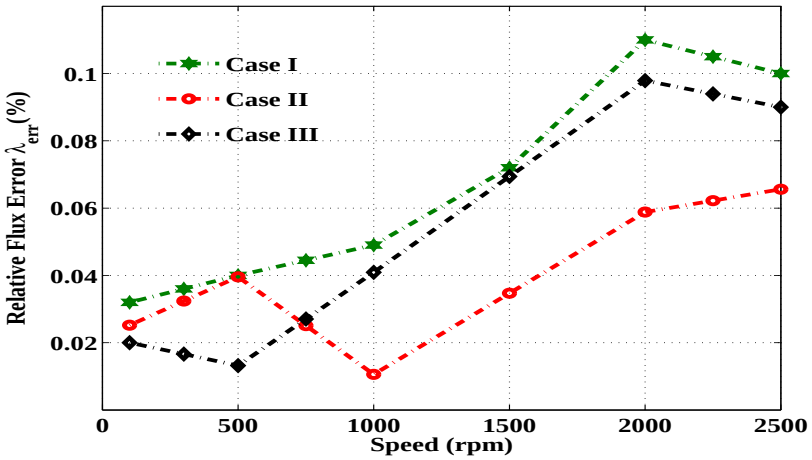

(c)

Fig. 4.32: Performance analysis at constant load torque of 1.5 Nm (a) Torque ripple (σT_e) (b) Torque error (T_{err}) (c) Flux error (λ_{err}).

4.5.3 Energy Consumption Analysis

The input energy consumption for considered cases is determined using (4.12). In this calculation, input dc source voltage (V_{dc}) and dc source current (I_{dc}) are obtained wrt time.

$$E_{in} = \sum (V_{dc} * I_{dc} * \Delta t) \tag{4.12}$$

Table 4.22 shows the input energy consumptions in Watt-hour (Wh) for two different loads. The % saving in input energy consumption wrt case III for the two driving cycles are listed in Table 4.22, and is calculated using (4.13).

$$Energy\ saving\ (\%) = \left(\frac{E_{in,i} - E_{in,3}}{E_{in,i}}\right) * 100 \tag{4.13}$$

where $E_{in,i}$ is the input energy consumption with i represents for different cases, and $E_{in,3}$ is input energy consumption for case III.

Table. 4.22: Comparative analysis on input energy consumption in Wh at 0.5 Nm and at 1.5 Nm loads

	0.5 Nm Load					1.5 Nm Load				
Driving cycle	Case I	Case II	Case III	Energy-saving(%) in Case III		Case I	Case II	Case III	Energy- saving(%) in Case III	
				For Case I	For Case II				For Case I	For Case II
NYCC	5.71	5.00	3.89	46.79	28.54	15.44	14.70	13.14	17.51	11.80
NEDC	13.30	11.66	10.6	25.47	10.00	69.23	68.39	58.22	18.91	17.45

The comparative analysis listed in Table 4.22 shows that case III possesses the lowest consumption of input energy compared to cases I and II. A significant savings of energy are achieved in case III wrt the other cases. The reduction in consumption of the input energy establishes the accuracy of the proposed technique.

Further, multiple sets of experiments are conducted in the laboratory to analyze the said cases' efficiency performance and briefly discussed in the next subsequent section.

4.5.4 Efficiency analysis

The efficiency analysis for the said cases is inspected with wide operating speeds and at different load torques. These efficiencies are calculated using instantaneous values of input and output powers over a period. The instantaneous values of inverter input power is calculated by measuring V_{dc} and I_{dc} at their respective node points using a differential voltage probe (YOKOGAWA-700924) and the current probe (YOKOGAWA-701933). The motor's output power is obtained by measuring the shaft torque and speed using the KISTLER-4503B/CoMo-4700 torque sensor. The technical details of the used differential probe, current probe, and torque sensor are given in Appendix A.4.

The efficiency maps provide more insight information for a wide operating range. These efficiency maps are calculated for speed variations from 100 rpm to 2000 rpm and load torque variations from 0.5 Nm to 2.5 Nm. The evaluated efficiency maps are shown in Fig. 4.33. The observations show that case III yields a higher efficiency as compared to the other cases.

The efficiency improvement for Case III is primarily due to the minimum input power consumption compared to the other cases for the fixed power output. Fig. 4.34 shows efficiency graphs with variations in speed and load torque. These observations confirm that the proposed method results in improved efficiency as compared to the other considered cases.

From the presented results and observations, it is found that the proposed method has comparatively no convergence issues. It does not required the comprehensive calculation of λ_s^* at every instant (as calculated offline and stored in its LUT). It has lower torque ripples. The proposed approach is accepted for practical applications where the torque reference changes quickly (see Fig. 4.19 and 4.25). This proposed approach also accounts for any operating condition described by motor torque and speed with minimal consumption of input energy. Further, it is observed that the proposed technique results in improved efficiency over a wide operating range.

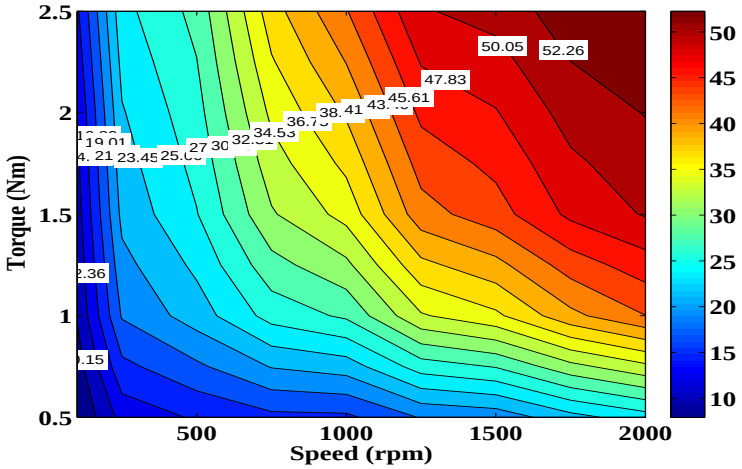

(a)

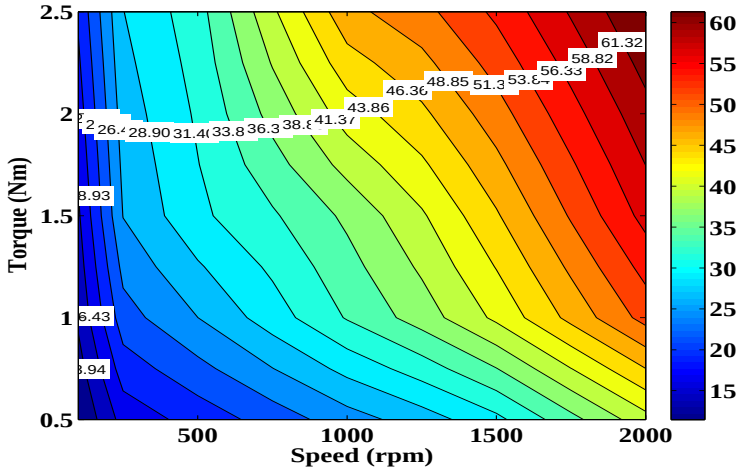

(b)

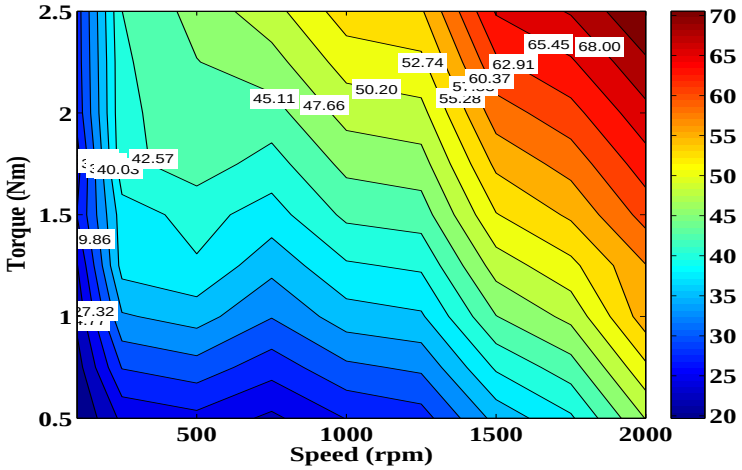

(c)

Fig. 4.33: Efficiency maps (a) Case I (b) Case II (c) Case III.

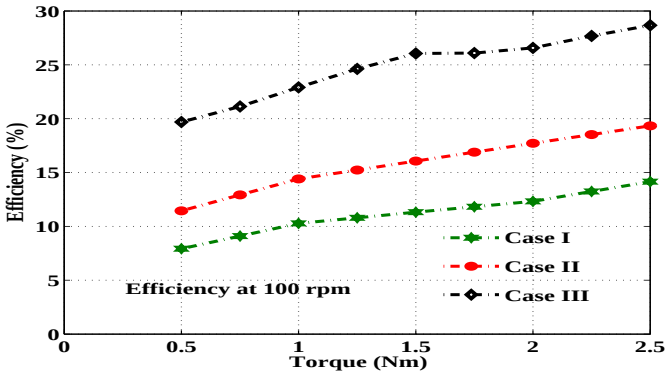

(a)

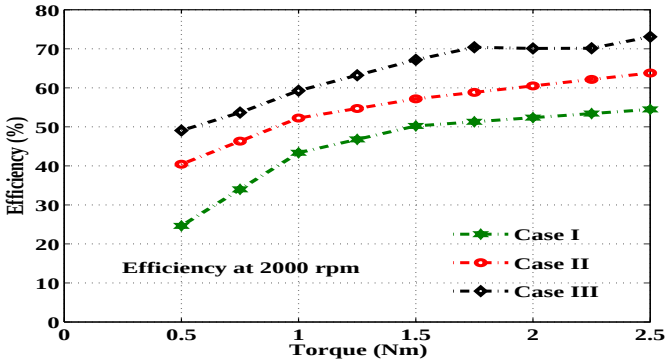

(b)

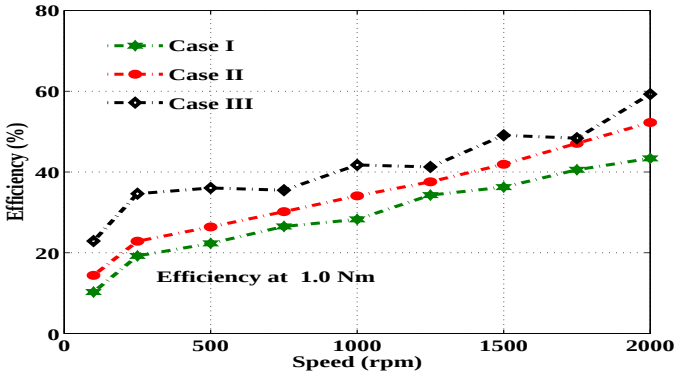

(c)

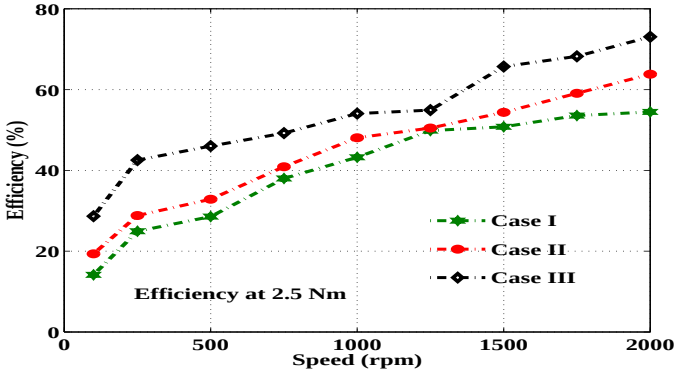

(d)

Fig. 4.34: Efficiency at (a) 100 rpm (b) 2000 rpm (c) 1.0 Nm (d) 2.5 Nm.

4.6 Conclusion

This chapter presents an offline LUT-based approach to determine the reference flux of the DTC strategy for IM drive. The method uses the FEA-based IM model to calculate suitable values of flux linkages. The FEA model ensures that the effect of magnetic saturation is taken into account. The multiple sets of FEA simulations are carried out to obtain the accurate values of flux linkage. The obtained flux linkage values are stored in lookup table format and fed to the DTC algorithm as reference flux linkage. The proposed approach ensures that the obtained flux linkage values in lookup table format give accurate information of reference flux at the required speed and given torque with dc voltage constraint. Thus proposed approach calculates reference flux linkage considering the reference speed, torque, and DC voltage. Further, it is compared with the existing conventional technique and variable flux approach to check the proposed method's robustness. The comparison is based on tracking speed, torque, and flux for different vehicle driving cycles. The observation shows that the proposed method is less sensitive to the motor's parameter variation, such as stator resistance and leakage inductance, and magnetization inductance. The experimental observations show that the proposed method yields improvement in drive efficiency with minimal input energy consumption. The proposed method is made acceptable for EV application with few modifications in the DTC algorithm.

However, this method required a pre-knowledge about the motor's geometry, i.e., winding scheme, slot dimensions details and lamination designs, to develop an FEA model of IM, which helps obtain accurate values of reference flux and maximum torque in LUTs format. This limitation is overthrown if a non-linear equivalent circuit model of IM will be developed and used. Therefore, the determination of reference flux linkage using a non-linear equivalent circuit model of IM is developed and discussed in the next chapter.

भारतीय प्रौद्योगिकी संस्थान गुवाहाटी
Indian Institute of Technology Guwahati

भारतीय प्रौद्योगिकी संस्थान गुवाहाटी
Indian Institute of Technology Guwahati

भारतीय प्रौद्योगिकी संस्थान गुवाहाटी
Indian Institute of Technology Guwahati

CHAPTER 5

REFERENCE FLUX LINKAGE DETERMINATION FOR DIRECT TORQUE CONTROL INDUCTION MOTOR DRIVE BASED ON NON-LINEAR EQUIVALENT CIRCUIT APPROACH

5.1 Introduction

In the context of an EV application, an offline lookup table (LUT) based method has been proposed to determine λ_s^*, and presented in chapter- 4. The technique proposed in the chapter- 4 used an FEA-based IM model to calculate an appropriate λ_s^* value. These values obtained are calculated offline and stored in the LUT format and fed to the DTC algorithm as reference flux.

The demerit of the method presented in chapter-4 is a pre-knowledge about the motor's geometry details (i.e., winding scheme, slot dimensions details, and lamination designs) and material's B vs. H curve to built an FEA model of IM. This limitation is overthrown if a non-linear equivalent circuit model of IM will be developed and used. Therefore, the determination of reference flux linkage using a non-linear equivalent circuit model of IM is developed and discussed in this chapter.

The method proposed in this chapter uses a non-linear equivalent circuit model of IM to achieve the above goal. The procedure to determine non-linear equivalent circuit parameters is explained in detail in section 5.2. The non-linear equivalent circuit is used to calculate λ_s as a function of voltage, speed, and torque. Further, the non-linear equivalent circuit takes into account the magnetic satura-

tion. The λ_s^* values are calculated offline using the non-linear equivalent circuit and implemented in the controller as a LUT.

The summary of the contributions of this chapter are:

- A method for determining the proper λ_s^* values for the DTC-based IM drive over a wide range of operations.
- The proposed technique uses a non-linear equivalent circuit model of IM to consider the magnetic saturation effect for calculating an appropriate λ_s^* value.
- The proposed approach calculates λ_s^* considering the reference speed (N_r^*), reference torque (T_e^*), and DC source voltage.
- The offline determined values of λ_s are collected and stored in the lookup table format and are fed to the DTC algorithm as reference flux linkage, λ_s^*.

The remainder of the chapter is organized as follows: Section 5.2 discusses the procedure for determining of non-linear equivalent circuit parameter (i.e., magnetizing inductance, L_m) of IM. A set of experiments are performed in the laboratory to obtain the magnetization curve of the IM. Section 5.3 explains the method to determine λ_s^* values for the DTC algorithm. The non-linear equivalent circuit of IM is solved, and the suitable values of λ_s are determined over a wide range of speeds. The obtained λ_s values are stored in LUT format and implemented in the DTC algorithm as reference flux (λ_s^*). The detailed procedure to determine the suitable values of λ_s is presented in Section 5.3. Parameter sensitivity analysis of the proposed method is investigated in Section 5.4. Section 5.5 shows the comparative analysis of the proposed approach with (i) loss model-based technique and (ii) FEA-based method (as presented in chapter-4), and the experimental results over a wide range of speed for the vehicle driving cycles (i.e., NYCC and NEDC). Further, the input energy and efficiency analysis of the considered driving cycles are demonstrated in section 5.5. Finally, the conclusions are presented in Section 5.6.

5.2 Determination of the Magnetizing Inductance of Induction Motor

This section presents the detailed procedure to determine non-linear equivalent circuit parameter, the magnetizing inductance of IM. The per-phase non-linear equivalent circuit model of IM is shown in Fig. 5.1, where L_m is magnetizing inductance. The stator input current (i_{as}) is the sum of rotor current (i_{ar}) and magnetizing current (i_m) and is given by (5.1):

$$i_{as} = i_{ar} + i_m \tag{5.1}$$

When the motor's i_m increases due to magnetic saturation in the iron core, its relative permeability decreases; as a consequence, decrement in L_m is observed.

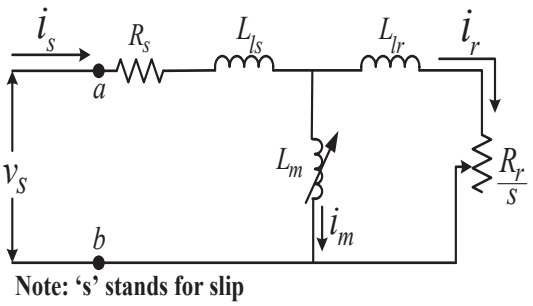

Fig. 5.1: Per-phase non-linear equivalent circuit of IM.

The parameters of IM considered in this work are listed in Appendix A.2. The parameters are obtained from the IEEE Standard (112 – 2017) no-load test and blocked rotor test of IM. With the equivalent circuit parameters of the IM used in this work ($L_m = 0.5275$ H and core loss resistance, $R_c \simeq 1.76$ kΩ), it is observed that $i_m \gg i_c$, where i_c is the iron loss branch's current (not shown in Fig. 5.1). Therefore, i_c is ignored in further analysis, and core loss resistance is not shown in Fig. 5.1.

A set of experiments are performed in the laboratory to determine the non-linear magnetization curve. An IM runs at its synchronous speed by using the dc shunt motor, which is mechanically coupled (MC) to IM. The schematic of the experimental setup for determining the non-linear magnetization curve is shown in Fig. 5.2. The $R1$ and $R2$ are the external resistances connected in series with the dc shunt motor's armature and field winding, respectively. The measurement of current

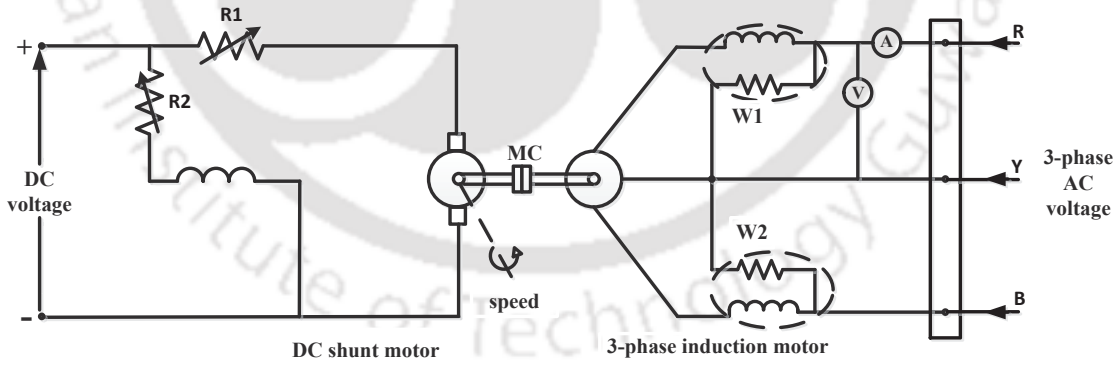

Fig. 5.2: Schematic representation of experimental setup for determining non-linear magnetization curve.

drawn by IM is recorded corresponding to increasing voltage up to about 125% of rated voltage to result in core saturation.

For every increment in the applied voltage to the IM, IM's speed is maintained at its synchronous speed with the help of the dc motor. This ensures that the induced current in the rotor of IM remains

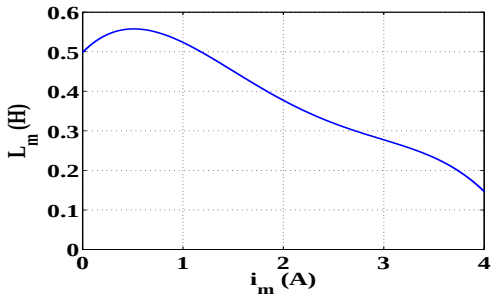

Fig. 5.3: Magnetizing inductance of the induction motor tested experimentally.

zero. Therefore, the overall air-gap λ_s is produced only due to i_{as}. Moreover, zero net active power reading by the wattmeters (W1 and W2) ensures that the IM has driven at its synchronous speed. The experiment is performed at the no-load condition to obtain the non-linear magnetization curve.

The rms values of applied voltage and the current drawn by the IM are noted. As the experiment is performed at no-load condition, the current drawn by the IM is mainly consists of the i_m since the core loss current is usually minimum. Therefore, the no-load current value is noted here and treated as i_m.

The stator winding impedance drop is neglected, as the per-phase R_s is only about 2.52% of the magnetizing reactance. Also, the stator winding leakage reactance (L_{ls}=0.0141 H) is very small compared to the magnetizing reactance (L_m=0.5275 H). Therefore, the applied voltage (V_s) to the stator is viewed as the induced voltage in the stator winding, which is the product of magnetizing reactance and i_m, and is given by (5.2):

$$|V_s| = |\omega_s L_m i_m| \tag{5.2}$$

where ω_s is the frequency of the V_s in radians per second.

Since a set of values of V_s and the i_m drawn by the IM are noted. Using (5.2), the values of L_m are obtained for corresponding values of i_m. Thus, the non-linear magnetization curve of IM is plotted and shown in Fig. 5.3. Based on the obtained experimental data and a polynomial fit, variation of L_m can be represented as shown in (5.3):

$$L_m = (\frac{1}{100\pi})(-3.882{i_m}^4 + 34.75{i_m}^3 - 104.1{i_m}^2 + 81.25i_m + 156.5) \tag{5.3}$$

The expression (5.3) shows the dependency of L_m with i_m. The flow chart to obtain the non-linear magnetization curve of IM is shown in Fig. 5.4. Thus, the obtained non-linear equivalent circuit model of IM with varying L_m is used further to determine the λ_s in LUT format and discussed in

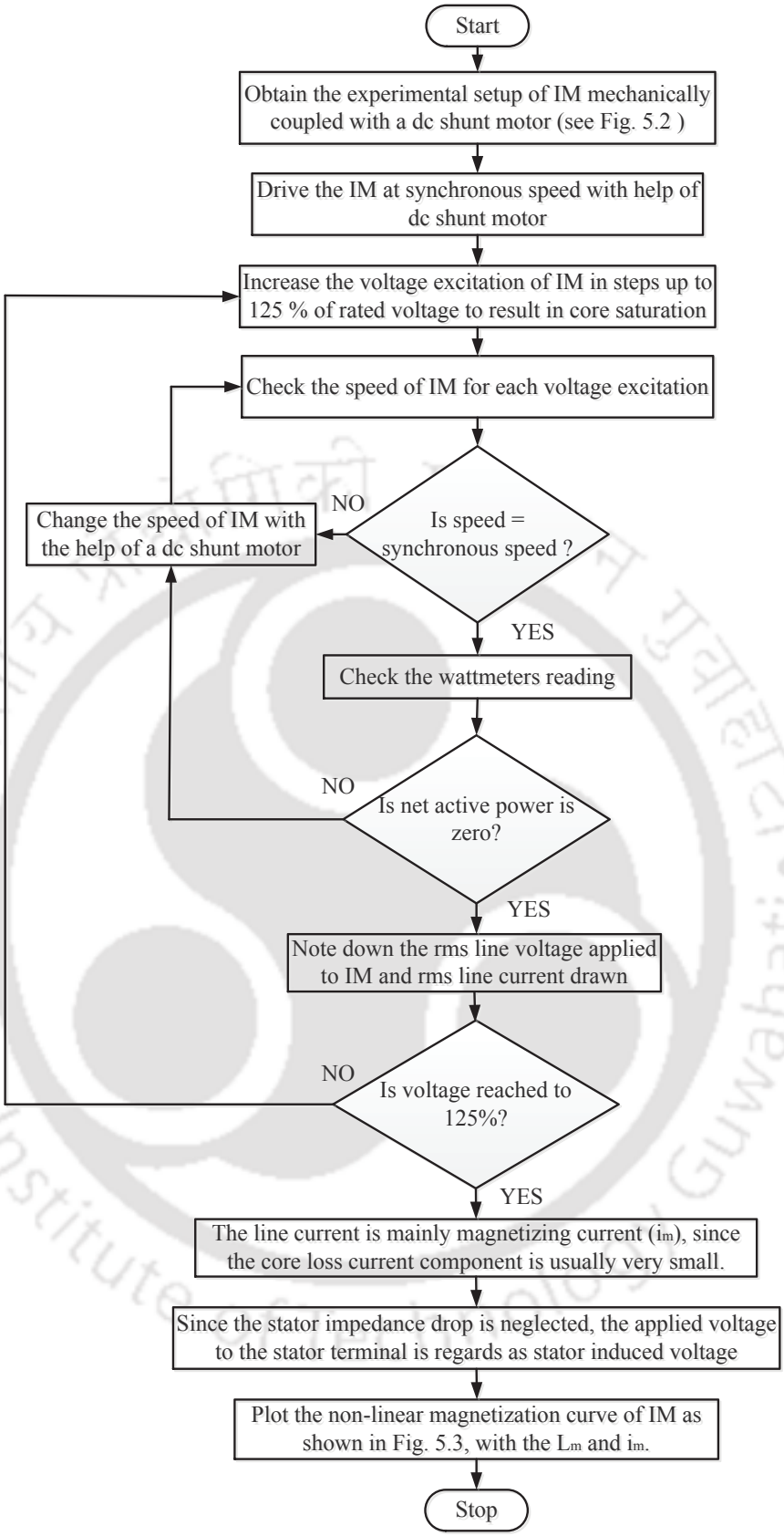

Fig. 5.4: Flow chart for the determination of the non-linear magnetization curve.

section 5.3.

5.3 Determination of Reference Flux Linkage

This section explains an offline technique for determining λ_s^* in context to DTC-based IM drive over a wide range of operations in EV applications. The approach uses a non-linear equivalent circuit model of IM to calculate an appropriate value of λ_s^*. The non-linear equivalent circuit model of IM with varying L_m is discussed in detail in Section 5.2. The section's primary objective is to obtain the suitable values of λ_s over a wide range of speed. The obtained values of λ_s are stored in LUT format and fed to the DTC algorithm as reference flux (λ_s^*). This LUT gives information about the proper λ_s^* at the required speed and given torque with voltage and current constraints.

To obtain the suitable values of λ_s over a wide range of operation, the per-phase non-linear equivalent circuit shown in Fig. 5.1 is solved, with variations in V_s, N_r, and f_s. For solving the per-phase non-linear equivalent circuit, the following points have been considered:

- Determine the equivalent circuit parameters (R_s, L_{ls}, R_r, L_{lr}) using the no-load and blocked rotor tests.
- Solve the equivalent circuit shown in Fig. 5.1 and obtain the magnitude of I_m as;

$$|I_m| = \left| \frac{V_s}{Z_{eq}} \times \frac{Z_m Z_r}{Z_m + Z_r} \right| \tag{5.4}$$

  where, $Z_r = \frac{R_r}{S} + j\omega_s L_{lr}$, $Z_m = j\omega_s L_m$, $Z_{eq} = Z_s + \frac{Z_m Z_r}{Z_m + Z_r}$, $Z_s = R_s + j\omega_s L_{ls}$, and $\omega_s = 2\pi f_s$.
- Substitute L_m as given in relation (5.3) in equation (5.4).
- Using numeric computation, solve the non-linear equivalent circuit as shown in Fig. 5.1 with the variations in V_s, N_r, and f_s.

Numerical methods can be used for solving the non-linear equations (5.4) and (5.3) with the variations in V_s, N_r, and f_s. In this presented work, Newton-Raphson (NR) method is used to solve these equations for finding the root with the error of approximately 10^{-3}. By NR iterative process, the value of I_m is determined first. With the obtained value of I_m, L_m can be determined using relation (5.3). Further, the non-linear equivalent circuit of IM is solved to determine the values of I_s and I_r with the variations in V_s, N_r, and f_s. The values of I_s and I_r are determined using the relations (5.5) and (5.6) respectively.

$$|I_s| = \left| \frac{V_s}{Z_{eq}} \right| \tag{5.5}$$

$$|I_r| = \left| \frac{V_s - I_s Z_s}{Z_r} \right| \tag{5.6}$$

The flow chart for NR iterative process is shown in Fig. 5.5.

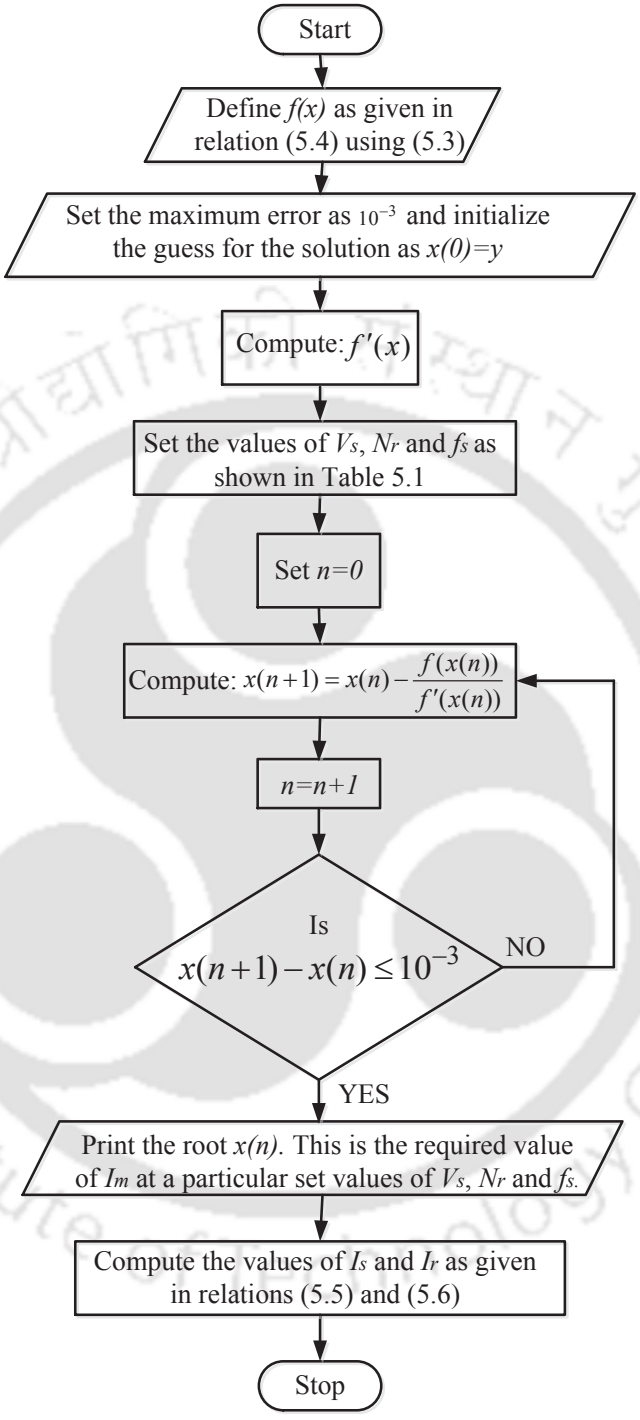

Fig. 5.5: Flow chart of Newton-Raphson iterative process for determining magnetizing current (I_m).

For each variation in V_s, N_r, and f_s, the corresponding values of T_e are determined. To obtain the

value of T_e, firstly, the mechanical power (P_m) is determined as in (5.7):

$$P_m = \frac{3I_r^2 R_r(1-s)}{s} \tag{5.7}$$

Once the mechanical power is calculated, the torque T_e is determined using (5.8):

$$T_e = \frac{P_m}{\omega_r} \tag{5.8}$$

where ω_r is equal to $\frac{2\pi}{60}N_r$, the friction and windage losses, and stray load loss are ignored [107].

The per-phase voltage equation of IM is given by (5.9)

$$v_s = i_s R_s + \frac{d\lambda_{as}}{dt} \tag{5.9}$$

By integrating (5.9), the per-phase flux linkage is given by (5.10)

$$\lambda_{as} = \int (v_s - i_s R_s)\, dt \tag{5.10}$$

where, v_s and i_s are per-phase instantaneous values of stator voltage and current, respectively, and are determine as shown in (5.11) and (5.12),

$$v_s = V_{\max} \sin \omega_s t \tag{5.11}$$

$$i_s = \mathrm{I}_{max} \sin(\omega_s t - \phi) \tag{5.12}$$

where, V_{max}, I_{max} is the maximum value of stator voltage and current, respectively, and ϕ is the phase angle between v_s and i_s, is defined as shown in (5.13):

$$\phi = \tan^{-1} \frac{X_{eq}}{\mathrm{R}_{eq}} \tag{5.13}$$

where R_{eq} and X_{eq} are the equivalent values of resistance and reactance viewed from the terminal (a,b) as shown in Fig. 5.1.

Thus, by substituting (5.11) and (5.12) in (5.10) and solving it for λ_{as} gives:

$$\lambda_{as} = -\frac{V_{\max}}{\omega_s} \cos\, \omega_s t + \frac{\mathrm{I}_{max} R_s}{\omega_s} \cos(\omega_s t - \phi) \tag{5.14}$$

Similarly, λ_{as} and λ_{bs} are determined, as:

$$\lambda_{bs} = -\frac{V_{\max}}{\omega_s} \cos\left(\omega_s t - \frac{2\pi}{3}\right) + \frac{\mathrm{I}_{max} R_s}{\omega_s} \cos\left(\omega_s t - \phi - \frac{2\pi}{3}\right) \tag{5.15}$$

$$\lambda_{cs} = -\frac{V_{\max}}{\omega_s} \cos\left(\omega_s t - \frac{4\pi}{3}\right) + \frac{\mathrm{I}_{max} R_s}{\omega_s} \cos\left(\omega_s t - \phi - \frac{4\pi}{3}\right) \tag{5.16}$$

By transforming $a-b-c$ to $\alpha\beta$ on a stationary frame of reference, $\lambda_{\alpha s}$ and $\lambda_{\beta s}$ are:

$$\lambda_{\alpha s} = \frac{\sqrt{3}}{2}(\lambda_{cs} - \lambda_{bs}) \tag{5.17}$$

$$\lambda_{\beta s} = \frac{2}{3}\left[\lambda_{as} - \frac{1}{2}(\lambda_{bs} + \lambda_{cs})\right] \tag{5.18}$$

Once $\lambda_{\alpha s}$ and $\lambda_{\beta s}$ are known, the total λ_s by the stator winding is given by:

$$|\lambda_s| = \sqrt{\left(\lambda_{\alpha s}^2 + \lambda_{\beta s}^2\right)} \tag{5.19}$$

The V_s is varied from 10 V to 110 V with steps of 10V. The motor is supplied with 50% of the rated phase voltage. This is due to the limited dc input voltage for the inverter. The nameplate ratings of f_s and N_r are 50 Hz and 2850 rpm, respectively. Based on the rating, the N_r has been chosen in 50 rpm steps ranging from 50 rpm to 2850 rpm. The f_s is chosen in 2.5 Hz steps ranging from 2.5 Hz to 50 Hz. With synchronous speed (N_s) of 3000 rpm, the slip (minimum) of the motor is 0.05 or 5%. Therefore, the possible combinations of f_s and N_r are such that the motor's slip should not be less than 0.05. Table 5.1 shows the few possible combinations of f_s, N_r, and motor slip (s) for V_s variations from 10 V to 110 V at steps of 10 V.

Table. 5.1: Few possible combinations of f_s, N_r, and slip (s) for computer computation with V_s variations from 10 V to 110 V at 10 V step size.

f_s (Hz)	N_r (rpm)	N_s (rpm)	slip (s)
2.5	50 to 142	150	0.67 to 0.053
5	50 to 285	300	0.83 to 0.05
7.5	50 to 427	450	0.89 to 0.051
10	50 to 570	600	0.92 to 0.05
50	50 to 2850	3000	0.98 to 0.05

For each variation in V_s, N_r, and f_s, the values of I_s, λ_s, and T_e are determined. The determined values of I_s, T_e, and λ_s are noted in tabular form, and few tabulated values are listed in Tables 5.2 and 5.3.

Table 5.2 shows the calculated values at motor speed 50 rpm and f_s at 2.5 Hz. Similarly, at the motor speed of 50 rpm, the values of I_{as}, T_e, and λ_s are calculated with V_s variations from 10 V to 110 V, for the rest of f_s (see Table 5.1). Likewise, for all N_r shown as in Table 5.1, the values of I_{as}, T_e, and λ_s are calculated with variations in f_s and V_s.

The tabulated values show that the high values of I_s and λ_s are observed at lower speeds, which are impracticable for the IM used in this experiment. Since the nameplate current rating of IM is 2.5

Table. 5.2: Calculated values at 50 rpm motor speed and 2.5 Hz stator voltage frequency

Stator current(rms) (A)	Flux linkage (wb)	Torque (Nm)	Input phase voltage(rms) (V)
0.97	0.54	0.69	10
2.02	1.01	2.65	20
3.32	1.26	5.12	30
4.83	1.35	7.49	40
6.39	1.39	9.78	50
7.96	1.43	12.15	60
9.43	1.54	15.35	70
10.95	1.62	18.47	80
12.51	1.67	21.48	90
14.05	1.73	24.70	100
15.59	1.79	28.13	110

Table. 5.3: Calculated values at a 2850 rpm motor speed and 50 Hz stator voltage frequency

Stator current(rms) (A)	Flux linkage (wb)	Torque (Nm)	Input phase voltage(rms) (V)
0.15	0.06	0.01	10
0.30	0.12	0.05	20
0.45	0.18	0.11	30
0.60	0.25	0.19	40
0.75	0.31	0.29	50
0.89	0.37	0.42	60
1.04	0.43	0.57	70
1.19	0.49	0.75	80
1.33	0.55	0.95	90
1.48	0.61	1.17	100
1.63	0.67	1.41	110

A. The main concerned of this work is for EV application, where the drive needs to operate over a wide speed and torque range with varying load conditions. So, limiting the current to its nominal rated values is not a preferable condition. Therefore, considering the IM used in this work with its electrical design constraint, it is overburden to twice the rated current value.

Thus, considering IM's overloading factor to twice its rated current value, processing of calculated data values of I_s, T_e, and λ_s are concluded. An overload factor of IM to twice its rated current value

ensures the inductance's variation due to magnetic saturation in the motor. While processing the calculated values, the data points corresponding to the high values of $I_s > 5$ A, are discarded from all the obtained tabulated values. For example, Table 5.2 has few values corresponding to $I_s > 5$ A. For such cases, the obtained tabulated values are again sorted with the current limit, ensuring the corresponding values to high current are discarded from the respective tables. The sorted values are again tabulated, as shown in Table 5.4.

Table. 5.4: Sorted values at a 50 rpm motor speed and 2.5 Hz stator voltage frequency

Stator current(rms) (A)	Flux linkage (wb)	Torque (Nm)	Input phase voltage(rms) (V)
0.97	0.54	0.69	10
2.02	1.01	2.65	20
3.32	1.26	5.12	30
4.83	1.35	7.49	40

Further, some tables have the calculated values within the acceptable current limit, as shown in Table 5.3. In Table 5.3, all the values are within the acceptable current limit. For such tables, further sorting of data points is not required. In like manner, the processing and sorting of calculated values for all the tables are completed and arranged in tabular form, and a few of them are as shown in Tables 5.3 and 5.4.

These sorted data are further tabulated based on V_s variations. Since the variations in V_s are observed from 10 V to 110 V with 10 V steps, a total of 11 tables are further framed. The variations in N_r and f_s are observed in each table, from 50 rpm to 2850 rpm and 2.5 Hz to 50 Hz, respectively. For example, Table 5.5 is shown for 40 V.

Table 5.5 is obtained by choosing corresponding 40 V data from Table 5.3, 5.4, and the rest of similar Tables (not shown). However, Table 5.4 does not have 40 V data. In such cases, the particular table can be ignored.

Similarly, these eleven voltage tables are framed for 10 V to 110 V. For each V_s, the torque and flux linkage curves are plotted as shown in Figures 5.6 and 5.7.

- Fig. 5.6 shows T_e vs. N_r: The torque curves are plotted wrt N_r, for each V_s. This is used as torque LUT. Using curve fitting, these curves are further refined, as shown in Fig. 5.8.
- Fig. 5.7 shows λ_s vs. N_r: This curve shows the flux linkage curves wrt N_r, for each V_s. However, to get flux linkage LUT, λ_s vs. N_r curves are needed at different T_e values, which is

Table. 5.5: Few chosen values at 40 V phase voltage

Rotor speed(rpm)	Stator current(A)	Torque (Nm)	Flux Linkage(wb)
250	2.89	0.31	0.17
500	2.69	0.27	0.15
750	2.77	0.35	0.17
1000	2.58	0.29	0.16
2250	1.85	0.39	0.19
2750	0.89	0.27	0.23
2850	0.74	0.28	0.30
250	2.82	0.28	0.16
1000	2.76	0.47	0.19
2000	1.52	0.49	0.26
1900	0.64	0.28	0.35
150	3.70	3.79	0.77

discussed in detail in the last paragraph of this section.

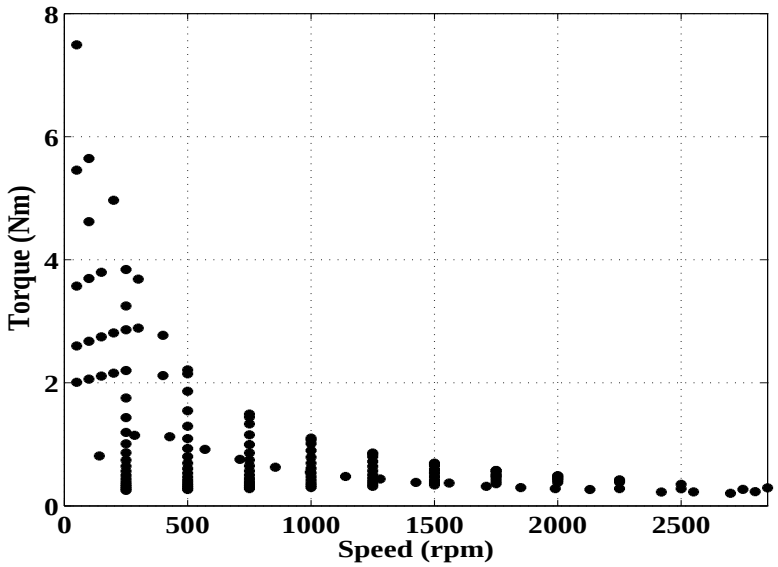

Fig. 5.6: T_e variations at 40 V wrt N_r.

These graphs (see Fig(s). 5.6 and 5.7) are plotted with variations in N_r and f_s (for T_e and λ_s) at a particular V_s. As a result, multiple data points are observed at a particular value of N_r. If these sets of data points are fed to the machine controller, pulsations in speed and torque can be seen, which, of course, is unacceptable for a drive system. Thus, the graphs are shown in Fig(s). 5.6 and 5.7 are further defined with limits such as λ_s limit, base speed, and T_e limit. These limits are explained in detail using relations (3.11) to (3.17) in chapter- 3. In the next subsequent sections, using these

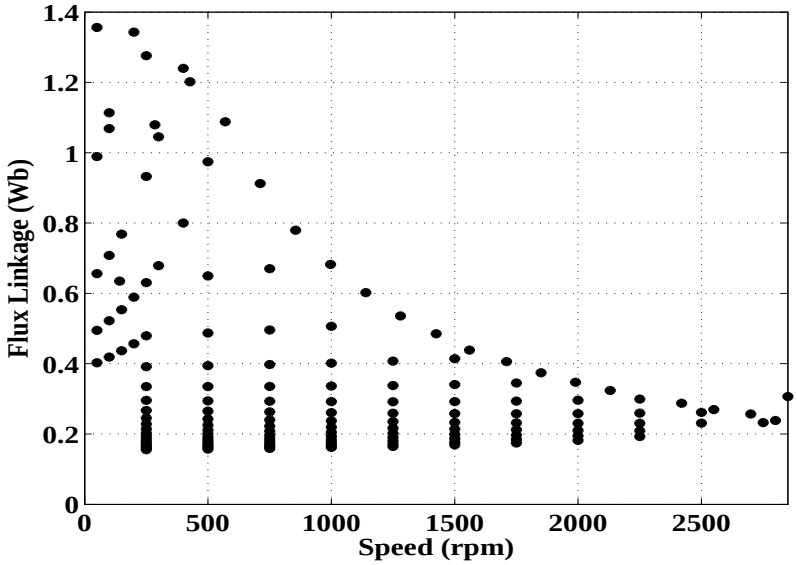

Fig. 5.7: λ_s variation at 40 V wrt N_r.

relations, the λ_s limit, and T_e limit are defined to obtain suitable values of λ_s and T_e in LUT format.

5.3.1 Flux linkage limit calculation

In this section, the same relations are used for the calculation of flux linkage limit as discussed in chapter-4. The flux linkage limit is calculated, considering (3.15), which can be written as shown in (5.20),

$$\lambda_s = \frac{V_s - I_s R_s}{\omega_s} \tag{5.20}$$

In this work, the IM used is excited with 50% of its rated phase voltage, i.e., 110 V (rms). Therefore, the stator λ_s must be calculated at 110 V voltage to obtain the maximum flux linked by the stator coil. So, (5.20) can be re-framed as shown in (5.21),

$$\left|\lambda_{s(110\,V)}\right| = \left|\frac{V_{ind}}{\omega_s}\right| \tag{5.21}$$

where V_{ind} is the maximum voltage across the stator winding of induction motor [107] and also termed as stator winding back-emf. The stator winding back-emf is the voltage difference of stator input voltage and stator resistance drop. Thus, V_{ind} is defined using (4.3) as discussed in chapter-4 and is obtained as:

$$V_{ind} = \left(\sqrt{2}\sqrt{3}\,V_s\right) - \left(\sqrt{2}\,I_s\,R_s\right) \tag{5.22}$$

where, V_s and I_s are the phase rms values of stator input voltage and current, respectively. The stator

winding of the IM used is connected in a star fashion. Under the above-stated conditions, the λ_s is calculated and is found to 0.8 Wb. Therefore, in this thesis, 0.8 Wb is considered as the maximum flux linked by the stator coil. The same value of flux linkage is used wherever the rated λ_s is required.

5.3.2 Torque limit calculation, and LUTs for T_e and λ_s

This section determines the suitable values of λ_s and T_e in the lookup table (LUT) format. The calculated T_e defines the maximal value of T_e at a reference speed and dc source voltage in the DTC algorithm. Therefore, it is mandatory to limit the torque value. Using relation (3.11), the maximum value of torque is obtained. This will ensure the limit of torque value for corresponding λ_s, V_s, and N_r. The observation chart for T_e and λ_s wrt rotor speed at different phase voltages is shown in Table 5.6. Few torque LUT entries are shown in Table 5.6, and the complete detailed LUT table is given in Appendix A.1.4.

Table. 5.6: Torque lookup table and flux linkage table wrt motor speed at different phase voltages

$N_r\ (rpm)/$ $V_{as}\ (V)$		50 rpm	500 rpm	1000 rpm	1500 rpm	2850 rpm
10	T_e	0.210	0.210	0.140	0.110	0.040
	λ_s	0.029	0.029	0.020	0.018	0.016
50	T_e	2.410	2.410	1.620	1.270	0.510
	λ_s	0.341	0.341	0.258	0.234	0.207
70	T_e	3.480	3.480	2.280	1.800	0.750
	λ_s	0.497	0.497	0.394	0.364	0.325
90	T_e	4.510	4.510	3.160	2.450	1.490
	λ_s	0.653	0.653	0.571	0.508	0.476
110	T_e	5.500	5.500	3.890	2.940	1.880
	λ_s	0.809	0.809	0.719	0.651	0.608

The torque lines are shown in Fig. 5.8 ensure that, at given V_s (say 50 V, 70 V, 110 V), the motor can develop the torque (maximum) shown by these lines. For example, if the motor is operating at 50 V, it can achieve a maximal torque of 2.4 Nm upto base speed. As speed increases, the torque capability developed by the motor reduces. If a torque of 2.4 Nm is needed at any other speed ($>$ base speed), the voltage level must be increased to meet torque demand.

Fig. 5.9 shows λ_s variations wrt N_r, and V_s. The λ_s LUT is obtained by determining the λ_s vs. N_r curves at distinct values of T_e. Therefore, curve fitting is further executed on the obtained sets of data to accomplish λ_s vs. N_r plots.

For example, at 500 rpm, complete data points of T_e and λ_s values are available with V_s variations,

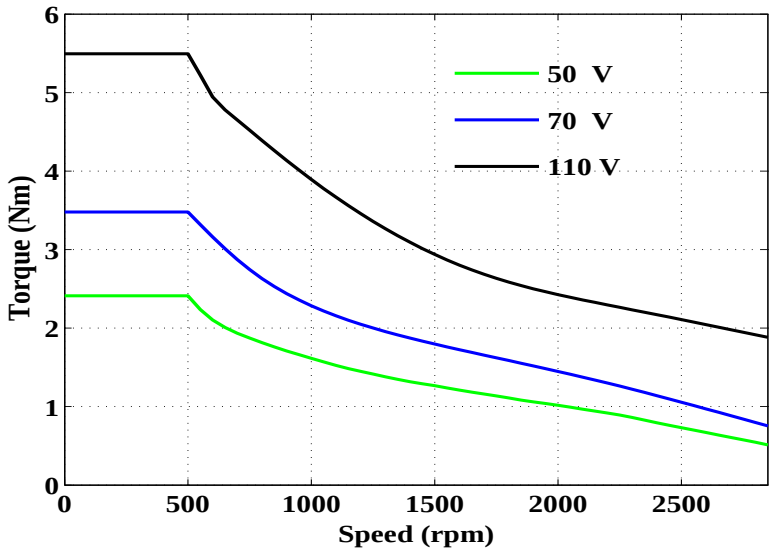

Fig. 5.8: Torque variations wrt speed at different phase voltages. The torque curves are smooth, and it is acceptable for the DTC.

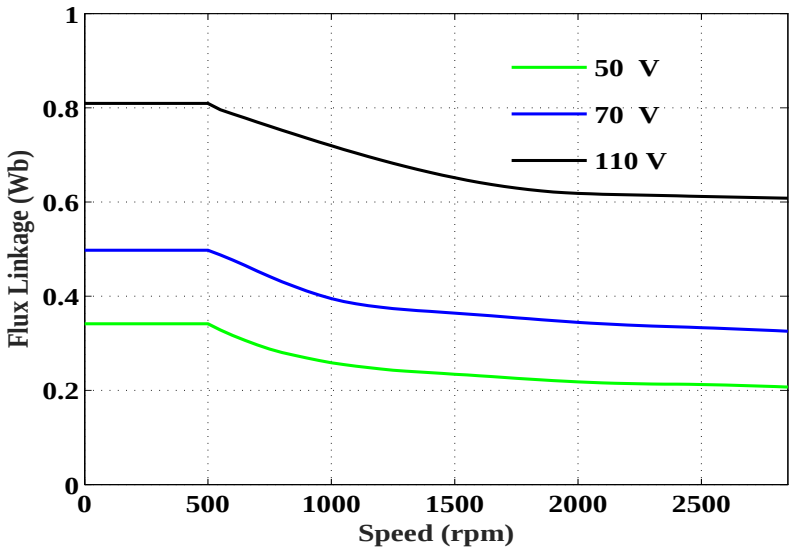

Fig. 5.9: Flux linkage variations wrt speed at different phase voltages. The flux linkage curves are smooth, and it is acceptable for the DTC.

as shown in Table 5.6. Using curve fitting, the fitted-model at 500 rpm is determined. This fitted-model shows λ_s variation wrt T_e at 500 rpm. Similar steps are carried out for the remaining N_r values to obtain the fitted-models. These fitted-models show variations between λ_s and T_e values at all possible speeds from 50 rpm to 2850 rpm. The obtained λ_s and T_e values at distinct speeds are arranged in tabular form to get the required λ_s LUT. Few λ_s LUT entries are shown in Table 5.7, and the complete detailed LUT table is given in Appendix A.1.3. A Flow chart to determine the suitable

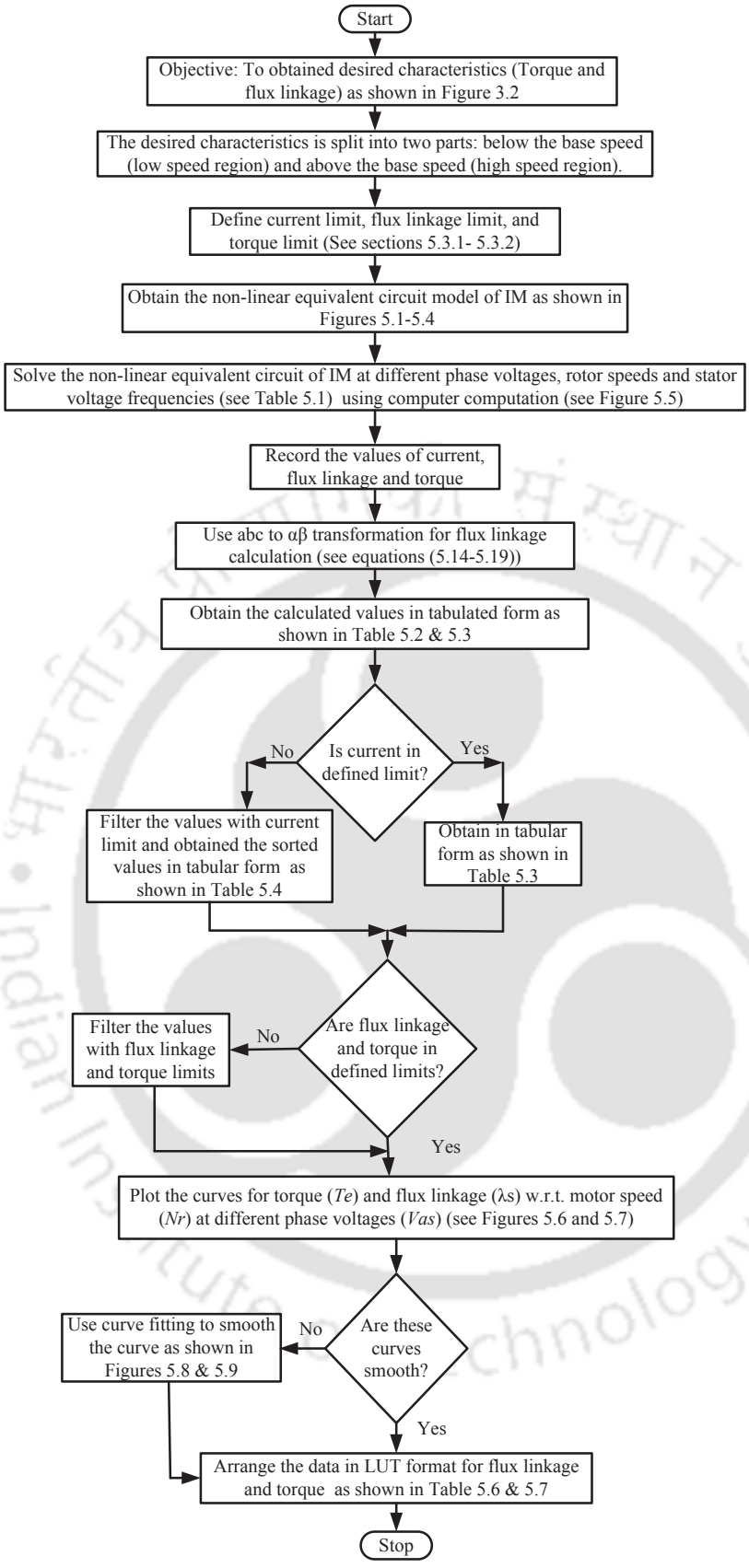

Fig. 5.10: Flow chart to determine the flux linkage (λ_s) and torque (T_e) values in lookup table format.

values of λ_s and T_e in LUT format is shown in Fig. 5.10.

Table. 5.7: Flux linkage lookup table which is used as reference flux in the DTC scheme

$N_r\ (rpm)/$ $T_e\ (Nm)$	50 rpm	500 rpm	1000 rpm	1500 rpm	2850 rpm
0.1	0.530	0.530	0.255	0.199	0.177
0.3	0.550	0.550	0.285	0.234	0.216
1	0.618	0.618	0.390	0.358	0.352
1.5	0.667	0.667	0.464	0.444	0.405

The method discussed in this section to determine λ_s and T_e values in LUTs format is simple and does not require any complex mathematical equations.

Furthermore, it is noticed from Fig. 5.7 that the λ_s value starts to decrease from 500 rpm onwards. A similar observation is observed for the T_e value. As shown in Figures 5.6 and 5.7, these observations conclude that the base speed can be considered 500 rpm. For the base speed determination, the relation between ω_s and ω_r has been examined and is presented in chapter -4, section 4.2.2.

It is found that with variable λ_s, base speed is not changing, and it remains constant for all values of V_s. Table 5.8 shows the calculation of base speed wrt variable λ_s. In this thesis, the base speed is calculated as 47.37 rad/sec. Thus, the equivalent speed in rpm, i.e., 500 rpm, is considered as base speed. It is concluded that the method proposed in this chapter for λ_s^* determination does not require base speed calculation, which in general depends on the dc-link voltage, motor current, motor λ_s, and machine parameters [69].

Table. 5.8: Calculation of base speed with variable flux

λ_s (wb)	0.809	0.731	0.653	0.575	0.497	0.419	0.341
V_{as} (V)	110	100	90	80	70	60	50
V_{ind} (V)	254.28	229.78	205.29	180.79	156.30	131.80	107.31
ω_s (rad/sec)	181.38	181.38	181.38	181.38	181.38	181.38	181.38
ω_r (rad/sec)	47.36	47.36	47.36	47.36	47.36	47.36	47.36

The obtained LUT for λ_s shows flux variations wrt N_r and T_e. The T_e LUT shows motor torque variations wrt N_r and V_s. In the case of EV applications, the variation in DC voltage is experienced wrt the discharge of the battery and operating conditions [80]. Therefore, for inverter fed IM, the relation between the stator excitation voltage (V_s) and inverter input dc voltage (V_{dc}) must be considered and is calculated using (4.6) [113] as discussed in chapter-4 and is obtained as:

$$|V_s| = \frac{0.8 * V_{dc}}{\sqrt{3}} \tag{5.23}$$

Using (5.23), V_{dc} is calculated as:

$$V_{dc} = \frac{\sqrt{3}|V_s|}{0.8} \tag{5.24}$$

The suitable value of λ_s^* is chosen from its LUT at reference speed and T_e. In addition, a proper value of maximum T_e (i.e., T_{em}) is also chosen from its LUT at reference speed and dc source input voltage.

The conclusions of this section are summarized as:

- The proposed method acknowledges the inductance's variation due to magnetic saturation in the motor while processing the calculated T_e and λ_s values.
- It is simple and does not require any complex mathematical equations to determine the λ_s and T_e values in LUTs format.
- It does not demand base speed calculation, which in general depends on the dc-link voltage, motor current, motor λ_s, and machine parameters.

To check the robustness of the proposed method, the parameters (i.e., R_s and L_{1s}) sensitivity analysis has been performed and is discussed in the next section.

5.4 Parameter sensitivity

In this section, the robustness of the proposed method is examined by performing parameter sensitivity analysis. The effect of parameter sensitivity on the proposed method is observed with $\pm$5 percent (%) variations in R_s and L_{ls}. Using computer programming, a non-linear equivalent circuit is solved with these variations (as discussed in section 5.3), the values are calculated, as shown in Tables 5.9-5.12. Tables 5.9-5.12 show the obtained values with parameter variations at 50 rpm and 2850 rpm, wrt Table 5.2 and 5.3.

Table 5.9 and 5.10 show calculated values at stator voltage frequency 2.5 Hz and motor speed 50 rpm, with $\pm$5% variations in R_s and L_{ls}, respectively, wrt Table 5.2. In Table 5.9 and 5.10, the first four values are within the acceptable current limit (i.e., 5 A). As discussed in section 5.3, the values that are not in the current limit range are discarded from the respective tables. Therefore, the values corresponding to high current are discarded from the tables (Table 5.9 and 5.10). Fig. 5.11 shows the plot for calculated values of Table 5.9 at 50 rpm and 2.5 Hz with $\pm$5% R_s variations and at constant L_{ls} (wrt Table 5.2). Fig. 5.12 shows the plot for calculated values of Table 5.10 at 50 rpm and 2.5 Hz with $\pm$5% L_{ls} variations and at constant R_s (wrt Table 5.2). In Fig(s). 5.11 and 5.12, an arrow is pointed to

Table. 5.9: Calculated values at 50 rpm motor speed and 2.5 Hz stator voltage frequency with $\pm 5\%$ R_s variations and constant L_{ls} wrt Table 5.2 (here, $\pm\delta$ indicates $\pm 5\%$).

Stator current(I_{as}) (A)		Flux linkage (λ_s) (wb)		Torque (T_e) (Nm)		Input phase voltage(rms)(V)
With $(R_s + \delta R_s)$	With $(R_s - \delta R_s)$	With $(R_s + \delta R_s)$	With $(R_s - \delta R_s)$	With $(R_s + \delta R_s)$	With $(R_s - \delta R_s)$	
0.955	0.997	0.526	0.555	0.665	0.703	10
1.991	2.084	0.985	0.104	2.62	2.719	20
3.268	3.405	1.24	1.27	4.996	5.215	30
4.749	4.914	1.328	1.38	7.197	7.750	40
6.276	6.509	1.353	1.45	9.5	10.617	50
7.811	8.116	1.38	1.48	11.317	13.041	60
9.245	9.623	1.491	1.59	14.393	16.374	70
10.729	11.182	1.572	1.67	17.389	19.628	80
12.251	12.781	1.623	1.72	20.277	22.769	90
13.754	14.361	1.682	1.78	23.361	26.135	100
15.256	15.94	1.742	1.84	26.642	29.725	110

Table. 5.10: Calculated values at 50 rpm motor speed and 2.5 Hz stator voltage frequency with $\pm 5\%$ L_{ls} variations and constant R_s wrt table 5.2 (here, $\pm\delta$ indicates $\pm 5\%$).

Stator current(I_{as}) (A)		Flux linkage(λ_s) (wb)		Torque(T_e) (Nm)		Input phase voltage(rms)(V)
With $(L_{ls} + \delta L_{ls})$	With $(L_{ls} - \delta L_{ls})$	With $(L_{ls} + \delta L_{ls})$	With $(L_{ls} - \delta L_{ls})$	With $(L_{ls} + \delta L_{ls})$	With $(L_{ls} - \delta L_{ls})$	
0.96	0.987	0.538	0.549	0.689	0.691	10
1.99	2.049	0.981	1.031	2.647	2.653	20
3.271	3.352	1.256	1.287	5.116	5.124	30
4.69	4.977	1.335	1.389	7.482	7.498	40
6.191	6.429	1.369	1.413	9.768	9.792	50
7.862	7.985	1.401	1.459	12.134	12.165	60
9.143	9.477	1.524	1.587	15.329	15.370	70
9.853	10.992	1.602	1.632	18.444	18.495	80
11.514	12.562	1.58	1.685	21.448	21.511	90
13.455	14.085	1.69	1.784	24.662	24.736	100
14.195	16.184	1.751	1.824	28.086	28.173	110

show the values within the acceptable current limit of 5 A, and remaining values beyond the limit are discarded. The percentage changes in calculated values with variations in parameters for 50 rpm and 2.5 Hz wrt Table 5.2 are shown in Table 5.13 and 5.14. The tables show that the maximum change in percentage, within the acceptable current limit, for the calculated values are ($+2.89$ to -3.16) % for I_s, ($+2.87$ to -2.89) % for λ_s, ($+3.91$ to -3.47) % for T_e.

Table 5.11 and 5.12 show calculated values at 2850 rpm and 50 Hz, with $\pm 5\%$ R_s and L_{ls} variations, respectively, wrt Table 5.3. The obtained values in these tables are within the acceptable current

Table. 5.11: Calculated values at 2850 rpm motor speed and 50 Hz stator voltage frequency with $\pm 5\%$ R_s variations and constant L_{ls} wrt table 5.3 (here, $\pm\delta$ indicates $\pm 5\%$).

Stator current(I_{as}) (A)		Flux linkage(λ_s) (wb)		Torque(T_e) (Nm)		Input phase voltage(rms)(V)
With $(R_s + \delta R_s)$	With $(R_s - \delta R_s)$	With $(R_s + \delta R_s)$	With $(R_s - \delta R_s)$	With $(R_s + \delta R_s)$	With $(R_s - \delta R_s)$	
0.146	0.155	0.0589	0.061	0.01	0.01	10
0.296	0.305	0.118	0.122	0.05	0.051	20
0.439	0.458	0.178	0.182	0.108	0.113	30
0.588	0.608	0.246	0.253	0.188	0.193	40
0.738	0.758	0.304	0.315	0.286	0.294	50
0.878	0.915	0.363	0.374	0.415	0.423	60
1.027	1.057	0.425	0.435	0.563	0.575	70
1.177	1.192	0.482	0.498	0.741	0.751	80
1.317	1.340	0.541	0.558	0.94	0.951	90
1.467	1.489	0.602	0.618	1.158	1.174	100
1.615	1.638	0.661	0.677	1.392	1.42	110

Table. 5.12: Calculated values at 2850 rpm motor speed and 50 Hz stator voltage frequency with $\pm 5\%$ L_{ls} variations and constant R_s wrt table 5.3 (here, $\pm\delta$ indicates $\pm 5\%$).

Stator current(I_{as}) (A)		Flux linkage(λ_s) (wb)		Torque(T_e) (Nm)		Input phase voltage(rms)(V)
With $(L_{ls} + \delta L_{ls})$	With $(L_{ls} - \delta L_{ls})$	With $(L_{ls} + \delta L_{ls})$	With $(L_{ls} - \delta L_{ls})$	With $(L_{ls} + \delta L_{ls})$	With $(L_{ls} - \delta L_{ls})$	
0.149	0.151	0.059	0.061	0.01	0.01	10
0.299	0.301	0.119	0.122	0.05	0.05	20
0.449	0.449	0.179	0.182	0.11	0.108	30
0.599	0.598	0.249	0.248	0.189	0.187	40
0.749	0.746	0.309	0.307	0.288	0.293	50
0.889	0.893	0.369	0.368	0.417	0.422	60
1.039	1.041	0.429	0.429	0.566	0.574	70
1.189	1.189	0.49	0.491	0.745	0.749	80
1.33	1.337	0.55	0.552	0.943	0.948	90
1.481	1.485	0.611	0.614	1.161	1.17	100
1.629	1.635	0.671	0.675	1.40	1.416	110

limit. Fig. 5.13 shows the plot for the calculated values of Table 5.11 at 2850 rpm and 50 Hz, with $\pm 5\%$ R_s variations and constant L_{ls}, wrt Table 5.3. Fig. 5.14 shows the plot for calculated values of Table 5.12 at 2850 rpm and 50 Hz, with $\pm 5\%$ L_{ls} variations and constant R_s (wrt Table 5.3). The percentage changes in calculated values with variations in parameters for 2850 rpm and 50 Hz wrt Table 5.3 are shown in Table 5.15 and 5.16. The tables show that the maximum change in percentage for the calculated values are ($+2.67$ to -3.33) % for I_s, ($+1.94$ to -1.67) % for λ_s, ($+1.82$ to -2.73) % for T_e.

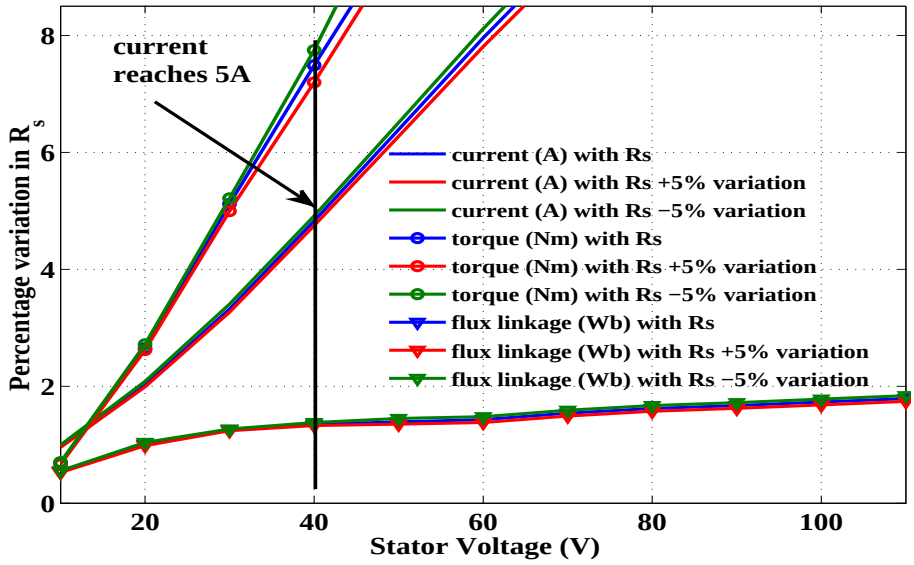

Fig. 5.11: Calculated values (Table 5.9) with ±5% variations in stator resistance (R_s) at 50 rpm motor speed and 2.5 Hz stator voltage frequency wrt Table 5.2.

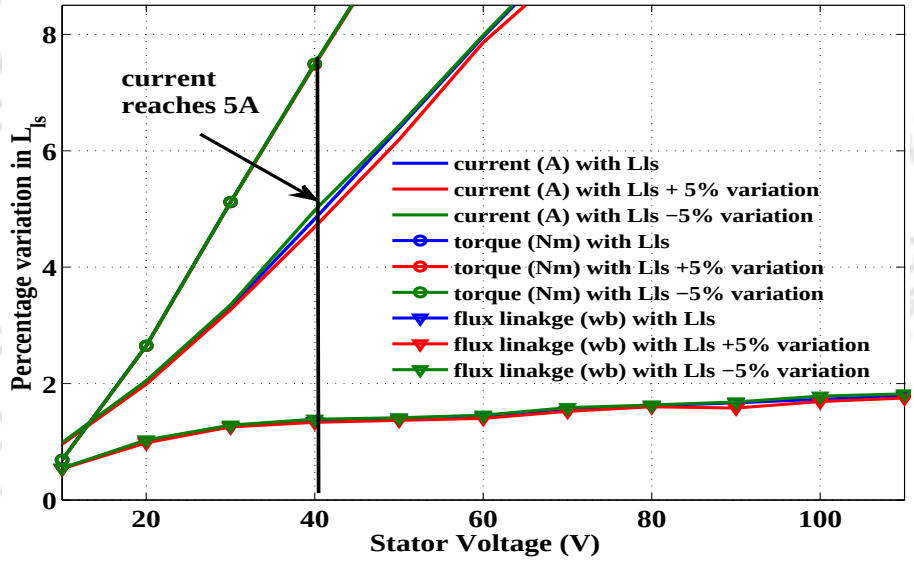

Fig. 5.12: Calculated values (Table 5.10) with ±5% variations in stator leakage inductance (L_{ls}) at 50 rpm motor speed and 2.5 Hz stator voltage frequency wrt Table 5.2.

These observations show that, for ±5% parameter variations, the maximum variations in λ_s and T_e are (+2.87 to −2.89) % and (+3.91 to −3.47)%, respectively up to the base speed. Beyond the base speed, the variations in λ_s and T_e are (+1.94 to −1.67) % and (+1.82 to −2.73) %, respectively. The observations confirm that the proposed approach is least sensitive to the variations of parameters. These offline obtained values of λ_s^* and T_e are arranged in LUT format and are fed to the DTC algorithm, which is discussed in chapter-4, section 4.4. To check the proposed approach's effective-

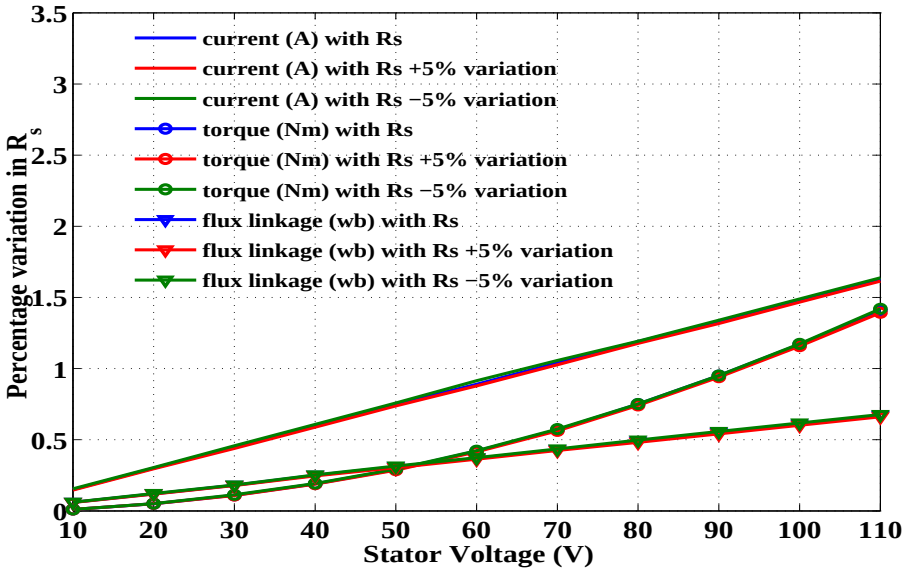

Fig. 5.13: Calculated values (Table 5.11) with ±5% variations in stator resistance (R_s) at 2850 rpm motor speed and 50 Hz stator voltage frequency wrt Table 5.3.

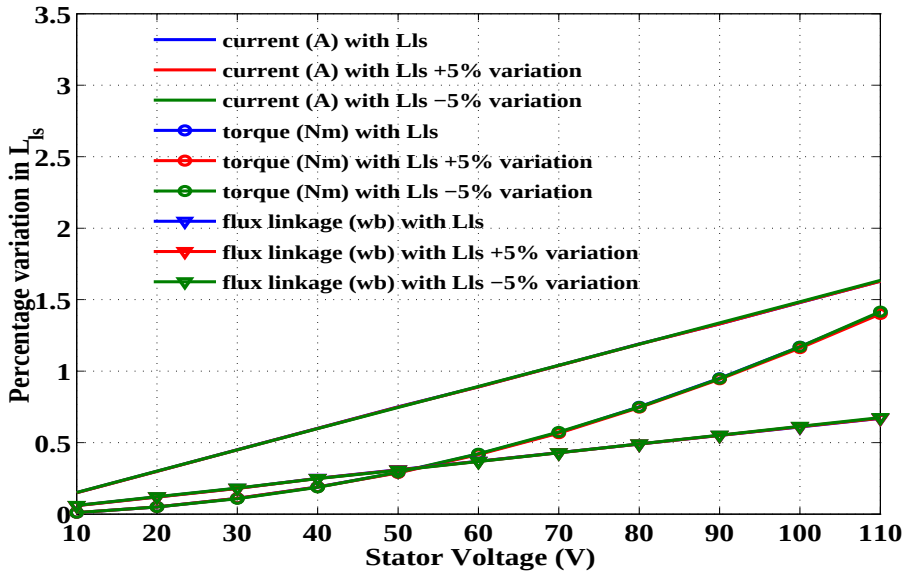

Fig. 5.14: Calculated values (Table 5.12) with ±5% variations in stator leakage inductance (L_{ls}) at 2850 rpm motor speed and 50 Hz stator voltage frequency wrt Table 5.3.

ness, the comparisons with the existing technique are carried out, and the experimental results are demonstrated in the next section.

Table. 5.13: Percentage (%) change in calculated values (table 5.9) at 50 rpm motor speed and 2.5 Hz stator voltage frequency with $\pm 5\%$ R_s variations and constant L_{ls} wrt table 5.2 (here, $\pm\delta$ indicates $\pm 5\%$).

% change in stator current (I_{as})		% change in flux linkage (λ_s)		% change in torque (T_e)		Input phase voltage(V_{as})(V)
With $(R_s + \delta R_s)$	With $(R_s - \delta R_s)$	With $(R_s + \delta R_s)$	With $(R_s - \delta R_s)$	With $(R_s + \delta R_s)$	With $(R_s - \delta R_s)$	
1.55	−2.78	2.59	−2.71	3.62	−1.88	10
1.44	−3.16	2.47	−2.59	1.13	−2.60	20
1.57	−2.56	1.58	−0.91	2.42	−1.86	30
1.67	−1.73	1.63	−2.41	3.91	−3.47	40
1.78	−1.86	2.66	−4.20	2.86	−8.86	50
1.87	−1.96	3.49	−3.61	6.86	−7.33	60
1.96	−2.05	3.18	−3.29	6.23	−6.67	70
2.02	−2.12	2.96	−3.10	5.85	−6.27	80
2.07	−2.17	2.81	−2.97	5.60	−6.00	90
2.11	−2.21	2.77	−2.86	5.42	−5.81	100
2.14	−2.25	2.68	−2.82	5.29	−5.67	110

Table. 5.14: Percentage (%) change in calculated values (table 5.10) at 50 rpm motor speed and 2.5 Hz stator voltage frequency with $\pm 5\%$ L_{ls} variations and constant R_s wrt table 5.2 (here, $\pm\delta$ indicates $\pm 5\%$).

% change in stator current (I_{as})		% change in flux linkage (λ_s)		% change in torque (T_e)		Input phase voltage(V_{as})(V)
With $(L_{ls} + \delta L_{ls})$	With $(L_{ls} - \delta L_{ls})$	With $(L_{ls} + \delta L_{ls})$	With $(L_{ls} - \delta L_{ls})$	With $(L_{ls} + \delta L_{ls})$	With $(L_{ls} - \delta L_{ls})$	
1.03	−1.75	0.37	−1.67	0.15	−0.15	10
1.49	−1.44	2.87	−2.08	0.12	−0.11	20
1.48	−0.96	0.32	−2.14	0.08	−0.08	30
2.89	−3.04	1.11	−2.89	0.11	−0.11	40
3.11	−0.61	1.51	−1.65	0.12	−0.12	50
1.23	−0.31	2.03	−2.02	0.13	−0.12	60
3.04	−0.50	1.04	−3.05	0.14	−0.13	70
10.02	−0.38	1.11	−0.74	0.14	−0.14	80
7.96	−0.42	5.39	−0.90	0.15	−0.14	90
4.23	−0.25	2.31	−3.12	0.15	−0.15	100
8.95	−3.81	2.18	−1.90	0.16	−0.15	110

5.5 Result and Discussion

The experimental setup of speed control for IM drive with the DTC scheme is shown in Appendix A.6. The complete system has been developed in the laboratory test-bed to mimic the EV conditions as far as possible. The developed setup is facilitated to run the motor for different driving cycles. It has tested and examined the performance of the controller over a wide torque and speed range. The

Table. 5.15: Percentage (%) change in calculated values (table 5.11) at 2850 rpm motor speed and 50 Hz stator voltage frequency with $\pm 5\%$ R_s variations and constant L_{ls} wrt table 5.3 (here, $\pm\delta$ indicates $\pm 5\%$).

% change in stator current (I_{as})		% change in flux linkage (λ_s)		% change in torque (T_e)		Input phase voltage(V_{as})(V)
With $(R_s+\delta R_s)$	With $(R_s-\delta R_s)$	With $(R_s+\delta R_s)$	With $(R_s-\delta R_s)$	With $(R_s+\delta R_s)$	With $(R_s-\delta R_s)$	
2.67	−3.33	1.83	−1.67	0	0	10
1.33	−1.67	1.67	−1.67	0	−2	20
2.44	−1.78	1.11	−1.11	1.82	−2.73	30
2	−1.33	1.6	−1.2	1.05	−1.58	40
1.6	−1.07	1.94	−1.61	1.38	−1.38	50
1.35	−2.81	1.89	−1.08	1.19	−0.71	60
1.25	−1.63	1.16	−1.62	1.23	−0.88	70
1.09	−0.17	1.63	−1.63	1.2	−0.133	80
0.98	−0.75	1.64	−1.45	1.05	−0.11	90
0.88	−0.61	1.31	−1.31	1.03	−0.34	100
0.92	−0.49	1.34	−1.04	1.28	−0.71	110

Table. 5.16: Percentage (%) change in calculated values (table 5.12) at 2850 rpm motor speed and 50 Hz stator voltage frequency with $\pm 5\%$ L_{ls} variations and constant R_s wrt table 5.3 (here, $\pm\delta$ indicates $\pm 5\%$).

% change in stator current (I_{as})		% change in flux linkage (λ_s)		% change in torque (T_e)		Input phase voltage(V_{as})(V)
With $(L_{ls}+\delta L_{ls})$	With $(L_{ls}-\delta L_{ls})$	With $(L_{ls}+\delta L_{ls})$	With $(L_{ls}-\delta L_{ls})$	With $(L_{ls}+\delta L_{ls})$	With $(L_{ls}-\delta L_{ls})$	
0.67	−0.67	1.67	−1.67	0	0	10
0.33	−0.33	0.83	−1.67	0	0	20
0.22	0.22	0.56	−1.11	0	1.82	30
0.17	0.33	0.40	0.80	0.52	1.58	40
0.13	0.53	0.32	0.97	0.69	−1.03	50
0.11	−0.34	0.27	0.54	0.71	−0.48	60
0.10	−0.10	0.23	0.23	0.70	−0.70	70
0.10	−0.10	0	−0.20	0.67	0.13	80
0	−0.53	0	−0.36	0.74	0.21	90
−0.07	−0.34	−0.16	−0.66	0.77	0	100
0.06	−0.31	−0.51	−0.75	0.71	−0.43	110

control algorithm is realized on a dSPACE1103 platform, and its sampling time is chosen as 40 μsec.

To check the effectiveness of the proposed method, comparisons with the existing technique are carried out, and experimental results are demonstrated in this section. The existing technique is:

- **Case I**: Loss model-based technique (as discussed in chapter-3, section 3.3.2) proposed in [62] for determining the accurate reference flux value at required operating conditions. In [62],

the suitable λ_s^* value is calculated from the IM loss minimization algorithm, and a loss model is developed in terms of λ_s, T_e, N_r, and motor parameters. Here, the developed loss model is sensitive to the L_m variation. Thus, in this work, to compare with the proposed method (regarded as **case III**), the variation in L_m (5.3) has been incorporated with the obtained loss model, and results are demonstrated in the next subsequent section.

- **Case II**: The method proposed in chapter-4, which used an FEA-based IM model to calculate the suitable λ_s^* value.

A multiple series of experiments are conducted and investigated in the laboratory with the developed test-bed setup. Comparative evaluations are figure-out and discussed in the next subsequent sections. The proposed techniques (Cases II and III) is compared with the existing method (Case I), in terms of performance indices of the drive (such as N_r, T_e, and λ_s responses), ripples in T_e and λ_s. Besides, input energy consumption and efficiency analysis are also discussed in detail and presented in sections 5.5.3 and 5.5.4, respectively.

5.5.1 Drive cycle response

The IM drive's performance is demonstrated in this section for the following vehicle driving cycles;

- New York City Cycle (NYCC)
- New European Driving Cycle (NEDC)

The responses of speed, torque, and flux linkage with the considered cases are presented for NYCC and NEDC driving cycles. Besides, the root mean square errors (RMSEs) for the response are calculated using (5.25) with each considered cases, and a comparative analysis is shown in Table 5.17.

$$\%RMSE = \sqrt{\frac{\sum_{i=1}^{n} e^2[i]}{n}} * 100\% \tag{5.25}$$

where e is the error between reference and estimated values, and m is the sample's number of points.

Table. 5.17: RMSE results chart

	NYCC			NEDC		
	Case I	Case II	Case III	Case I	Case II	Case III
Speed (rpm)	67.02	63.00	61.90	16.34	15.57	15.32
Torque (Nm)	0.1726	0.07	0.0584	0.11	0.06	0.04
Flux linkage (wb)	0.0411	0.04	0.0237	0.10	0.08	0.054

Fig. 5.15 shows the speed responses of the considered cases for the NYCC. Fig.(s) 5.15(c) and 5.15(b) are the DTC speed responses for case III (non-linear equivalent circuit-based approach) and case II (FEA-based approach), respectively. Fig. 5.15(a) is the speed response for case I (loss model-based approach).

The observations for torque and flux are presented in Fig(s). 5.16 and 5.17, respectively. The torque response for the case I (loss model-based approach) is shown in Fig. 5.16(a). The observation indicates that the measured torque response with case I is not acceptable as accurate tracking of reference torque is not possible for a wide range of operations. The torque ripples are observed in case I, with a %RMSE value of 17.26%. Since the motor cannot produce the required torque, as the selection of reference flux in this case is not accurate, as shown in Fig. 5.17(a). The Fig. 5.16(c) shows an acceptable result in torque response for Case III (non-linear equivalent circuit-based approach) with a %RMSE value of 5.84%. Here, the ripple in measured torque is low compared to the case I and is improved compared to case II (FEA-based approach). The %RMSE value of torque for case II is 7%. The flux linkage response for case III is shown in Fig. 5.17(c). The observation shows that the proper λ_s^* is selected for the method proposed in case III. As a result, the motor is able to develop the required torque with case III. The flux response is shown in Fig.5.17(c) confirms that the variations in flux (reference as well as estimated) is desirable for a wide range of operation. The %RMSE value in flux response for Case I is 4.11%. Whereas, for cases II and III, %RMSE values in flux response are 4% and 2.37%, respectively.

Besides, close observation of 15 sec is made for the NYCC as shown in 5.18-5.20. The chattering of speeds to settle down to zero rpm are seen with the case I, as shown in Fig. 5.18(a) (marked by the arrow in the respective figures). Whereas the speed response with case III is quite satisfactory. Moreover, the torque and flux responses are not satisfactory for case I, as shown in Fig.(s) 5.19(a) and 5.20(a). These results show that case I has convergence issues; as a consequence, the accurate tracking of reference speed, torque, and flux is not acceptable. Whereas case III shows comparatively fair performance in terms of speed tracking, torque, and flux tracking. The observations confirm that case III yields an acceptable performance. In addition, Case III ensures improvement in tracking speed, torque, and flux responses compared to Case II over a wide range of operations.

Similar observations have been reported with NEDC, and the observations are presented as in Fig.(s) 5.21-5.23. As observed, case I with the DTC strategy is unacceptable for a wide speed range. In comparison, observations are fair with cases II and III (in terms of speed, torque and flux responses). Moreover, the ripples in measured torque are small with case III and appropriate λ_s^* selec-

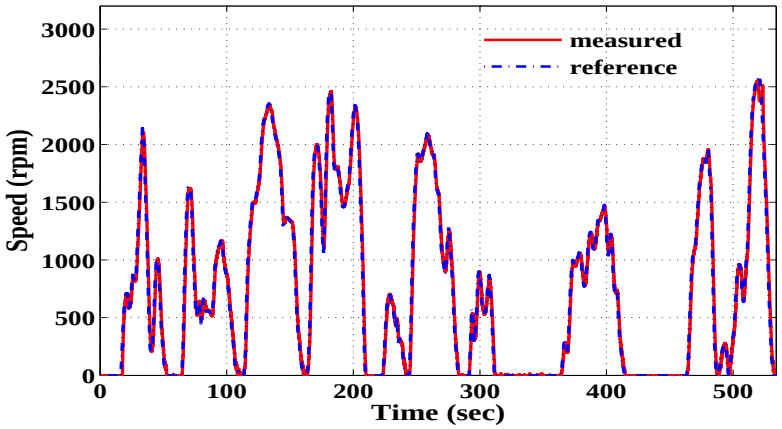

(a)

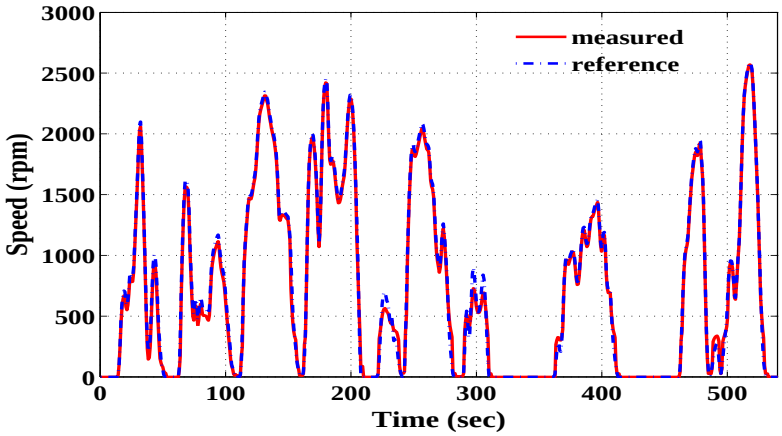

(b)

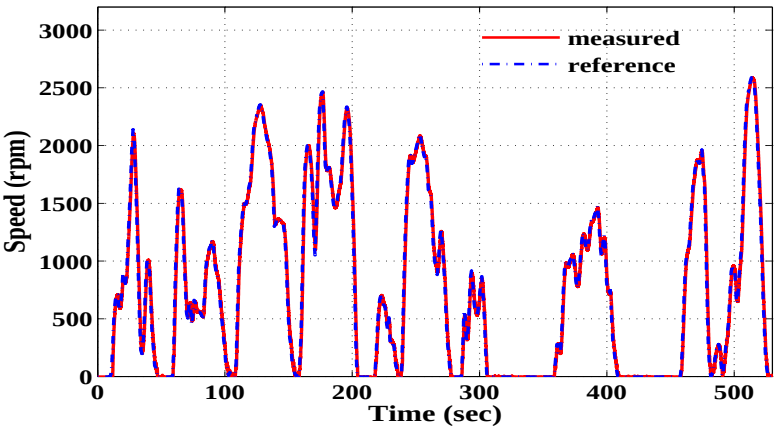

(c)

Fig. 5.15: Speed response for NYCC (a) Case I (b) Case II (c) Case III. The RMSE for Case III is 61.9 and for case II is 63.00. Whereas, for case I is 67.02.

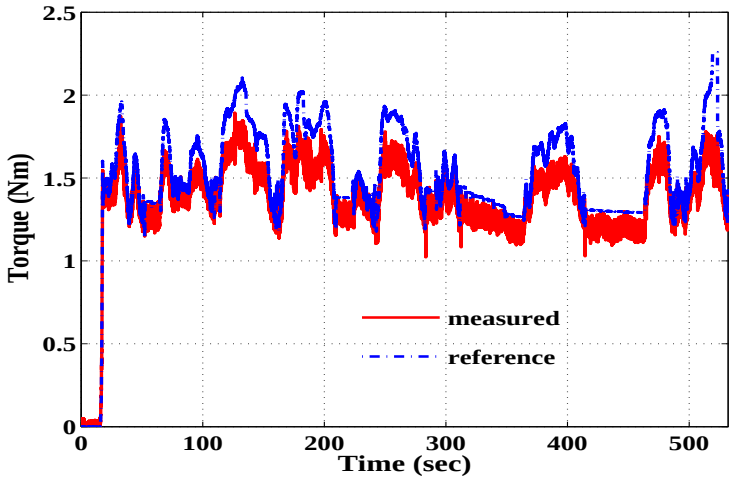

(a)

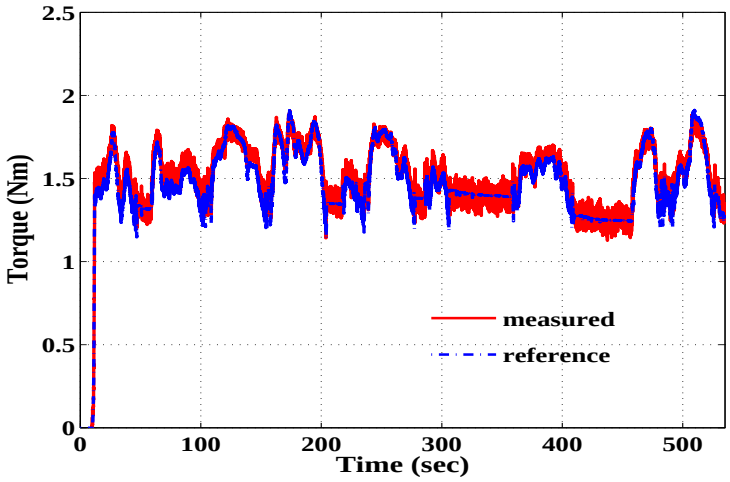

(b)

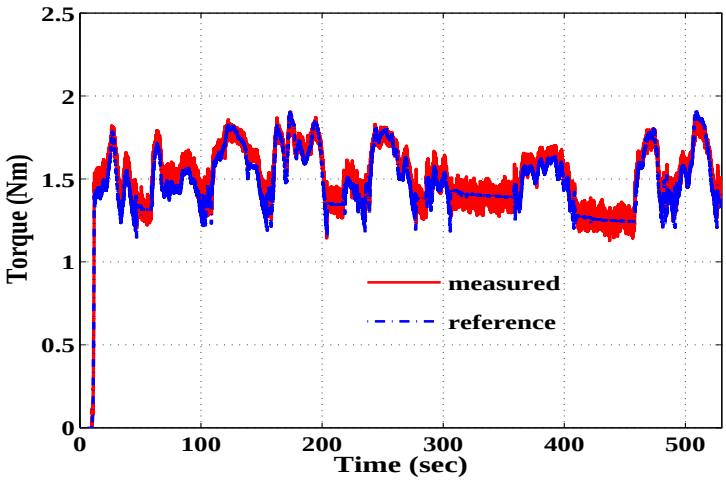

(c)

Fig. 5.16: Torque response for NYCC (a) Case I(b) Case II (c) Case III. The RMSE for Case III is 0.0584, and for Case II is 0.07. While for Case I is 0.1726.

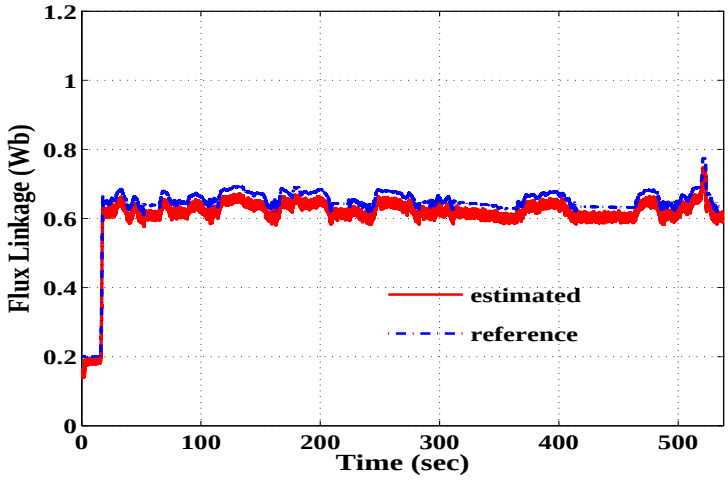

(a)

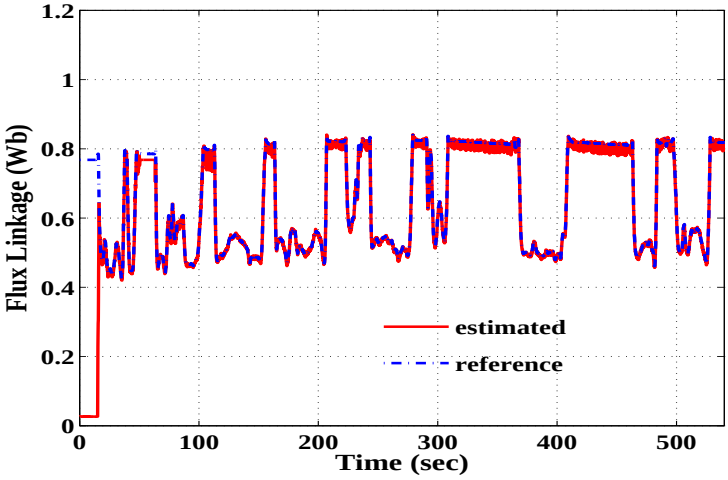

(b)

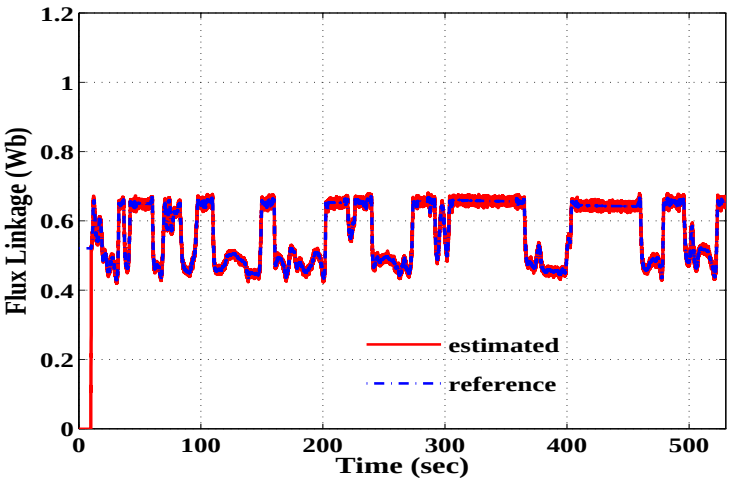

(c)

Fig. 5.17: Flux linkage response for NYCC (a) Case I (b) Case II (c) Case III. The flux linkage response with Case III is satisfactory. The RMSE for Case III is 0.0237, and for Case II is 0.04. While for Case I is 0.0411.

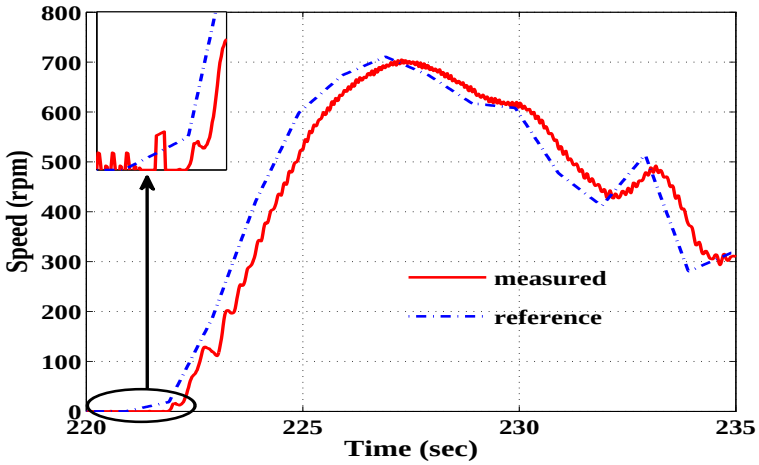

(a)

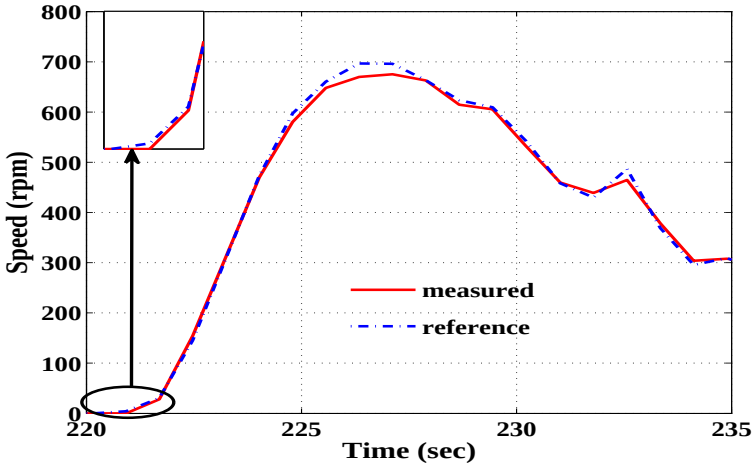

(b)

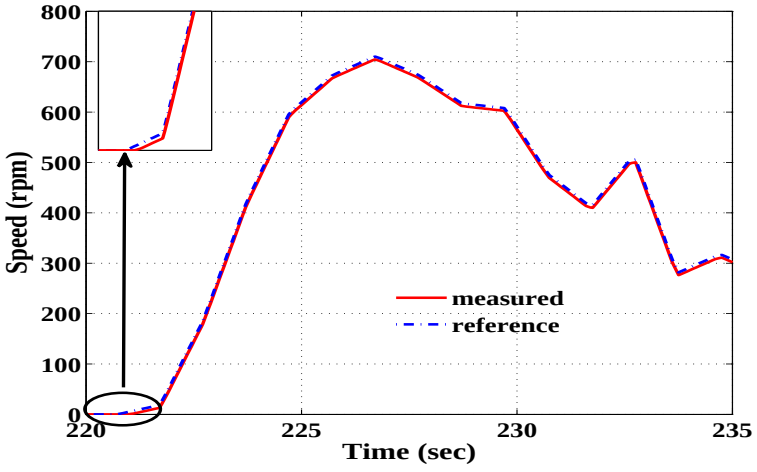

(c)

Fig. 5.18: NYCC speed response for a period of 15 sec (a) Case I (b) Case II (c) Case III. With Case I, the performance of IM drive is not satisfactory. The chattering of measured speed to settle down at zero rpm is observed. Whereas, with Case III, the drive shows satisfactory performance as compared to the Case II.

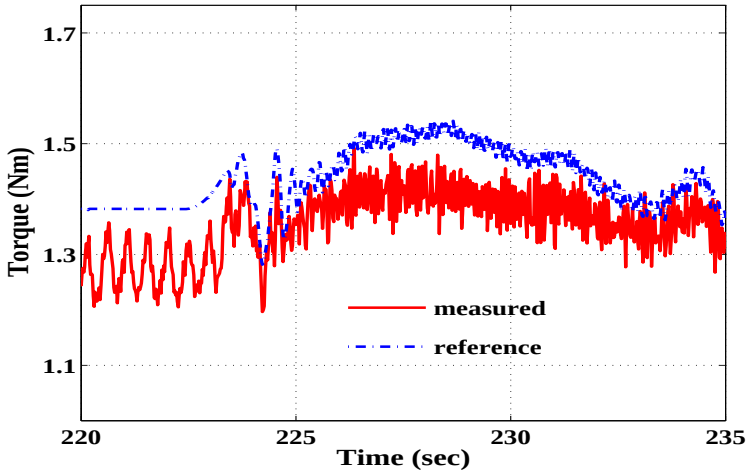

(a)

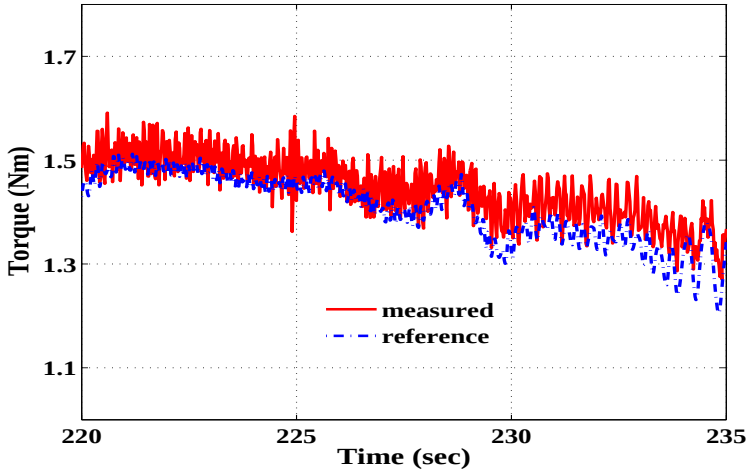

(b)

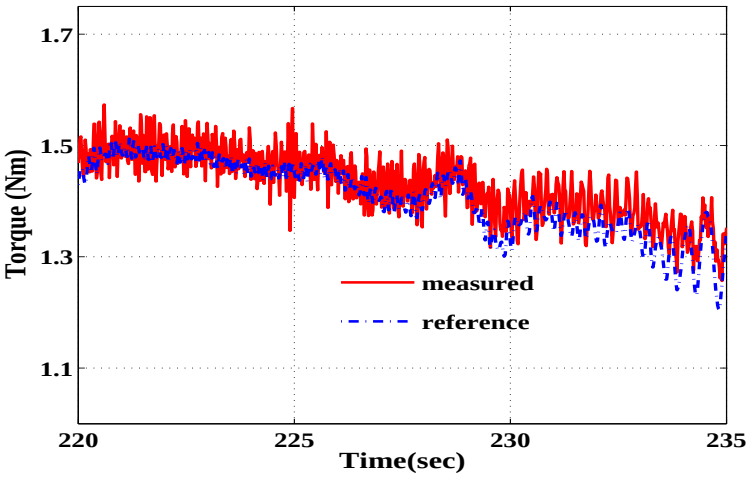

(c)

Fig. 5.19: NYCC torque response for a period of 15 sec (a) Case I(b) Case II (c) Case III. With Case III torque response is satisfactory and also RMSE in torque is less, as compared to cases I and II.

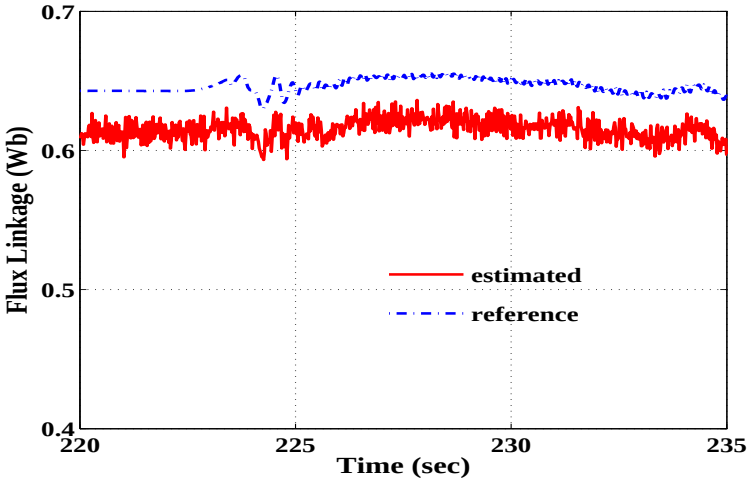

(a)

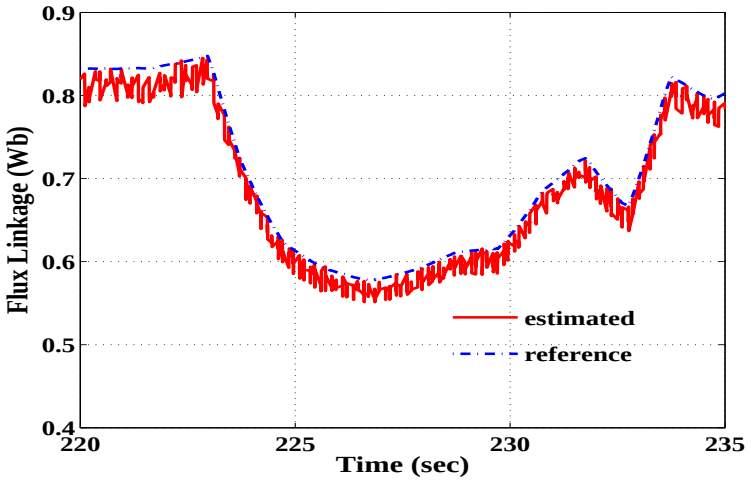

(b)

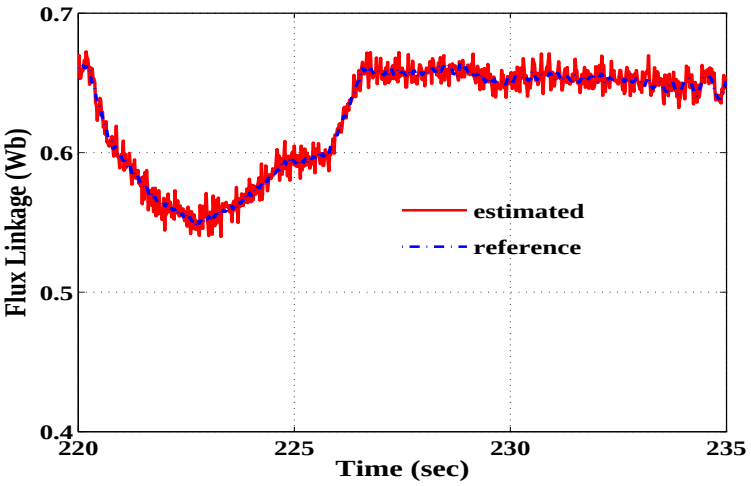

(c)

Fig. 5.20: NYCC flux linkage response for a period of 15 sec (a) Case I (b) Case II (c) Case III. Case I: Chattering of flux linkages (estimated) are observed, for the same instant as observed for speed and torque responses. The flux response with case III is satisfactory as compared to Case II.

tion (so as estimated λ_s) is achievable to develop the motor's required T_e. Besides, cases II and III determine the low value of flux compared to the case I for speed higher than the base speed. This is acceptable for EV applications with a wide speed range.

Table 5.17 shows the RMSE values for speed response, torque, and flux response with the considered cases. The RMSE results chart shows that the values with case I are comparatively high. And torque ripples are seen for case I. As the flux level with case I is either constant over the changing operating conditions or does not get the acceptable range of variations to settle for an optimal value. The result ensures that case I is not able to determine the accurate λ_s^* value. Thus, case I may not be acceptable for drives with fast dynamics. Table 5.17 clearly marks that case III provides comparatively satisfactory and improved performance compared to cases I and II. Further, to check the proposed method's reliability, the dynamic and steady-state responses are observed and discussed in the next subsequent section.

5.5.2 Dynamic and steady state response

The steady-state response and the transient at starting with step response at different speeds are analyzed and demonstrated in this section. The performance indicators such as torque ripple expressed in standard deviation (σT_e), relative torque error (T_{err}), and relative flux error (λ_{err}) are calculated for the considered cases. Fig. 5.24 illustrates the dynamic speed response of the DTC-based IM drive with step-change in speed. The speed response is tested by changing the speed from 0 rpm to 1000 rpm and back to 250 rpm, as shown in Fig. 5.24.

The torque responses (reference and measured) with the case III shown in Fig.5.24(c) are comparatively fair. Also, have fewer torque ripples are observed with case III as compared to the case I. It is seen that the drive performance in Case III is improved as compared to case II.

To understand the proposed technique's impact on flux and torque ripples, torque ripple expressed in standard deviation (σT_e), relative torque error (T_{err}), and relative flux error (λ_{err}) are determined using (5.26)-(5.28) [114] for the considered cases at different operating points. The experimental observations at 100 rpm with considered cases are shown in Fig(s). 5.25- 5.28.

$$\%\sigma_{\hat{T}_e} = \sqrt{\frac{1}{n-1}\sum_{i=1}^{n}\left(\hat{T}_{ei} - \hat{T}_{emn}\right)^2} \times 100 \tag{5.26}$$

$$\hat{T}_{emn} = \frac{1}{n}\sum_{i=1}^{n}\hat{T}_{ei} \tag{5.27}$$

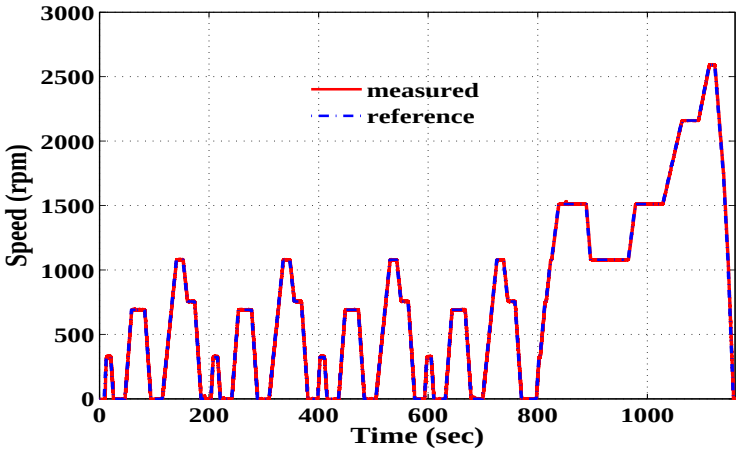

(a)

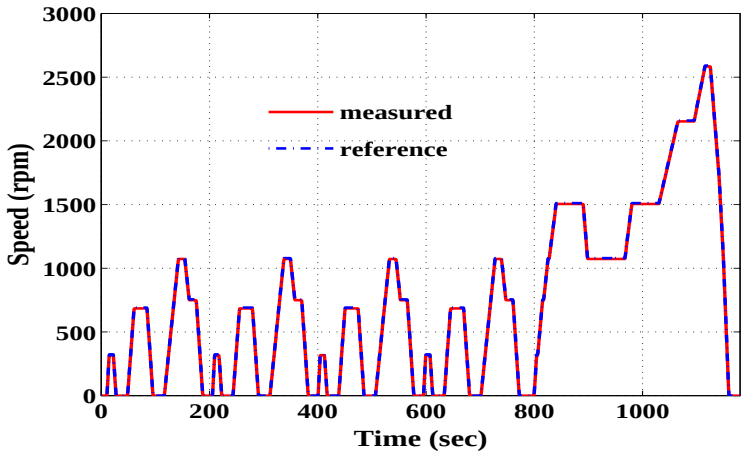

(b)

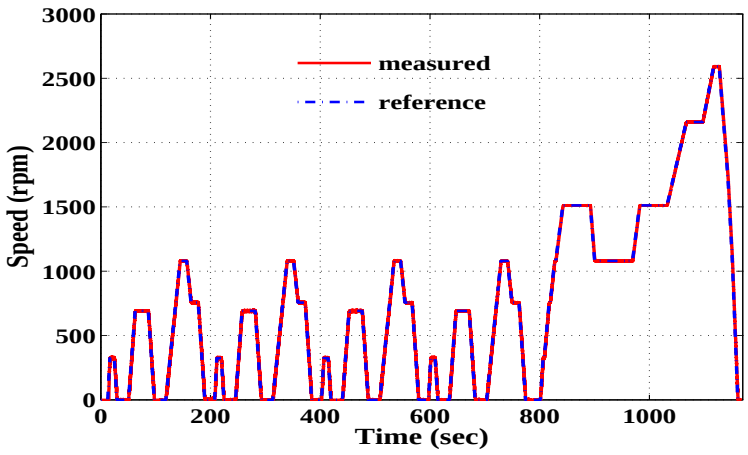

(c)

Fig. 5.21: Speed response for NEDC (a) Case I (b) Case II (c) Case III. Speed tracking is satisfactory for all the considered cases. The RMSE for Case I is 16.35, while for Cases II and III are 15.57 and 15.32, respectively.

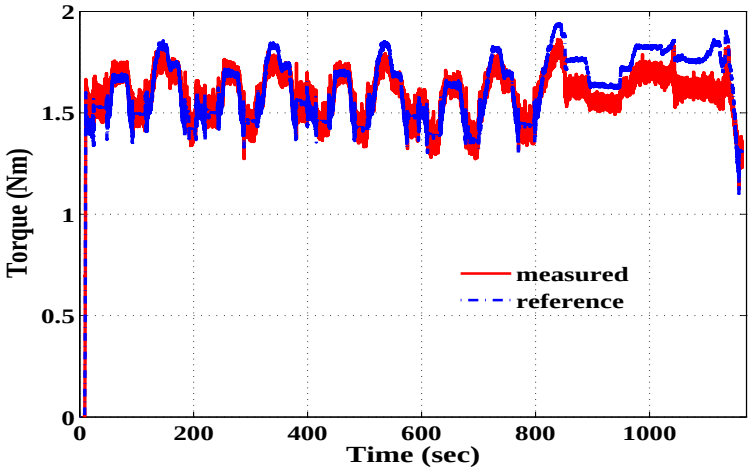

(a)

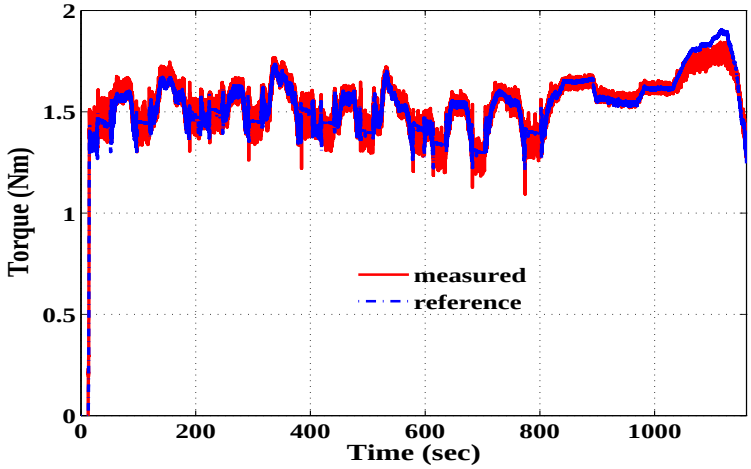

(b)

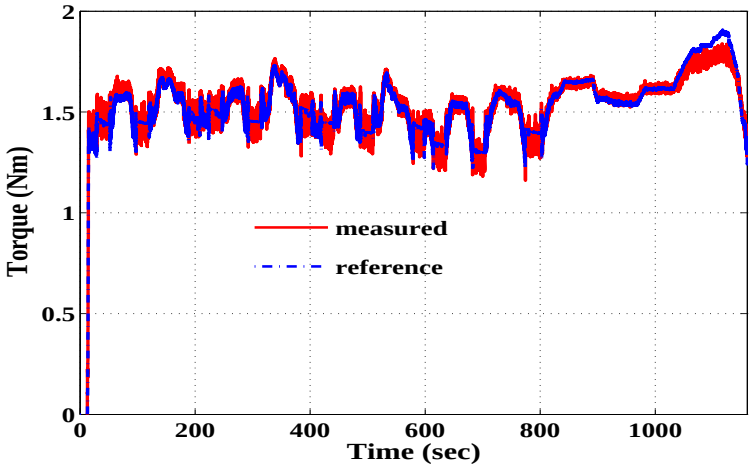

(c)

Fig. 5.22: Torque response for NEDC (a) Case I(b) Case II (c) Case III. Proper tracking of T_e^* is not possible with case I for a wide speed range. Torque response is satisfactory with cases II and III. The RMSEs for cases II and III are 0.06 and 0.04, respectively, while for the case I is 0.11.

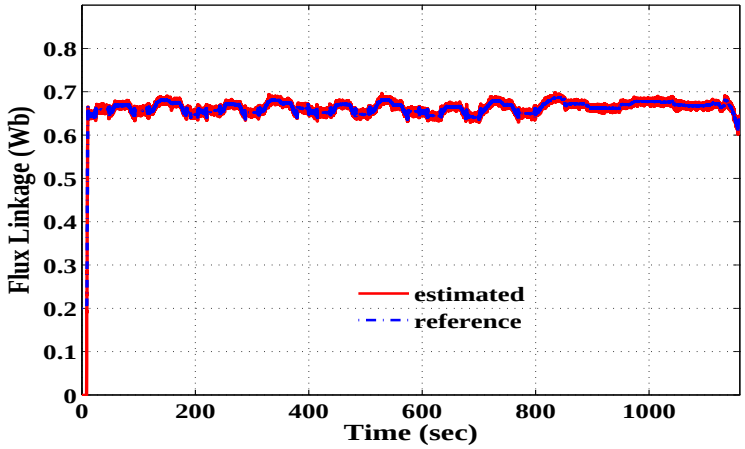

(a)

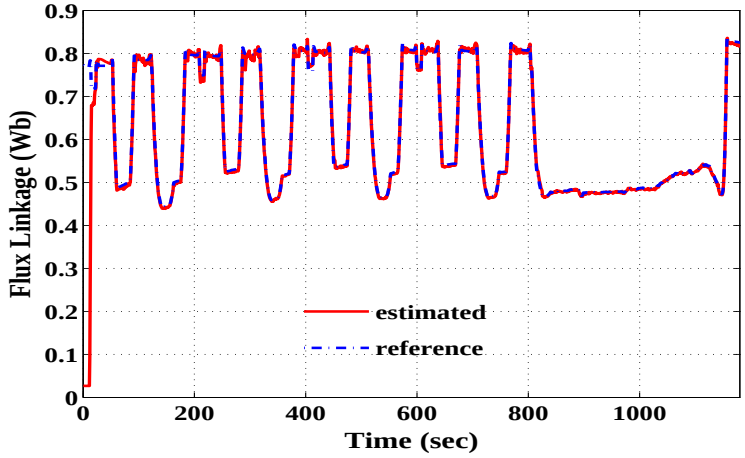

(b)

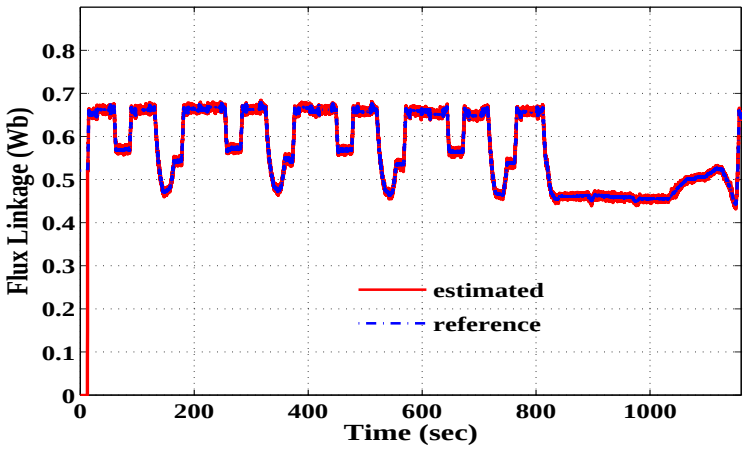

(c)

Fig. 5.23: Flux linkage response for NEDC (a) Case I (b) Case II (c) Case III. The RMSE for Case I is 0.10, while for cases II and III are 0.08 and 0.054, respectively.

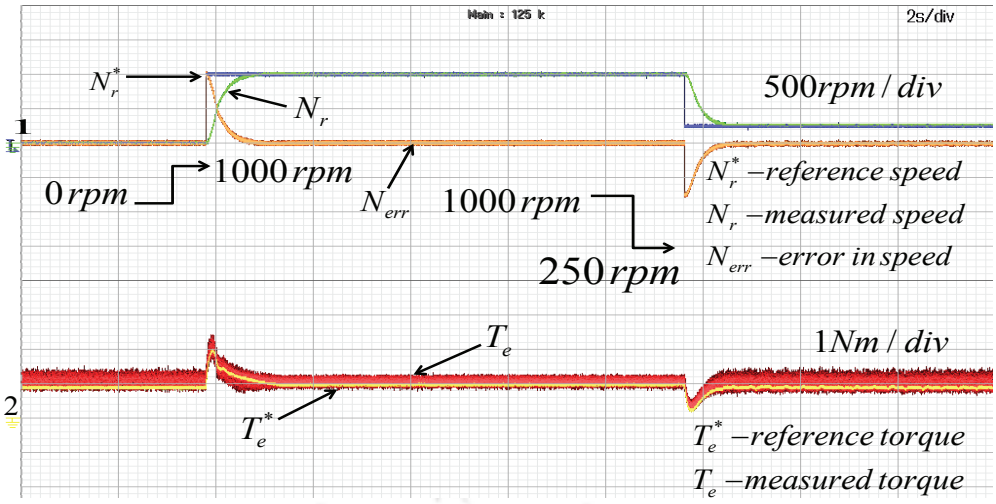

(a)

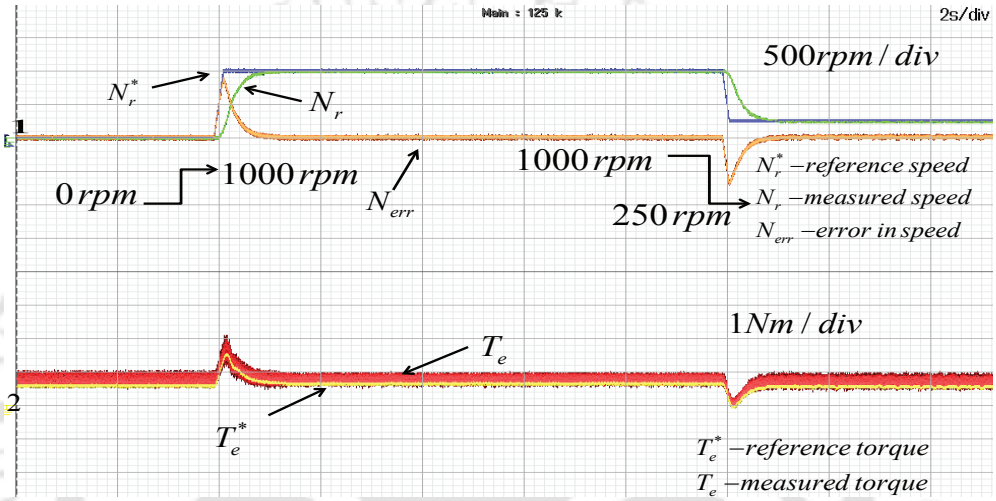

(b)

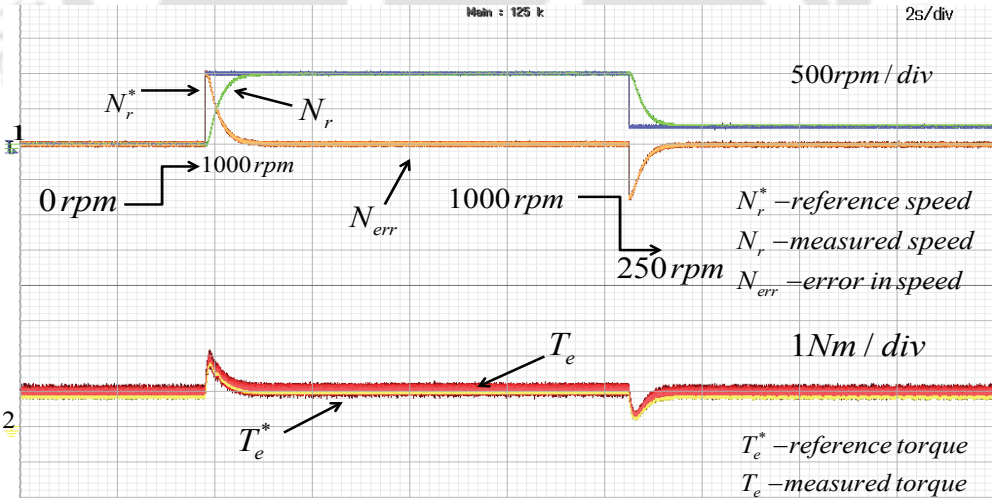

(c)

Fig. 5.24: Dynamic response with step change in speed (a) Case I (b) Case II (c) Case III.

$$\%X_{error} = \frac{Avg(X_{ref}) - Avg(X_{esti})}{Avg(X_{ref})} \times 100 \tag{5.28}$$

where $\hat{T}_{ei}$ is the actual sample, n represents sample's number, X represents flux linkage or torque used for the error calculations, Avg is an average value, ref is the reference value, and $esti$ is either estimated or measured value. The comparative analysis chart based on torque ripple expressed in % standard deviation (σT_e), % relative torque error (T_{err}), and % relative flux error (λ_{err}) over a wide speed range are shown in Table 5.18.

Table. 5.18: Comparative chart based on torque ripple expressed in standard deviation (σT_e), relative torque error (T_{err}) and relative flux error (λ_{err})

Torque ripple expressed in % standard deviation (σT_e)						
	100 rpm	500 rpm	1000 rpm	1500 rpm	2000 rpm	2500 rpm
Case I	7.66	7.02	6.69	6.79	6.90	3.70
Case II	6.89	5.51	3.83	3.80	2.87	2.43
Case III	6.01	5.31	3.97	3.37	2.77	2.26
% Relative torque error (T_{err})						
	100 rpm	500 rpm	1000 rpm	1500 rpm	2000 rpm	2500 rpm
Case I	11.47	7.10	2.50	3.32	4.14	2.49
Case II	8.12	7.96	1.85	1.40	1.09	0.52
Case III	7.73	6.64	1.81	1.37	0.93	0.47
% Relative flux error (λ_{err})						
	100 rpm	500 rpm	1000 rpm	1500 rpm	2000 rpm	2500 rpm
Case I	0.012	0.002	0.013	0.056	0.10	0.06
Case II	0.005	0.013	0.04	0.06	0.09	0.09
Case III	0.004	0.01	0.06	0.06	0.07	0.08

Fig. 5.29 shows the torque ripple expressed in % standard deviation (σT_e), % relative torque error (T_{err}) and % relative flux error (λ_{err}) for the considered cases. These observations show that the T_e and λ_s ripples with Case III have reduced compared to the case I and are improved compared to case II. Fig. 5.29 indicates that Case III provides improved performance. Further, consumption in input energy and efficiency analysis are explained for the considered cases over a wide speed and torque range and presented in the next section.

5.5.3 Energy consumption analysis

The consumption in input energy for the considered cases is determined using (5.29). For the determination of input energy consumption, the instantaneous inverter input voltage (V_{dc}) and current (I_{dc}) are recorded in dSPACE1103 wrt time. Table 5.19 shows the input energy consumptions in Watt-hour (Wh) at two different loads.

$$E_{in} = \sum (V_{dc} \times I_{dc} \times \Delta t) \tag{5.29}$$

Table. 5.19: Comparative analysis on input energy consumption in Wh at 2.0 Nm and at 2.5 Nm loads

Driving cycle	2.0 Nm Load					2.5 Nm Load				
	Case I	Case II	Case III	Energy-saving(%) in Case III		Case I	Case II	Case III	Energy- saving(%) in Case III	
				For Case I	For Case II				For Case I	For Case II
NYCC	51.30	50.96	49.50	3.51	2.87	59.61	57.82	55.72	6.52	3.63
NEDC	100.70	98.58	95.19	5.46	3.44	142.44	139.73	131.67	7.55	5.77

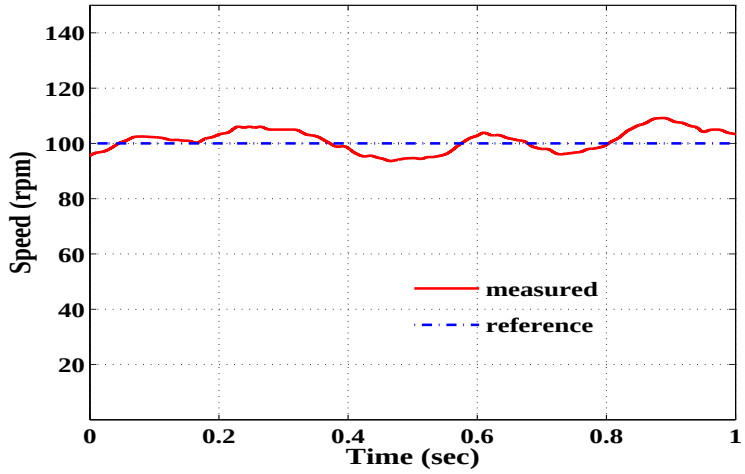

(a)

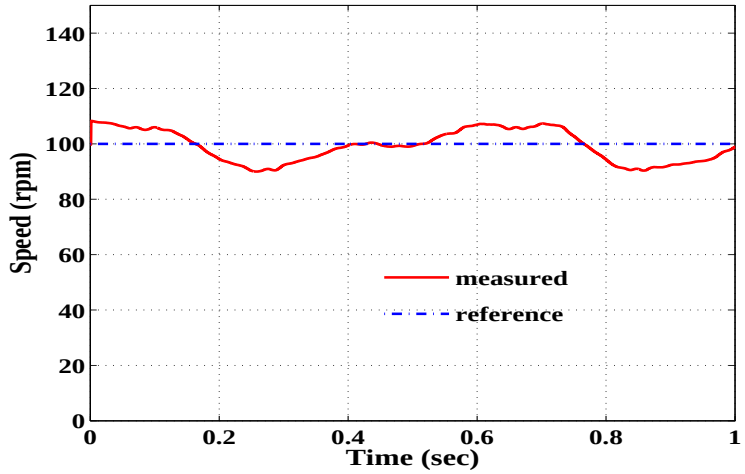

(b)

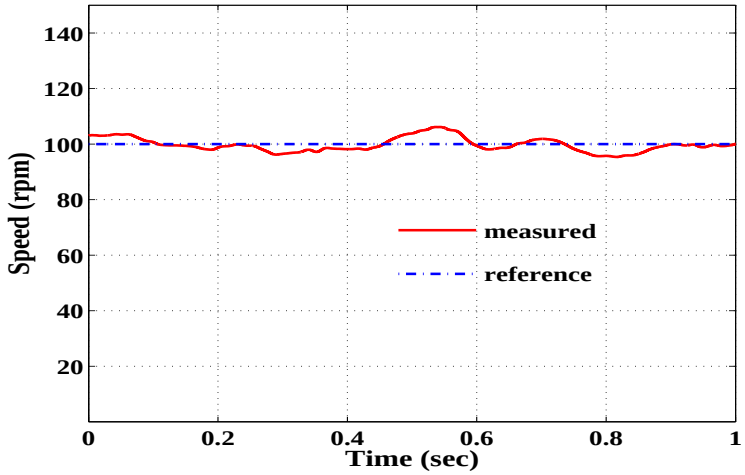

(c)

Fig. 5.25: Steady state speed response at 100 rpm (a) Case I (b) Case II (c) Case III.

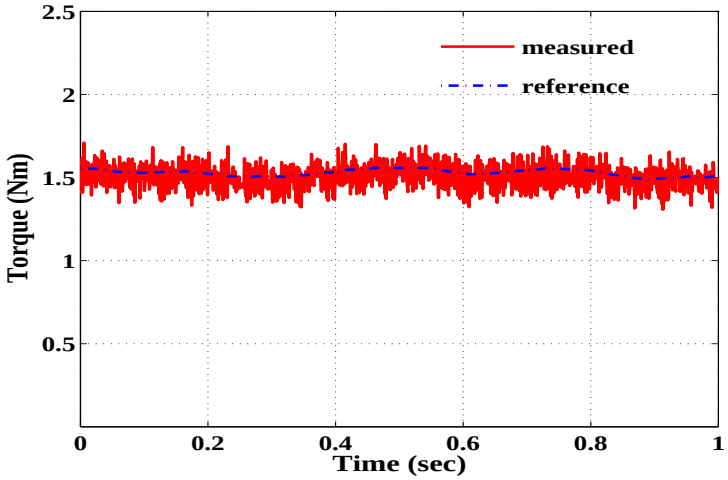

(a)

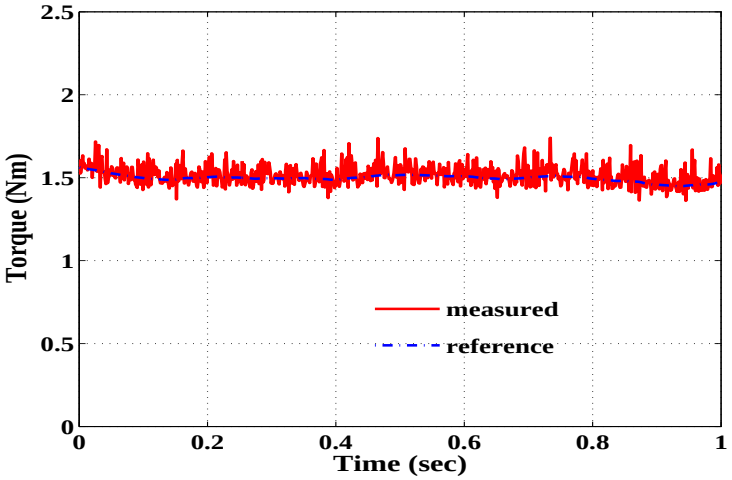

(b)

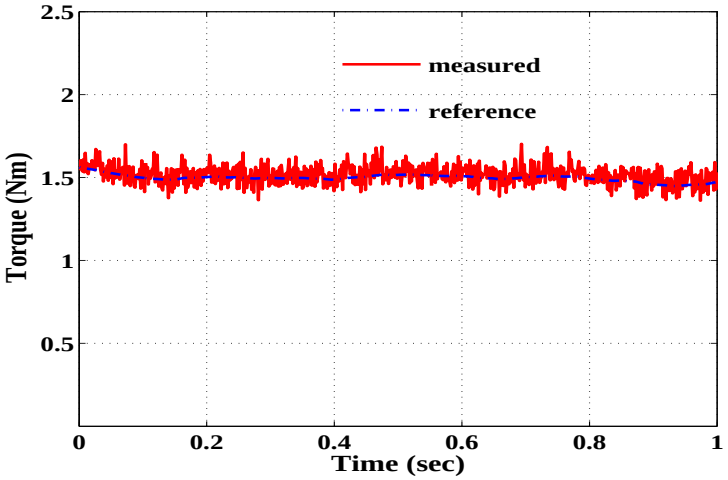

(c)

Fig. 5.26: Steady state torque response at 100 rpm (a) Case I (b) Case II (c) Case III. The % torque ripple (σT_e) in standard deviation with case III is 6.01%, while for cases I and II are 7.66% and 6.89%, respectively.

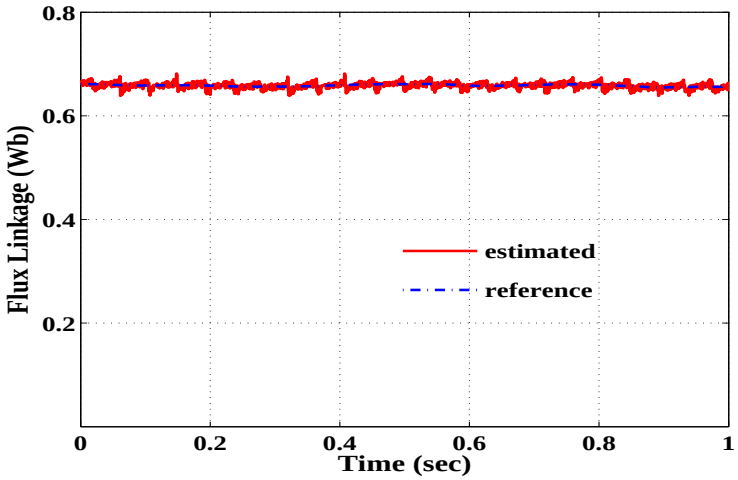

(a)

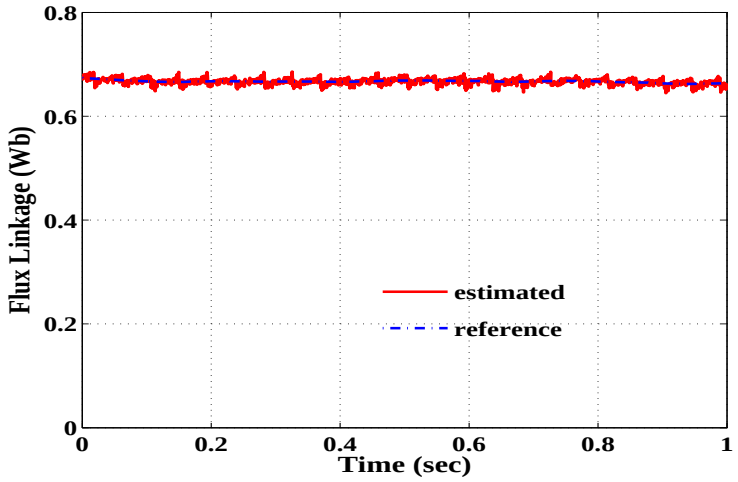

(b)

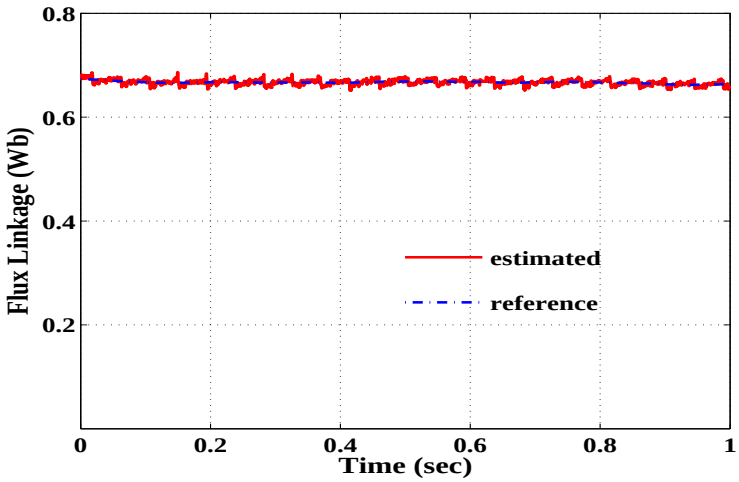

(c)

Fig. 5.27: Steady state flux linkage response at 100 rpm (a) Case I (b) Case II (c) Case III. The % relative flux error (λ_{err}) with case III is 0.0048%, while for cases I and II are 0.012% and 0.0059%, respectively.

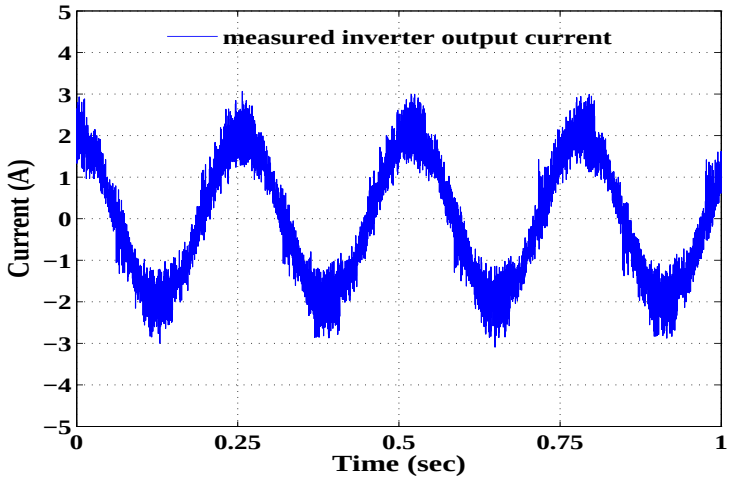

(a)

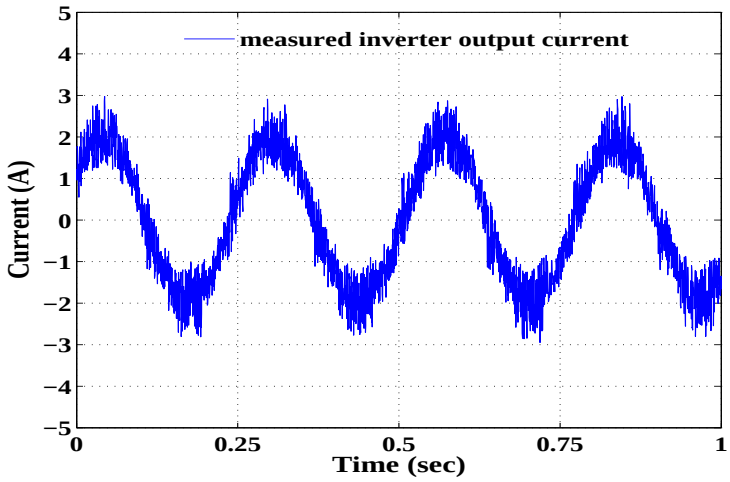

(b)

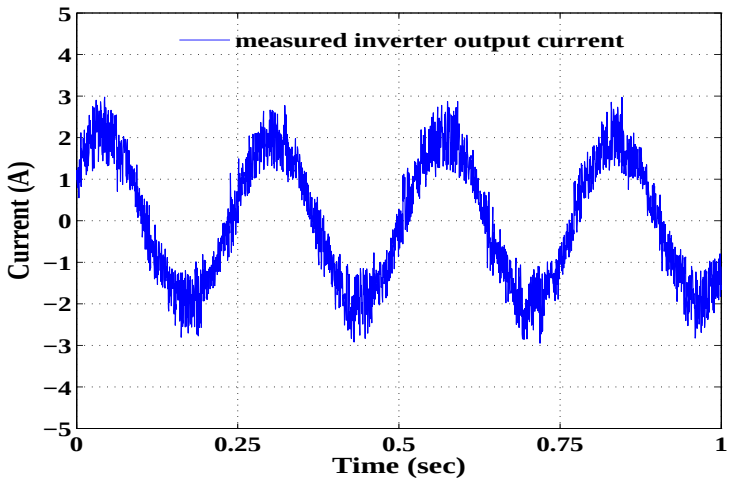

(c)

Fig. 5.28: Steady state current response at 100 rpm (a) Case I (b) Case II (c) Case III.

The % saving in input energy consumption wrt case III for the two driving cycles are listed in

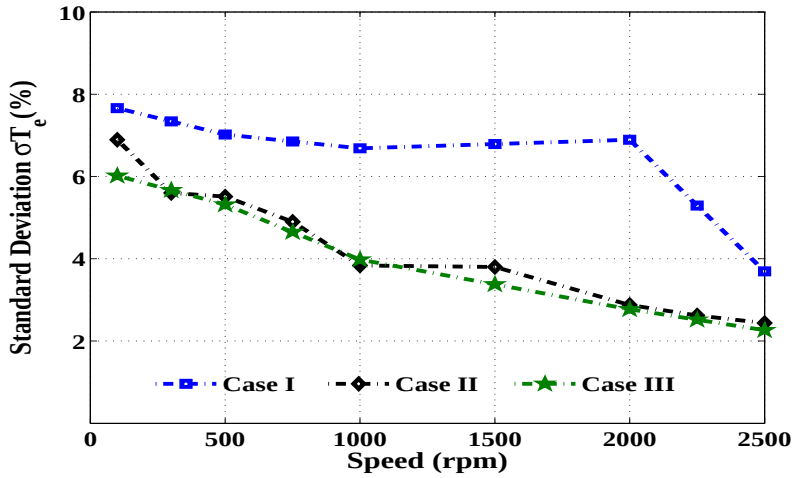

(a)

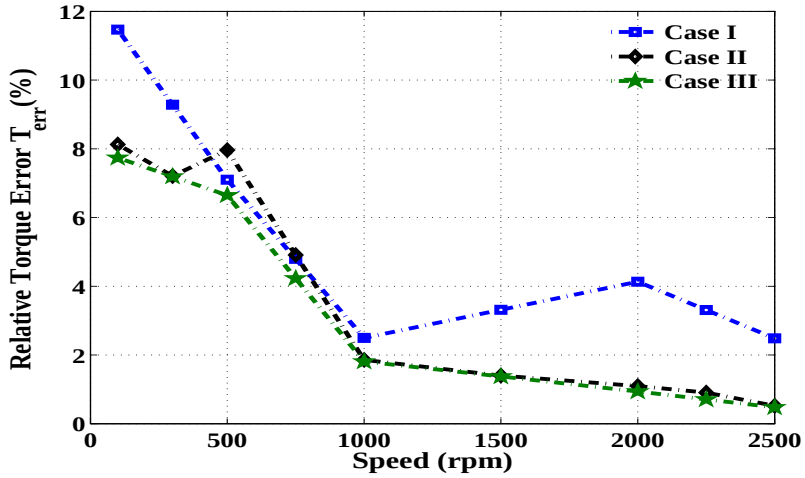

(b)

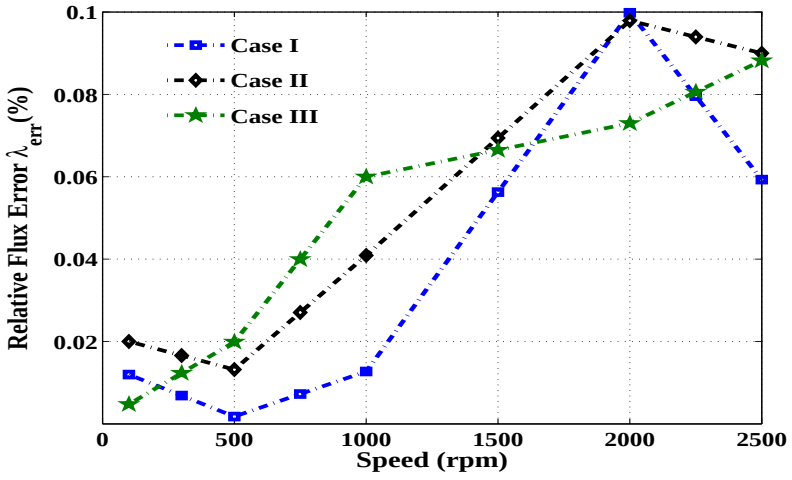

(c)

Fig. 5.29: Performance analysis at 1.5 Nm load torque (a) Torque ripple (σT_e) (b) Torque error (T_{err}) (c) Flux error (λ_{err}).

Table 5.19, and is calculated using (5.30).

$$Energy\ saving(\%) = \left(\frac{E_{in,i} - E_{in,3}}{E_{in,i}}\right) * 100 \tag{5.30}$$

where $E_{in,i}$ is the input energy consumption with i represents for different cases, and $E_{in,3}$ is consumption of input energy in case III.

The comparative analysis listed in Table 5.19 shows that case III possesses the lowest consumption of input energy compared to cases I and II. A significant savings of energy (5.46 % for 2.0 Nm load and 7.55 % for 2.5 Nm load) are achieved in case III for NEDC compared to the other cases. Besides, the percentage of energy-saving has improved in Case III as compared to Case II. The reduction in consumption of the input energy establishes the accuracy of the proposed technique.

Further, multiple sets of experiments are conducted in the laboratory to analyze the said cases' efficiency performance and briefly discussed in the next subsequent section.

5.5.4 Efficiency analysis

The efficiency analysis for the said cases is inspected with wide operating speeds and at different load torques. These efficiencies are calculated using instantaneous values of input and output powers over a period. The instantaneous values of inverter input power are calculated by measuring V_{dc} and I_{dc} at their respective node points using a differential voltage probe (YOKOGAWA-700924) and the current probe (YOKOGAWA-701933). The motor's output power is obtained by measuring the shaft torque and speed using the KISTLER-4503B/CoMo-4700 torque sensor. The technical details of the used differential probe, current probe, and torque sensor are given in Appendix A.4.

The comparative analysis on the efficiency over the wide speed range and varying load torque for the considered cases is presented in Table 5.20. The efficiency maps provide more insight information for a wide operating range. These efficiency maps are calculated for speed variations from 100 rpm to 2000 rpm and load torque variations from 0.5 Nm to 2.5 Nm. The evaluated efficiency maps are shown in Fig. 5.30. The observations show that case III yields a higher efficiency as compared to the case I. The efficiency improvement for Case III is primarily due to the minimum input power consumption for the fixed power output. Fig. 5.31 shows efficiency graphs with variations in speed and load torque. These observations confirm that the proposed method (case III, non-linear equivalent circuit approach) results in improved efficiency compared to case I. Moreover, the efficiencies obtained using Case II and Case III are quite similar.

From the presented results and observations, it is found that the proposed methods (case II and

Table. 5.20: Efficiency's comparative analysis chart over the wide speed range and varying load torque for the considered cases

% Efficiency at 100 rpm with varying load					
	0.5 Nm	1.0 Nm	1.5 Nm	2.0 Nm	2.5 Nm
Case I	16.76	20.17	22.58	23.97	25.45
Case II	19.69	22.91	26.06	26.58	28.67
Case III	20.16	23.40	24.80	26.43	28.02
% Efficiency at 2000 rpm with varying load					
	0.5 Nm	1.0 Nm	1.5 Nm	2.0 Nm	2.5 Nm
Case I	48.29	60.20	63.46	67.04	70.53
Case II	49.08	59.27	67.20	70.10	73.08
Case III	49.03	61.98	68.49	71.53	74.74
% Efficiency at 1 Nm over the wide speed range					
	100 rpm	500 rpm	1000 rpm	1500 rpm	2000 rpm
Case I	20.17	33.58	40.66	49.65	60.20
Case II	22.91	36.04	41.74	49.09	59.27
Case III	23.40	39.33	41.69	49.41	61.98
% Efficiency at 2.5 Nm over the wide speed range					
	100 rpm	500 rpm	1000 rpm	1500 rpm	2000 rpm
Case I	25.45	42.77	49.88	63.54	70.53
Case II	28.67	46.04	54.07	65.72	73.08
Case III	28.02	44.68	54.83	62.92	74.74

III) have comparatively no convergence issues. As they do not require the comprehensive calculation of λ_s^* at every instant (as calculated offline and stored in its LUT). They have fewer torque ripples. The proposed approaches are accepted for practical applications where the torque reference changes quickly (see Fig. 5.16). These methods also account for any operating condition described by motor torque and speed with minimal input energy consumption. Further, the method proposed in this chapter has an advantage over the method proposed in chapter-4. As the non-linear equivalent circuit approach does not need a pre-knowledge about the geometry of the motor, i.e., winding scheme, slot dimensions details and lamination designs to determine the accurate values of reference flux in the DTC algorithm.

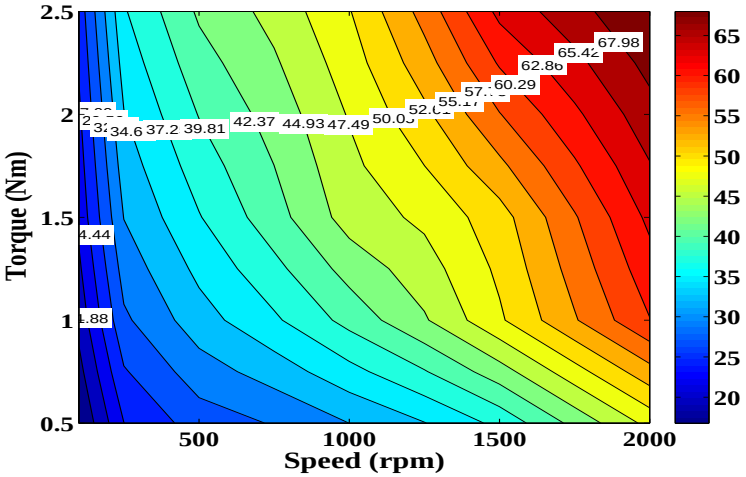

(a)

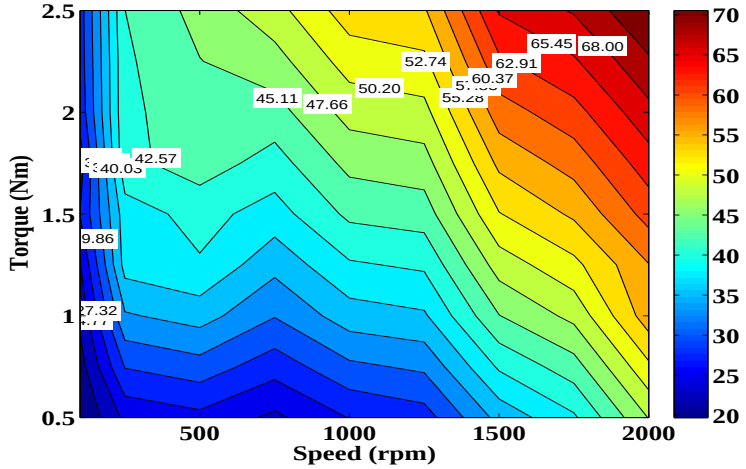

(b)

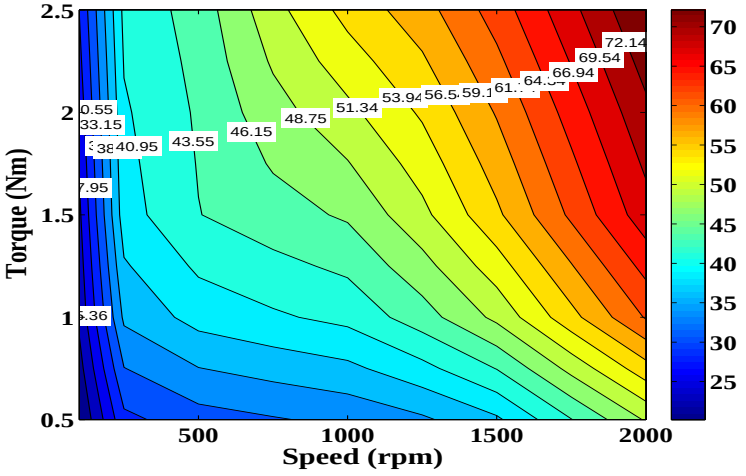

(c)

Fig. 5.30: Efficiency maps (a) Case I (b) Case II (c) Case III.

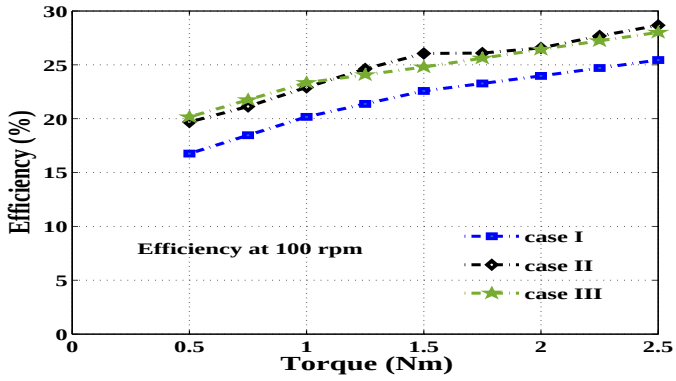

(a)

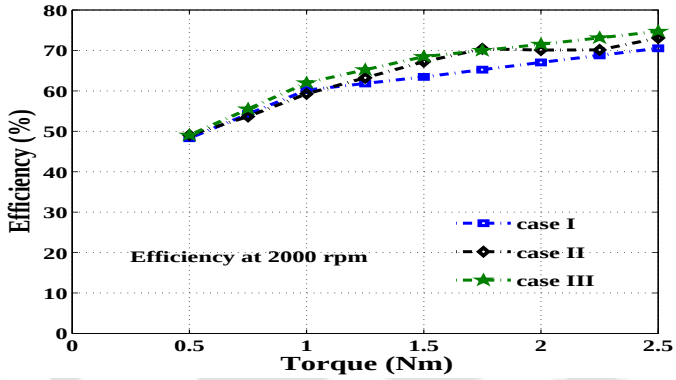

(b)

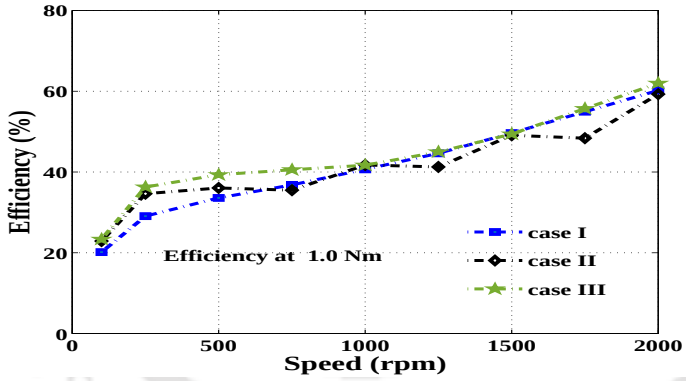

(c)

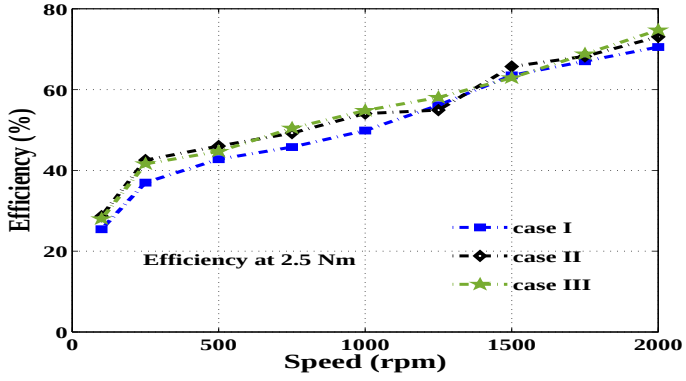

(d)

Fig. 5.31: Comparative efficiency analysis at (a) 100 rpm (b) 2000 rpm (c) 1.0 Nm (d) 2.5 Nm.

5.6 Conclusion

This chapter discusses the offline lookup table-based approach to determine the reference flux linkage of the DTC strategy for IM drive. The method uses a non-linear equivalent circuit model of IM to determine the suitable values of flux linkage. The non-linear model ensures that the effect of saturation is taken into account. A set of experiments are performed in the laboratory to obtain the magnetization curve of the IM. Further, the relation between the motor's magnetizing inductance and magnetizing current is established. Besides, the IEEE Standard (112 – 2017) no-load test and blocked rotor test are performed on the tested motor to obtain its equivalent circuit parameters. The obtained equivalent circuit with varying magnetizing inductance exhibits the non-linear model of IM.

The obtained non-linear equivalent circuit is solved with variations in applied stator voltage, rotor speed, and stator voltage frequency to get the accurate flux linkage values. The obtained flux linkage values are stored in the lookup table format and fed to the DTC algorithm as the reference flux linkage. The proposed technique ensures that the obtained flux linkage values in lookup table format give accurate information of reference flux at the required speed and given torque with dc voltage constraint. Thus proposed approach calculates reference flux linkage considering the reference speed, torque, and DC voltage. Further, to check the proposed method's effectiveness, it is compared with the loss model-based technique and FEA-based approach (presented in chapter-4), based on the tracking of speed, torque, and flux linkage with different vehicle driving cycles. The observations confirm that the proposed technique is suitable for dynamic speed range as the tracking of speed, torque, and flux linkage are satisfactory for the given vehicle driving cycles.

Further, the proposed technique is simple and does not require any complex mathematical equations to determine reference flux linkage values in lookup table format. It does not demand base speed calculation, which in general depends on the dc-link voltage, motor current, motor flux linkage, and machine parameters. The proposed method is least sensitive to variations in motor parameters. The dynamic and steady-state responses for the considered cases are demonstrated, and it is observed that the proposed approach has fewer torque ripples. Besides, it is found experimentally that the proposed technique yields improvement in the drive efficiency compared to the loss model-based technique and FEA-based approach, with minimal input energy consumption. The method presented in this chapter overcomes the drawback of the FEA-based approach proposed in chapter-4. However, this method requires intensive offline calculations to develop the lookup table for the reference flux linkage.

भारतीय प्रौद्योगिकी संस्थान गुवाहाटी
Indian Institute of Technology Guwahati

CHAPTER 6

CONCLUSIONS AND FUTURE WORK

6.1 Conclusions

The thesis's framework is based on implementing a low-cost and efficient DTC IM drive for EV applications. This work started with the choice of the control structure that is best suited to the EV application. Generally, for the high-performance control algorithms, the FOC scheme is widely employed. However, the FOC scheme has a complex control structure and requires coordinate transformation and pulse width modulator (PWM) signal generator. Therefore, an alternative strategy, the DTC scheme, is chosen because it is simple in structure and competence to provide a high dynamic response and does not demand any coordinate transformations and pulse width modulation (PWM) techniques. Moreover, for an efficient and low-cost drivetrain, the selection of EM is important as EM is one of the main subsystems of the EV drivetrains. In this work, the low-cost and rugged IM is preferred as an alternative to PM motor to drive the EV. Besides, the IM drives' efficiency can be improved in two ways; 1) by changing the motor geometry and material, 2) by incorporating the optimal reference flux (stator or rotor) selection method in the used control scheme, which reduces the motor losses. In this thesis work, the two approaches are proposed for the selection of suitable λ_s^*:

1. Determination of λ_s^* using a Finite Element Analysis (FEA) based IM model.
2. Determination of λ_s^* using a non-linear equivalent circuit model of IM.

For the implementation of the DTC algorithm for an IM, it is required to understand the dynamic model of IM subjected to control. Therefore, in this thesis, chapter-2 covers the mathematical modeling of IM and the vector control schemes. The DTC scheme is used in this work due to its advantage over another control scheme (FOC). Besides the advantages of DTC, it has some drawbacks, and one of them's the selection of λ_s^*. It is found that the value of λ_s^* significantly impacts the DTC perfor-

mance and plays an important role in improving the efficiency of the drivetrain. Hence, in this thesis, chapter-3 focused mainly on the impact of variable λ_s^* on DTC-based IM drive performance.

In chapter-3, a detailed analysis has been presented to explain the effects of variable λ_s on the motor's behavior. Besides, this chapter focussed on the DTC scheme with variable λ_s^*. It is observed that a variable λ_s^* is desirable in the DTC scheme for a wide range of speed and torque. Further, a brief explanation of methods for determining the λ_s^* in context to the DTC scheme is presented. Finally, based on the determination methods of λ_s^*, the detailed discussion on its limitations in context to EV applications are summarized. The selection of optimal λ_s^* is critical and has a substantial impact on IM drive performance for EV applications over a wide range of operations and the efficiency improvement of the EV drivetrain. It is found that there is no generalized accepted method for determining the reference flux linkage. Thus, the determination of optimal λ_s^* is one of the challenging issues in DTC of IM for a wide range of operations and variable load conditions. Based on this chapter's finding, the determination methods of λ_s^* are proposed for DTC-based IM drive over a wide range of operations and are explained in the next subsequent chapters.

In chapter-4, an offline LUT based approach to determine the λ_s^* of the DTC strategy for IM drive is presented. The method proposed in this chapter uses the FEA-based IM model to calculate suitable values of flux linkages. The FEA model ensures that the effect of magnetic saturation is taken into account. The multiple sets of FEA simulations are carried out to obtain the accurate values of flux linkage. The obtained flux linkage values are stored in LUT format and fed to the DTC algorithm as reference flux. The proposed approach ensures that the obtained flux linkage values in LUT format gives accurate information of λ_s^* at the required speed and given torque with dc voltage constraint. Moreover, the proposed approach calculates λ_s^* considering the reference speed, torque, and DC source voltage. Further, to check the robustness of the proposed method, it is compared with the existing conventional technique and variable flux approach. The comparison is based on tracking speed, torque, and flux for different vehicle driving cycles. The observation shows that the proposed method is less sensitive to the motor's parameter variation, such as stator resistance and leakage inductance, and magnetization inductance. The experimental observations show that the proposed method yields improvement in drive efficiency with minimal input energy consumption. The proposed method is made acceptable for EV application with few modifications in the DTC algorithm. This chapter's work contributed towards the publication in SCI journal listed in the list of publications, serial number-4.

However, this method proposed in chapter-4 required a pre-knowledge about the geometry of the motor, i.e., winding scheme, slot dimensions details, and lamination designs, to develop an FEA model of IM, which helps to obtain accurate values of reference flux and maximum torque in LUTs format. This limitation is overthrown if a non-linear equivalent circuit model of IM will be developed and used. Therefore, the determination of reference flux linkage using a non-linear equivalent circuit model of IM is developed and discussed in the next chapter.

The chapter-5 discussed the non-linear equivalent circuit model approach to determine the λ_s^* of the DTC strategy for IM drive. The method proposed in this chapter uses a non-linear equivalent circuit model of IM to determine the suitable values of flux linkage. The non-linear model ensures that the effect of saturation is taken into account. A set of experiments are performed in the laboratory to obtain the magnetization curve of the IM. Further, the relation between the motor's magnetizing inductance and magnetizing current is established. Besides, the IEEE Standard (112 – 2017) no-load and blocked rotor tests are performed on the tested motor to obtain its equivalent circuit parameters. The obtained equivalent circuit with varying magnetizing inductance exhibits the non-linear model of IM. The obtained non-linear equivalent circuit is solved with variations in applied stator voltage, rotor speed, and stator voltage frequency to get the accurate flux linkage values. The obtained flux linkage values are stored in the LUT format and fed to the DTC algorithm as the reference flux linkage. The proposed technique ensures that the obtained flux linkage values in LUT format give accurate information of reference flux at the required speed and given torque with dc voltage constraint. The proposed approach calculates reference flux linkage considering the reference speed, torque, and DC voltage. Further, to check the proposed method's effectiveness, it is compared with the loss model-based technique and FEA-based approach (presented in chapter-4), based on tracking speed, torque, and flux linkage with different vehicle driving cycles. The observations confirm that the proposed technique is suitable for dynamic speed range as the tracking of speed, torque, and flux linkage are satisfactory for the given vehicle driving cycles. This chapter's work contributed towards the publication in SCI journal listed in the list of publications, serial number-1.

Moreover, the technique proposed in chapter-5 is simple and does not require any complex mathematical equations to determine λ_s^* values in LUT format. It does not demand base speed calculation, which in general depends on the dc-link voltage, motor current, motor flux linkage, and machine parameters. The proposed method is least sensitive to variations in motor parameters. The dynamic and steady-state responses for the considered cases are demonstrated, and it is observed that the proposed approach has fewer torque ripples. Besides, it is found experimentally that the proposed

technique yields improvement in the drive efficiency compared to the loss model-based technique and FEA-based approach, with minimal input energy consumption. The method presented in this chapter overcomes the drawback of the FEA-based approach proposed in chapter-4.

6.2 Scope for Future Work

The thesis aims to design, develop, and implement a speed control DTC-based IM drive that can operate for a wide speed range and stable at various operating modes. For the fulfillment of these objectives, few design methods are presented and discussed. Some of the issues that have not addressed in this thesis and may be the subject of future research are listed below:

- Inverter nonlinearities are ignored in this thesis work. One can use techniques to introduce nonlinearity compensation for the proper voltage signals' estimation.
- Further different inverter topologies can be used with the proposed design.
- The regenerative braking can be one of the perspectives for further extension in this work. A setup can be developed to implement a control strategy with electrical braking over a wide range of operations.
- With the proposed design, a drivetrain configuration for a small passenger car can be developed and prototyped for testing on the actual road driving conditions scenario.
- Different DC-DC converter topologies can be further studied and examined as the extension of the proposed design for efficiency and overall performance improvement.

LIST OF PUBLICATIONS

Journal Publications

1. **Singh, A.**,Prabhakar, K., Reddy, U., and Kumar, P., "A Lookup Table-Based Reference Flux Linkage Selection of Direct Torque Control Induction Motor Drive for Electric Vehicle Applications: An Offline Strategy," SAE Int. J. Alt. Power, 9(1):2020, doi:10.4271/08-09-01-0005.
2. K. K. Prabhakar, C. U. Reddy, **A. K. Singh** and P. Kumar, "A New Reference Flux Linkage Selection Technique for Efficiency Improvement of Direct Torque Controlled IM Drive," in IEEE Journal of Emerging and Selected Topics in Power Electronics, 2020, DOI 10.1109/JESTPE.2020.2979235.
3. Prabhakar, K., Reddy, U., **Singh, A.**, and Kumar, P., "System Performance Comparison of Direct Torque Control Strategies Based on Flux Linkage and DC-Link Voltage for EV Drivetrains," SAE Int. J. Alt. Power, 8(2):103118, 2019, doi:10.4271/08-08-02-0007.
4. **Singh, A.**, Reddy, U., Prabhakar, K., and Kumar, P., "Selection of Reference Flux Linkage for Direct Torque Control Based Induction Motor Drive in Electric Vehicles Applications," SAE Int. J. Alt. Power, 8(1):2019, doi:10.4271/08-08-01-0001.
5. C. U. Reddy, K. K. Prabhakar, **A. K. Singh** and P. Kumar, "Speed Estimation Technique Using Modified Stator Current Error Based MRAS for Direct Torque Controlled Induction Motor Drives," in IEEE Journal of Emerging and Selected Topics in Power Electronics, 2019, DOI: 10.1109/JESTPE.2019.2901523.
6. C. Upendra Reddy; Prabhakar, Kashyap; **Singh, Amit Kumar**; Kumar, Praveen: "Direct Torque Control Induction Motor Drive Performance Evaluation Based on Torque Error Status Selection Methods," IET Electrical Systems in Transportation, 2019, DOI: 10.1049/iet-est.2018.5005.
7. K. Prabhakar, U. R. Chinthakunta, **A. K. Singh** and P. Kumar, "Efficiency and performance analysis of DTC-based IM drivetrain using variable dc-link voltage for electric vehicle applications," in IET Electrical Systems in Transportation, vol. 8, no. 3, pp. 205-214, 9, 2018,

DOI: 10.1049/iet-est.2017.0086.

Conference Publications

1. C. U. Reddy, K. K. Prabhakar, **A. K. Singh** and P. Kumar, “Performance evaluation of DTC IM drive for an EV application,” 2017 IEEE Power and Energy Society General Meeting, Chicago, IL, 2017, pp. 1-5.
2. K. K. Prabhakar, C. U. Reddy, **A. K. Singh** and P. Kumar, “Inverter switching frequency prediction in DTC of induction motor drive for an EV drivetrain,” 2017 IEEE Power and Energy Society General Meeting, Chicago, IL, 2017, pp. 1-4.
3. C Upendra Reddy, Kashyap Kumar Prabhakar, **Amit Kumar Singh** and Praveen Kumar, “Flux estimation in DTC for wide speed range,” 2016 IEEE Power and Energy Society General Meeting (PESGM), Boston, MA, 2016, pp. 1-5. doi: 10.1109/PESGM.2016.7741637.
4. K. K. Prabhakar, M. Ramesh, A. Dalal, C. U. Reddy, **A. K. Singh** and P. Kumar, “Efficiency investigation for electric vehicle powertrain with variable DC-link bus voltage,” IECON 2016 - 42nd Annual Conference of the IEEE Industrial Electronics Society, Florence, Italy, 2016, pp. 1796-1801.
5. **A. K. Singh**, P. Kumar, C. U. Reddy and K. Prabhakar, “Simulation of direct torque control of induction motor using Simulink, simplorer and maxwell software,” 2015 IEEE International Transportation Electrification Conference (ITEC), Chennai, India, 2015, pp. 1-6.
6. **A. K. Singh**, C. U. Reddy, K. K. Prabhakar and P. Kumar, “FPGA implementation of direct torque control of induction motor with reduced ripples in torque and flux,” 2015 IEEE International Transportation Electrification Conference (ITEC), Chennai, India, 2015, pp. 1-8.
7. **Singh, A.K.**; Dalal, A.; Roy, R.; Kumar, P., ”Improved dynamic model of induction motor including the effects of saturation,” 2014 IEEE International Conference on Power Electronics, Drives and Energy Systems (PEDES), Mumbai, India, 2014, pp.1-5.
8. **Singh, A.K.**; Dalal, A.; Kumar, P., ”Analysis of induction motor for electric vehicle application based on drive cycle analysis,” 2014 IEEE International Conference on Power Electronics, Drives and Energy Systems (PEDES), Mumbai, India, 2014, pp.1-6.
9. K. K. Prabhakar, **A. K. Singh**, C. U. Reddy and P. Kumar, “Drive system for electric vehicle power train application using DC to AC matrix converter,” 2014 IEEE International Conference on Power Electronics, Drives and Energy Systems (PEDES), Mumbai, India, 2014, pp.

1-4.

10. Ansari, M.N.; **Singh, A.K.**; Kumar, P., ”Performance analysis of a hybrid dual rotor motor for electric vehicle application,” 2012 XXth International Conference on Electrical Machines (ICEM), Marseille, France, 2012, pp.2002-2007.

भारतीय प्रौद्योगिकी संस्थान गुवाहाटी
Indian Institute of Technology Guwahati

APPENDIX A

APPENDIX

A.1 Proposed Lookup Tables

A.1.1 FEA Based Lookup Table For Flux Linkage

The FEA-based lookup table for flux linkage proposed in chapter-4 is listed in this section. The complete lookup table is ranging from 0 rpm to 2850 rpm. Due to page-width constraints, the lookup table is listed in subsections as shown below.

Table. A.1.1: FEA based lookup table for flux linkage upto 950 rpm

$N_r\ (rpm)/$ $T_e\ (Nm)$	0 rpm	50 rpm	100 rpm	150 rpm	200 rpm	250 rpm	300 rpm	350 rpm	400 rpm	450 rpm	500 rpm	550 rpm	600 rpm	650 rpm	700 rpm	750 rpm	800 rpm	850 rpm	900 rpm	950 rpm
0.1 Nm	0.148	0.148	0.148	0.148	0.148	0.148	0.148	0.148	0.148	0.148	0.148	0.146	0.141	0.135	0.129	0.124	0.118	0.114	0.110	0.107
0.2 Nm	0.218	0.218	0.218	0.218	0.218	0.218	0.218	0.218	0.218	0.218	0.218	0.215	0.207	0.198	0.189	0.183	0.175	0.169	0.164	0.160
0.3 Nm	0.299	0.299	0.299	0.299	0.299	0.299	0.299	0.299	0.299	0.299	0.299	0.289	0.279	0.267	0.256	0.247	0.237	0.228	0.221	0.215
0.4 Nm	0.314	0.314	0.314	0.314	0.314	0.314	0.314	0.314	0.314	0.314	0.314	0.310	0.298	0.284	0.271	0.260	0.248	0.237	0.229	0.222
0.5 Nm	0.349	0.349	0.349	0.349	0.349	0.349	0.349	0.349	0.349	0.349	0.349	0.344	0.331	0.316	0.301	0.289	0.276	0.264	0.255	0.248
0.6 Nm	0.382	0.382	0.382	0.382	0.382	0.382	0.382	0.382	0.382	0.382	0.377	0.363	0.346	0.329	0.317	0.303	0.290	0.280	0.273	0.268
0.7 Nm	0.451	0.451	0.451	0.451	0.451	0.451	0.451	0.451	0.451	0.451	0.451	0.432	0.416	0.398	0.380	0.372	0.366	0.351	0.338	0.327
0.8 Nm	0.464	0.464	0.464	0.464	0.464	0.464	0.464	0.464	0.464	0.464	0.464	0.439	0.422	0.403	0.384	0.376	0.370	0.355	0.342	0.331
0.9 Nm	0.475	0.475	0.475	0.475	0.475	0.475	0.475	0.475	0.475	0.475	0.475	0.468	0.450	0.429	0.408	0.392	0.374	0.359	0.346	0.337
1.0 Nm	0.506	0.506	0.506	0.506	0.506	0.506	0.506	0.506	0.506	0.506	0.506	0.496	0.476	0.454	0.432	0.414	0.395	0.379	0.366	0.356
1.1 Nm	0.537	0.537	0.537	0.537	0.537	0.537	0.537	0.537	0.537	0.537	0.537	0.523	0.501	0.477	0.454	0.436	0.416	0.410	0.408	0.404
1.5 Nm	0.719	0.719	0.719	0.719	0.719	0.719	0.719	0.719	0.719	0.719	0.719	0.689	0.666	0.623	0.586	0.556	0.532	0.513	0.498	0.488

Table. A.1.2: FEA based lookup table for flux linkage from 1000 rpm to 1950 rpm

$N_r\ (rpm)/$ $T_e\ (Nm)$	1000 rpm	1050 rpm	1100 rpm	1150 rpm	1200 rpm	1250 rpm	1300 rpm	1350 rpm	1400 rpm	1450 rpm	1500 rpm	1550 rpm	1600 rpm	1650 rpm	1700 rpm	1750 rpm	1800 rpm	1850 rpm	1900 rpm	1950 rpm
0.1 Nm	0.105	0.103	0.102	0.102	0.101	0.101	0.100	0.100	0.099	0.097	0.096	0.096	0.095	0.094	0.094	0.093	0.093	0.092	0.091	0.091
0.2 Nm	0.157	0.155	0.154	0.153	0.152	0.152	0.151	0.150	0.148	0.146	0.144	0.142	0.141	0.140	0.138	0.137	0.135	0.134	0.132	0.130
0.3 Nm	0.209	0.195	0.193	0.191	0.190	0.189	0.188	0.186	0.184	0.181	0.179	0.171	0.170	0.168	0.166	0.165	0.164	0.162	0.160	0.159
0.4 Nm	0.218	0.214	0.212	0.210	0.209	0.208	0.207	0.205	0.203	0.200	0.198	0.196	0.194	0.193	0.191	0.190	0.188	0.187	0.185	0.183
0.5 Nm	0.243	0.240	0.237	0.236	0.234	0.233	0.232	0.230	0.227	0.224	0.222	0.220	0.218	0.216	0.214	0.213	0.211	0.209	0.207	0.205
0.6 Nm	0.264	0.261	0.259	0.258	0.257	0.255	0.253	0.250	0.247	0.244	0.241	0.239	0.237	0.235	0.233	0.231	0.229	0.227	0.224	0.222
0.7 Nm	0.319	0.313	0.294	0.291	0.290	0.286	0.285	0.285	0.274	0.279	0.275	0.272	0.270	0.268	0.265	0.263	0.261	0.259	0.256	0.254
0.8 Nm	0.323	0.317	0.303	0.301	0.299	0.298	0.296	0.293	0.290	0.286	0.282	0.279	0.277	0.274	0.272	0.270	0.268	0.265	0.262	0.259
0.9 Nm	0.330	0.325	0.322	0.319	0.318	0.316	0.314	0.311	0.307	0.303	0.299	0.296	0.293	0.291	0.289	0.286	0.284	0.281	0.278	0.275
1.0 Nm	0.349	0.343	0.340	0.337	0.335	0.333	0.331	0.328	0.324	0.320	0.316	0.312	0.309	0.307	0.304	0.302	0.299	0.297	0.294	0.290
1.1 Nm	0.401	0.398	0.385	0.374	0.366	0.361	0.357	0.354	0.352	0.350	0.348	0.345	0.340	0.336	0.332	0.328	0.325	0.322	0.319	0.317
1.5 Nm	0.482	0.441	0.436	0.433	0.431	0.429	0.426	0.423	0.418	0.415	0.412	0.407	0.403	0.400	0.397	0.392	0.388	0.384	0.380	0.376

Table. A.1.3: FEA based lookup table for flux linkage from 2000 rpm to 2850 rpm

$N_r\ (rpm)/$ $T_e\ (Nm)$	2000 rpm	2050 rpm	2100 rpm	2150 rpm	2200 rpm	2250 rpm	2300 rpm	2350 rpm	2400 rpm	2450 rpm	2500 rpm	2550 rpm	2600 rpm	2650 rpm	2700 rpm	2750 rpm	2800 rpm	2850 rpm
0.1 Nm	0.090	0.089	0.089	0.088	0.087	0.087	0.087	0.086	0.086	0.085	0.085	0.084	0.084	0.084	0.083	0.083	0.082	0.081
0.2 Nm	0.128	0.126	0.124	0.123	0.122	0.121	0.120	0.119	0.119	0.118	0.118	0.117	0.117	0.116	0.116	0.115	0.115	0.114
0.3 Nm	0.158	0.156	0.156	0.155	0.154	0.154	0.152	0.152	0.151	0.150	0.149	0.148	0.146	0.145	0.143	0.142	0.141	0.140
0.4 Nm	0.181	0.179	0.177	0.176	0.176	0.173	0.172	0.171	0.171	0.169	0.168	0.168	0.166	0.166	0.165	0.164	0.163	0.161
0.5 Nm	0.202	0.200	0.197	0.195	0.193	0.192	0.190	0.189	0.189	0.188	0.187	0.187	0.186	0.186	0.185	0.183	0.182	0.180
0.6 Nm	0.219	0.216	0.214	0.212	0.210	0.209	0.208	0.207	0.205	0.205	0.204	0.204	0.203	0.203	0.202	0.201	0.199	0.198
0.7 Nm	0.250	0.247	0.245	0.242	0.240	0.239	0.236	0.233	0.231	0.231	0.228	0.225	0.222	0.220	0.219	0.217	0.215	0.213
0.8 Nm	0.256	0.253	0.250	0.247	0.245	0.245	0.243	0.241	0.241	0.240	0.240	0.238	0.237	0.236	0.234	0.232	0.230	0.228
0.9 Nm	0.272	0.268	0.265	0.265	0.262	0.262	0.260	0.259	0.258	0.256	0.254	0.252	0.252	0.250	0.248	0.246	0.244	0.242
1.0 Nm	0.286	0.286	0.283	0.283	0.279	0.279	0.276	0.276	0.274	0.274	0.272	0.270	0.268	0.266	0.262	0.260	0.257	0.255
1.1 Nm	0.314	0.311	0.308	0.306	0.304	0.302	0.300	0.297	0.293	0.290	0.287	0.285	0.283	0.280	0.274	0.272	0.270	0.268
1.5 Nm	0.373	0.368	0.364	0.359	0.354	0.349	0.345	0.341	0.338	0.335	0.328	0.326	0.323	0.322	0.321	0.319	0.316	0.313

A.1.2 FEA Based Lookup Table For Torque

The FEA-based lookup table for torque proposed in chapter-4 is listed in this section. The complete lookup table is ranging from 0 rpm to 2850 rpm. Due to page-width constraints, the lookup table is listed in subsections as shown below.

Table. A.1.4: FEA based lookup table for torque upto 950 rpm

$N_r\ (rpm)/$ $V_{as}\ (V)$	0 rpm	50 rpm	100 rpm	150 rpm	200 rpm	250 rpm	300 rpm	350 rpm	400 rpm	450 rpm	500 rpm	550 rpm	600 rpm	650 rpm	700 rpm	750 rpm	800 rpm	850 rpm	900 rpm	950 rpm
10 V	0.039	0.039	0.039	0.039	0.039	0.039	0.039	0.039	0.039	0.039	0.039	0.039	0.039	0.038	0.038	0.037	0.037	0.036	0.035	0.034
20 V	0.203	0.203	0.203	0.203	0.203	0.203	0.203	0.203	0.203	0.203	0.203	0.203	0.202	0.201	0.199	0.196	0.192	0.187	0.182	0.176
30 V	0.487	0.487	0.487	0.487	0.487	0.487	0.487	0.487	0.487	0.487	0.487	0.463	0.452	0.450	0.448	0.440	0.430	0.428	0.404	0.391
40 V	0.931	0.931	0.931	0.931	0.931	0.931	0.931	0.931	0.931	0.931	0.931	0.882	0.880	0.886	0.873	0.859	0.841	0.821	0.804	0.797
50 V	1.219	1.219	1.219	1.219	1.219	1.219	1.219	1.219	1.219	1.219	1.219	1.192	1.192	1.190	1.180	1.161	1.136	1.108	1.098	1.085
60 V	1.651	1.651	1.651	1.651	1.651	1.651	1.651	1.651	1.651	1.651	1.651	1.647	1.641	1.631	1.615	1.594	1.569	1.540	1.509	1.477
70 V	2.197	2.197	2.197	2.197	2.197	2.197	2.197	2.197	2.197	2.197	2.197	2.187	2.173	2.155	2.132	2.105	2.074	2.039	2.003	1.965
80 V	2.569	2.569	2.569	2.569	2.569	2.569	2.569	2.569	2.569	2.569	2.569	2.552	2.530	2.505	2.474	2.440	2.402	2.362	2.321	2.278
90 V	3.226	3.226	3.226	3.226	3.226	3.226	3.226	3.226	3.226	3.226	3.226	3.193	3.156	3.115	3.069	3.020	2.969	2.915	2.859	2.804
100 V	3.774	3.774	3.774	3.774	3.774	3.774	3.774	3.774	3.774	3.774	3.774	3.729	3.682	3.632	3.580	3.525	3.469	3.411	3.353	3.294
110 V	4.288	4.288	4.288	4.288	4.288	4.288	4.288	4.288	4.288	4.288	4.288	4.235	4.179	4.119	4.057	3.993	3.926	3.858	3.789	3.720

Table. A.1.5: FEA based lookup table for torque ranging from 1000 rpm to 1950 rpm

$N_r\ (rpm)/$ $V_{as}\ (V)$	1000 rpm	1050 rpm	1100 rpm	1150 rpm	1200 rpm	1250 rpm	1300 rpm	1350 rpm	1400 rpm	1450 rpm	1500 rpm	1550 rpm	1600 rpm	1650 rpm	1700 rpm	1750 rpm	1800 rpm	1850 rpm	1900 rpm	1950 rpm
10 V	0.033	0.031	0.030	0.029	0.028	0.026	0.025	0.024	0.023	0.021	0.020	0.019	0.018	0.016	0.015	0.014	0.013	0.012	0.010	0.0099
20 V	0.171	0.166	0.161	0.155	0.151	0.146	0.141	0.137	0.132	0.128	0.124	0.120	0.117	0.113	0.110	0.106	0.103	0.100	0.098	0.095
30 V	0.388	0.355	0.343	0.332	0.322	0.312	0.302	0.293	0.285	0.277	0.270	0.263	0.257	0.251	0.245	0.239	0.234	0.229	0.224	0.220
40 V	0.778	0.731	0.710	0.690	0.672	0.655	0.638	0.623	0.608	0.594	0.571	0.559	0.547	0.536	0.515	0.505	0.498	0.480	0.465	0.450
50 V	1.078	1.067	1.059	1.032	1.007	0.982	0.959	0.937	0.915	0.895	0.842	0.806	0.783	0.751	0.704	0.688	0.672	0.656	0.641	0.626
60 V	1.444	1.412	1.381	1.351	1.321	1.292	1.264	1.236	1.209	1.182	1.156	1.130	1.104	1.079	1.054	1.029	1.005	0.981	0.957	0.932
70 V	1.927	1.890	1.852	1.816	1.780	1.744	1.708	1.673	1.638	1.604	1.570	1.535	1.502	1.468	1.435	1.401	1.368	1.335	1.302	1.269
80 V	2.236	2.194	2.153	2.113	2.073	2.034	1.996	1.958	1.921	1.884	1.848	1.812	1.777	1.741	1.706	1.671	1.637	1.602	1.567	1.533
90 V	2.748	2.694	2.640	2.588	2.537	2.486	2.437	2.388	2.340	2.293	2.246	2.200	2.155	2.111	2.066	2.023	1.980	1.937	1.894	1.852
100 V	3.236	3.178	3.121	3.064	3.008	2.952	2.897	2.842	2.788	2.734	2.681	2.628	2.575	2.523	2.471	2.419	2.368	2.317	2.266	2.215
110 V	3.652	3.584	3.518	3.452	3.387	3.323	3.260	3.198	3.136	3.075	3.015	2.956	2.897	2.839	2.781	2.723	2.666	2.610	2.554	2.498

Table. A.1.6: FEA based lookup table for torque ranging from 2000 rpm to 2850 rpm

$N_r\ (rpm)/$ $V_{as}\ (V)$	2000 rpm	2050 rpm	2100 rpm	2150 rpm	2200 rpm	2250 rpm	2300 rpm	2350 rpm	2400 rpm	2450 rpm	2500 rpm	2550 rpm	2600 rpm	2650 rpm	2700 rpm	2750 rpm	2800 rpm	2850 rpm
10 V	0.0088	0.0079	0.0070	0.0061	0.0053	0.0046	0.0040	0.0034	0.0029	0.0025	0.0022	0.0019	0.0018	0.0017	0.0016	0.0016	0.0016	0.0015
20 V	0.093	0.090	0.088	0.086	0.084	0.083	0.081	0.080	0.079	0.078	0.077	0.077	0.076	0.076	0.076	0.075	0.075	0.075
30 V	0.215	0.211	0.207	0.202	0.198	0.194	0.189	0.185	0.180	0.175	0.143	0.155	0.150	0.144	0.138	0.132	0.128	0.121
40 V	0.440	0.422	0.410	0.399	0.380	0.365	0.348	0.337	0.325	0.315	0.309	0.302	0.294	0.290	0.285	0.281	0.277	0.272
50 V	0.611	0.597	0.582	0.568	0.553	0.538	0.523	0.508	0.492	0.476	0.450	0.442	0.425	0.407	0.401	0.398	0.390	0.385
60 V	0.908	0.884	0.860	0.836	0.812	0.788	0.763	0.738	0.713	0.687	0.662	0.635	0.609	0.582	0.555	0.528	0.500	0.473
70 V	1.236	1.202	1.169	1.136	1.102	1.069	1.035	1.001	0.967	0.933	0.898	0.863	0.828	0.792	0.756	0.721	0.685	0.649
80 V	1.498	1.464	1.429	1.394	1.359	1.323	1.287	1.251	1.214	1.177	1.140	1.102	1.063	1.024	0.985	0.945	0.905	0.866
90 V	1.810	1.768	1.726	1.685	1.643	1.602	1.560	1.518	1.476	1.434	1.392	1.350	1.307	1.264	1.221	1.177	1.134	1.091
100 V	2.164	2.114	2.063	2.013	1.963	1.912	1.862	1.812	1.762	1.712	1.661	1.611	1.560	1.510	1.459	1.408	1.358	1.307
110 V	2.443	2.388	2.333	2.278	2.223	2.169	2.114	2.060	2.005	1.951	1.896	1.841	1.787	1.732	1.677	1.622	1.567	1.512

A.1.3 Non-Linear Equivalent Circuit Based Lookup Table For Flux Linkage

The non-linear equivalent circuit-based lookup table for flux linkage proposed in chapter-5 is listed in this section. The complete lookup table is ranging from 0 rpm to 2850 rpm. Due to page-width constraints, the lookup table is listed in subsections as shown below.

Table. A.1.7: Non-linear equivalent circuit based lookup table for flux linkage upto 950 rpm

$N_r\ (rpm)/$ $T_e\ (Nm)$	0 rpm	50 rpm	100 rpm	150 rpm	200 rpm	250 rpm	300 rpm	350 rpm	400 rpm	450 rpm	500 rpm	550 rpm	600 rpm	650 rpm	700 rpm	750 rpm	800 rpm	850 rpm	900 rpm	950 rpm
0.1 Nm	0.530	0.530	0.530	0.530	0.530	0.530	0.530	0.530	0.530	0.530	0.530	0.489	0.450	0.415	0.383	0.354	0.328	0.306	0.286	0.269
0.2 Nm	0.540	0.540	0.540	0.540	0.540	0.540	0.540	0.540	0.540	0.540	0.540	0.499	0.461	0.426	0.395	0.367	0.342	0.320	0.301	0.284
0.3 Nm	0.550	0.550	0.550	0.550	0.550	0.550	0.550	0.550	0.550	0.550	0.550	0.509	0.472	0.438	0.407	0.380	0.355	0.334	0.315	0.299
0.4 Nm	0.559	0.559	0.559	0.559	0.559	0.559	0.559	0.559	0.559	0.559	0.559	0.520	0.483	0.450	0.420	0.393	0.369	0.347	0.329	0.313
0.5 Nm	0.569	0.569	0.569	0.569	0.569	0.569	0.569	0.569	0.569	0.569	0.569	0.530	0.495	0.462	0.432	0.405	0.382	0.361	0.343	0.328
0.6 Nm	0.579	0.579	0.579	0.579	0.579	0.579	0.579	0.579	0.579	0.579	0.579	0.541	0.506	0.474	0.444	0.418	0.395	0.375	0.358	0.343
0.7 Nm	0.589	0.589	0.589	0.589	0.589	0.589	0.589	0.589	0.589	0.589	0.589	0.551	0.517	0.485	0.457	0.431	0.409	0.389	0.372	0.357
0.8 Nm	0.598	0.598	0.598	0.598	0.598	0.598	0.598	0.598	0.598	0.598	0.598	0.562	0.528	0.497	0.469	0.444	0.422	0.403	0.386	0.372
0.9 Nm	0.608	0.608	0.608	0.608	0.608	0.608	0.608	0.608	0.608	0.608	0.608	0.572	0.539	0.509	0.482	0.457	0.436	0.417	0.400	0.386
1.0 Nm	0.618	0.618	0.618	0.618	0.618	0.618	0.618	0.618	0.618	0.618	0.618	0.583	0.550	0.521	0.494	0.470	0.449	0.431	0.415	0.401
1.1 Nm	0.628	0.628	0.628	0.628	0.628	0.628	0.628	0.628	0.628	0.628	0.628	0.593	0.561	0.532	0.506	0.483	0.462	0.444	0.429	0.416
1.2 Nm	0.637	0.637	0.637	0.637	0.637	0.637	0.637	0.637	0.637	0.637	0.637	0.604	0.573	0.544	0.519	0.496	0.476	0.458	0.443	0.430
1.3 Nm	0.647	0.647	0.647	0.647	0.647	0.647	0.647	0.647	0.647	0.647	0.647	0.614	0.584	0.556	0.531	0.509	0.489	0.472	0.457	0.445
1.4 Nm	0.657	0.657	0.657	0.657	0.657	0.657	0.657	0.657	0.657	0.657	0.657	0.625	0.595	0.568	0.543	0.522	0.503	0.486	0.472	0.460
1.5 Nm	0.667	0.667	0.667	0.667	0.667	0.667	0.667	0.667	0.667	0.667	0.667	0.635	0.606	0.580	0.556	0.535	0.516	0.500	0.486	0.474

Table. A.1.8: Non-linear equivalent circuit based lookup table for flux linkage ranging from 1000 rpm to 1950 rpm

$N_r\ (rpm)/$ $T_e\ (Nm)$	1000 rpm	1050 rpm	1100 rpm	1150 rpm	1200 rpm	1250 rpm	1300 rpm	1350 rpm	1400 rpm	1450 rpm	1500 rpm	1550 rpm	1600 rpm	1650 rpm	1700 rpm	1750 rpm	1800 rpm	1850 rpm	1900 rpm	1950 rpm
0.1 Nm	0.255	0.243	0.233	0.225	0.218	0.213	0.209	0.206	0.204	0.202	0.199	0.198	0.198	0.198	0.197	0.197	0.196	0.196	0.195	0.195
0.2 Nm	0.270	0.258	0.248	0.240	0.234	0.229	0.225	0.222	0.220	0.219	0.218	0.218	0.217	0.217	0.217	0.217	0.217	0.217	0.216	0.216
0.3 Nm	0.285	0.273	0.264	0.256	0.250	0.245	0.241	0.239	0.237	0.236	0.235	0.234	0.234	0.234	0.234	0.234	0.234	0.234	0.234	0.234
0.4 Nm	0.300	0.289	0.279	0.272	0.266	0.261	0.258	0.255	0.253	0.252	0.252	0.251	0.251	0.251	0.251	0.252	0.251	0.251	0.251	0.251
0.5 Nm	0.315	0.304	0.295	0.288	0.282	0.277	0.274	0.272	0.270	0.269	0.269	0.269	0.269	0.269	0.269	0.269	0.268	0.268	0.268	0.268
0.6 Nm	0.330	0.319	0.310	0.303	0.298	0.293	0.290	0.288	0.287	0.286	0.286	0.286	0.286	0.286	0.286	0.286	0.286	0.286	0.286	0.286
0.7 Nm	0.345	0.334	0.326	0.319	0.314	0.310	0.307	0.304	0.304	0.304	0.304	0.304	0.304	0.304	0.304	0.304	0.304	0.303	0.303	0.303
0.8 Nm	0.360	0.350	0.341	0.335	0.330	0.326	0.323	0.322	0.322	0.322	0.322	0.322	0.322	0.322	0.322	0.321	0.321	0.321	0.321	0.321
0.9 Nm	0.375	0.365	0.357	0.350	0.345	0.342	0.340	0.340	0.340	0.340	0.340	0.340	0.340	0.339	0.339	0.339	0.339	0.339	0.339	0.338
1.0 Nm	0.390	0.380	0.372	0.366	0.361	0.358	0.358	0.358	0.358	0.358	0.358	0.358	0.358	0.357	0.357	0.357	0.357	0.357	0.356	0.356
1.1 Nm	0.405	0.395	0.388	0.382	0.377	0.376	0.376	0.376	0.376	0.376	0.376	0.376	0.376	0.376	0.375	0.375	0.375	0.374	0.374	0.374
1.2 Nm	0.419	0.411	0.403	0.398	0.395	0.395	0.395	0.395	0.394	0.394	0.394	0.394	0.394	0.393	0.393	0.393	0.393	0.393	0.392	0.392
1.3 Nm	0.434	0.426	0.419	0.413	0.413	0.413	0.413	0.413	0.413	0.413	0.413	0.412	0.412	0.412	0.412	0.411	0.411	0.411	0.411	0.410
1.4 Nm	0.449	0.441	0.434	0.432	0.432	0.432	0.432	0.431	0.431	0.431	0.431	0.431	0.431	0.430	0.430	0.430	0.429	0.429	0.429	0.428
1.5 Nm	0.464	0.456	0.451	0.451	0.451	0.450	0.450	0.450	0.450	0.450	0.444	0.442	0.441	0.440	0.439	0.437	0.437	0.433	0.432	0.430

Table. A.1.9: Non-linear equivalent circuit based lookup table for flux linkage ranging from 2000 rpm to 2850 rpm

$N_r\ (rpm)/$ $T_e\ (Nm)$	2000 rpm	2050 rpm	2100 rpm	2150 rpm	2200 rpm	2250 rpm	2300 rpm	2350 rpm	2400 rpm	2450 rpm	2500 rpm	2550 rpm	2600 rpm	2650 rpm	2700 rpm	2750 rpm	2800 rpm	2850 rpm
0.1 Nm	0.194	0.194	0.193	0.193	0.193	0.192	0.192	0.191	0.191	0.190	0.189	0.189	0.188	0.186	0.184	0.182	0.179	0.177
0.2 Nm	0.216	0.216	0.216	0.215	0.215	0.214	0.214	0.213	0.212	0.211	0.210	0.209	0.207	0.205	0.203	0.201	0.199	0.196
0.3 Nm	0.234	0.234	0.233	0.233	0.233	0.232	0.232	0.231	0.230	0.229	0.228	0.227	0.226	0.224	0.222	0.220	0.218	0.216
0.4 Nm	0.252	0.251	0.251	0.251	0.251	0.250	0.250	0.249	0.249	0.248	0.247	0.246	0.244	0.243	0.241	0.239	0.237	0.235
0.5 Nm	0.268	0.268	0.268	0.268	0.268	0.268	0.268	0.267	0.267	0.266	0.265	0.264	0.263	0.262	0.260	0.259	0.257	0.255
0.6 Nm	0.286	0.285	0.285	0.285	0.285	0.285	0.285	0.285	0.285	0.285	0.284	0.283	0.282	0.281	0.279	0.278	0.276	0.274
0.7 Nm	0.303	0.303	0.303	0.302	0.302	0.302	0.302	0.302	0.302	0.302	0.302	0.302	0.301	0.300	0.298	0.297	0.294	0.291
0.8 Nm	0.321	0.320	0.320	0.320	0.320	0.320	0.319	0.319	0.319	0.319	0.319	0.318	0.318	0.318	0.317	0.316	0.315	0.313
0.9 Nm	0.338	0.338	0.338	0.337	0.337	0.337	0.337	0.336	0.336	0.336	0.336	0.335	0.335	0.335	0.335	0.335	0.334	0.333
1.0 Nm	0.356	0.355	0.355	0.355	0.355	0.354	0.354	0.354	0.354	0.353	0.353	0.353	0.353	0.352	0.352	0.352	0.352	0.352
1.1 Nm	0.374	0.374	0.373	0.373	0.373	0.372	0.372	0.372	0.372	0.371	0.370	0.370	0.370	0.369	0.369	0.369	0.369	0.369
1.2 Nm	0.392	0.391	0.391	0.391	0.390	0.390	0.389	0.389	0.388	0.388	0.387	0.387	0.386	0.386	0.386	0.386	0.385	0.385
1.3 Nm	0.410	0.409	0.409	0.408	0.407	0.407	0.406	0.406	0.405	0.404	0.404	0.404	0.403	0.403	0.403	0.402	0.402	0.402
1.4 Nm	0.427	0.426	0.426	0.425	0.425	0.424	0.423	0.422	0.422	0.422	0.421	0.420	0.420	0.419	0.419	0.419	0.419	0.419
1.5 Nm	0.429	0.429	0.425	0.423	0.423	0.422	0.422	0.420	0.419	0.419	0.417	0.416	0.412	0.410	0.409	0.409	0.406	0.405

A.1.4 Non-Linear Equivalent Circuit Based Lookup Table For Torque

The non-linear equivalent circuit-based lookup table for torque proposed in chapter-5 is listed in this section. The complete lookup table is ranging from 0 rpm to 2850 rpm. Due to page-width constraints, the lookup table is listed in subsections as shown below.

Table. A.1.10: Non-linear equivalent circuit based lookup table for torque upto 950 rpm

$N_r\ (rpm)/$ $V_{as}\ (V)$	0 rpm	50 rpm	100 rpm	150 rpm	200 rpm	250 rpm	300 rpm	350 rpm	400 rpm	450 rpm	500 rpm	550 rpm	600 rpm	650 rpm	700 rpm	750 rpm	800 rpm	850 rpm	900 rpm	950 rpm
10 V	0.211	0.211	0.211	0.211	0.211	0.211	0.211	0.211	0.211	0.211	0.211	0.193	0.181	0.172	0.166	0.161	0.156	0.151	0.146	0.142
20 V	0.765	0.765	0.765	0.765	0.765	0.765	0.765	0.765	0.765	0.765	0.765	0.708	0.666	0.635	0.611	0.592	0.573	0.556	0.540	0.524
30 V	1.317	1.317	1.317	1.317	1.317	1.317	1.317	1.317	1.317	1.317	1.317	1.216	1.141	1.086	1.045	1.011	0.980	0.950	0.922	0.896
40 V	1.866	1.866	1.866	1.866	1.866	1.866	1.866	1.866	1.866	1.866	1.866	1.725	1.620	1.542	1.483	1.435	1.389	1.346	1.307	1.271
50 V	2.410	2.410	2.410	2.410	2.410	2.410	2.410	2.410	2.410	2.410	2.410	2.234	2.104	2.007	1.934	1.873	1.814	1.759	1.708	1.661
60 V	2.948	2.948	2.948	2.948	2.948	2.948	2.948	2.948	2.948	2.948	2.948	2.703	2.523	2.395	2.307	2.245	2.197	2.159	2.127	2.097
70 V	3.479	3.479	3.479	3.479	3.479	3.479	3.479	3.479	3.479	3.479	3.479	3.317	3.160	3.011	2.872	2.745	2.631	2.529	2.439	2.358
80 V	4.000	4.000	4.000	4.000	4.000	4.000	4.000	4.000	4.000	4.000	4.000	3.769	3.544	3.351	3.194	3.065	2.963	2.883	2.821	2.771
90 V	4.511	4.511	4.511	4.511	4.511	4.511	4.511	4.511	4.511	4.511	4.511	4.283	4.127	3.920	3.808	3.694	3.580	3.468	3.360	3.257
100 V	5.010	5.010	5.010	5.010	5.010	5.010	5.010	5.010	5.010	5.010	5.010	4.798	4.629	4.459	4.313	4.188	4.075	3.966	3.860	3.755
110 V	5.495	5.495	5.495	5.495	5.495	5.495	5.495	5.495	5.495	5.495	5.495	5.221	4.943	4.779	4.650	4.520	4.389	4.261	4.134	4.012

Table. A.1.11: Non-linear equivalent circuit based lookup table for torque ranging from 1000 rpm to 1950 rpm

$N_r\ (rpm)/$ $V_{as}\ (V)$	1000 rpm	1050 rpm	1100 rpm	1150 rpm	1200 rpm	1250 rpm	1300 rpm	1350 rpm	1400 rpm	1450 rpm	1500 rpm	1550 rpm	1600 rpm	1650 rpm	1700 rpm	1750 rpm	1800 rpm	1850 rpm	1900 rpm	1950 rpm
10 V	0.140	0.134	0.130	0.127	0.124	0.121	0.118	0.115	0.112	0.110	0.108	0.105	0.103	0.101	0.099	0.097	0.094	0.092	0.090	0.088
20 V	0.510	0.495	0.481	0.468	0.457	0.446	0.435	0.425	0.415	0.407	0.399	0.390	0.381	0.373	0.365	0.358	0.349	0.341	0.334	0.327
30 V	0.872	0.847	0.823	0.801	0.782	0.763	0.744	0.726	0.710	0.696	0.682	0.667	0.652	0.638	0.625	0.612	0.598	0.583	0.571	0.559
40 V	1.236	1.201	1.167	1.136	1.109	1.083	1.056	1.030	1.007	0.987	0.968	0.947	0.925	0.905	0.887	0.869	0.849	0.828	0.810	0.794
50 V	1.615	1.569	1.524	1.484	1.449	1.415	1.380	1.346	1.316	1.290	1.266	1.237	1.209	1.183	1.159	1.136	1.109	1.083	1.059	1.038
60 V	2.061	2.015	1.963	1.910	1.861	1.812	1.764	1.719	1.679	1.645	1.613	1.577	1.542	1.509	1.478	1.449	1.415	1.381	1.352	1.325
70 V	2.280	2.217	2.156	2.100	2.049	2.001	1.955	1.913	1.872	1.834	1.796	1.760	1.724	1.689	1.655	1.621	1.586	1.552	1.517	1.483
80 V	2.724	2.677	2.631	2.586	2.542	2.498	2.455	2.412	2.370	2.327	2.285	2.243	2.202	2.160	2.118	2.076	2.034	1.992	1.949	1.906
90 V	3.159	3.068	2.981	2.899	2.823	2.750	2.682	2.618	2.558	2.502	2.449	2.398	2.351	2.306	2.264	2.224	2.186	2.149	2.114	2.080
100 V	3.652	3.549	3.448	3.348	3.250	3.154	3.061	2.970	2.882	2.798	2.717	2.641	2.568	2.501	2.446	2.402	2.363	2.328	2.293	2.260
110 V	3.892	3.777	3.666	3.560	3.458	3.360	3.266	3.177	3.093	3.013	2.938	2.867	2.802	2.741	2.685	2.633	2.585	2.541	2.500	2.462

Table. A.1.12: Non-linear equivalent circuit based lookup table for torque ranging from 2000 rpm to 2850 rpm

$N_r\ (rpm)/$ $V_{as}\ (V)$	2000 rpm	2050 rpm	2100 rpm	2150 rpm	2200 rpm	2250 rpm	2300 rpm	2350 rpm	2400 rpm	2450 rpm	2500 rpm	2550 rpm	2600 rpm	2650 rpm	2700 rpm	2750 rpm	2800 rpm	2850 rpm
10 V	0.087	0.084	0.082	0.080	0.078	0.076	0.073	0.069	0.066	0.062	0.059	0.057	0.054	0.052	0.050	0.047	0.045	0.040
20 V	0.320	0.312	0.304	0.296	0.289	0.280	0.271	0.260	0.249	0.239	0.229	0.219	0.209	0.199	0.190	0.180	0.170	0.160
30 V	0.548	0.535	0.520	0.507	0.494	0.480	0.464	0.445	0.427	0.409	0.392	0.376	0.359	0.342	0.326	0.309	0.292	0.275
40 V	0.777	0.758	0.738	0.718	0.700	0.679	0.655	0.628	0.602	0.578	0.556	0.536	0.516	0.496	0.477	0.457	0.437	0.417
50 V	1.017	0.992	0.966	0.942	0.918	0.892	0.862	0.828	0.794	0.761	0.731	0.700	0.669	0.638	0.607	0.576	0.545	0.510
60 V	1.297	1.266	1.233	1.202	1.172	1.139	1.100	1.057	1.014	0.972	0.933	0.894	0.854	0.815	0.775	0.736	0.696	0.655
70 V	1.447	1.411	1.375	1.337	1.300	1.261	1.221	1.180	1.139	1.097	1.055	1.013	0.970	0.927	0.884	0.840	0.797	0.754
80 V	1.862	1.818	1.773	1.728	1.682	1.635	1.587	1.538	1.489	1.438	1.386	1.332	1.278	1.222	1.165	1.107	1.049	0.992
90 V	2.046	2.014	1.982	1.950	1.918	1.886	1.854	1.822	1.790	1.757	1.724	1.690	1.657	1.623	1.589	1.555	1.521	1.486
100 V	2.226	2.194	2.162	2.130	2.098	2.066	2.034	2.002	1.970	1.937	1.904	1.870	1.837	1.803	1.769	1.735	1.701	1.666
110 V	2.426	2.392	2.358	2.326	2.295	2.264	2.233	2.202	2.171	2.139	2.108	2.076	2.044	2.012	1.979	1.947	1.915	1.882

A.2 Induction Motor Rating Details and Equivalent Parameters

The used IM nameplate data and its electrical equivalent circuit parameters, which are determined from standard no-load and locked rotor tests are listed in Table A.2.1.

Table. A.2.1: Induction motor parameters values

Nameplate and Parameters	Value
Manufacturer	DE LORENZO
Connection type	**Y** (star)
Number of Phases	3ph
Power	1.1 kW
Voltage (phase)	220 V
Rated current	2.5 A
Number of Poles	2
Frequency	50 Hz
Rated speed	2850 rpm
Stator Resistance	4.29 Ω
Rotor Resistance	3.73 Ω
Stator Leakage Inductance	0.0141 H
Rotor Leakage Inductance	0.0141 H
Magnetizing Inductance	0.5275 H

A.3 Machines used for Loading the Induction Motor

Powder brake and DC machine (used in regenerative mode) have been used to load the induction motor. The nameplate details of these machines are:

Table. A.3.1: Powder break nameplate details

Nameplate Data	Value
Manufacturer	DE LORENZO
Voltage (DC)	0-20 V
Rated speed	4000 rpm
Rated torque	20 Nm

The nameplate details of DC machine are:

Table. A.3.2: DC machine nameplate details

Nameplate Data	Value
Manufacturer	DE LORENZO
Winding type	Shunt
Rated power	1.1 kW
Armature voltage	220v
Rated current	6.8 A
Rated speed	3000 rpm
Field voltage	160 V
Rated current	0.26 A

A.4 Measuring Equipments

The list of the equipments used are:

Table. A.4.1: List of measurement equipment

Apparatus	Model
Differential voltage probe	YOKOGAWA 700924
Current probe	YOKOGAWA 701933
Digital oscilloscope	YOKOGAWA DLM2054
Torque Sensor	Kistler 4503*B*

A.5 Voltage Source Inverter Components

The hardware components used for building 3-phase inverter are given in Table. A.5.1.

Table. A.5.1: List of hardware components

Components	Description	Quantity
Dc link capacitor	450 V; 500 μF	1
Inverter switch (IGBT)	FGH40N60	6
Inverter gate driver IC	IR2130	1
Optocoupler IC	HCPL2601	6

- Fairchild semiconductor 'FGH40N60SFD 600 V, 40 A field Stop IGBT', Technical Datasheet, 2008.
- International rectifier 'IR2130 3-Phase Bridge Driver', Technical Datasheet, 2004.
- Fairchild semiconductor 'HCPL2601 optocoupler (4.5-5.5) V', Technical Datasheet, 2011.

A.6 Experimental Test Bed

The schematic shown in Fig.A.6.1, and experimental setup shown in Fig.A.6.2, consists of a three-phase squirrel cage IM (parameters are given in Table A.2.1), powder brake (for IM loading), a VSI, and dSpace DS1103 platform. The heart of this lab drive is the DSP board, DS1103 board, which is employed to execute the computation of the control schemes. The DS1103 board is a real-time controller made by dSPACE GmbH for motion control purposes. The control algorithm is realized on a dSPACE1103 platform, and its sampling time is chosen as 40 μsec.

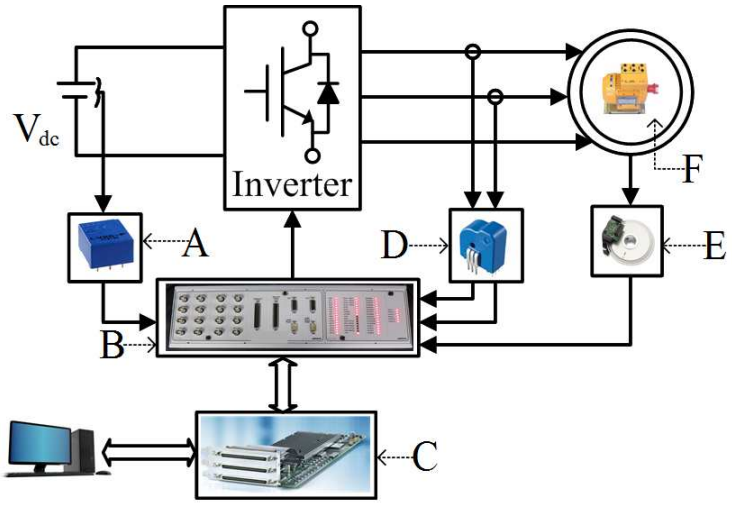

A: Voltage sensor, **B**: Interface board, **C**: dSPACE1103,
D: Current sensor, **E**: Speed encoder, **F**: IM

Fig. A.6.1: Schematic diagram of experimental setup

The control scheme uses two phase currents (i_a , i_b) and DC-link voltage ($V_{dc} = 320$ V), which are measured using hall effect current sensors (LTS-6NP) and voltage transducer (LV-25P). Further, the values of $k_p = 0.0425$ and $k_i = 0.825$ are used in the speed control loop in DTC based drivetrain configuration as shown in Fig. 4.17.

A.6.1 DSP Board, dSPACE DS1103

The DS1103 board is based on the Motorola PowerPC 604e/333MHz processor, which forms the main processing unit and intended to interface with Personal Computers (PC). The purpose of the PC is to download the control scheme on to the board. The Real-Time interface (RTI) given by dSpace links the experimental setup and the simulink (Matlab 2013a MathWorks, Inc.) model through the Control Desk platform. Thus, the variables of simulink model can be accessed by the Control Desk (a

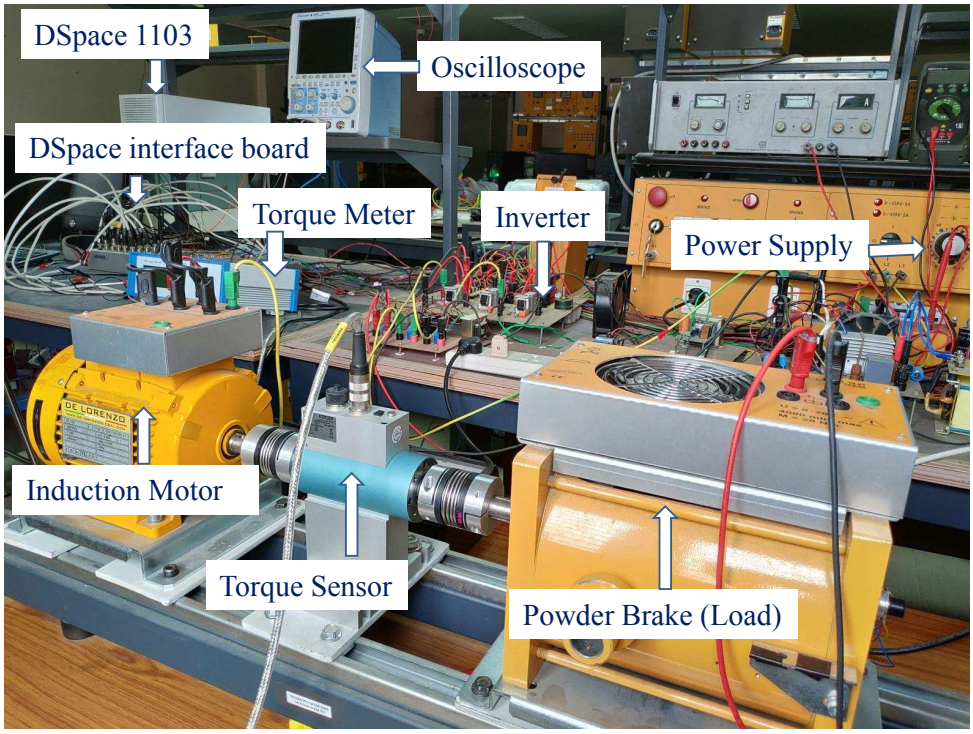

Fig. A.6.2: Real time implementation test bed

platform links simulink and RTI), which also interacts with the DSP during the running of the control algorithm. Consequently, the control signals inside the DSP can be observed, captured, and varied by the Control Desk.

Three of the sixteen Analog to digital (A/D) conversion units available on the DS1103 board are used for measuring the input signals (two stator currents and DC voltage). Each unit of A/D has a 16-bit resolution with 4 μs sampling time, and the acceptable input voltage range of each A/D conversion unit is $\pm$ 10V. Also, the DS1103board has eight digital to analog (D/A) units available for the visualization of signals. The resolution of D/A converter is 14-bit with the voltage range $\pm$10V. For further information about dSpace DS1103 can be found in “DS1103 Controller Board Features Release 2014-A - May 2014”, and “dSPACE DS1103 User’s Guide”.

A.6.2 Stator Current Measurement

Two stator currents are measured in the laboratory test-bed setup using hall effect current transducers of LEM viz. LTS 6-NP. The sensor converts a current of $+-$6A into a voltage of $+-$5V. The output of the current transducer is a low current value based on the conversion ratio of 1:2000. The current is passed through a resistor of 208.33 Ω as specified by the datasheet. The voltage across the resistance is the output of the current sensor, which is the input to the A/D converter unit of the dSPACE-1103

Control Desk. A gain of 9.302 is initially multiplied to the input voltage signal to obtain the actual current in the control algorithm. The gain is updated to 9.4 based on the experimental calibration. The actual current obtained after multiplication is used in the control algorithm.

A.6.3 Voltage Measurement

The DC voltage, which is the input to the inverter in the setup is the only measured voltage. The DC voltage is measured using a hall effect transducer of LEM viz.LV 25P. The primary voltage rating of the transducer is 10V to 500V, which is converted to a voltage range of 0 to $+-5$V on the secondary side. The transducer has a conversion ratio of 2500:1000, and the output is current in the range of 0 to 25 mA, as specified in the datasheet. The current is passed to a resistance of 200 Ω to convert current to an equivalent voltage. The equivalent voltage is fed to the A/D converter of the dSPACE-1103 Control Desk. A gain of 114.5 (obtained using experiments) is multiplied to the measured voltage at the A/D to obtain the actual measured voltage. The actual measured voltage and the PWM pulses (S_a, S_b, and S_c) are given as an input to the control algorithm.

A.6.4 Speed Measurement

The speed is measured using an incremental optical encoder, HEDS 9040, which is mounted on the common shaft of the machine set. The resolution of the encoder is 1024 pulse per revolution. The output from the is directly fed to the DS1103 position encoder measurement unit, which gives the measured speed of the induction motor. For further information about DS1103 speed encoder can be found in “DS1103 Controller Board Features Release 2014-A - May 2014”, and “dSPACE DS1103 User’s Guide”.

भारतीय प्रौद्योगिकी संस्थान गुवाहाटी
Indian Institute of Technology Guwahati

REFERENCES

[1] S. K. Guttikunda, R. Goel, and P. Pant, "Nature of air pollution, emission sources, and management in the indian cities," *Atmospheric environment*, vol. 95, pp. 501–510, 2014.

[2] W. H. Organization, "Who global ambient air quality database (update 2018)," *World Health Organization: Geneva, Switzerland*, 2018.

[3] "Global ev outlook 2017," *International Energy Agency*, pp. 1–71, 2017.

[4] U. Tietge, P. Mock, N. Lutsey, and A. Campestrini, "Comparison of leading electric vehicle policy and deployment in europe," *Int. Council Clean Transp.*, vol. 49, no. 30, pp. 847 129–102, 2016.

[5] B. F. d'Arcier and Y. Lecler, "Promoting next generation vehicles in japan: the smart communities and their experimentations," *Int. J. Automotive Technology and Management*, vol. 14, no. 3-4, pp. 324–346, 2014.

[6] M. B. Dror, "Zero emission vehicle credits: China program design inputs brief," *Innov. Center Energy Transp*, pp. 1–26, 2015.

[7] N. L. Dale Hall, Marissa Moultak, "Electric vehicle capitals of the world: Demonstrating the path to electric drive," *The Int. Council Clean Transp.*, 2017.

[8] V. Gulati, "National electric mobility mission plan 2020," *Department of Heavy Industry, Ministry of Heavy Industries & Public Enterprises, Government of India*, 2012.

[9] S. Juyal, M. Singh, S. Singh, and S. Pal, "India leaps ahead: Transformative mobility solutions for all," *NITI Aayog INDIA and RMI*, 2017.

[10] C. M. Martinez, X. Hu, D. Cao, E. Velenis, B. Gao, and M. Wellers, "Energy management in plug-in hybrid electric vehicles: Recent progress and a connected vehicles perspective," *IEEE Trans. Veh. Technol.*, vol. 66, no. 6, pp. 4534–4549, 2016.

[11] A. Emadi, Y. Lee, and K. Rajashekara, "Power electronics and motor drives in electric, hybrid electric, and plug-in hybrid electric vehicles," *IEEE Trans. Ind. Electron*, vol. 55, no. 6, pp. 2237–2245, 2008.

[12] M. Zeraoulia, M. E. H. Benbouzid, and D. Diallo, "Electric motor drive selection issues for hev propulsion systems: A comparative study," *IEEE Trans. Veh. Technol.*, vol. 55, no. 6, pp. 1756–1764, Nov. 2006.

[13] J. Cui, M. Kramer, L. Zhou, F. Liu, A. Gabay, G. Hadjipanayis, B. Balasubramanian, and D. Sellmyer, "Current progress and future challenges in rare-earth-free permanent magnets," *Acta Materialia*, vol. 158, pp. 118–137, 2018.

[14] M. Riddle, C. M. Macal, G. Conzelmann, T. E. Combs, D. Bauer, and F. Fields, "Global critical materials markets: An agent-based modeling approach," *Resources Policy*, vol. 45, pp. 307–321, 2015.

[15] S. A. Odhano, R. Bojoi, A. Boglietti, S. G. Rosu, and G. Griva, "Maximum efficiency per torque direct flux vector control of induction motor drives," *IEEE Trans. Ind. Appl.*, vol. 51, no. 6, pp. 4415–4424, Nov. 2015.

[16] T. J. BARLOW, S. Latham, I. McCrae, and P. Boulter, "A reference book of driving cycles for use in the measurement of road vehicle emissions," *TRL Published Project Report*, 2009.

[17] C. Chan, "The state of the art of electric and hybrid vehicles," *Proceedings of the IEEE*, vol. 90, no. 2, pp. 247–275, 2002.

[18] J. G. West, "Dc, induction, reluctance and pm motors for electric vehicles," *Power Engineering Journal*, vol. 8, no. 2, pp. 77–88, 1994.

[19] K. Rajashekara, "Present status and future trends in electric vehicle propulsion technologies," *IEEE J. of Emerging and Sel. Topics in Power Electron.*, vol. 1, no. 1, pp. 3–10, 2013.

[20] I. Boldea, L. N. Tutelea, L. Parsa, and D. Dorrell, "Automotive electric propulsion systems with reduced or no permanent magnets: An overview," *IEEE Trans. Ind. Electron.*, vol. 61, no. 10, pp. 5696–5711, 2014.

[21] D. Traore, J. D. Leon, A. Glumineau, and L. Loron, "Speed sensorless field-oriented control of induction motor with interconnected observers: experimental tests on low frequencies benchmark," *IET Control Theory Appl.*, vol. 1, no. 6, pp. 1681–1692, Nov. 2007.

[22] M. P. Kazmierkowski and A. B. Kasprowicz, "Improved direct torque and flux vector control of pwm inverter-fed induction motor drives," *IEEE Trans. Ind. Electron.*, vol. 42, no. 4, pp. 344–350, 1995.

[23] D. Casadei, G. Serra, A. Tani, and L. Zarri, "Direct torque control for induction machines: A technology status review," in *Electrical Machines Design Control and Diagnosis (WEMDCD), 2013 IEEE Workshop*, March 2013, pp. 117–129.

[24] R. Kumar, S. Das, and A. K. Chattopadhyay, "Comparative assessment of two different model reference adaptive system schemes for speed-sensorless control of induction motor drives," *IET Electr. Power Appl.*, vol. 10, no. 2, pp. 141–154, 2016.

[25] H. u. Rehman and L. Xu, "Alternative energy vehicles drive system: Control, flux and torque estimation, and efficiency optimization," *IEEE Trans. Veh. Technol.*, vol. 60, no. 8, pp. 3625–3634, Oct. 2011.

[26] D. Casadei, F. Profumo, G. Serra, and A. Tani, “Foc and dtc: two viable schemes for induction motors torque control,” *IEEE Trans. Power Electron.*, vol. 17, no. 5, pp. 779–787, 2002.

[27] G. S. Buja and M. P. Kazmierkowski, “Direct torque control of pwm inverter-fed ac motors-a survey,” *IEEE Trans. Ind. Electron.*, vol. 51, no. 4, pp. 744–757, 2004.

[28] I. Takahashi and T. Noguchi, “A new quick-response and high-efficiency control strategy of an induction motor,” *IEEE Trans. Ind. Appl.*, vol. IA-22, no. 5, pp. 820–827, Sept. 1986.

[29] E. Levi, R. Bojoi, F. Profumo, H. A. Toliyat, and S. Williamson, “Multiphase induction motor drives - a technology status review,” *IET Electr. Power Appl.*, vol. 1, no. 4, pp. 489–516, July 2007.

[30] A. Haddoun, M. E. H. Benbouzid, D. Diallo, R. Abdessemed, J. Ghouili, and K. Srairi, “A loss-minimization dtc scheme for ev induction motors,” *IEEE Trans. Veh. Technol.*, vol. 56, no. 1, pp. 81–88, Jan. 2007.

[31] M. Depenbrock, “Direct self-control (dsc) of inverter-fed induction machine,” in *IEEE Trans. Power Electron.*, vol. Vol.3,, no. No.4., Oct.1988.

[32] C. A. Martins, X. Roboam, T. A. Meynard, and A. S. Carvalho, “Switching frequency imposition and ripple reduction in dtc drives by using a multilevel converter,” *IEEE Trans. Power Electron.*, vol. 17, no. 2, pp. 286–297, 2002.

[33] C. Martins, T. Meynard, X. Roboam, and A. Carvalho, “A predictive sampling scale model for direct torque control of the induction machine fed by multilevel voltage-source inverters,” *Eur. Phys. J. AP*, vol. 5, no. 1, pp. 51–61, 1999.

[34] D. Casadei, G. Serra, and K. Tani, “Implementation of a direct control algorithm for induction motors based on discrete space vector modulation,” *IEEE Trans. Power Electron.*, vol. 15, no. 4, pp. 769–777, 2000.

[35] I. Takahashi and Y. Ohmori, “High-performance direct torque control of an induction motor,” *IEEE Trans. Ind. Appl.*, vol. 25, no. 2, pp. 257–264, 1989.

[36] C. G. Mei, S. Panda, J. Xu, and K. Lim, “Direct torque control of induction motor-variable switching sectors,” in *Proc. IEEE 1999 Int. Conf. Power Electron. Drive Systems. PEDS’99 (Cat. No. 99TH8475)*, vol. 1. IEEE, 1999, pp. 80–85.

[37] J.-W. Kang and S.-K. Sul, “Analysis and prediction of inverter switching frequency in direct torque control of induction machine based on hysteresis bands and machine parameters,” *IEEE Trans. Ind. Electron.*, vol. 48, no. 3, pp. 545–553, 2001.

[38] B. K. Bose, “An adaptive hysteresis-band current control technique of a voltage-fed pwm inverter for machine drive system,” *IEEE Trans. Ind. Electron.*, vol. 37, no. 5, pp. 402–408, 1990.

[39] G. Brando, A. Dannier, A. D. Pizzo, R. Rizzo, and I. Spina, "Generalised look-up table concept for direct torque control in induction drives with multilevel inverters," *IET Electr. Power Appl.*, vol. 9, no. 8, pp. 556–567, 2015.

[40] ——, "Torque derivative control in induction motor drives supplied by multilevel inverters," *IET Power Electron.*, vol. 9, no. 11, pp. 2249–2261, 2016.

[41] K.-B. Lee, J.-H. Song, I. Choy, and J.-Y. Yoo, "Improvement of low-speed operation performance of dtc for three-level inverter-fed induction motors," *IEEE Trans. Ind. Electron.*, vol. 48, no. 5, pp. 1006–1014, 2001.

[42] T. Ahammad, A. R. Beig, and K. Al-Hosani, "Sliding mode based dtc of three-level inverter fed induction motor using switching vector table," in *2013 9th Asian Control Conf. (ASCC)*. IEEE, 2013, pp. 1–6.

[43] C. Lascu, I. Boldea, and F. Blaabjerg, "Direct torque control of sensorless induction motor drives: a sliding-mode approach," *IEEE Trans. Ind. Appl.*, vol. 40, no. 2, pp. 582–590, 2004.

[44] S. Mukherjee and G. Poddar, "Direct torque control of squirrel cage induction motor for optimum current ripple using three-level inverter," *IET Power Electron.*, vol. 3, no. 6, pp. 904–914, Nov. 2010.

[45] J. Beerten, J. Verveckken, and J. Driesen, "Predictive direct torque control for flux and torque ripple reduction," *IEEE Trans. Ind. Electron.*, vol. 57, no. 1, pp. 404–412, Jan. 2010.

[46] G. Cirrincione, M. Cirrincione, C. Lu, and M. Pucci, "Direct torque control of induction motors by use of the gmr neural network," in *Proc. Int. Joint Conf. on Neural Networks, 2003.*, vol. 3. IEEE, 2003, pp. 2106–2111.

[47] R. Toufouti, S. Meziane, and H. Benalla, "Direct torque control for induction motor using intelligent techniques." *Journal of Theoretical and Applied Information Technology*, vol. 3, no. 3, 2007.

[48] R. T. S. Meziane and H. Benalla, "Direct torque control for induction motor using fuzzy logic," *ICGST Trans. on ACSE*, vol. 6, no. 2, pp. 17–24, 2006.

[49] H.-W. Wang, W.-P. Cui, X. Zhang, and J.-Q. Ren, "An improved method of low speed torque ripple based on adaptive fuzzy torque tracking controller," in *Proc. of 2004 Int. Conf. on Machine Learning and Cybernetics (IEEE Cat. No. 04EX826)*, vol. 1. IEEE, 2004, pp. 519–522.

[50] D. S. Kirschen, D. W. Novotny, and T. A. Lipo, "Optimal efficiency control of an induction motor drive," *IEEE Trans. Energy Convers.*, no. 1, pp. 70–76, 1987.

[51] S. Kaboli, M. R. Zolghadri, and E. Vahdati-Khajeh, "A fast flux search controller for dtc-based induction motor drives," *IEEE Trans. Ind. Electron.*, vol. 54, no. 5, pp. 2407–2416, Oct. 2007.

[52] S. N. Vukosavic and E. Levi, "Robust dsp-based efficiency optimization of a variable speed induction motor drive," *IEEE Trans. Ind. Electron.*, vol. 50, no. 3, pp. 560–570, 2003.

[53] C. Chakraborty and Y. Hori, "Fast efficiency optimization techniques for the indirect vector-controlled induction motor drives," *IEEE Trans. Ind. Appl.*, vol. 39, no. 4, pp. 1070–1076, 2003.

[54] A. M. Bazzi and P. T. Krein, "Review of methods for real-time loss minimization in induction machines," *IEEE Trans. Ind. Appl.*, vol. 46, no. 6, pp. 2319–2328, 2010.

[55] E. S. Sergaki and G. S. Stavrakakis, "Online search based fuzzy optimum efficiency operation in steady and transient states for dc and ac vector controlled motors," in *2008 18th Int. Conf. on Electrical Machines*. IEEE, 2008, pp. 1–7.

[56] F. Abrahamsen, F. Blaabjerg, J. K. Pedersen, and P. B. Thoegersen, "Efficiency-optimized control of medium-size induction motor drives," *IEEE Trans. Ind. Appl.*, vol. 37, no. 6, pp. 1761–1767, Nov. 2001.

[57] I. Kioskeridis and N. Margaris, "Loss minimization in scalar-controlled induction motor drives with search controllers," *IEEE Trans. Power Electron.*, vol. 11, no. 2, pp. 213–220, Mar. 1996.

[58] G. C. Sousa, B. K. Bose, and J. G. Cleland, "Fuzzy logic based on-line efficiency optimization control of an indirect vector-controlled induction motor drive," *IEEE Trans. Ind. Electron.*, vol. 42, no. 2, pp. 192–198, 1995.

[59] B. K. Bose, N. R. Patel, and K. Rajashekara, "A neuro-fuzzy-based on-line efficiency optimization control of a stator flux-oriented direct vector-controlled induction motor drive," *IEEE Trans. Ind. Electron.*, vol. 44, no. 2, pp. 270–273, 1997.

[60] D. de Almeida Souza, W. C. de Aragao Filho, and G. C. D. Sousa, "Adaptive fuzzy controller for efficiency optimization of induction motors," *IEEE Trans. Ind. Electron.*, vol. 54, no. 4, pp. 2157–2164, 2007.

[61] S. Sridharan and P. T. Krein, "Minimization of system-level losses in vsi-based induction motor drives: offline strategies," *IEEE Trans. Ind. Appl.*, vol. 53, no. 2, pp. 1096–1105, 2016.

[62] Y. Wang, T. Ito, and R. D. Lorenz, "Loss manipulation capabilities of deadbeat direct torque and flux control induction machine drives," *IEEE Trans. Ind. Appl.*, vol. 51, no. 6, pp. 4554–4566, Nov./Dec. 2015.

[63] M. Farasat, A. M. Trzynadlowski, and M. S. Fadali, "Efficiency improved sensorless control scheme for electric vehicle induction motors," *IET Electr. Syst. Transp.*, vol. 4, no. 4, pp. 122–131, 2014.

[64] F. Tazerart, Z. Mokrani, D. Rekioua, and T. Rekioua, "Direct torque control implementation with losses minimization of induction motor for electric vehicle applications with high operating life of the battery," *Int. J. Hydrog. Energy*, vol. 40, no. 39, pp. 13 827 – 13 838, 2015. [Online]. Available: http://www.sciencedirect.com/science/article/pii/S0360319915009404

[65] S. Bozhko, S. Dymko, S. Kovbasa, and S. M. Peresada, "Maximum torque-per-amp control for traction im drives: Theory and experimental results," *IEEE Trans. Ind. Appl.*, vol. 53, no. 1, pp. 181–193, Jan. 2017.

[66] A. A. C. Rebolledo and M. A. Valenzuela, "Expected savings using loss-minimizing flux on im drives-part i: Optimum flux and power savings for minimum losses," *IEEE Trans. Ind. Appl.*, vol. 51, no. 2, pp. 1408–1416, March 2015.

[67] M. H. Nasir Uddin, "Flc-based dtc scheme to improve the dynamic performance of an im drive," *IEEE Trans. Ind. Appl.*, vol. 48, no. 2, March/April 2012.

[68] X. Xu and D. Novotny, "Selection of the flux reference for induction machine drives in the field weakening region," *IEEE Trans. Ind. Appl.*, vol. 28, no. 6, pp. 1353–1358, Nov. 1992.

[69] D. Casadei, G. Serra, A. Stefani, A. Tani, and L. Zarri, "Dtc drives for wide speed range applications using a robust flux-weakening algorithm," *IEEE Trans. Ind. Electron.*, vol. 54, no. 5, pp. 2451–2461, Oct. 2007.

[70] J. Faiz and M. B. B. Sharifian, "Different techniques for real time estimation of an induction motor rotor resistance in sensorless direct torque control for electric vehicle," *IEEE Trans. Energy Convers.*, vol. 16, no. 1, pp. 104–109, March 2001.

[71] X. del Toro, M. Jayne, P. Witting, V. Sala, A. Arias, and J. Romeral, "New dtc control scheme for the induction motor fed with a three-level inverter," in *Ind. Electron., 2005. ISIE 2005. Proc. IEEE Int. Symp.*, vol. 3, June 2005, pp. 893–897 vol. 3.

[72] U. V. Patil, H. M. Suryawanshi, and M. M. Renge, "Closed-loop hybrid direct torque control for medium voltage induction motor drive for performance improvement," *IET Power Electron.*, vol. 7, no. 1, pp. 31–40, Jan. 2014.

[73] B. Singh, S. Jain, and S. Dwivedi, "Torque ripple reduction technique with improved flux response for a direct torque control induction motor drive," *IET Power Electron.*, vol. 6, no. 2, pp. 326–342, Feb 2013.

[74] Y. Zhang, J. Zhu, Z. Zhao, W. Xu, and D. G. Dorrell, "An improved direct torque control for three-level inverter-fed induction motor sensorless drive," *IEEE Trans. Power Electron.*, vol. 27, no. 3, pp. 1502–1513, 2010.

[75] D. Casadei, G. Serra, and A. Tani, "Direct flux and torque control of induction machine for electric vehicle applications," in *Electrical Machines and Drives, 1995. Seventh Int. Conf. (Conf. Publ. No. 412)*, Sept. 1995, pp. 349–353.

[76] T. Windisch and W. Hofmann, "Loss minimizing and saturation dependent control of induction machines in vehicle applications," in *IECON 2015 - 41st Annual Conf. IEEE Ind. Electron. Soc.*, Nov 2015, pp. 001 530–001 535.

[77] I. Kioskeridis and N. Margaris, "Loss minimization in induction motor adjustable-speed drives," *IEEE Trans. Ind. Electron.*, vol. 43, no. 1, pp. 226–231, Feb. 1996.

[78] F. Fernandez-Bernal, A. Garcia-Cerrada, and R. Faure, "Model-based loss minimization for dc and ac vector-controlled motors including core saturation," *IEEE Trans. Ind. Appl.*, vol. 36, no. 3, pp. 755–763, May 2000.

[79] O. S. Ebrahim, M. A. Badr, A. S. Elgendy, and P. K. Jain, "Ann-based optimal energy control of induction motor drive in pumping applications," *IEEE Trans. Energy Convers.*, vol. 25, no. 3, pp. 652–660, Sept. 2010.

[80] S. D. Breucker, K. Engelen, R. D'hulst, and J. Driesen, "Impact of current ripple on li-ion battery ageing," in *2013 World Electr. Veh. Symp. Exh. (EVS27)*, Nov. 2013, pp. 1–9.

[81] P. C. Perera, F. Blaabjerg, J. K. Pedersen, and P. Thogersen, "A sensorless, stable v/f control method for permanent-magnet synchronous motor drives," *IEEE Trans. Ind. Appl.*, vol. 39, no. 3, pp. 783–791, 2003.

[82] A. Chikhi, M. Djarallah, and K. Chikhi, "A comparative study of field-oriented control and direct-torque control of induction motors using an adaptive flux observer," *Serbian Journal of Electrical Engineering*, vol. 7, no. 1, pp. 41–55, 2010.

[83] S. J. Rind, Y. Ren, Y. Hu, J. Wang, and L. Jiang, "Configurations and control of traction motors for electric vehicles: A review," *Chinese Journal of Electrical Engineering*, vol. 3, no. 3, pp. 1–17, 2017.

[84] R.Krishnan, *Electric Motor Drives Modeling, Analysis, and Control*. Prentice Hall of India, 2002.

[85] P. C. Krause, O. Wasynczuk, S. D. Sudhoff, and S. Pekarek, *Analysis of electric machinery and drive systems*. Wiley Online Library, 2002, vol. 2.

[86] B.K.Bose, *Modern Power Electronics and AC Drives*. Prentice Hall, New Jersey., 2002.

[87] H. C. Stanley, "An analysis of the induction machine," *Electrical Engineering*, vol. 57, no. 12, pp. 751–757, 1938.

[88] G. Shen, X. Zhu, J. Zhang, and D. Xu, "A new feedback method for pr current control of lcl-filter-based grid-connected inverter," *IEEE Trans. Ind. Electron.*, vol. 57, no. 6, pp. 2033–2041, 2010.

[89] N. He, D. Xu, Y. Zhu, J. Zhang, G. Shen, Y. Zhang, J. Ma, and C. Liu, "Weighted average current control in a three-phase grid inverter with an lcl filter," *IEEE Trans. Power Electron.*, vol. 28, no. 6, pp. 2785–2797, 2012.

[90] H. Le-Huy, "Comparison of field-oriented control and direct torque control for induction motor drives," in *Conference record of the 1999 IEEE industry applications conference. Thirty-forth IAS annual meeting (Cat. No. 99CH36370)*, vol. 2. IEEE, 1999, pp. 1245–1252.

[91] M. P. Kazmierkowski, L. G. Franquelo, J. Rodriguez, M. A. Perez, and J. I. Leon, "High-performance motor drives," *IEEE Ind. Electron. Magazine*, vol. 5, no. 3, pp. 6–26, 2011.

[92] O. Hegazy, R. Barrero, J. Van Mierlo, M. El Baghdad, P. Lataire, and T. Coosemans, "Control, analysis and comparison of different control strategies of electric motor for battery electric vehicles applications," in *2013 15th European Conference on Power Electronics and Applications (EPE)*. IEEE, 2013, pp. 1–13.

[93] A. M. Trzynadlowski, *The field orientation principle in control of induction motors*. Springer Science & Business Media, 2013.

[94] B. K. Bose, *Power electronics and motor drives: advances and trends*. Elsevier, 2010.

[95] K. Chau, *Electric vehicle machines and drives: design, analysis and application*. John Wiley & Sons, 2015.

[96] K. Bouhoune, K. Yazid, M. S. Boucherit, and M. Menaa, "Fuzzy logic-based direct torque control for induction machine drive," in *2017 25th Mediterranean Conference on Control and Automation (MED)*. IEEE, 2017, pp. 577–582.

[97] K. Bouhoune, K. Yazid, and M. S. Boucherit, "Ann-based dtc scheme to improve the dynamic performance of an im drive," in *7th IET Int. Conf. Power Electron., Machines and Drives (PEMD 2014)*, 2014, pp. 1–6.

[98] J. Rodriguez, M. P. Kazmierkowski, J. R. Espinoza, P. Zanchetta, H. Abu-Rub, H. A. Young, and C. A. Rojas, "State of the art of finite control set model predictive control in power electronics," *IEEE Trans. Ind. Informat.*, vol. 9, no. 2, pp. 1003–1016, 2012.

[99] F. Wang, Z. Zhang, S. A. Davari, R. Fotouhi, D. A. Khaburi, J. Rodríguez, and R. Kennel, "An encoderless predictive torque control for an induction machine with a revised prediction model and efosmo," *IEEE Trans. Ind. Electron.*, vol. 61, no. 12, pp. 6635–6644, 2014.

[100] Y. Cho, Y. Bak, and K.-B. Lee, "Torque-ripple reduction and fast torque response strategy for predictive torque control of induction motors," *IEEE Trans. Power Electron.*, vol. 33, no. 3, pp. 2458–2470, 2017.

[101] C. Schauder, "Adaptive speed identification for vector control of induction motors without rotational transducers," in *Conference Record of the IEEE Ind. Appl. Society Annual Meeting,*. IEEE, Oct. 1989, pp. 493–499.

[102] V. Ambrozic, G. Buja, and R. Menis, "Band-constrained technique for direct torque control of induction motor," *IEEE Trans. Ind. Electron.*, vol. 51, no. 4, pp. 776–784, Aug. 2004.

[103] T. Noguchi, M. Yamamoto, S. Kondo, and I. Takahashi, "Enlarging switching frequency in direct torque-controlled inverter by means of dithering," *IEEE Trans. Ind. Appl.*, vol. 35, no. 6, pp. 1358–1366, 1999.

[104] N. R. N. Idris and A. H. M. Yatim, "Direct torque control of induction machines with constant switching frequency and reduced torque ripple," *IEEE Trans. Ind. Electron.*, vol. 51, no. 4, pp. 758–767, 2004.

[105] A. E. M. Ehsani, Y. Gao, *Modern Electric, Hybrid Electric, and Fuel Cell Vehicles*. CRC Press, 2011.

[106] X. Zhang and W. Qu, "A novel compensation method of stator flux estimation in low speed region," in *Sixth Int. Conf. on Electr. Machines Syst., 2003. ICEMS 2003.*, 2003.

[107] S. J. Chapman, *Electrical Machinery Fundamentals*. McGraw-Hill, 2005.

[108] A. Dalal and P. Kumar, "Analytical model for permanent magnet motor with slotting effect, armature reaction and ferromagnetic material property," *IEEE Trans. Magn.*, vol. PP, no. 99, pp. 1–1, 2015.

[109] B. Zhang, Q. Ge, Q. Chang, and S. Zhang, "Research on a sensorless svm-dtc strategy for induction motors based on modified stator model," in *2014 9th IEEE Conf. Ind. Electron. Appl.* IEEE, 2014, pp. 1724–1729.

[110] J.-H. Kim, J.-W. Choi, and S.-K. Sul, "Novel rotor-flux observer using observer characteristic function in complex vector space for field-oriented induction motor drives," *IEEE Trans. Ind. Appl.*, vol. 38, no. 5, pp. 1334–1343, 2002.

[111] D. Casadei, G. Serra, A. Tani, and L. Zarri, "A robust method for flux weakening operation of dtc induction motor drive with on-line estimation of the break-down torque," in *2005 European Conf. on Power Electron. Appl.*, Sept. 2005, pp. 10 pp.–P.10.

[112] J.-H. Choi, J.-H. Shin, and Y.-S. Kim, "The efficiency optimization control of an indirect vector-controlled induction motor drive," in *Proceedings of the KIEE Conference*. The Korean Institute of Electrical Engineers, 2000, pp. 352–354.

[113] M. H. Rashid, *Power Electronics: Circuits, Devices & Applications*. Prentice Hall, 2014.

[114] U. R. Chinthakunta, K. K. Prabhakar, A. K. Singh, and P. Kumar, "Direct torque control induction motor drive performance evaluation based on torque error status selection methods," *IET Electr. Syst. Transp.*, vol. 9, pp. 113–127(14), September. 2019. [Online]. Available: https://digital-library.theiet.org/content/journals/10.1049/iet-est.2018.5005